

UNIVERSITÉ DU QUÉBEC

THÈSE PRÉSENTÉE À
L'UNIVERSITÉ DU QUÉBEC À TROIS-RIVIÈRES

COMME EXIGENCE PARTIELLE
DU DOCTORAT EN GÉNIE PAPETIER

PAR
DANIEL MATTE

PRECOAT'S INFLUENCE ON TOPCOAT'S PHYSICAL
PROPERTIES AND PRINTABILITY

Février 2012

Université du Québec à Trois-Rivières

Service de la bibliothèque

Avertissement

L'auteur de ce mémoire ou de cette thèse a autorisé l'Université du Québec à Trois-Rivières à diffuser, à des fins non lucratives, une copie de son mémoire ou de sa thèse.

Cette diffusion n'entraîne pas une renonciation de la part de l'auteur à ses droits de propriété intellectuelle, incluant le droit d'auteur, sur ce mémoire ou cette thèse. Notamment, la reproduction ou la publication de la totalité ou d'une partie importante de ce mémoire ou de cette thèse requiert son autorisation.

UNIVERSITÉ DU QUÉBEC À TROIS-RIVIÈRES**DOCTORAT EN GÉNIE PAPETIER (Ph.D.)**

Programme offert par l'Université du QUÉBEC À TROIS-RIVIÈRES

**PRECOAT'S INFLUENCE ON TOPCOAT'S PHYSICAL PROPERTIES AND
PRINTABILITY****INFLUENCE DE LA PRÉ-COUCHE SUR LES PROPRIÉTÉS PHYSIQUES ET
D'IMPRESSION DE LA COUCHE SUPÉRIEURE****PAR****Daniel Matte**

Claude DANEULT

Directeur de recherche

Université du Québec à Trois-Rivières

Bruno CHABOT

Président du jury

Université du Québec à Trois-Rivières

Patrice MANGIN

Co-directeur de recherche

Université du Québec à Trois-Rivières

Jean-Philippe BOISVERT

Évaluateur externe

Centre de recherche Lafarge,
St-Quentin Fallavier, France

François BERTRAND

Évaluateur externe

École Polytechnique de Montréal,
Département de génie chimique

Thèse soutenue le 20 décembre 2011

Preface

The objective of present thesis is to verify the possibility to establish interactions between different properties of the precoat and/or topcoat layers in order to relate these properties to printability. To reach the thesis objective we designed an experiment based on the analysis of various groups of coated samples. The study is divided in 4 different groups representing for each one a different precoat, coating layer, pigment-latex, and calendering combinations.

The first group (Group 1) is used to study the replacement of 20 parts of GCC (Ground Calcium Carbonate; 1.4 μm average particle size) by 4 clays of different average particle size. The second group (Group 2) serves to study the calendering effect on the base paper or on the precoated layer. Two temperature conditions combined with 2 different pressures for a total of 8 conditions are included in Group 2. The third group (Group 3) has only 2 conditions: for the first condition, the latex S/B (Styrene/Butadiene) is replaced by an acrylic in the precoat; for the second condition, the CMC (Carboxy Methyl Cellulose) is replaced by an amphoteric protein. Finally, the last group (Group 4) is used to study what occurs when the GCC pigment is totally replaced in the precoat formulation by other pigments. Group 4 has five different formulations: one with PCC (Precipitated Calcium Carbonate), one with Brazilian Clay and 3 with GCC different particle size and different particle size distribution. The topcoat applied over each of these 20 precoat conditions is exactly the same.

The latex is changed for the topcoat using 3 different latexes for a total of 60 conditions. The latexes used are Styrene/Butadiene/Acrylonitrile (S/B/ACN), Styrene/Acrylic (S/A), Styrene/Acrylic/ Acrylonitrile (S/A/ACN). All these conditions are analyzed for pore structure, contact angle, SEM (Scanning electron microscopy), and offset printability test (DELTACK).

Acknowledgements

My first thoughts go to my family who believed in me from the very beginning of this project. Their support and help were a huge part in supporting me to successfully complete such a huge undertaking. I want to thank all my family members, my wife Johanne, and my children Kathleen, Marilyn, Pier-Luc, and Jean-Christophe, for their support and their good comments during all the time and the long hours I worked on my thesis.

Big thanks are due to Professors Claude Daneault and Patrice Mangin for their comments, support, and help. Without them, I would certainly have not been able to complete the work in its present form. They showed me various ways to improve myself in this “adventure”. Very special thanks are due to Patrice Mangin for the time he spent with me to re-write and re-organise the document, and to teach me how to analyse data in further depth, with a scientific mind, before reaching the final defence of the thesis. All his comments and suggestions surely improved this document to a high scientific level.

I also want to thank Centre International de Couchage (CIC) and the people at CIC for their support and their help. Thanks are due to Omya Development AG for the great support offered, especially for all the testing performed on my behalf, and finally thanks are due to Kamin LLC for allowing me to utilise some results from their trials.

Very special thanks are due to Nancy Jacob, CIC for all the data compilation and her patience with the changes in the direction of my research. Special thoughts are conveyed to Charlie Mazza, CIC, and Patrice Mangin, CIPP/UQTR for their help in improving the English structure of my document.

The author also wishes to thank Dr Patrick Gane and Dr Cathy Ridgway, Omya Development AG for their help and support in the mercury testing and their useful comments on the different methods. Discussions were particularly valuable in conducting and preparing the research work and strategy. Their input is very much appreciated.

The last words and thanks go for all the persons listed below who helped me in different ways and at different times during the project, namely:

Joseph Ishley	for comments on the English document,
Sylvie St Amour	for mercury intrusion and CLC testing,
Sylvie Sauriol	for CLC testing and printability measurements,
Martin Dubé	for profilometry, mathematical and pore analysis,
Agnès Lejeune	for Scanning Electron Microscopy (SEM) wonderful pictures,
Josée Doucet	for contact angle measurement,
Amy Dimmick	for comments and corrections on the English document, and
Robert Lanouette	for PLS analysis, comments, and useful discussions.

February 2012

Résumé en français

La fabrication du papier enduit ou papier couché connaît des développements importants depuis une vingtaine d'années. Une partie de ces développements concerne les papiers enduits de plus d'une couche, communément appelés «*papier multicouches*.» Durant toutes ces années, la caractérisation de la structure des couches, les unes par rapport aux autres, n'a fait l'objet que de quelques études qui traitaient principalement de la couche finale appliquée sur le papier. L'influence de la pré-couche sur les caractéristiques finales d'impression n'a quant à elle pratiquement jamais été abordée de façon fondamentale. Une étude sur les interactions entre les couches pour un carton de pâte kraft blanchie mentionne l'effet de la pré-couche mais aucune étude systématique ne traite le papier sans bois (wood free).

L'objectif premier de ce travail a donc été de déterminer et de comprendre l'effet de la pré-couche sur les caractéristiques finales d'impression de la feuille. Pour ce faire, vingt (20) différentes conditions de préparation de pré-couche ont été analysées avant d'y appliquer trois types d'enduits de surface différents. Les différentes conditions d'application des pré-couches ont été réalisés sur une coucheuse pilote selon des conditions d'opération industrielles normales pour ce type de papier. L'application de la couche supérieure a été réalisée sur un équipement de laboratoire qui reproduits des conditions industrielles d'opérations : le CLC pour «*Cylindrical Laboratory Coater*». L'impression de type offset des papiers ainsi préparés a été faite à l'aide d'un appareil Prüfbau adapté pour la mesure du maximum de tirant lors de la prise d'encre (DELTACK). Les structures ont été déterminées par intrusion au mercure et par microscopie électronique à balayage complétée par des mesures d'angle de contact. Outre les mesures normalisées sur les propriétés des papiers, ces mesures ont servi à évaluer les propriétés structurelles et de surface des papiers en vue de l'analyse et de la compréhension des comportements des différentes pré-couches d'un point de vue structurel.

Le support de couche utilisé est un papier sans bois avec un grammage ou poids de base de 61 g/m², soit le papier commercial «*Thermal Transfert*» (Fraser Paper Company). Quatre différents groupes de papiers pré-couchés ont été produits en usine pilote afin

d'obtenir une qualité et une stabilité jugées primordiales avant l'application en laboratoire à l'aide du CLC d'une couche finale ou couche supérieure, au-dessus de la pré-couche. Toutes les formulations de pré-couche ont été ajustées à une concentration de départ de 66 % avec cependant parfois une dilution additionnelle afin de permettre une application de qualité lors de la production en usine pilote. La pré-couche de 12 g/m² par côté, le côté rugueux étant couché en premier, a été appliquée avec la station de couchage jet/lame de la coucheuse pilote. La vitesse de la coucheuse était de 1400 m/min et la lame choisie pour le contrôle de poids de couche correspondait à une nomenclature industrielle « 0.457 mm / 84 mm / 45° » (dimension et angle de la lame d'application).

Pour chacune des conditions expérimentales de l'étude, les tests d'intrusion au mercure ont été effectués sur le support de couche, sur le papier pré-couché, sur le papier double couche pré-couché et couché et sur le papier double couche calandré. L'objectif final de ces analyses était d'obtenir les renseignements sur la partie couchée, pré-couche et couche supérieure, uniquement. En effet, lorsque le test est effectué, la structure complète de la feuille est analysée, soit le support de couche et les deux couches. Une caractéristique spécifique de cette étude est d'avoir utilisé une particularité du programme Autopore® de la mesure d'intrusion au mercure pour optimiser l'analyse des données de la double-couche. En effet, le programme Autopore® permet de soustraire à l'analyse de porosité les données relatives à une mesure à vide du bulbe contenant l'échantillon afin de tenir compte de l'expansion du bulbe sous l'effet de la pression d'intrusion ainsi que du tube indiquant le volume d'intrusion lors du test à haute pression. Nous avons utilisé cette particularité afin de « retrancher » les données de porosité du papier support de couche en le considérant alors comme une valeur de porosité de base ou une porosité hors étude « à enlever » pour faciliter l'analyse de la pré-couche. Ainsi, il devenait possible de conserver uniquement les valeurs reliées directement à la pré-couche sans une distorsion qui serait causée par le support de couche. La même procédure a été appliquée pour la couche supérieure et la couche calandree afin de pouvoir isoler les résultats pertinents pour chacune des composantes expérimentales au niveau de la structure de la feuille. Cette nouvelle méthode, avec ses limites (la mesure étant destructive, ce n'est jamais « exactement le même échantillon de papier » qui peut être évalué avant et après couchage ou calandrage), permet cependant d'isoler chacune des couches les unes des

autres en plus d'avoir une vue d'ensemble complète de la structure étudiée. Il devient alors plus facile d'analyser les résultats des traitements mécaniques ou modifications appliqués.

Le tableau suivant présente la liste de toutes les conditions qui composent les 4 groupes de l'étude, conçus avec pour objectif principal l'étude des différentes modifications de la pré-couche, soit : (1) 20 parties de substitution de kaolin de la pré-couche, (2) pré-calandrage du support de couche et de la pré-couche, (3) substitution du latex et de l'épaississant de la pré-couche et (4) 100 parties de substitution du/des pigments de la pré-couche. Nous avons choisi de présenter dans ce sommaire étendu en plus en détail les résultats et l'analyse effectués lors de la substitution de 20 parties de kaolin dans la pré-couche (groupe 1) et seulement une brève conclusion pour chacun des trois autres groupes. Ce choix a été fait afin de démontrer comment sont présentés et analysés les résultats tout en préservant le modèle du résumé en français.

Dans le groupe 1 qui comporte 4 conditions de substitution de 20 parties de kaolin par des pigments de différentes grosseurs de particules et de forme, la recette « standard » ou de base pour la pré-couche, aussi valable pour l'ensemble de l'étude, comprend 100 parties de GCC (1,4 μm). Pour ce groupe 1, les kaolins de substitution sont : un kaolin No.1 (brillance élevée, particule fine de dimension moyenne 0.469 μm), un kaolin No.2 (brillance régulière, dimension 2.13 μm), un kaolin grossier délaminé (brillance régulière, dimension 5.312 μm) et un kaolin d'ingénierie grossier (rapport longueur/épaisseur élevé, dimension 6.329 μm). L'analyse des résultats du groupe 1 démontre que substituer 20 parties de kaolin dans une formulation contenant 100 parties de GCC dans la formulation de la pré-couche permet de moduler la structure de la pré-couche et d'obtenir les propriétés d'impression désirées. De la même façon, nous avons montré que l'absorption capillaire, le mouvement préférentiel de divers éléments de la pré-couche et de la couche ou la pénétration forcée des liquides de la couche supérieure dans la pré-couche sont des mécanismes potentiels pour expliquer comment la structure de la couche supérieure est modifiée par la présence de la pré-couche. Nous avançons de plus l'hypothèse que la pénétration forcée ou une partie de celle-ci est probablement causée par le remouillage de la pré-couche lorsqu'une couche y est appliquée par-dessus.

Tableau Formulations de pré-couches reliées à chacun des groupes de l'étude.

Formulations de pré-couche	Groupe	Nombre de formulations
100 parties GCC (1.4 μm)	Contrôle	3 couches = 3 échantillons
20 parties de kaolin No. 1 - Brillance élevée et particule	Groupe 1 20 parties de substitution de kaolin	3 couches x 4 pré-couches = 12 conditions
20 parties de kaolin No. 2 - Brillance régulière (2.13 μm)		
20 parties de kaolin grossier délaminé (5.312 μm)		
20 parties de kaolin d'ing. grossier -facteur de forme élevé (6.329 μm)		
Support de couche calandré 100°C - 50 kN/m	Group 2 Pré-calandrage du support de couche et de la pré-couche	3 couches x 4 calandrage du support de couche et 4 calandrage de la pré-couche = 24 conditions
Support de couche calandré 100°C - 200 kN/m		
Pré-couche calandree 100°C - 50 kN/m		
Pré-couche calandree 100°C - 200 kN/m		
Support de couche calandré 200°C - 50 kN/m		
Support de couche calandré 200°C - 200 kN/m		
Pré-couche calandree 200°C - 50 kN/m		
Pré-couche calandree 200°C - 200 kN/m		
Pré-couche 100 parties GCC (1.4 μm) + Latex acrylique	Groupe 3 Substitution S/A + Protéine	3 couches x 2 pré-couches 6 = conditions
Pré-couche 100 parties GCC (1.4 μm) + Protéine		
100 parties BPSD GCC (0.659 μm)	Group 4 Substitution de 100 parties de pigment	3 couches x 5 pré-couches = 15 conditions
100 parties BPSD GCC (0.3598 μm)		
100 parties PCC (0.499 μm)		
100 parties de kaolin brésilien (0.548 μm)		
100 parties NPSD GCC (0.6593 μm)		

BPSD= pigment avec une distribution de particules larges

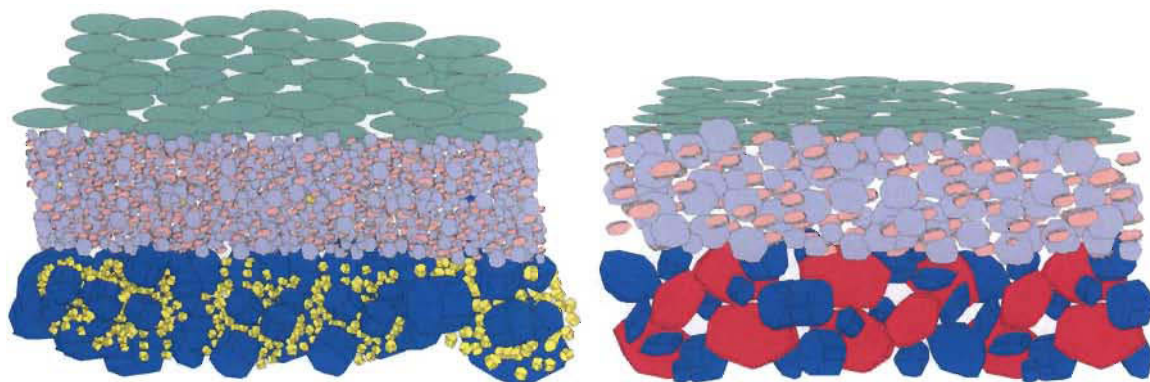
NPSD= pigment avec une distribution de particules étroites

Une autre conclusion clé de notre étude est d'avoir mis en évidence l'importance des différents types de latex utilisés pour la fabrication de la couche supérieure dans la prise d'encre (cf. l'analyse des propriétés d'impression DELTACK). Le latex avec une base de butadiène résulte toujours en une force maximale de triant d'encre plus élevé que pour le latex à base d'acrylique. Les deux latex à base d'acrylique utilisés dans la fabrication de la couche supérieure ont un comportement similaire sur la prise d'encre comme il est possible de le déduire sur l'analyse de courbes DELTACK d'aspect similaire. Finalement, nous avons montré qu'il est possible d'obtenir la même prise d'encre avec

des structures poreuses très différentes. Les deux situations observées sont (a) le cas de structures avec des volumes de pores identiques mais des diamètres de pores moyens très différents ou (b) le cas de volumes de pores très différents avec des diamètres moyens de pores identiques.

Nous avons proposé un mécanisme fondamental qui permet d'expliquer simplement ce phénomène particulier sur la base des changements dans la structure de la couche ayant pour origine les différentes pré-couches utilisées. De façon globale, les changements structuraux que l'on retrouve dans un complexe de structure pré-couche/couche sont en mesure de modifier comment l'encre et/ou les solvants de l'encre pénètrent préférentiellement à l'intérieur des deux différents types de structure, le tout résultant en des compositions finales du film d'encre très différentes. Le film d'encre peut être épais ou mince mais cependant posséder la même force de tirant reliée à la prise d'encre dans des structures différentes.

L'illustration suivante permet de visualiser le mécanisme proposé pour la fixation de l'encre dans les 2 cas. Elle représente l'épaisseur du film d'encre en relation avec une force de tirant maximum égale et la structure de la pré-couche : structure de pré-couche fermée à gauche et ouverte à droite démontrant la possibilité de filtration/pénétration préférentielle des composantes de l'encre.



Bas = pré-couche / milieu = couche/ dessus = film d'encre (vert)

Le groupe deux (2) de notre étude a été conçu afin de vérifier l'effet du pré-calendrage du support de couche et de la pré-couche sur un papier double-couche basé sur l'hypothèse que ce pré-calendrage pouvait affecter la structure supérieure sur la base d'effets physiques de pénétration des fluides vus pour la prise d'encre mais ici appliqués à la pré-couche ou à la couche supérieure. Pour toutes les conditions, le pré-calendrage résulte en une diminution de la dimension des pores et conséquemment, d'une réduction du volume total de pores lorsque comparé à la condition de contrôle qui n'a subi aucun pré-calendrage. L'analyse des courbes de distribution des pores n'a cependant pas permis d'identifier de tendance généralisable pouvant expliquer comment une structure double-couche pouvait être affectée par le pré-calendrage. Par contre, l'analyse du volume total de pores a montré des tendances généralisables en ce qui concerne les effets de température ou de pression; ce qui s'avère un outil puissant pour comprendre comment le pré-calendrage peut modifier les structures de papier double-couche.

En effet, nous avons trouvé que le pré-calendrage à 100°C résulte en un volume de pores de la structure de la pré-couche plus élevé que lors d'un pré-calendrage à 200°C. Comme anticipé, le pré-calendrage à 200 kN/m produit quant à lui un volume de pores total plus faible que le pré-calendrage à 50 kN/m. Les résultats obtenus pour la structure de la couche sont plus surprenants et ce, pour le pré-calendrage du support de pré-couche et de la pré-couche elle-même. Nous avons observé deux effets qui semblent *a priori* en opposition mais que nous avons pu expliciter simplement par transposition d'effet de filtration d'une structure à l'autre. En effet, (a) lorsque le support de couche a été pré-calendré, le volume total de la couche est plus élevé à 100°C qu'à 200°C, et (b) à l'opposé, lorsque la pré-couche a été pré-calendrée, le volume total de la couche est plus élevé à 200°C qu'à 100°C.

Le mécanisme que nous proposons afin d'expliquer de tels résultats en apparence contradictoire est basé sur la filtration et la compaction d'une structure qui survient lors des opérations de couchage, les effets étant dus au mouvement de l'eau et des matériaux constituants de la couche lorsqu'une couche humide est appliquée par-dessus une autre surface. Assurément, la surface d'une structure poreuse devient plus ou moins ouverte selon le calendrage appliqué et peut ainsi contrôler la filtration et la compaction. Le pré-

calandrage à haute température de la pré-couche a un impact direct sur la structure de la couche (fermeture des pores). Le pré-calandrage du support de couche a le même effet lorsque la pré-couche est appliquée mais la situation est nécessairement inversée lorsque la couche est appliquée; il y a donc transposition d'effet de filtration d'une couche à l'autre ou « effet domino ». En effet, considérant que le papier couché double-couche comporte trois couches, soit papier de base, pré-couche et couche supérieure : une structure de base (papier de base ou pré-couche) plus fermée rend par filtration préférentielle la couche supérieure plus ou moins ouverte avec un effet subséquent (« domino ») sur la couche supérieure finale. Finalement, nous expliquons qu'il est possible d'obtenir les mêmes caractéristiques d'impressions avec les différentes structures créées par pré-calandrage. Une fois encore, l'effet de la température du pré-calandrage est ici le facteur prédominant. En conclusion, nous avons donc pu montrer qu'il est possible de contrôler la microstructure et même la nanostructure (jusqu'à 30 nm) d'un papier double-couche par le pré-calandrage, et ainsi, qu'il est possible de contrôler les caractéristiques d'impressions des papiers double-couches.

Concernant l'utilisation de protéine ou de latex S/A dans la pré-couche en substitution d'une combinaison initiale S/B+CMC (groupe 3), la conclusion générale est que cette pratique n'apporte pas d'avantages significatifs, spécialement pour la substitution du latex S/A. Par contre, dans le cas de la substitution du CMC par la protéine, nous avons pu montrer que la protéine change la structure en élargissant la distribution des pores de la pré-couche. Il serait par contre hasardeux de généraliser les avantages de l'utilisation de ce produit car une seule condition a été réalisée. Une étude plus approfondie impliquant d'autres conditions expérimentales serait nécessaire pour de futurs travaux. Les résultats d'impression n'ont quant à eux apporté aucune conclusion qui soit différente des autres conditions des autres groupes d'étude.

Concernant la substitution de 100 parties de pigment (groupe 4) de la pré-couche, l'analyse effectuée nous permet de confirmer que la structure de la pré-couche influence grandement la structure finale d'un papier double couche. Nous avons observé entre autres l'importance clé de la distribution et le diamètre moyen de particules afin de déterminer comment ces facteurs influencent la structure globale constitué par l'ensemble

pré-couche/couche supérieure. Plus spécifiquement, nous avons trouvé et expliqué comment le volume de pores total est inversement proportionnel à la distribution des particules de pigment. Nous avons aussi montré que la surface totale des pores décroît avec la dimension de particules et qu'elle est inversement proportionnelle à la dimension de particules dans le cas de distribution de particules élargie. Finalement, nous avons confirmé notre hypothèse, à savoir que le diamètre moyen des particules est directement relié à la dimension du pigment utilisé dans la pré-couche.

En conclusion générale, nous avons proposé un mécanisme en deux phases, qui a pu être validé dans d'autres conditions au niveau de la formation de la pré-couche et de la couche supérieure pour expliquer comment la même force de tirant, résultant de prises d'encre donc de mécanismes d'absorption, pouvait être obtenue avec structures de couche très différentes. En effet, la filtration d'une encre ou d'une sauce de couchage est basée sur les mêmes mécanismes physiques. Concernant la prise d'encre, nous avons montré que, dans un cas, des volumes de pores similaires combinés à des diamètres de pores moyens très différents et, dans un autre cas, des volumes de pores passablement différents combinés à des diamètres moyens de pores similaires pouvait résulter en une même force de tirant maximum reliée au film d'encre transférée au papier double-couche. Le mécanisme proposé pour expliquer cet effet est basé sur la pénétration préférentielle des solvants de l'encre qui contrôle la prise d'encre ainsi que la variation du transfert de l'encre relié aux différentes structures de couche qui contrôle l'épaisseur du film d'encre : les deux ayant des effets opposés. La filtration de la sauce de couchage obéit quant à elle au même mécanisme.

Abstract

The main objective of present study was to establish how modification in the design and structure of the precoat in double-coated papers would control the final properties, mainly printing characteristics, of the double-coated paper. To achieve such an objective we needed first to develop different precoat structures based on commercially feasible and applicable practices and second to fine tune the mercury intrusion method to be able to differentiate sometimes minute but important structural differences brought about by modifications in the precoat formulation, application, and treatment.

Mercury intrusion is a well established method which is used extensively within the pulp and paper industry. The test provides a great deal of information to the papermaker about the paper and coating structure which may vary widely depending on the choice of materials used in the coated paper production. The mercury intrusion test has been shown to be invaluable in predicting or troubleshooting many areas such as blister resistance and printing issues. As mercury intrusion is time consuming and expensive, every effort must be made to ensure that the data collected is fully investigated and interpreted to take complete advantage of the information on pores structure and pores distribution.

The specifically designed method of mercury intrusion curves analysis was developed to examine and analyse a wide range of commercial operating conditions, including base paper calendering, different pigment and binder combinations. In essence, we determine cut-off values for the different sections of the mercury intrusion curves to be able to compare these curves on a same base-line. The mercury intrusion curves thus modified are designed as “normalized”.

Present study of double-coated layer structures focuses on the effect of the precoat portion of a double layer wood free coated paper. Many different precoat and surface treatment conditions are analyzed to verify, and understand the relationships between the various precoat combinations and printing characteristics in order to provide the best printability.

In the experimental design, 12 different precoat formulations and 8 calendering conditions are analysed. The pigment of the precoat varies for each of the 12 precoat, and consists of different pigments, including broad ground calcium carbonate, fine number one (#1) clay, delaminated clay, number 2 (#2) clay, structured clays, and fine precipitated calcium carbonate. The binder and additive system for all of the coatings are kept constant, with one exception where the latex is modified. The latex used for the majority of the coatings is standard styrene butadiene (S/B) latex.

Additionally, one selected precoat serves as a standard or reference. Eight different calendering iterations are used, i.e. calendering the base paper at four different temperature and pressure combinations, and calendering the precoat paper at 4 different temperature and pressure combinations. All of the precoat application and calendering is performed at a pilot scale at the Centre International de Couchage (CIC) in Trois-Rivières, Quebec, Canada. Each precoat is applied to both sides of the base paper by blade coating at 12 g/m².

Including the calendering iterations, there are then 20 total precoat conditions. Three different topcoats are applied to each precoat, bringing the total number of conditions examined to 60. The pigment slip and additive portion of the topcoats are kept constant, and only the latex varies. The three different latexes used are styrene-butadiene acrylonitrile (S/B/ACN), styrene acrylate (S/A), and styrene-acrylate acrylonitrile (S/A/ACN). The topcoats are applied to one side of the precoat paper at 12 g/m² via the laboratory CLC equipment. All these topcoats conditions are tested with the Prüfbau DELTACK and a curve of each condition is used to examine which conditions would have the best surfaces for offset printing.

Finally, we have proposed and validated a physical mechanism based on preferential filtration, structural rearrangement, and filtration domino effect of one structure to the next to explain how the precoat structure influences both the structure and the printing characteristics of the double-coated paper.

Keywords

English:

Coated paper, double-coated paper, precalendering, calendering, soft nip calendering, pilot coater, pigment, latex, filtration mechanisms, coating structure, layered structure, pigment packing, pore size, pore distribution, pore volume, micro-structure, nano-structure, printing characteristics, print quality, mercury intrusion, contact angle, Prüfbau DELTACK, microscopic evaluation, projection on latent structure (PLS), normalization method.

Français :

Papier couché, papier couché double-couche, pré-calandrage, calandrage, calandrage à pince molle, coucheuse pilote, pigment, latex, mécanismes de filtration, structure de la couche, structure stratifiée, empilement des pigments, tailles de pores, distribution des pores, volume des pores, microstructure, nanostructure, caractéristiques d'impression, qualité d'impression, intrusion au mercure, angle de contact, Prüfbau DELTACK, évaluation microscopique, projection sur structure latente (PLS), méthode de normalisation.

Table of Contents

Preface	iii
Acknowledgements	iv
Résumé en français	ii
Abstract	x
Keywords	xii
Table of Contents	xiii
List of Figures	xvii
List of Tables.....	xxiv
List of Equations	xxvi
List of Appendix	xxviii
Abbreviations and Symbols	xxix
Abbreviations.....	xxix
Symbols	xxxii
Chapter 1 - Introduction.....	35
Chapter 2 - Literature review	36
2.1 Paper (Base stock)	37
2.2 Pigments and latex	39
2.2.1 Clay.....	43
2.2.2 Calcium Carbonate	45
2.2.3 Latex	47
2.3 Calendering.....	54
2.4 Multilayer coated paper	59
2.5 Conclusions and implications	61

Chapter 3 - Discussion and analysis of the characterization methods	64
3.1 Introduction.....	64
3.2 Contact angle method	67
3.2.1 Contact angle theory	69
3.2.2 Contact angle: test description.....	70
3.3 Mercury intrusion	71
3.3.1 Darcy's Law.....	71
3.3.2 Washburn Equation	72
3.3.3 Mercury porosimetry	74
3.3.4 Further considerations on liquid penetration of complex structures.....	75
3.4 Equipment and methods – Mercury intrusion.....	77
3.4.1 Repeatability of the mercury intrusion test.....	81
3.5 Normalisation and optimization of the mercury intrusion data analysis.....	83
3.5.1 The hexadecane imbibition method and analysis	83
3.5.2 Coating layer cut off point.....	86
3.5.3 Separation of the precoat and the topcoat layers	90
3.6 Mercury Intrusion normalisation method	93
3.7 Scanning Electron Microscopy (SEM)	106
3.8 Prüfbau DELTACK method	108
3.8.1 Description of the method	108
3.8.2 DELTACK curve analysis.....	111
3.8.3 Maximum in ink tack force.....	112
Chapter 4 - Experimental design.....	114
4.1 Experimental levels selection	114
4.2 Precoated paper roll preparation	116
4.3 Top Coated Samples	118
4.3.1 Control of the top coat weight for the CLC samples.....	119
4.4 Calendering the top coated samples.....	120
Chapter 5 - Results and Analysis	121
5.1 Introduction.....	121

5.2	Effects of 20 parts clay substitution in the precoat layer (Group 1)	123
5.2.1	Analysis of the precoat and topcoat structures: 20 parts clay substitution (Group 1).....	123
5.2.1.1	Analysis of the precoat and topcoat structure through pore size distribution.....	123
5.2.1.2	Influence of the precoat (20 parts substitution) on the topcoat/precoat combined structure	126
5.2.1.3	Influence of the precoat structure (20 parts substitution) on the topcoat structure	130
5.2.2	Printability variations related to 20 parts clay substitution in the precoat (Group 1).....	134
5.2.3	Contact Angle results comparison from Group 1 (20 parts clay substitution).....	141
5.2.4	Summary: 20 parts substitution in the precoat layer (Group 1).....	143
5.3	Effect of calendering the base stock or the precoat layer (Group 2)	144
5.3.1	Analysis of the precoat and topcoat structures: calendering base paper and precoated layer (Group 2)	145
5.3.1.1	Analysis of the precoat and topcoat structure through pore size distribution.....	146
5.3.2	Printability variations related to precalendering the base stock or the precoat layer (group 2).....	154
5.3.3	Summary: base paper and precoated layer calendering group (Group 2)	155
5.4	Effect on Styrene/Acrylic and Protein substitution in precoat layer (Group 3).....	157
5.4.1	Analysis of the precoat and topcoat structures through pore size distribution: Styrene/Acrylic and Protein substitution (Group 3)	157
5.4.2	DELTACK results comparison from Group 3 (SA latex and protein substitution).....	164
5.4.3	Summary: Latex and thickener substitution in precoat layer (Group 3)	168
5.5	Effect on 100 parts substitution in the precoat layer (group 4)	168
5.5.1	Analysis of the uncalendered precoat and topcoat structures, pore size distribution: 100 parts precoat pigment substitution (group 4).....	169

5.5.2	Analysis of the calendered precoat and topcoat structures total pore volume, total pore area, and average pore diameter: 100 parts precoat pigment substitution (group 4).....	173
5.5.3	DELTACK results comparison from Group 4 (100 parts pigments substitution).....	175
5.5.4	Summary: 100 parts substitution in the precoat layer (Group 4).....	179
5.6	DELTACK and ink tack comparison of Groups and latex – Average Curves	179
5.7	Projection on a Latent Structure (Partial least Square) Study	185
5.7.1	General presentation of the PLS method	185
5.7.2	PLS Results.....	188
5.7.3	PLS Study for 2 components - Effect of precoat pore volume on the final results.....	189
5.7.4	Effect of the latex.....	190
5.7.5	PLS study for 3 components.....	193
5.7.6	PLS study for 4 components.....	194
	Chapter 6 - Conclusion.....	201
	Bibliography.....	207
	Appendix	216
	Appendix 1	216
	Appendix 2	219
	Appendix 3	226

List of Figures

Figure 2-1	A MSP (left) and blade (right) coated ULWC paper, where a 28 g/m ² wood containing base paper is coated with 5 g/m ²	39
Figure 2-2	Scanning electron microscopy of talc	41
Figure 2-3	Pore size comparison for large and small particle size pigments	42
Figure 2-4	Packing efficiency of pigments with two different particle size diameter	43
Figure 2-5	Packing efficiency for a platy and blocky pigments.....	44
Figure 2-6	Coating layer structure with high aspect ratio clay.....	44
Figure 2-7	Packing efficiency of precipitated calcium carbonate compared with a blocky pigment.....	45
Figure 2-8	Pore structure for a GCC with a broad particle size distribution.....	47
Figure 2-9	Pore structure for a PCC with a narrow particle size distribution	47
Figure 2-10	Glass transition temperature (T _g) related to the level of styrene in the latex	50
Figure 2-11	Film forming during drying process for two different T _g	51
Figure 2-12	Effect of the calendering on the pore structure	55
Figure 2-13	Water movement for a platy pigment for an uncalendered (left) and calendered (right) coating layer.....	57
Figure 2-14	Double coated paper and base stock	59
Figure 3-1	Water drop with an angle lower than 90° (left) and greater than 90° (right).....	67
Figure 3-2	Contact angle θ between a substrate and a liquid	68
Figure 3-3	Droplet of non-wetting liquid on solid surface.....	69
Figure 3-4	Droplet on a solid surface at various absorption stages: (a) initial deposition, (b) during absorption, and (c) at equilibrium, end of the absorption.	70
Figure 3-5	Droplet deposit, measurement and final results for angle lower (left) and greater (right) than 90°	71
Figure 3-6	Wetting and non-wetting fluid in a capillary	73
Figure 3-7	Mercury Intrusion equipment	78
Figure 3-8	Sample holder with his stem mounted for the mercury intrusion test	79
Figure 3-9	Paper sample set up for the mercury intrusion test.....	80
Figure 3-10	Paper sample in his penetrometer	81

Figure 3-11	Mercury intrusion curves with samples from the same piece of paper.....	82
Figure 3-12	Example of surface defect affecting the mercury intrusion volume	84
Figure 3-13	Hexadecane absorption by a base paper sample	85
Figure 3-14	Mercury intrusion curves without normalization.....	88
Figure 3-15	Base paper pore structure with coating structure	88
Figure 3-16	Mercury intrusion curves with base paper blank – cut off point for coating	89
Figure 3-17	Base paper pore structure with coating structure	89
Figure 3-18	Precoated subtraction for the coating structure.....	91
Figure 3-19	Example of curves with the precoat used as blank in the Autopore program	92
Figure 3-20	Top coating layers for the 3 different latexes with condition 1	92
Figure 3-21	Top coating layers for Standard precoat-100 parts GCC (1.4 μm) and 20 parts clay substitution: High Glossing clay (0.469 μm), No. 2 clay (2.13 μm), delaminated clay (5.312 μm), and High Aspect Ratio clay (6.329 μm)	93
Figure 3-22	Reference file to store the results related to a condition.....	94
Figure 3-23	Screen to open the mercury intrusion file with the Autopore® program	95
Figure 3-24	Dialog box to choose the desired file to analyse	95
Figure 3-25	Mercury intrusion file while open with Autopore®	96
Figure 3-26	Mercury intrusion file after clicking on advanced button.....	97
Figure 3-27	Dialog boxes to obtain the results normalised for the base paper	99
Figure 3-28	Dialog boxes to obtain the results normalised for the precoated layer.....	100
Figure 3-29	Dialog boxes to obtain the results normalised for the uncalendered double coated paper	101
Figure 3-30	Dialog boxes to obtain the results normalised for the calendered double coated paper.....	102
Figure 3-32	Dialog box to start to generate excel spreadsheet with Autopore® program	103
Figure 3-33	Dialog box used to choose the .smp file to convert in excel spreadsheet	104
Figure 3-34	Dialog box to choose the reports to convert in excel file	105
Figure 3-35	Converted file	105

Figure 3-36	Save the document on excel spreadsheet form	106
Figure 3-37	Defect in the calendered coating layer	107
Figure 3-38	Defect generated by blade coating.....	107
Figure 3-39	SEM measurement equipment	108
Figure 3-40	DELTACK measurement instrument	110
Figure 3-41	Example of tack development from a DELTACK test curve.....	111
Figure 3-42	Example of a complete DELTACK curve.....	112
Figure 3-43	Truncated DELTACK Curve to fit the Polynomial Curve	113
Figure 3-44	DELTACK Curves means and polynomial curves fitting	113
Figure 4-1	Schematic of the experimental design	115
Figure 4-2	Styrene/Acrylic latex molecule.....	116
Figure 4-3-	Styrene/Butadiene latex molecule	116
Figure 4-4	Schematic representation of the cross section of the final paper samples produced for the study.....	119
Figure 5-1	Mercury Intrusion in Precoated layer – Precoat 20 parts clay substitution Group.....	124
Figure 5-2	Mercury Intrusion in Coating structure for condition with Standard Precoat - 100 parts GCC (1.4 μ m) - uncalendered	125
Figure 5-3	Mercury Intrusion in Topcoating Layer - 20 parts clay substitution group - S/B/ACN latex – uncalendered.....	127
Figure 5-4	Mercury Intrusion in Topcoating Layer - 20 parts clay substitution group - S/A latex – uncalendered	127
Figure 5-5	Mercury Intrusion in Topcoating Layer - 20 parts clay substitution group - Latex S/A/ACN – uncalendered	128
Figure 5-6	Total Pore Volume (TPV) Uncalendered Paper for Group 1 - Comparing the 3 latexes.....	129
Figure 5-7	Total Pore Volume (TPV) Calendered Paper for Group 1 - Comparing the 3 latexes.....	129
Figure 5-8	Average Pore Diameter (APD) Calendered Paper for Group 1 - Comparing the 3 latexes.....	130
Figure 5-9	Total Pore Volume (TPV) Topcoated layer for Group 1 as a function of the particle size of the precoat layer - Comparing the 3 latexes.....	131
Figure 5-10	Average Pore Diameter (APD) Topcoated layer for Group 1 as a function of the particle size of the precoat layer - Comparing the 3 latexes.....	133

Figure 5-11	Capillary theory related to smaller pores in the precoat. Topcoat: GCC is in purple-blue, clay in light red. Precoat: GCC is in orange and N°1 fine clay is in yellow.	133
Figure 5-12	Preferential movement theory related to bigger pores in the precoat. Topcoat: GCC is in purple-blue, clay in light red. Precoat: GCC is in orange and high aspect ratio clay is in grey.	134
Figure 5-13	DELTACK – 20% clay substitution Group, S/B/ACN latex.....	135
Figure 5-14	Time to reach the maximum force function of the maximum force	136
Figure 5-15	Total Pore Volume function Time to reach the maximum force	136
Figure 5-16	Ink film thickness related to an equal ink tack force and the precoat structure: close precoat structure (left) and open precoat structure (right).....	138
Figure 5-17	DELTACK maximum force versus total pore volume for 20 parts clay substitution group	139
Figure 5-18	DELTACK maximum force versus average pore diameter for 20 parts clay substitution group	140
Figure 5-19	Contact angle for Coated Paper– 20% clay substitution Group	142
Figure 5-20	Contact angle for calendered Paper– 20% clay substitution Group	143
Figure 5-21	Uncalendered (left) and calendered (right) base stock use in this study	145
Figure 5-22	Mercury Intrusion in Precoated layer – Base Paper and Precoat Calendered Group	146
Figure 5-23	Mercury Intrusion in Topcoated layer – Base Paper and Precoat Calendered Group Separated – S/B/ACN latex	148
Figure 5-24	Mercury Intrusion in Coating Structure – Base Paper and Precoat Calendered Group	151
Figure 5-25	Total pore volume (mL/g) for the standard reference (yellow), calendered base paper (blue) and precoat layer (purple) for the different pressures and 100°C used in calendering.....	152
Figure 5-26	Total pore volume (mL/g) for the standard reference (yellow), calendered base paper (blue) and precoat layer (purple) for the different pressures and 200°C used in calendering.....	153
Figure 5-27	DELTACK mean for each latex (8 calendering conditions)	154
Figure 5-28	Localisation of the dots for the precalendering, both base paper and precoat, at 100°C and 200°C for the S/B/ACN, S/A, and S/A/ACN latex	155
Figure 5-29	Mercury Intrusion in Precoating layer with 100 parts GCC (1.4 µm) –SA Latex and Amphoteric Thickener (protein).....	158

Figure 5-30	Mercury Intrusion in Coating structure for condition with 100 parts GCC (1.4 μm) and Acrylic Latex - uncalendered	160
Figure 5-31	Mercury Intrusion in Coating structure for condition with 100 parts GCC (1.4 μm) – Amphoteric Thickener (protein) – Uncalendered.....	160
Figure 5-32	Mercury Intrusion in Calendered Structure with 100 parts GCC (1.4 μm) –S/B/ACN Latex and Amphoteric Thickener (protein).....	161
Figure 5-33	Mercury Intrusion in Calendered Structure with 100 parts GCC (1.4 μm) –SA Latex and Amphoteric Thickener (protein)	162
Figure 5-34	Mercury Intrusion in Calendered Structure with 100 parts GCC (1.4 μm) –S/A/ACN Latex and Amphoteric Thickener (protein).....	162
Figure 5-35	Total Pore Volume (TPV) Coated Paper for Group 3 - Comparing the 3 latexes. Precoat: all 3 groups 100 parts GCC (1.4 μm and (A): SBR+CMC, (B): S/A+CMC, and (C) SBR+Protein.	163
Figure 5-36	DELTACK – S/A Precoating layer and protein Group, latex, S/B/ACN	165
Figure 5-37	DELTACK – S/A Precoating layer and protein Group, S/A latex	166
Figure 5-38	DELTACK – S/A Precoating layer and protein Group, latex, S/A/ACN latex	166
Figure 5-41	Mercury Intrusion in precoat layer – 100 parts substitution Group. The reference curve GCC is in red.....	170
Figure 5-42	Mercury Intrusion in Coating Structure layer – 100 parts substitution Group. Uncalendered samples.....	171
Figure 5-43	Mercury Intrusion in Topcoat Structure – 100 parts substitution Group – S/B/ACN latex. Uncalendered samples.	171
Figure 5-44	Mercury Intrusion in Topcoat Structure – 100 parts substitution Group – SA latex. Uncalendered samples.	172
Figure 5-45	Mercury Intrusion in Topcoat Structure – 100 parts substitution Group – S/A/ACN latex. Uncalendered samples.	172
Figure 5-46	Total Pore Volume (TPV) of the calendered precoat/topcoat structure for Group 4 - Comparing the 3 latexes. The samples are ordered in decreasing particle size distribution.....	174
Figure 5-47	Total Pore Area (TPA) Coated Paper for Group 4 - Comparing the 3 latexes. The samples are ordered in decreasing particle size distribution.	174
Figure 5-48	Average Pore Diameter (APD) Coated Paper for Group 4 - Comparing the 3 latexes. Samples are ordered as a function of the particle size.....	175

Figure 5-49 DELTACK mean for each latex (5 conditions – 100 parts substitution).....	176
Figure 5-50 DELTACK maximum force versus total pore volume for 100 parts pigments substitution group- all conditions	178
Figure 5-51 DELTACK maximum force versus average pore diameter for 100 parts pigments substitution group – all conditions.....	178
Figure 5-52 General DELTACK Comparison curves for the 3 latex.....	181
Figure 5-53 DELTACK Curve for the control precoating layer – 100 parts GCC (1.4 μ m)	182
Figure 5-54 DELTACK Average Curves for the 3 latexes for the 20 parts substitution Group.....	182
Figure 5-55 DELTACK Average Curves for the 3 latexes for the base paper and precoating layer calendering Group	183
Figure 5-56 DELTACK Average Curves for the 3 latexes for the Acrylic latex and Protein substitution Group	183
Figure 5-57 DELTACK Average Curves for the 3 latexes for the 100 parts substitution Groups - Carbonates	184
Figure 5-58 DELTACK average curves for the 3 latex – Brazilian clay	184
Figure 5-59 2 principal axis on a fish picture.....	186
Figure 5-60 Graphic showing 2 principal components, the best correlation with Y and the projection on a surface.....	187
Figure 5-61 PLS Regression – Projection graphic with the +/- 0.2 square low correlation area.....	188
Figure 5-62 Graphic projection for the Component 1 and 2 without precoated pore volume variable.....	191
Figure 5-63 Graphic projection for the Component 1 and 2 with precoated pore volume variable.....	191
Figure 5-64 PLS Result (2 Components) – Graphic for the 3 latex	192
Figure 5-65 PLS Result (2 Components) – Correlation factor R^2 projection graphic.....	192
Figure 5-66 PLS Result (3 Components) – Most important variables in order of their importance	194
Figure 5-67 PLS Result (3 Components) – Correlation factor R^2 projection graphic.....	194
Figure 5-69 PLS Result (4 Components) – Most important variables in order of their importance	196
Figure 5-70 PLS Result (4 Components) – Graphic projection for the Component 1 and 2 with precoated variable.....	196

Figure 5-71	PLS Result (4 Components) – Graphic projection for the Component 3 and 4 with precoated variable.....	198
Figure 5-72	PLS Result (4 Components) – Ink Tack Force	198
Figure 5-73	PLS Result (4 Components) – Time to get the maximum force with DELTACK	199
Figure 5-74	PLS Result (4 Components) – Pore Volume for uncalendered paper.....	199
Figure 5-75	PLS Result (4 Components) – Pore Volume for calendered paper	200
Figure 5-76	PLS Result (4 Components) – Contact Angle	200
Figure 6-3	DELTACK Average Curves for S/B/ACN latex, S/A latex and S/A/ACN, 100 parts GCC (1.4 μm).....	219
Figure 6-4	DELTACK – 20% clay substitution Group, S/B/ACN latex.....	219
Figure 6-5	DELTACK – 20% clay substitution Group, S/A latex	220
Figure 6-6	DELTACK – 20% clay substitution Group, S/A/ACN latex	220
Figure 6-7	DELTACK – Base Paper and Precoated layer Calendering Group, S/B/ACN latex	221
Figure 6-8	DELTACK – Base Paper and Precoated layer Calendering Group, S/A latex.....	221
Figure 6-9	DELTACK – Base Paper and Precoated layer Calendering Group, S/A/ACN latex	222
Figure 6-10	DELTACK – S/A Precoating layer and protein Group, latex, S/B/ACN	222
Figure 6-11	DELTACK – S/A Precoating layer and protein Group, S/A latex	223
Figure 6-12	DELTACK – S/A Precoating layer and protein Group, latex, S/A/ACN latex	223
Figure 6-13	DELTACK – 100% Pigment substitution Group, latex, S/B/ACN	224
Figure 6-14	DELTACK – 100% Pigment substitution Group, S/A latex	224
Figure 6-15	DELTACK – 100% Pigment substitution Group, S/A/ACN latex.....	225
Figure 6-16	Correlation using equation 6-2 and 6-3 and showing correlating latent factor.....	228

List of Tables

Table 2-1	Monomers used to make S/B latex	48
Table 2-2	Monomers used to make S/A latex	49
Table 2-3	Influence of different monomer latex composition on printing properties.....	49
Table 3-1	Repeatability of the mercury intrusion test.....	82
Table 3-2	Surface Tension (mN/m) and Contact Angle (°) of the chemicals used in this study	84
Table 3-3	Hexadecane test results BS 2007-1-1	85
Table 3-4	Base paper hexadecane and pore diameter cut off points.....	86
Table 3-5	Coating layers cut off points (larger pores)	90
Table 3-6	Autopore® files use to explain the mercury intrusion method. Related to BS1Latex1	93
Table 3-7	Prüfbau Instrument Settings for Sheet Offset and Web Offset.....	109
Table 3-8	Ink Test Settings for DELTACK Prüfbau test.....	109
Table 3-9	Prüfbau test settings	110
Table 4-1	Latex characteristics used in the study	115
Table 4-2	Precoated standard formulations and 20 parts substitution	117
Table 4-3	Calendering and Soft Nips Settings	117
Table 4-4	Precoat formulations – Latex and Amphoteric thickener	117
Table 4-5	Precoat formulations – 100 parts substitution.....	118
Table 4-6	Precoat Operation Parameters - Coater.....	118
Table 4-7	Topcoat Formulations used with the CLC	120
Table 4-8	Laboratory Calendering Conditions.....	120
Table 5-1	Precoated formulations related with the group and the condition number.....	122
Table 5-2	Conditions for the 20 parts clay substitution - Group 1	123
Table 5-3	Mean Contact Angle (°) values for Group 1 – Coated and Calendered Paper	143
Table 5-4	Conditions for the calendering group - Group 2.....	145
Table 5-5	Average volume structure (mL/g) for the precoat layer (Group 2)	147
Table 5-6	Average pore volume (mL/g) for the topcoat layer for each latex (Group 2).....	150

Table 5-7	Conditions for the S/A precoat latex and amphoteric thickener - Group 3	157
Table 5-8	Conditions for 100 parts substitution - Group 4	168
Table 5-9	Maximum ink tack force and time for all conditions for the 3 latexes used in this study.....	181
Table 5-10	Modeling structure related to the components used	189
Table 5-11	Correlation factor R^2 for 2 components – Results	191
Table 5-12	Correlation factor R^2 for 3 components – Results	193
Table 5-13	Correlation factor R^2 for 4 components – Results	195

List of Equations

$\frac{1}{Tg} = \frac{W_1}{Tg_1} + \frac{W_2}{Tg_2}$	Equation 2-1	51
$S = \gamma_s - \gamma_l - \gamma_{sl}$	Equation 3-1	67
$\cos \theta = \frac{\gamma_s - \gamma_{SL}}{\gamma_L}$	Equation 3-2	68
$\gamma_{S-V} + \gamma_{L-V} \cos(\theta) = \gamma_{S-L}$	Equation 3-3	69
$Q = \frac{k}{\eta} \frac{\Delta P}{L} A$	Equation 3-4	71
$k = \frac{Q}{A} \frac{L}{\Delta P} \eta$ (with unit m ²)	Equation 3-5	72
$K = \frac{k}{\eta}$	Equation 3-6	72
$F_{out} = 2 \pi r \gamma \cos \theta$	Equation 3-1	73
$P = \frac{F_{out}}{\pi r^2}$	Equation 3-2	73
$P = \frac{-2 \pi r \gamma \cos \theta}{\pi r^2}$	Equation 3-3	74
$P = \frac{-4 \gamma \cos \theta}{D}$	Equation 3-4	74
$D = \frac{712,54}{P}$	Equation 3-5	77
$V_{int} = V_{obs} - \delta V_{blank} + \left[0,175(V_{bulk}^1) \log_{10} \left(1 + \frac{P}{1820} \right) \right] - V_{bulk}^1 (1 - \Phi^1) \left(1 - \exp \left[\frac{P^1 - P}{M_{ss}} \right] \right)$	Equation 3-6	78
$(MaximumValue - MinimumValue) \div Mean \times 100$	Equation 3-7	81

$W_{\text{absorbed hexa}} = W_{\text{hexa saturated base paper}} - W_{\text{dry base paper}}$	Equation 3-8.....	84
$V_{\text{absorbed hexa}} = W_{\text{absorbed hexa}} / 0.77$	Equation 3-9	84
Total Pore Volume = $V_{\text{absorbed hexa}} / W_{\text{dry base paper}}$	Equation 3-10	84
$y = ax^2 + bx + c$	Equation 3-11	112
$Y = b_0 + b_1 X_1 + b_2 X_2 + \dots + b_p X_p$	Equation 6-1	227
$[X]_N^K = [T]_N^A * [P]_A^K + [E]_N^K$	Equation 6-2	227
$[Y]_N^M = [U]_N^A * [C]_A^M + [F]_N^M$	Equation 6-3	227
$u_{n,a} = b_a t_{n,a} + h_{n,a}$	Equation 6-4	227

List of Appendix

Appendix 1 Mercury Intrusion Test Procedure by Micromeritics and calculating values description	216
Appendix 2 DELTACK Curves	219
Appendix 3 Projection on Latent structure (PLS)	226

Abbreviations and Symbols

Abbreviations

3D	Three Dimensional Space
AVP	Average Pore Diameter
BPSD	Broad particle size distribution
CA	Contact Angle
CLC	Cylindrical Laboratory Coater
CMC	Carboxy-methyl cellulose
COV	Coefficient of variation
Force	Maximum force (DELTACK Test)
GCC	Ground Calcium Carbonate
IA	Image Area
IGT	Surface strength printability test
kN/m	Kilo-Newton per meter (5.714 PLI per kN/m)
MPa	MegaPascal (1MPa=145.03 PSI)
MPDV	Median Pore Diameter Volume
MPDA	Median Pore Diameter Area
MSP	Metering size press
NPSD	Narrow particle size distribution

NIA	Non-Image Area
P	Porosity
PCA	Principal Component Analysis
P_Cal_PC	Precoating layer calendering pressure
PCC	Precipitated Calcium Carbonate
PLI	Pounds per linear inches
PLS	Projection on a latent Structure or Partial Least Squares
PPS	Parker Print Surf – roughness of the sheet
PrVP	Precoated layer Pore Volume
PSI	Pounds per square inches
RDP	Research, Development and Production
RMS	Root mean square
S/A	Styrene/Acrylic Latex
S/A/ACN	Styrene/Acrylic/Acrylonitrile Latex
S/B	Styrene/Butadiene Latex
S/B/ACN	Styrene/Butadiene/Acrylonitrile latex
SBR	Styrene/Butadiene latex
SEM	Surface electronic microscopy
T _g	Glass transition temperature
Time	Time need to reach the maximum force (DELTACK Test)

TPA	Total Pore Area
T Cal PC	Precoating layer calendering temperature
TPV	Total Pore Volume
TPA	Total Pore Area
VP	Pore Volume for uncalendered paper
VPC	Pore Volume for calendered paper
W	Weight

Symbols

A	filtration area
b	flow coefficient
b	correlation factor
C	concentration
D	coefficient of diffusion
d_{eff}	effective particle diameter
ΔP	pressure drop, pressure differential (Pa)
F	filtration elements
h	distance
H	residual matrix of error
k	permeability
K	coefficient of permeability or hydraulic conductivity.
L	length or layer thickness
$L_{\text{filter cake}}$	thickness of filter cake layer
[Matrix]	symbol for a matrix calculation; the name of the matrix is symbolized by a capital letter.
P	applied pressure
p_e	additional pressure applied with the capillary pressure
$\Delta P/L$	pressure drop across the sample length (L)
Q	flow
Q_{liquid}	amount of liquid phase removed through dewatering

r	capillary radius
W	circumference of the ring (μm , around 10 cm)
Q	air flow ($\mu\text{m}^3 \cdot \text{s}^{-1}$)
R_a	roughness average
r_h	hydraulic radius
R_q	root mean square (RMS) roughness
R_t	maximum peak to valley height
R_{pps}	Parker print surf roughness of paper (μm)
S	spreading coefficient
S	area of the porous medium cylinder defined by πR^2 (R is the radius)
t	time
u and t	vector reducing number of planes between x and y
V_{IMB}	volume of ink imbibed by the layer
V_b	corresponding bulk volume
X	flow direction
θ	contact angle of the mercury on the pores (usually 130° - 140° for paper)
μ	dynamic viscosity (in this case, the coating color viscosity)
μ_f	pore coefficient
μ_l	path coefficient
φ	average mass flow
Φ	fractional void volume
ξ	porosity
Ψ	Kozeny constant

ρ	fluid density
μ	air viscosity at the measurement temperature (PA*s)
γ	surface tension
γ_S	superficial tension of the solid (free energy of the solid)
γ_L	superficial tension of the fluid (free energy of the fluid)
γ_{SL}	interfacial tension between the liquid and the solid.
γ_{Hg}	surface tension of mercury (usually 480-485 mPa°s)

Chapter 1 - Introduction

The need to improve paper properties is always what consumers request from the printers and the paper producers. As coated paper is a big part of the improvement, there is a need for high performance coatings. Coatings are applied to board and paper to provide a smooth surface and to improve the printing snap, often defined as the overall impression of the print quality as perceived through human eyes in the pressroom. Most studies are performed to identify the best pigment-binder combinations and thus obtain the right properties required by the papermaker for operations. The type and the amount of the various coating color components affect the mechanical, optical and liquid absorption characteristics of the coated paper in a very complex manner. Considering printing characteristics, it is why the biggest challenge for the researchers still remains to find an optimum balance of paper properties for an ink droplet to provide a sharply defined printed dot on the coated paper surface. The droplet needs to have an optimal spread/penetration ratio [1] and to set fast, *i.e.* within the runnability limits of the printing process in the coating structure. To achieve such ink setting properties, the coating color particles need to be located close to the paper surface [2]. This is particularly true for the offset printing process where a large amount of ink and water, up to 300% ink coverage through 4, and more, ink layer applications, are added to the paper during printing. A properly formulated coating offers several options and the papermaker is continuously looking for new ways to take advantage of formulation options to improve properties such as brightness, opacity, smoothness, surface strength, ink setting, ink drying, print gloss, etc [3]. The type of coating technology used also increases the challenge to meet new operation and quality objectives. For example, the runnability of high solids pigmented coating colors on the metering size press depends on a complex balance between rheology and water retention [4-7]. The pulse dynamics generated by the nip in a metering size press or a roll applicator acting on coating colors play an important role in film splitting phenomena. Therefore, the development strategy for the metering size press requires a new approach to create a necessary balance between dynamic water retention and rheology when using the new high viscosity (1000-1200 poise or $\text{Pa}\cdot\text{s}^{-1}$) formulations [8].

Chapter 2 - Literature review

One common way to increase the print quality of a paper sheet is through surface treatment, either coating and/or calendering. Papers designed to improve image sharpness and brightness need to be coated, *i.e.* one needs to apply a thin layer of aqueous suspension containing mineral pigments and chemicals over a base sheet. This suspension is dried after application, the drying method contributes to the characteristics, either good or bad, of the dry thin, actually micrometers thick, layer.

In the last 2 decades, several studies tried to explain the factors that control the printability of the coated paper. The pore structure of paper coatings that could be modified using a range of different mineral pigments and binder contents, has been found by many researchers to have a significant effect on the coated paper printing characteristics [9]. The first identified paper structure parameter was the architecture of the pore structure for the base paper and the coating layer which together drive the final print properties. Most physical and functional properties of pigment coated papers are influenced to a greater or lesser extent, by the porous structure of the coating layer. For example, the number and the size of microvoids contribute to macroscopic properties such as brightness, light scattering efficiency, and opacity. The void structure also affects the flow of liquids and gases through the coating layer. Absorption of inks and fountain solutions during printing is controlled by the structure of the pore space close to the coating layer surface. The porous structure of a coating layer depends on the coating color formulation, pigments and their combinations, synthetic and natural binders, chemical additives (*e.g.* associative thickeners), coating color application, and the drying processes [10]. Therefore, it is obvious that the coated paper structure can be considered as a combination of fibres, pigment(s), binder, and air volume. The air volume is directly influenced by the others parameters. A wide range of control of the coating pore size is possible using narrow particle size distribution kaolins and carbonates. Tuning the pore diameter to a desire target enables to control the print properties while still maintaining the desired gloss and optical properties. Once pore diameter and volume are controlled to the targeted, desired range, optimizing the binder package will further enhance the proper-

ties. While the pigments can create exceptional value to the final coated paper, mismatched pigments may negatively affect optical performance and result in a poor print performance [11]. We may conclude that the pore structure of the surface layer will determine both the optical and print performance of the coated paper [12]. It is however important to understand how the structure may be affected by the size and shape of the components in the coating layer and how they are packed together [12].

The literature analysis is then closely related to the pore structure or network: a concept with its own terminology. To discuss pore structure, two terms need to be defined; skeleton and skeletal element, as was done by Gane [13] : ‘‘If you think about a porous structure, what do you see? Imagine you are walking through the structure as you might walk through a network of caves underground. You perhaps see big rocks, sands and soil made walls of the cave. Perhaps you see other caves and channels on either side or even above and below. You are walking around in the pores; the solid material between the pores is the skeleton of the structure. Each part of the skeleton (big rocks, sands) between the pores/caves is a skeletal element. In other words, if you know the pore structure (the pore elements) you then need to know the solid structure to determine how the pores are arranged in space. The arrangement of the solid structure is known as the skeleton, and each part between the pore elements is a skeletal element’’.

2.1 Paper (Base stock)

The application of a coating layer is a complex process dependent of many interactions between the components and the process. Notwithstanding all factors, the application must still be achieved on a paper surface designed to adequately receive a layer of coating. The coating layer does not and will not hide a defect (Figure 2-1) or enhance the poor quality of the base paper. Base paper characteristics are very important to obtain a high quality final product and insure good printability [14, 15]. As an example, Al-Turaif [16] shows that gloss increases and roughness decreases when the substrate is changed from absorbent to non-absorbent. Another important aspect is the filler content in the base paper. Increasing the base paper filler content improves surface roughness, print gloss, paper gloss, and has a positive effect on print mottle [17].

The tendency to increase the filler level was initiated many years ago. Nowadays, it becomes more and more important when considering the price of the fibres. The two sidedness of the base paper may become critical, especially when reducing the coatweight and consequently, the possibilities for coat weight adjustment between both sides of the sheet [6]. Another aspect, especially for wood free papers, is the sizing of the base stock. Huang and Lepoutre [18] report that sizing is added to control the penetration of the fluids in the base sheet but, if absorbency is changed by hydrophobic sizing, just a small effect may be observed. However, if pore size and void fraction (pore volume) are modified, the effect on absorbency is large. Overall, hydrophobic sizing improves coated gloss slightly on dense base sheet, but not on porous sheets. It does not have an effect on coated roughness, irrespective of base sheet density. The fluid penetration causing the base paper roughening under the influence of moisture and the hydraulic of fluid penetration are a function of the dwell time and dewatering characteristics. They have been shown to be dominant factors with respect to modification and coverage in the final coated paper properties [19].

Physical coverage of a porous base paper is a complex function of the application method, solids concentration, coating formulation, pigment particle size, and shape distribution, including interactions with the void dimensions, the anisotropic rheology and the drainage during dewatering [20]. Another article by Allem and Uesaka [21] finds that for LWC papers, the coating thickness is primarily affected by the base sheet roughness. They show that other coating parameters are also related, albeit to a lesser extent, to the coating thickness.

It is important to recognize the distinction between micro and macro roughness when considering a base paper problem. Gane and Hooper [22] show that the macro roughness is primarily associated with initial base sheet roughness, surface void structure, and fibre compaction. The macro profile is in the important region related to coating coverage. Micro profile is related to the structural packing of the pigmented coating layer and is determined by the pigment size and shape distributions, and by the interactions between coating color and base sheet.

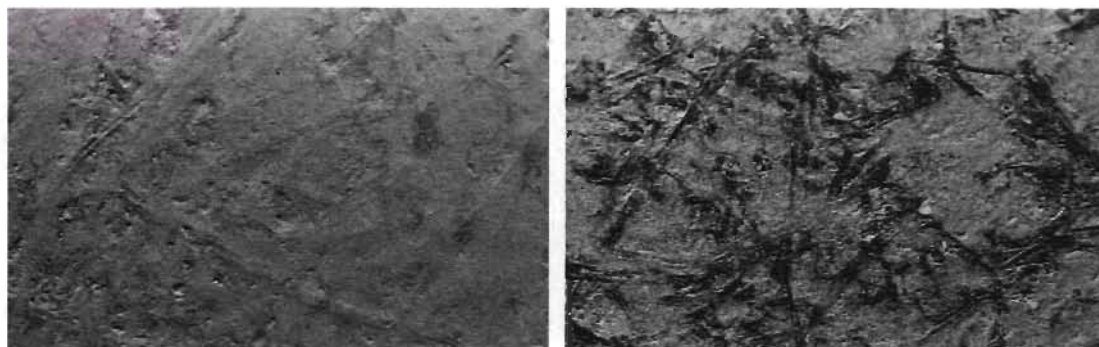


Figure 2-1 A MSP (left) and blade (right) coated ULWC paper, where a 28 g/m^2 wood containing base paper is coated with 5 g/m^2 .

The structure of the coating layer influences the macro roughness through the effective coating holdout and coverage associated with coating bulk and void bridging [22]. Base paper fibres, however, do not constitute a static interlocking network but introduce dynamic and chemicals interactions, particularly with the fluid component of the coating color. Acting together, such phenomena collectively control the overall absorbency of the base sheet, which in conjunction with the dewatering rate of the coating color, determines surface coverage, coating holdout, and roughness of the coated sheet for a given pigment system [22].

Therefore, control of the absorbency of the base paper is an important parameter because the relaxation of fibre stress occurs during the wetting generated by the coating color application. The relaxation phenomenon originates from the base sheet formation and/or any surface treatment performed on the base stock prior to the application of the coating layer. A good water holding, *i.e.* slow dewatering, combined with a fast immobilization limits the extent of the surface relaxation of the base sheet.

2.2 Pigments and latex

The coating layer applied on the base stock or another coating layer is mainly produced with minerals pigments. The pigments are the products of mining exploitation or are manufactured under controlled industrial process conditions. Today some pigments combine the two processes: they are called “engineered pigments”. Many pigments are

commercially available. Choosing the right one is a complex process where several factors must be considered to achieve the quality needed for a specific coated paper.

Poor dispersion of pigments in a coating color recipe is known to lead to problems such as blade scratches, excess rejects at screen, rheological fluctuations, and runnability disturbances at the coater [23]. It is however related to the process itself and fundamentals drive the final behaviour in a pressroom. Lee [24] shows that pigment particle size distribution, particle shape, binder type (film shrinkage), drying temperature and time, pigment wetting, coating holdout (especially at low coating weights), and varying coating weights contribute to micro scale roughness. The micro scale variations are partly responsible for instabilities, variations during the printing process. The characterization of the coating layer and understanding the mechanisms and interactions of the layer various parameters is a key factor to improving the printing characteristics and the printing quality.

Several studies designate the pore structure as the key factor, or at least, a very important aspect of the coating layer structure. On the one hand, Di Risio and Yan [25] find that pigment particle packing, one of the most important pigment properties, governs the coating pore structure, which in turn affects the optical, mechanical, and printing qualities of the coated paper.

On the other hand, David and Bertrand [26] report that the particle size and shape distributions control the packing ability of pigments; these parameters thus impacting the resulting coating structure. In addition, a relationship between the shape factor of the different pigments and the flow rate, as related to coating movement, in conjunction with the pore structure is rather straightforward. For high shape factor pigments, example talc (Figure 2-2 [27]), the coating penetration is small and does not depend on rheology.

It suggests that high shape factor pigments can block pores to reduce coating penetration. For moderate shape factor pigment, the results indicate that slowing the absorption of the water phase into the paper helps reduces coating penetration [28].

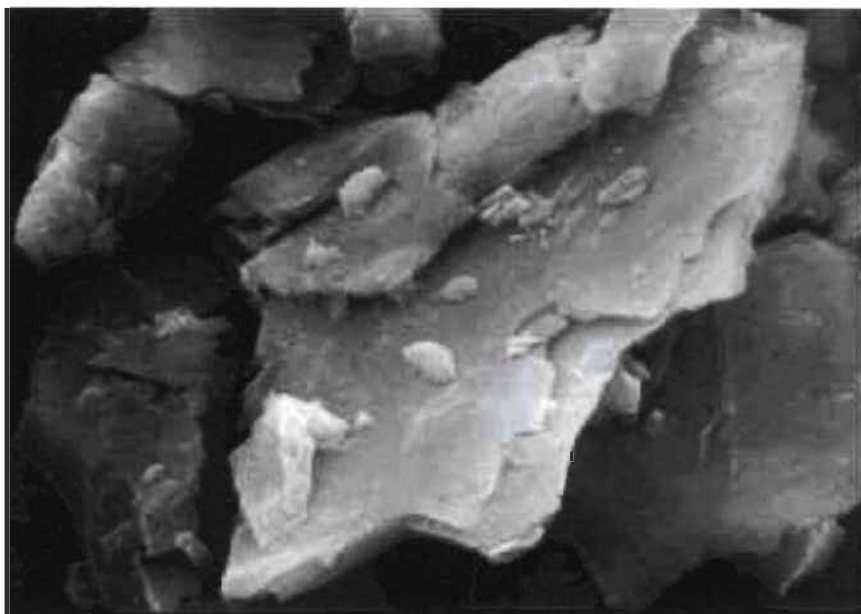


Figure 2-2 Scanning electron microscopy of talc

All of the concepts previously discussed indicate that it is feasible and possible to tailor-make coating structures [29]. Coating structure design may be achieved by modeling the pigment particle size and particle size distribution. The particle size determines the paper gloss, while the pore size is determined by both the particle size and the distribution (Figure 2-3). More specifically, decreasing the particle size increases gloss and decreases pore size, but it has only a minor influence on porosity. The last assertion is only true if the particle size distribution is kept constant, which is unlikely to happen if the particle size is changed by a modification of the pigments in the formulation. Generally, as the particle size decreases, the distribution narrows.

However, decreasing the particle size distributions increases pore size and porosity. The influence on paper gloss is minor or may be considered negligible [3]. The pore structure, as previously described, controls the porosity of the coating layer. The porosity of the coating layer itself can be controlled through modification of the pigment size and morphology, the binder type and level, and inter-particle interaction. The morphology of the particles is here related to particles with a regular shape as such type of particle packs tighter, closer than irregularly shaped particles [30].

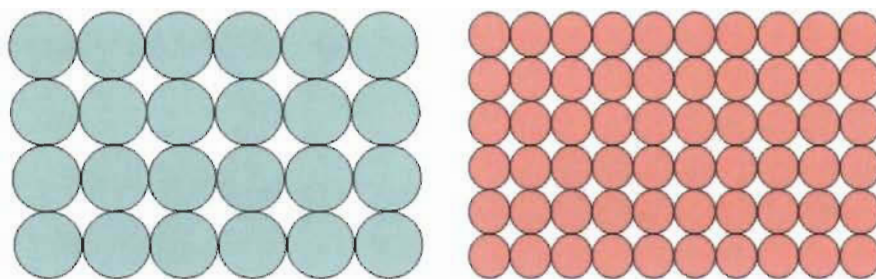


Figure 2-3 Pore size comparison for large and small particle size pigments

Previous considerations indicate the importance of understanding the coating structure and how the coating layer interacts with the base sheet and the coating process itself. It is well established that gloss is dependent on surface roughness and pore structure [31]. Therefore, these parameters must be considered upon designing a new coating or improving an existing one. To build a coating structure in accordance with our goals, the coating layer has to be designed with a thorough understanding of all parameters which affect its structure. Larsson and Engstrom [32] find that the thickness of the coating layer is governed by the pigment packing in the final dry coating layer, which in turn is governed by the particle shape and particle size distribution of the pigment and by the interactions between the constituents of the coating color. Pigments with narrow particle size distribution are known to give superior coverage. Okomori and Lepoutre [33] also show that the pigment size distribution and the pigment shape influence pigment packing. The only parameter with no effect is pigment surface area which does not affect the coating pore volume to any great extent [34]. Of course, the last statement is heavily dependent on what type of pigment, and what will be the change in coating morphology.

The shape, size and size distributions also affect the optical properties of the coated paper. Devisetti and Malla [35] investigating coarse pigments find that a high coated sheet brightness can be obtained despite the fact that the lower pigment brightness than that of other kaolins. This is probably due to the improved coverage of groundwood base stock with the use of coarse pigments.

The role and the way each kind of pigment behaves are pigment specific. Each pigment has unique morphologies, unique crystal structures. The ways a pigment and its morphology interact with the other components has a strong influence on the coated layer structure (Figure 2-4). For example, the benefits of a plate like particle morphology has

been frequently described in terms of contour-like coverage in lightweight coating, whereas blocky particles tend to fill surface voids and leads to uneven coverage [36]. Finally, all the differences among the pigments and certain orders of mixing components can result in a significant change in the shear viscosity and/or viscoelastic parameters characterizing the colors. Such interactions will influence the rheological properties of the coating color, and changes in the rheological behaviour may have consequences for the runnability of the color [37] in the costing operation.

The pigments can be separated into four groups; clay, carbonate, titanium, and special pigments. The 2 first groups are covered by many different studies because these pigments are, and have been, widely used for coating paper.

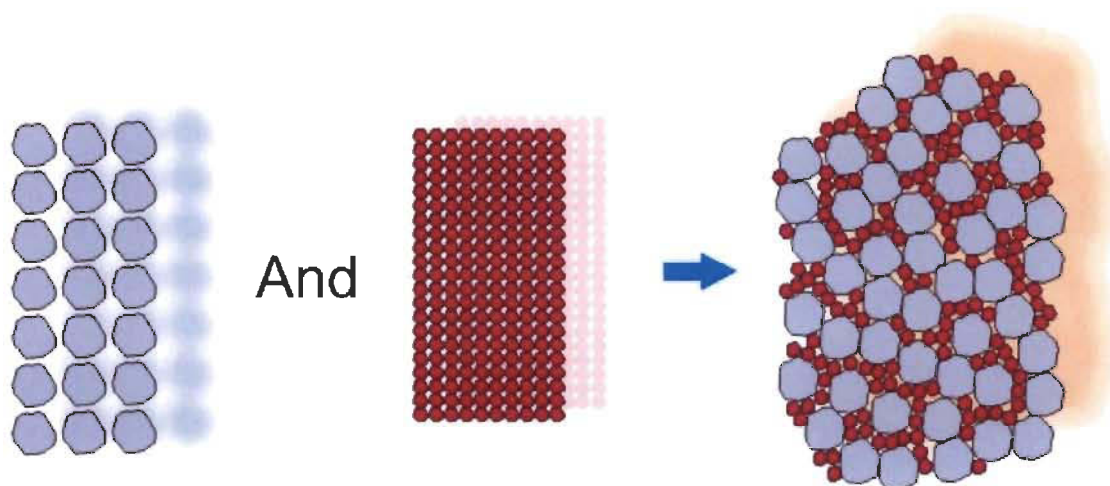


Figure 2-4 Packing efficiency of pigments with two different particle size diameter

2.2.1 Clay

Clay is a pigment that has been used in the coating for more than 100 years in the paper industry. It is mined around the world and the main producing areas are mainly England, Georgia in the United States of America, and Jari River district in Brazil. All these kaolins have their specific characteristics. They are used because they are locally available or because they have specific characteristics permitting to meet specific coating layer structures. Clay coating colors usually exhibit higher viscosities than ground calcium carbonate (GCC), for a given pigment concentration. The difference is mainly due to different particle morphologies. The platelet morphology of kaolinite confers poor

packing ability but, at the same time, good coverage properties of the base paper (Figure 2-5) [38].

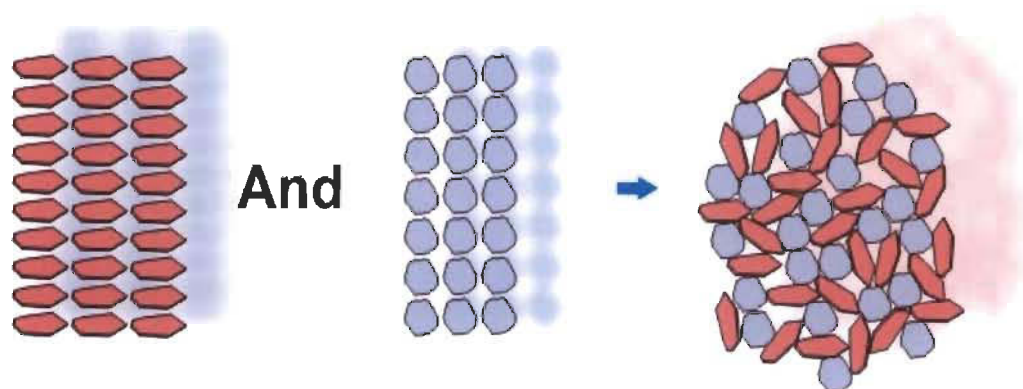


Figure 2-5 Packing efficiency for a platy and blocky pigments

The pore volume of the clay coated layer is reduced almost twice as much for the clay coating as for the GCC coating. The phenomenon is attributed to the greater capability of platy clay (Figure 2-6) to reorient and rearrange under compression than the isometric GCC particles [39]. Furthermore, the coarser kaolin particles seem to produce bigger pores than produced by the finer kaolin particles. For particles of a similar median size, narrow kaolin distribution generates pore distributions with more uniform pore sizes than generated by broader clay particle distributions [25].

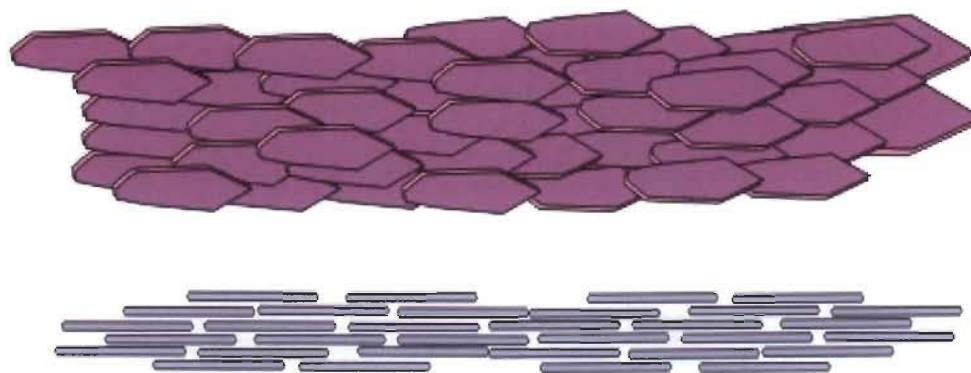


Figure 2-6 Coating layer structure with high aspect ratio clay

Di Risio and Yan [25] report that coarse clays particles produce coating layers with a similar number of pores but with a larger pore size than finer clay. For the same particle size, clay pigments with a broad particle size distribution produce a low pore volume. Notwithstanding the clay source, the effect of varying the aspect ratio from low to high is studied by Gane [40, 41] who finds that English platy clay runs clean at high speed,

without interactive binders and water retention aids, whereas the less water-retaining US clays and coarse ground carbonates requires some controlled level of water retention aid. The problem, thus, arises that many water retention aids and natural binders used today create an increased viscoelasticity in the coating color by interacting with pigments and creating depletion and flocculation together with partially or strongly associated water. These interactions will result in a predicted effect of relaxation induced dilatancy – dry stalagmites, dusting, scratching etc.

2.2.2 Calcium Carbonate

Calcium carbonate is a very useful common coating pigment. The calcium carbonate pigments are separated in 2 majors groups; either ground (GCC) or precipitated (PCC). Ground carbonate or GCC comes from chalk, limestone or marble which is the primary GCC source around the world. PCC is manufactured under controlled conditions to produce specific particle size, shape, and particle size distribution. Both forms of calcium carbonate are used to “build structure” in the coating layer. PCC enhances pore volume, but the average pore diameter is somehow similar when PCC and GCC have a similar size distribution (Figure 2-7). Coarse GCC increases the average pore diameter significantly, but pore volume and porosity decrease. Coating pore structure also impacts optical properties and the printability of low gloss coated paper[42].

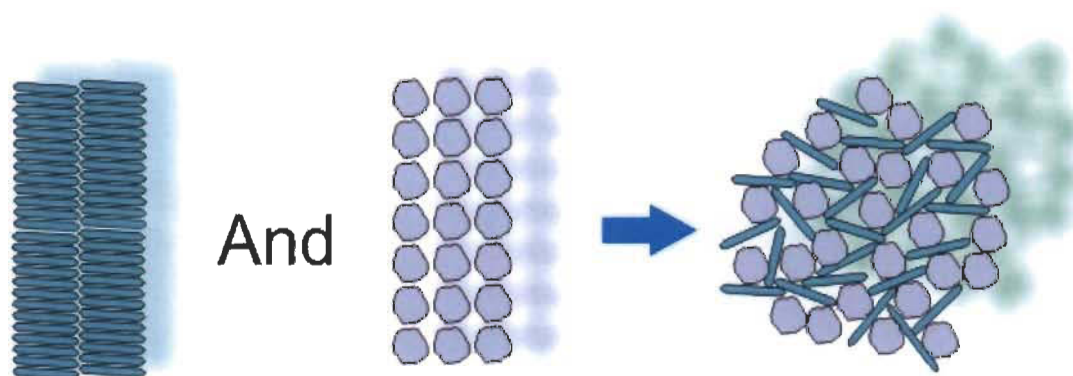


Figure 2-7 Packing efficiency of precipitated calcium carbonate compared with a blocky pigment

Yulong and Zhenlei [42] show that brightness depends strongly on the pore diameter of coating structure and that coatings with relatively large pore size enhance light scattering

and opacity. Sheet gloss is reduced significantly with a roughness increase, as measured with the Parker Print-Surf (PPS). Print gloss and delta gloss are improved with an appropriate balance between pore sizes and pores volume. Increasing average pore diameter and decreasing pore volume enhance print gloss and the gloss variation (delta gloss). Larsson and Engstrom [32] find that porosity of the final coating layer (GCC) is not controlled by the network structure, but by the packing of the aggregates and shrinkage during consolidation of the coating layer. The pigment packing is in turn controlled by the relative plastic viscosity of the suspension, by the particle size distribution of the pigments and its stabilization upon drying. Knappich *et al* [43] find a similar behaviour for GCC with narrow particle size distribution resulting in a coating structure with a large void diameter and a high total void volume. Therefore, the optical and physical properties of the coated paper are significantly improved. Fukui [44, 45] investigating blends of coarse and fine ground carbonate (GCC) in several ratios finds results in accordance with Osterhuber [44, 45]. Osterhuber, McFadden and Roman [29, 45] show that the pore volume, measured with mercury intrusion, remains relatively constant when particle size is varied within 0.45 - 0.85 μm . With a particle size above 0.85 μm , the pore volume decreases slightly, which could indicate an improved, almost ideal packing. The lowest pore volume is obtained using 100% coarse carbonate, while addition of fine carbonate increases the pore volume.

The type of calcium carbonate particles and the mixing ratio with other pigments directly determine how the structure of the coated paper will be developed. A carbonate with a broad distribution results in dense particle packing (Figure 2-8) which closes the coating. Conversely, the narrow particle size distribution of PCC generates a coating structure that contains substantially larger pores and higher pore volumes (Figure 2-9) than a broad particle size distribution GCC [45]. In addition, reducing [11, 46, 47] the particle diameter reduces the pore diameter. Works from Hagemeyer suggest that organic dispersant plus the chemical nature of the pigment have an even larger effect than the shape itself. Another aspect of the PCC is how it affects the final paper properties. Al-Turaif shows that introducing a prismatic shaped PCC pigment into the plate like kaolin pigment coating causes a gloss decrease and a roughness increase. Furthermore, adding PCC particles upsets the packing thus increasing the pathways within the coating

and subsequently increasing the movements of latex particles toward the surface [16]. The calcium carbonate is also a good pigment to control the blistering resistance. Okomori and Lepoutre [33, 48] find that using 100 parts CaCO_3 is considerably better for blistering resistance than using 100 parts clay. The blistering of coated paper depends greatly on the properties of the coating layer near the base stock surface.

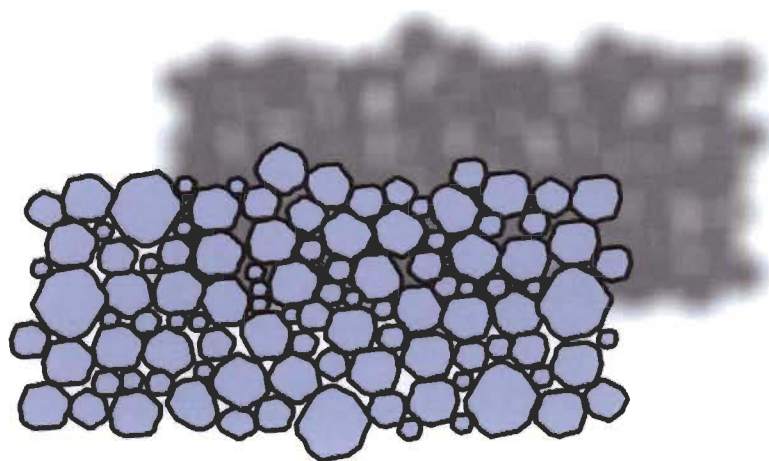


Figure 2-8 Pore structure for a GCC with a broad particle size distribution

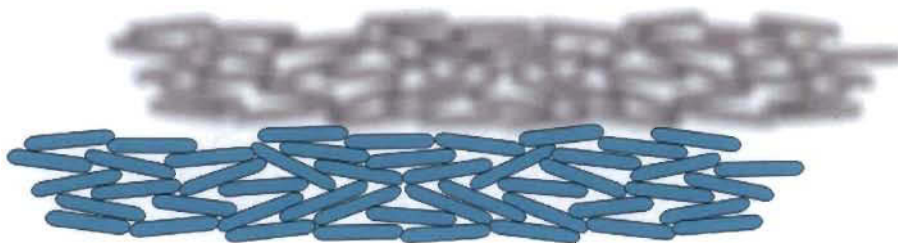


Figure 2-9 Pore structure for a PCC with a narrow particle size distribution

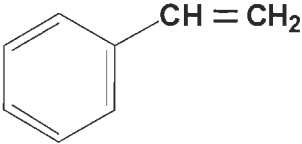
2.2.3 Latex

The latex is an important constituent of a coating structure. The pigments create the structure and the latex keeps the structure holding together after drying in the coating process. Latex has a complex chemical structure. It is composed of particles and liquid forming an emulsion. The type and particle size of the latex give the final properties of

the film formed when the sheet is dried. The latex is one of main components used to increase the strength of the coating structure. The type and particle size of the latex also affect the coating structure. It is the reason why coating strength increases as latex content increases and, at a given latex content level, it is why coating strength increases when pigment particle size distribution increases.

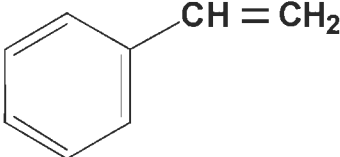
Latex emulsion is a dispersion of spherical particles (100-300 μm) in water. A latex solution is always produced by reaction with 2 or more different monomers. The lists of possible monomers for the two main groups of latex used in paper industry are listed in table 2-1 and 2-2 [49]. Latex always contains styrene monomer combined with one or more other monomers. Each latex is generally combined with other chemical components *e.g.* carboxylic acid ($-\text{COOH}$), amide (CONH_2), hydroxyl groups ($-\text{OH}$).

Table 2-1 Monomers used to make S/B latex

Styrene / Butadiene Latex	Basic chemical group
Styrene	
Butadiene	$\text{CH}_2 = \text{CH} - \text{CH} = \text{CH}_2$
Acrylamide	$\text{CH}_2 = \text{CH} - \overset{\text{O}}{\underset{\parallel}{\text{C}}} - \text{NH}_2$
Acrylic acid	$\text{CH}_2 = \text{CH} - \overset{\text{O}}{\underset{\parallel}{\text{C}}} - \text{OH}$
Acrylonitrile	$\text{CH}_2 = \text{CH} - \text{C} \equiv \text{N}$
Itaconic acid	$\text{CH}_2 = \underset{\text{CH}_2 = \text{C} - \text{OH}}{\overset{\parallel}{\text{C}}} - \overset{\text{O}}{\underset{\parallel}{\text{C}}} - \text{OH}$

The choice of the other monomers is related to the end use of the product and the desired end-properties. The general rule of thumb in the pulp and paper industry is that the S/B binders are mainly comprised of styrene and butadiene. In addition, acrylic binders have a wider variety of composition than S/B binders. The key parameters for binder performance are monomer composition, glass transition temperature T_g , gel content, and particle size.

Table 2-2 Monomers used to make S/A latex

Acrylic Latex	Basic chemical group
Styrene	
N – Butyl - acrylate	$\text{CH}_2 = \text{CH} - \overset{\text{O}}{\parallel} \text{C} - \text{O} - (\text{CH}_2)_3 - \text{CH}_3$
Methyl acrylate	$\text{CH}_2 = \text{CH} - \overset{\text{O}}{\parallel} \text{C} - \text{O} - \text{CH}_3$
Ethyl acrylate	$\text{CH}_2 = \text{CH} - \overset{\text{O}}{\parallel} \text{C} - \text{O} - \text{CH}_2 - \text{CH}_3$
Acrylonitrile	$\text{CH}_2 = \text{CH} - \text{C} \equiv \text{N}$

The choice of the monomers has a great impact in the final performance of the latex. The influence of the monomer composition for latex is listed in table 2-3. The table shows the printing properties for the most important monomers used in industry coating processes. Styrene is the monomer present in all latex used in coating industry. The glass transition temperature of the styrene is therefore an important factor. The relation between the percentage of styrene and the T_g is defined in Figure 2-10 [49].

Table 2-3 Influence of different monomer latex composition on printing properties

Butadiene	n-Butyl-acrylate	Styrene	Acrylonitrile
Elasticity, flexibility	Elasticity, flexibility	Stiffness	Stiffness
Fold endurance	Fold endurance	Gloss	Solvent resistance
Bond Strength	Bond Strength	Porosity	Bond Strength
	Resistance to UV		
	Print evenness in offset		

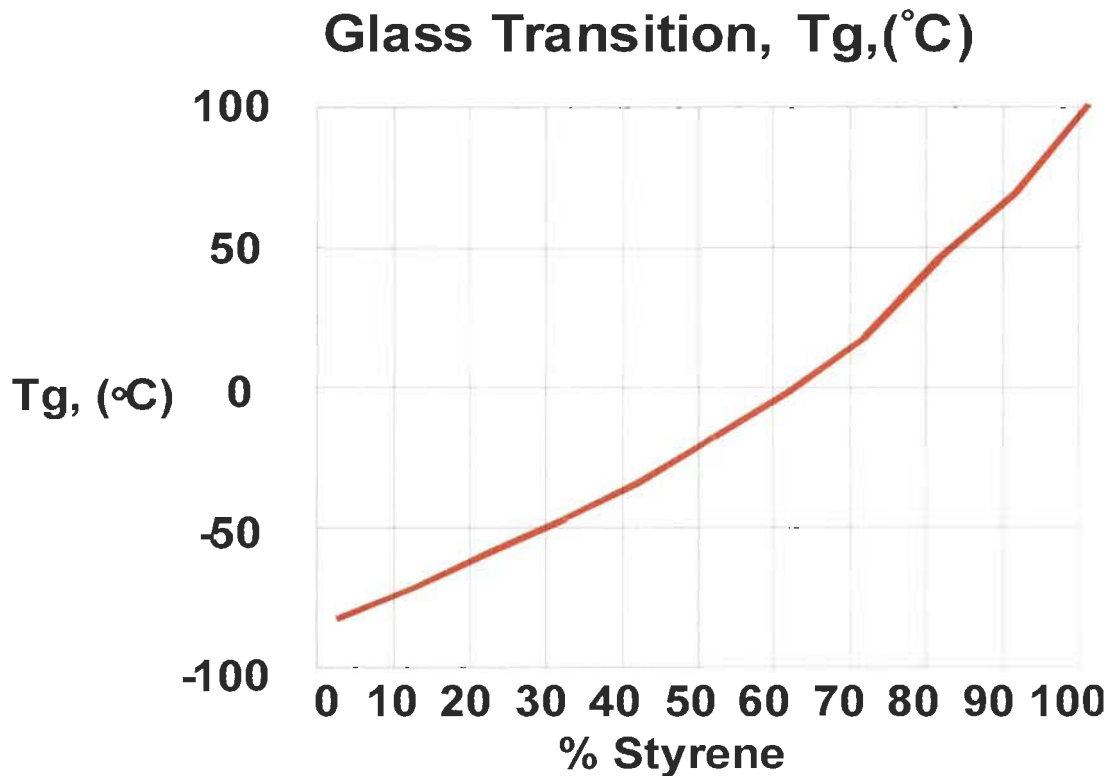


Figure 2-10 Glass transition temperature (T_g) related to the level of styrene in the latex

Therefore, it can be concluded that the lower the Glass transition temperature (T_g), the softer the latex. The T_g of a latex is calculated by the Gordon-Taylor equation (equation 2-1) [49] as follow:

$$\frac{1}{T_g} = \frac{W_1}{T_{g1}} + \frac{W_2}{T_{g2}} \quad \text{Equation 2-1}$$

Where T_g = glass transition temperature of the monomer
 W = weight fraction of the monomer

The particle size influences bond strength, ink gloss, blister resistance, and gloss. Increasing the particles size of a latex negatively affect (decrease) the two first parameters (bond strength and ink gloss) while the two last one (blister resistance and gloss) are positively affected (increase). The glass transition temperature T_g is important to evaluate the power needed in the drying process to make the film upon surface application. Figure 2-11 [49] shows how the film is formed with different drying temperatures for two different latexes with different glass transition temperatures T_g .





Tg temperature	Drying temperature	
	30 °C	80 °C
28 °C		
6 °C		

Figure 2-11 Film forming during drying process for two different T_g

A low specific area of the broad distribution pigments in a coating indicates a low proportion of unbounded pigment surface [33]. The mechanical properties of the coating layer are greatly affected by the mechanical properties of the binder [50]. The mechanical properties of the coating layer will thus depend on the cohesion of the latex bridges formed between the pigments particles and the void structure of the coating layer. For example, stiff latex should give strong bridges and prevent or reduce shrinking during drying and consolidation phase; therefore resulting in an improved porous structure [50]. The stiffness, as a latex property, is neither good nor bad. It must be aligned with the final sheet property required by the customer. An interesting characteristic used to evaluate the mechanical properties of a latex is still the glass transition temperature, “ T_g ”, Kugge *et al* [51] demonstrated that above T_g the polymer chains are considerably more mobile, enabling the latex particles to easily deform and readily film-form during drying, than below T_g . A low T_g latex greatly retards the film formation during the drying process. The differences in latex mechanical properties influence the mobility of the latex particles during the drying process and therefore strongly influence the distribution of latex within the coating [24, 52]. The latex binder T_g has therefore a considerable influence on the latex behaviour inside the coating layer. For example, high T_g latex is known to migrate more easily to the top surface during drying [53] than low T_g latex. Binder migration to the top layer during drying is effective resulting in a closed, smooth, high gloss top layer [51]. The amount of latex strongly influences the properties of pigment coating. Sufficient latex is required to confer mechanical strength to the coating layer. Excess addition of latex has adverse effects on a range of optical and physical properties.

Theoretical models often propose that latex particles are well dispersed through the wet coating layer and form a film including all pigments particles during the drying phase. However, Hiorns *et al* [12] show that the latexes do not necessarily form a film at the surface of the pigments. The latex plays an important role in the structure of the coated sheet. Carte *et al* [11] show that despite the large change in coating sheet properties, little change occurs in the pore structure of the coating, relatively to a change in the latex used in the formulation. This would indicate that chemical effects of the latex might have a dominant effect on the final properties of the coating.

Another important latex concept to consider is how the latex particles behave in a solution with other pigments particles. The size of the latex particles is very small compared to the majority of the pigment particles. The small latex particles increase the packing volume of the coating color. Therefore, the amount of binder impacts the structure of the coating and affects the porosity of paper coatings. This is confirmed by Knappich *et al* [43] where latex particles replace pigment fines in the wet coating. Both coating pore volume and average pore diameter are reduced when fines content and binder level are increased. Malla *et al* [54] confirm that pore volume is mostly affected by binder level while pore size is primarily affected by the amount of fines in the pigment. Finally Audette and Hiorns *et al* [12, 55] show that the use of hard latex, with increased Styrene in S/B latex, in the coating process usually provides benefits in terms of coating smoothness and hence sheet gloss. It is here important to consider the latex melting in the drying process. The impact is no longer comparable to the one of a hard sphere-like particle but to a liquid forming a film and filling the pore network.

The latex alone, or added to other chemicals, is known to influence the coating structure. Several papers mention the different ways how latex behaves in the coating structure. Lepoutre [56] reports the now well known effect that binders and thickeners affect the coating structure during coating layer consolidation. Larsson and Engstrom [32] agree. However, when using carboxy-methyl cellulose (CMC), they find that the CMC interacted with both, GCC-pigment and the latex, to build the network structure. Wallström and Järnström [57] find that at low binder levels, coating structure is mainly controlled by the packing of pigment particles. In addition, the binder redistribution may impact the pore structure. The binder redistribution is defined by two different concepts; the binder migration to the surface and the binder penetration into the paper. This is confirmed by Matsubayashi *et al* [48] who find that high concentration of latex occurs at the coating-base stock interface. It also indicates that latex tends to migrate into the base stock as well as into the coating structure. On this basis, pigments which increase the porosity of the coating should require more binder. Dimmick [58] believes such a statement is not supported by all researchers and might not be necessarily true as the binder does not completely cover the surface of the pigments. On the one hand, it is more like a spot welded theory where the binder welds the point of contacts between the

pigment particles. As a consequence, increasing the porosity does not necessarily increase the binder demand to keep the strength of the coating layer. Indeed, the spot welding effect does not automatically decrease. On other hand, and over a level of porosities, the statement is validated. However, Husband *et al* [59] indicate that such pigment types may lose binder readily into the base paper, which in turn might weaken the coating strength while, paradoxically, strengthening the coating – base sheet interface.

Identifying the right type of latex for a given application is important. For example, in a study of the effect of binder on rotogravure printability Fernandez *et al* [60] and Devisetti [35] show that soft, vinyl-acrylic latex provides optimum printability. Laudome *et al* [61] complete the information in an analysis of the different behaviour of latex and starch. They show that shrinkage during drying with starch-based formulations causes stresses far higher than those occurring in latex-based formulations.

2.3 Calendering

Paper has been calendered since the paper machine invention by Nicolas Robert over 200 years ago. The calendering has evolved to become a very important part of the final quality of uncoated and coated paper. Today, calendering is a main factor for the improvement of the surface of both paper and printing quality. As the factors controlling the surface properties are numerous and complex, a thorough understanding of the relationship between base stock, coating color and type of calendering is essential. It is well accepted that producing a good quality for printing requires a smooth and uniform surface. Coating application and subsequent calendering greatly improve the paper surface characteristics but, in counterpart, both operations must be performed according to the specifications and characteristics required for the end product and the end user. When coating layers are superposed, added one over the other as it is done for double coated and triple coated papers, the final product quality is significantly enhanced. During coating, the liquid phase in the coating color comes into contact with the base sheet. The fluid absorption by the fibre network and the fibres themselves increases both the thickness and roughens the surface of the base sheet. The increase in surface roughness of the base sheet may affect the coating mass distribution and so requires more calender-

ing energy to attain the desired smoothness [14]. When the base stock is precalendered, the entire effect of precalendering is lost due to the release of intra-fibre stresses. As the fibres come into contact with the water contained in the coating color, they have a tendency to recover their original shape: therefore the roughness of both the fibre surface and by consequence of the paper surface tends to increase [22, 62]. The effect is well documented and observed for light weight coated (LWC) paper grades [63].

When a calendering load is applied to a paper surface, most of the desired smoothing effect of the surface is already achieved at 110 kN/m. A further increase of the loading pressure only maintains the surface properties up to a maximum but also negative affects some paper properties. The pressure applied by calendering has an important effect on modifying the pore structure of the coating and globally the paper structure (Figure 2-12). Calendering has a greater influence, like reducing the pore size, on large pores than on small pores; the effect decreasing with the size of the pores. The reduction in pore volume and pore size results in a significant reduction of the light-scattering coefficient, up to 35%, of the coated sheet. The particle size distribution has a significant effect on the coating structure; for instance upon calendering, a GCC with a narrow particle size distribution results in a larger pore volume and larger pore size than a GCC with a broad particle size distribution. Although the coating with narrow particle size distribution pigments suffers a somewhat larger reduction in pore volume and pore size during calendering, it still presents a larger pore volume and pore size than a coating with broad particle size distribution pigments. The pore volume of a clay coating is reduced almost twice as much as a GCC coating [39].

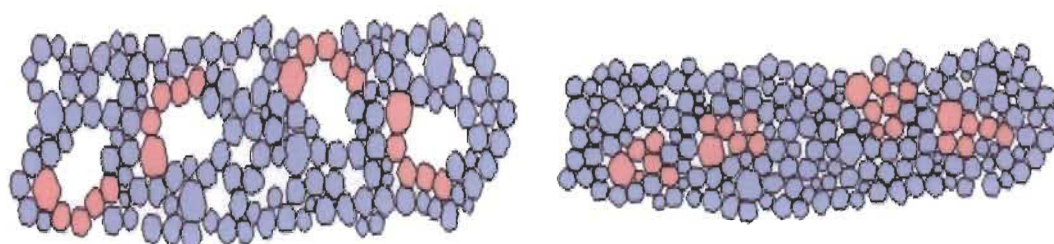


Figure 2-12 Effect of the calendering on the pore structure

As far as calendering temperature is concerned, paper properties are more sensitive to the effect of temperature than of calendering pressure. The main effect of high calender-

ing temperatures and low pressures is on the coating layer itself which will deform and smoothen under such conditions. Oppositely, the combination of a low temperature and high pressure implies that the whole sheet will compress evenly [12]. The smooth surface then results in an even thickness profile of the paper. Concomitantly, the bending stiffness and opacity of the paper are reduced due to combined effect of paper thickness reduction [50], fibres being crushed in the process, and the reduction in the void volume in the fibres, fibre network, and coating layer. The finest pore structure of the coating layer, *i.e.* a precoat or a topcoat layer, is the controlling factor for ink setting behaviour as it controls liquid penetration into the layer (Figure 2-13). Kugge [52] works confirm previous assertion as he surmises that both the topcoat, which is directly into contact with the ink, or the underlying precoat and even the precalendering and/or calendering may modify the latex distribution inside the coating layer. The rearrangement of the latex particles with water movement upon drying of the sheet may be the reason why the latex content on the surface of the coated sheets is affected by the precalendering conditions. The type of calendering (hard nip, soft nip, supercalendering, etc.) used is an important factor as it will further influence the quantity of latex ending-up on the coated sheet surface: the highest latex content on the surface being reached with soft nip precalendered sheets. The intensity of precalendering also affects the surface latex content. In addition, Venkata *et al* [62] find that different precalendering methods such as machine calendering, supercalendering, and soft nip calendering do not affect the distribution of latex on the surface of the coated sheet. The latex influences the whole coating process due to film forming behaviour and compressive response to calendering. The viscoelastic properties of the coatings correlate with the compressive behaviour of the calendering of coated paper and the bending behaviour (Gurley stiffness testing) [64].

Precalendering is then an interesting strategy to control the total calendering operation load applied onto a coated sheet. However, as we have just seen, different aspects of the process need to be taken into account [5]. In essence, following points may be outlined:

- precalendering is one of the effective methods to achieve a uniform coating layer and to reduce the roughness and porosity of the surface base paper,

- the intensity of calendering is the critical factor in achieving the final surface properties of the coated sheet,
- precalendering the base sheets as a pre-treatment is effective only if the coated sheet is not post calendered [62],
- precalendering at high temperature has the same effect as increasing the coat weight around 1 g/m² [65],
- the precalendering effect on the base paper with calendering at high temperature increases the number of small pores on the surface, and
- a base sheet without precalendering and with precalendering at low temperature gives the same coated paper properties [65].

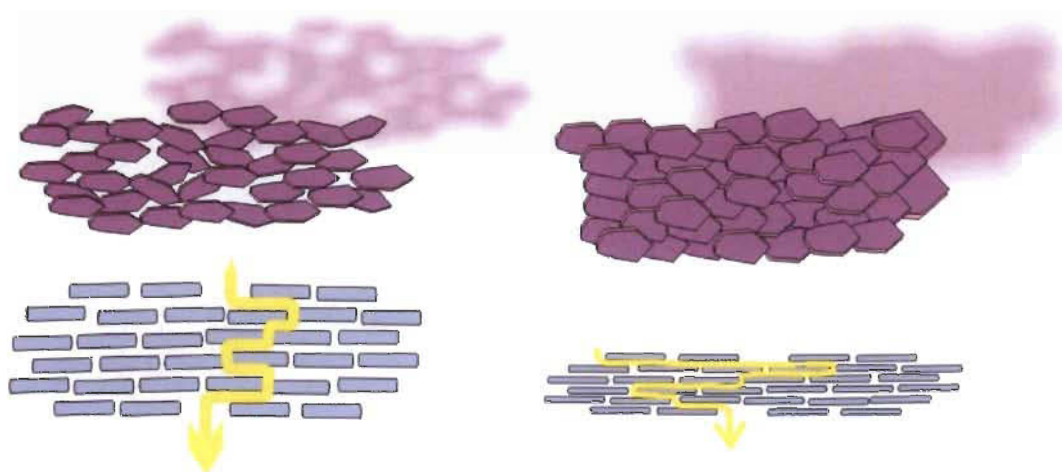


Figure 2-13 Water movement for a platy pigment for an uncalendered (left) and calendered (right) coating layer

The effect of precalendering has a different impact depending on the nature of the base paper, either wood free or mainly mechanical pulp (as for LWC) sheet. In the case of the wood free paper, precalendering before coating has generally positive effects on the properties of the coated end product. The gloss and the smoothness are somewhat enhanced. As expected, the coating mass distribution in coating layer is more homogenous when a precalendered paper is used [66]. For LWC paper precalendering does not always improve the coated sheet final properties. For instance, Ahlroos, Alexandersson, and Grön [17, 22], and Gane and Hooper [17, 22] show that during precalendering, ex-

pansion of fibre flocks may affect the coating mass distribution and deteriorate print quality. Here, precalendering the base sheet (for LWC) does not significantly improve surface roughness or gloss. Another example is provided by Engström and Lafaye [67]. They find that precalendering a wood containing base paper (LWC) results in a reduction in the covering ability of the coating with a subsequent increase of mottling in offset printing. In a study of the effect of precalendering and low coat weight application, as low as 2-3 g/m², Gane and Hooper [22] explain that surface of the base sheet must have a macro-roughness adapted to the application of the coating layer; the base stock being the same apart from the reduced macro roughness of the precalendered sample. They show that an improved coating coverage is achieved when coating a smooth precalendered base stock. It is clear that the rough base stock has a great proportion of uncovered surface fibres in the finished sheet. However, the gloss of the two samples is similar.

The same authors show that the surface profile generated after coating reproduced many of the surface features present in the uncalendered base stock. More critical is that the smoothing effect due to precalendering coupled to the regeneration of the original base profile via relaxation of the fibre network results in a coated sheet which does not achieve the gloss advantage that might have been expected from the improved coverage [22].

Today, soft nip calendering is a useful technology mainly used for LWC and board grades with some applications in wood free papers. The impact of soft nip calendering on density is small: the paper surface developed is a closed surface with small pores [65]. Furthermore, Nissinen [68] finds that the effects of soft calendering on quality characteristics are usually small, except for roughness and gloss. It is the reason why precoat soft calendering remains an interesting process variable. In their work, although they expected a negative effect on the coating process, topcoating, at 10 g/m², went surprisingly well with no streaking problems. However, the coatweight varies upon blade load modifications. Finally, they show that the uniformity of coating layer and post-calendering at low load are important for print quality characteristics, and more specifically mottling [65].

2.4 Multilayer coated paper

Double layer coating is used to obtain a paper with maximum gloss and printability characteristics (Figure 2-14) [69]. Usually, double-coating is used to apply high coat weight applications as it mainly provides a large flexibility for the coating colors and coat weights, in both the precoat and topcoat layer, applied on the paper. It should be emphasized that with the same total coatweight, double-coating provides a paper with a smoother surface after printing than single-coating where fibre swelling will increase the paper surface roughness [6, 70]. The interactions between the coating layers and the base paper are critical parameters to consider when producing a new or a modified coated paper grade. Multilayer coating is generally done to apply high coat weights in a strategy to minimize total production cost. Indeed, cost savings can be realized by the use of less expensive pigments and additives in the precoat, thus keeping the high glossing pigments and binder in the topcoat. Such a cost reduction strategy may be optimized by varying the coatweight ratio between precoat and topcoat with the same total coatweight applied to the base paper [71].

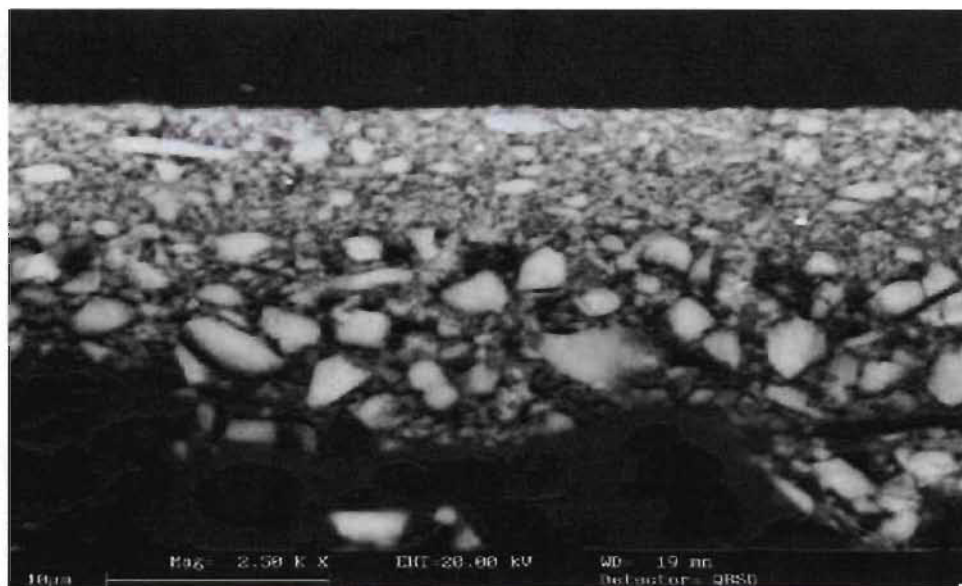


Figure 2-14 Double coated paper and base stock

The coatweight/coating color interaction between each layer and the base paper directly controls the final quality of the paper. For instance, the gloss difference between a pre-

coat layer containing carbonate and a precoat layer containing clay is maintained after application of the topcoat layer [71]. The gloss of the finished product appears to be dependent on the roughness of the precoated sheet rather than the particle size of the precoat pigments [71]. Another study by Renvall, Rautiainen and Rossitto concludes that the type and the particle size of the pigments in a precoat formulation directly influence the finished properties of the double coated sheet [70]. Although the two preceding studies have slightly different conclusions, we hypothesize that a combination of the roughness of the base paper and the particle size are the key factors in the design of a precoat layer. Some results show that, for a double-coated paper, the precoat application has such a predominant importance that the topcoat weight has a relatively small influence on the IGT surface strength. Overall, the coatweight of the precoat and the method of precoat application have also a predominant influence on the final product [70]. Using different binder system in the precoat layer, Burri *et al* [72] find no visible effect on the ink setting rate. Renvall, Rautiainen and Rossitto [70] show that, for a given coat weight level, when used for topcoat, the roll applicator provides a better gloss than the short dwell coater. Finally, Hostetler [73] suggests that the precoat formulations have significant effect on the topcoat dewatering.

The process runnability in topcoat layer application depends on the roughness of the precoat. In a study using Solid Bleached Sulphate (SBS) paperboard, Gagnon and Hiscock [74] report that increasing pore diameter at a comparable total volume reduces the “capillarity” of the precoat and tends to decrease the topcoat dewatering rates (*i.e.* dehydration velocity). Furthermore, the inclusion of coarse carbonate in the precoat reduces the incidence of streaking in double coated papers [71]. During coating color application, the topcoat performance is solely controlled by the precoat layer. Nevertheless, and it should be expected so, some final properties of the double coated paper are directly influenced by the topcoat layer. For instance, if cracking tendency is the key factor for sheet quality, the total coatweight applied becomes the most important controlling factor [70]. Similarly, the drying of the topcoat layer is very important for the final properties of double coated paper. Nissinen [68] points out that the quality of double coated fine paper mostly depends on the moisture level, mainly after topcoat application.

He notices that the final moisture, and even the middle layer moisture in three layers, is quite related to mottling.

2.5 Conclusions and implications

We have reviewed and analysed the effects of different concepts and methods on the coating paper properties: among others calendering, pigment replacement, pigment and chemical substitution. From the literature review, it is apparent that the double coated papers properties in relationship with above concepts have not been largely and fundamentally analysed. Our remark is especially true when considering the architecture of the pore structure in the various layers in relationship to the double-coated paper properties: little understanding of the true fundamentals exists. Most of the studies evaluate the effect of the precoat on the final printability but are limited to the single precoated paper: understanding of the interaction between the two layers and on the final topcoat is still somehow lacking.

The characterization of the different layers and understanding the mechanisms and interactions of how the layer truly affects the final coated paper property, *i.e. how the layer truly works*, is a key factor to improving the printing characteristics and quality of double-coated papers. In present literature review, we explain how the pore structure may be an important factor to understanding such phenomena. The porous structure of coating layer depends on coating color formulation, pigments and their combinations, but also on pigment particle size distribution and particle shape. The porous structure is also impacted by the binders, either synthetic or natural, by the chemical additives, *e.g.* associative thickeners, by the coating color application, and by the drying processes. We emphasize here that the particle packing, considered as one of the most important pigment properties, is directly related to the coating pore structure, which in turn affects the optical, mechanical, and printing qualities of the coated paper. Such results suggest that high shape factor pigments may block pores to reduce the penetration of the coating color. Therefore, the type of pigments particles and their mixing ration with other pigments directly determine how the structure of the coated paper is or can be developed. One study indicates that the type and the particle size of the pigments in a precoat for-

mulation may directly influence the finished properties of a double coated sheet. One author suggests that the precoat formulations have significant effect on topcoat dewatering while another concludes that “some final properties” of the double coated paper are directly influenced by the topcoat layer. Our review highlights the importance of the latex used in the topcoat formulation on the printing properties. Indeed, the latex alone, or in addition with other chemicals, is known to influence the coating structure.

Precalendering before coating is an interesting strategy to control the total calendering operation load applied onto a coated sheet. For wood free paper, it may result in positive effects on the properties of the coated end product. We have also shown that the interactions between the coating layers and the base paper are critical parameters to consider when producing a new or a modified coated paper grade.

As a consequence, on the basis of our own production and commercial experience comforted by present literature review, we have designed a study to verify how the precoat layer characteristics, mainly the structure parameters, could affect the final structure and printability of double coated papers. We thus designed experimental groups of paper to develop various coating structures in accordance with our research work objective and hypothesis. The objective is simple but quite complex: we surmise that it is possible to design the coating layers if a thorough understanding of the main parameters that affect the structure is achieved. With our industry perspective combined with present literature review, we focused the design parameters on partial or total pigment substitution in the precoat layer, precalendering of the precoat layer with a focus on temperature and calendering pressure, a point-study on the binder effect in the precoat. For the topcoat, due to the research work objective, we surmised that using the most commercially used latexes would bring the necessary additional topcoat parameters. Indeed, our hypothesis here is that the effect of the precoat may differ upon the various topcoat latexes.

Finally, as we focused the research on the structure of the various layers, we realized that we needed a method that would allow us to separate effects related to the finest pores in both the topcoat and precoat structures. Accordingly, we deemed it was feasible to improve the treatment of mercury intrusion data, and that is was indeed necessary, to be able to analyze in detail the pore size distribution and available pore volume of

each structure, *i.e.* the precoat and topcoat layers, both as a single combined layer and separately.

Chapter 3 - Discussion and analysis of the characterization methods

3.1 Introduction

We have seen that the pore structure of the paper and the coating layer are important concepts to characterize and to understand the final physical, optical, and printing properties of the coated paper. As the porous network controls both the ink absorption during paper printing and coating applications, in order to fully understand the basic differences brought about by precoating and calendaring, we selected characterization methods that involve liquid penetration.

The behaviour of a fluid in contact with a porous structure has been extensively studied in different industry sectors: petroleum, geology, agricultural etc. As both the base paper and the coating layer are porous structures, we may apply the penetration concepts that were developed in these other sectors. Nevertheless, the application of these concepts to the paper industry has to be tailored to describe more accurately the fluid behaviour on and within a base paper or any coating layer. Understanding the base paper structure and/or a coating structure are key factors to explain how the ink penetrates in a given substrate. Similarly, applying a coating layer over a substrate is done when the coating colour is still in a liquid form.

Therefore, it is very important to understand how the liquid movements behave after an application of a liquid over a structured substrate composed of a network of pores and capillaries (channels) with many varying shapes. The paper and/or coating layer pores and capillaries also present a large number of sizes and diameters. The wet coating layer is composed of pigment(s), binder(s), chemical(s), and water associated with these components and/or added to the coating mixture. The mixture rheological behaviour is controlled by the nature of the components and the interactions among the components. When the wet coating is applied to a substrate, the components and the water begin to move, rearrange themselves one versus the other (for instance “binder migration”); the

movements and rearrangements are controlled by the absorption behaviour of the fluid into the paper and/or the coating layer.

When a coating layer is applied over a substrate, the components may either deeply penetrate in the substrate or preferably stay on the surface. The quality of the final product changes greatly with either process, depending on whether the coating layer stays on the surface or penetrates into the media. Thickeners or rheology modifiers are widely used to modify (normally slowing down) the dewatering and/or to minimize the movements of the pigment(s) and binder(s). That is why, on one hand, the relationships between the properties of the coating suspension and the final (dry) coating layer [28] has been widely studied. On the other hand, the differences between a fluid applied over a base paper (fibres with filler) versus over another coating layer (most of the time a dry layer) are also critical.

These concepts have been treated by many researchers [75-80] as fluid movements are not straightforward. Indeed, each parameter controlling the flow behaviour must be analysed separately from the others in order to understand the basic mechanisms. Schoelkopf *et al* [81] propose equations describing the liquid flow through porous substrate containing a driving force. The driving force can either be a wetting force leading to capillary and/or an external pressure, which then competes against flow penetration resistance force or so-called drag term. Viscous friction is the classic drag component. Schoelkopf *et al* [81] also propose other contributions to account for flow dissipation mechanisms like turbulent flow and liquid flow discontinuity close to the meniscus in the case of capillarity.

The fundamentals of fluid movement are further explained by Gane *et al* [76] in terms of viscosity, surface tension, density, and of course vapour pressure. Viscosity acts to slow flow in small capillaries after liquid has penetrated the larger pores of the porous system. The effect is most influenced by the permeability of the substrate. Permeability is defined by the Darcy law and is an average measure of liquid flow through a saturated substrate under external pressure. Surface tension interacts with the surface energy of the material making up the substrate and/or the coating layer. In the coating layer, it is usually defined by mineral, surfactant/dispersant on the mineral surface and the binder

system. Both polar and non-polar liquids will wet most of the coatings. Wetting the surface provides the force which will then drive absorption of the coating in the substrate. Density is important when considering short timescale effects within the substrate. Indeed, after the coating colour impacts the substrate, the liquid is facing the choice between penetrating a fine pore and a large pore. The large pore will absorb more liquid mass and so inertia will attempt to delay absorption. The fine pore ($\sim 0.1 \mu\text{m}$) absorbs liquid rapidly for about 10 ns before viscosity acts to slow down the flow, but during that time interval the coating pore is already full of liquid [82].

Therefore, the fluid movement is separated into:

- 1- Coating color penetration or permeability (imbibition)
- 2- Coating penetration by capillarity
- 3- Thickening mechanism
- 4- Dewatering by filtration

In conclusion, although many methods are reported in the literature for characterizing pore structure and flow behaviour, for the reasons explained above, I have chosen the following methods to determine and/or characterize the porous structure of coated papers.

- Liquid drop contact angle
- Mercury porosimetry (normalized with the stain imbibition technique and data treatment within Autopore®)
- DELTACK Prüfbau

In my study, I have selected to use mainly mercury intrusion, although a very complex and even a quite complicated test to perform and to analyse, as it provides more detailed information on the pore structure and the pore structure distribution. The stain imbibition technique is nevertheless used to characterise and to normalize the base paper with the hexadecane method. The normalization method is explained later (heading 3.5)

3.2 Contact angle method

In order to measure contact angle, a very small droplet of liquid, around 5 picoliters, generally water, is applied on the surface of the substrate to be measured and the angle between the droplet and the substrate surface is accurately measured (Figure 3-1). The angle between the droplet and the substrate surface provides information on the substrate wettability (Figure 3-2).

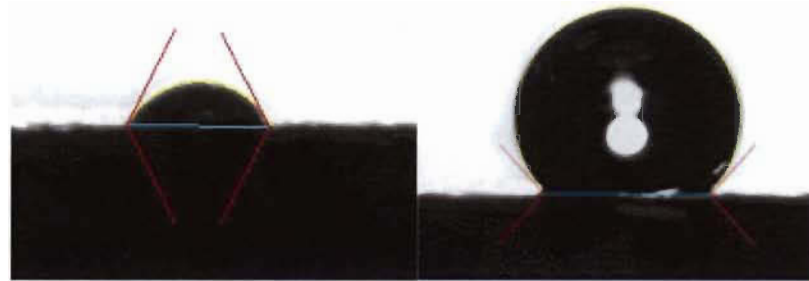


Figure 3-1 Water drop with an angle lower than 90° (left) and greater than 90° (right)

The wettability between a liquid and a surface is defined by equation 3-1

$$S = \gamma_s - \gamma_l - \gamma_{sl} \quad \text{Equation 3-1}$$

where

S = spreading coefficient

γ_s = superficial tension of the solid (free energy of the solid)

γ_l = superficial tension of the fluid (free energy of the fluid)

γ_{sl} = interfacial tension between the liquid and the solid.

When the spreading coefficient is positive, the liquid spreads on the surface. When the spreading coefficient is negative, the liquid does not spread on the surface. The phenomenon is illustrated in the Figure 3-1 and Figure 3-2. In other words, when $\cos \theta > 0$, the surface is hydrophilic: the liquid is absorbed by the substrate; when $\cos \theta < 0$, the surface is hydrophobic: the liquid does not spread on the surface of the substrate. The co-

sine of the angle between the droplet and the substrate (solid) is defined by the equation 3-2.

$$\cos \theta = \frac{\gamma_s - \gamma_{sl}}{\gamma_L} \quad \text{Equation 3-2}$$

where $\cos \theta$ = contact angle between the fluid and the solid

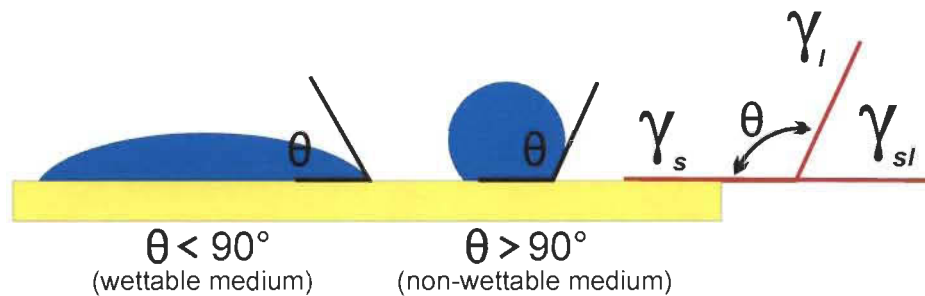


Figure 3-2 Contact angle θ between a substrate and a liquid

The contact angle may also be measured at different time intervals to analyse liquid absorption as a function of time. The phenomenon is illustrated in Figure 3-1. The red lines in the Figure 3-1 outline the contact angle and form a line around the droplet at the liquid-solid-vapour interface. The analysis of the variations of the red lines when a droplet is deposited on a horizontal solid surface from the start of the droplet deposition until the final stabilization describes the droplet absorption. Immediately after droplet deposition, the contact angle is necessarily close to 180° .

The angle measured at the liquid-solid-vapour interface determines the liquid-vapour tension vector. After complete deposition, the droplet contact angle decreases and therefore the horizontal component of the liquid-vapour tension decreases as energy balance should reach the minimum level. The equilibrium occurs when the sum of all vectors and horizontal components equal zero. If the contact angle is lower than 90° , the sign of the vector becomes negative. The liquid absorption theory will be further explained for the mercury intrusion method.

3.2.1 Contact angle theory

A drop of liquid on a solid surface is in contact with the substrate and with another fluid surrounding the droplet which is either the droplet liquid vapour or air. The configuration is illustrated in Figure 3-3 which presents the various interfaces: liquid-solid, liquid-vapour, and solid-vapour. Another interface is represented by a continuous line around the droplet that describes the liquid-vapour-solid boundary.

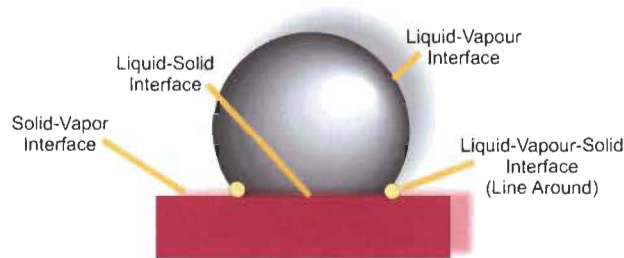


Figure 3-3 Droplet of non-wetting liquid on solid surface.

Each interface corresponds to an interfacial tension symbolised as γ_{l-v} for the liquid-vapour interface, γ_{l-s} for the liquid-solid interface, and γ_{s-v} for the solid-vapour interface. The force of surface tension is usually provided per unit length (dynes/cm) and act tangentially to the interface. The Young equation shown in equation Equation 3-3 gives the relation of the contact angle in the triple point energy, *i.e.* interfacial tensions, of the 3 interfaces: solid-vapour, solid-liquid, and liquid-vapour:

$$\gamma_{S-V} + \gamma_{L-V} \cos(\theta) = \gamma_{S-L} \quad \text{Equation 3-3}$$

The behaviour of a droplet deposited on a surface may be described by 3 vectors that change with time until equilibrium, minimal energy, is obtained. The phenomenon is described in Figure 3-4 [83]. In Figure 3-4 (a) the droplet has just been deposited on the surface. In Figure 3-4 (b), the droplet begins to spread and the forces are not yet balanced because the surface tension vectors of the interface solid-vapour and liquid-vapour are greater than the surface tension vector solid-liquid. When the contact angle goes over 90° , the sign of the cosine becomes positive. At energy equilibrium illustrated in Figure 3-4 (c), the droplet does not penetrate anymore in the substrate.

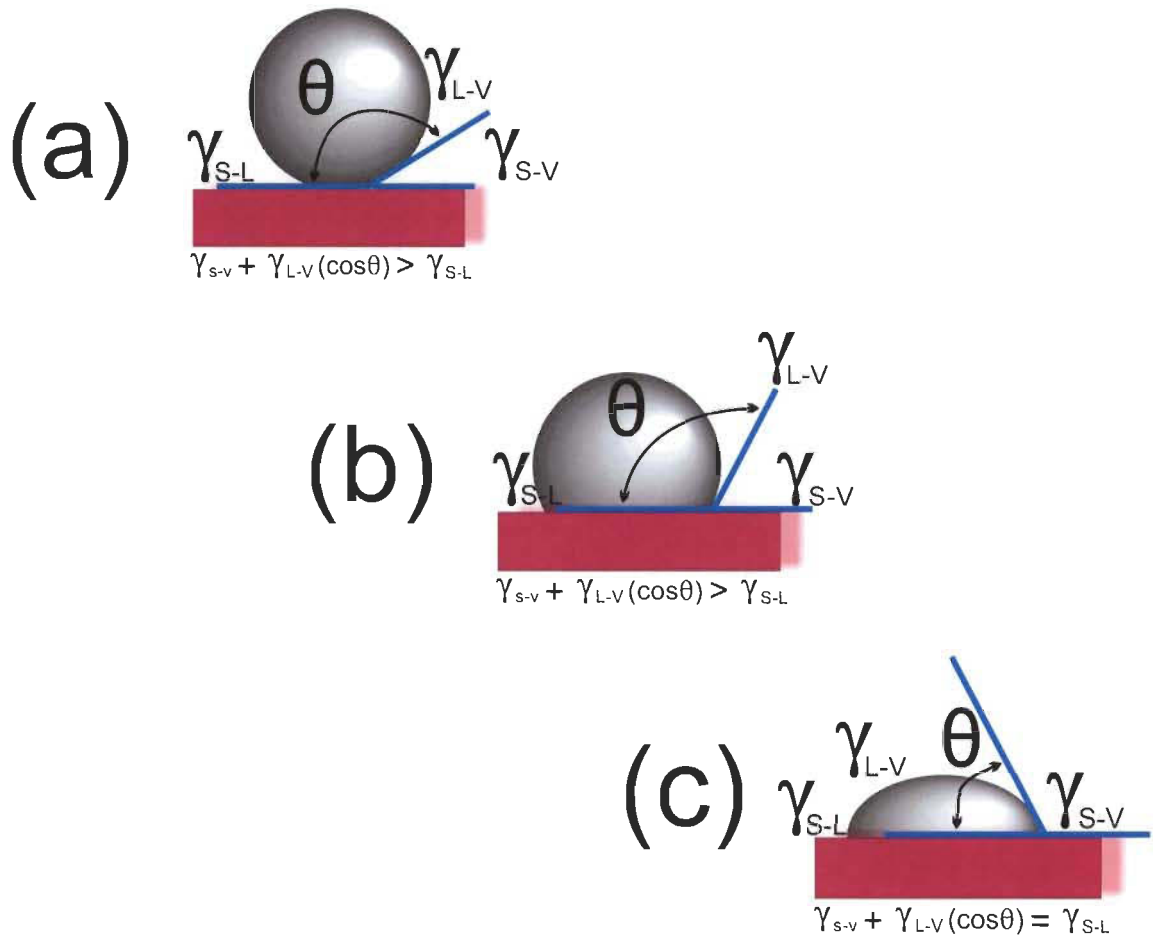


Figure 3-4 Droplet on a solid surface at various absorption stages: (a) initial deposition, (b) during absorption, and (c) at equilibrium, end of the absorption.

3.2.2 Contact angle: test description

In order to measure contact angle, a droplet, usually 10 nanoliters (nL) is deposited on a surface. The contact angle measuring apparatus takes measures as soon as the droplet hits the surface by evaluating the contact angles as a function of time. Water is normally used with paper but various liquids may be utilized to create the droplet. As seen in Figure 3-4, the angle is measured immediately after droplet deposition (a), and then again over a specific period of time (b), to evaluate the time needed for the droplet to stabilize (c) on the surface. The test procedure is illustrated in Figure 3-5. In the apparatus we used, the volume of the droplet is 10 nanoliters. The droplet is placed on the surface of the sample, securely fastened with tape, and a picture is taken every 100 ms. Three measurements are done for each test. If a measurement is significantly different from the

other, a new one is done. The contact angle result is the average of the 3 values measured on the CLC coated side from each sample.

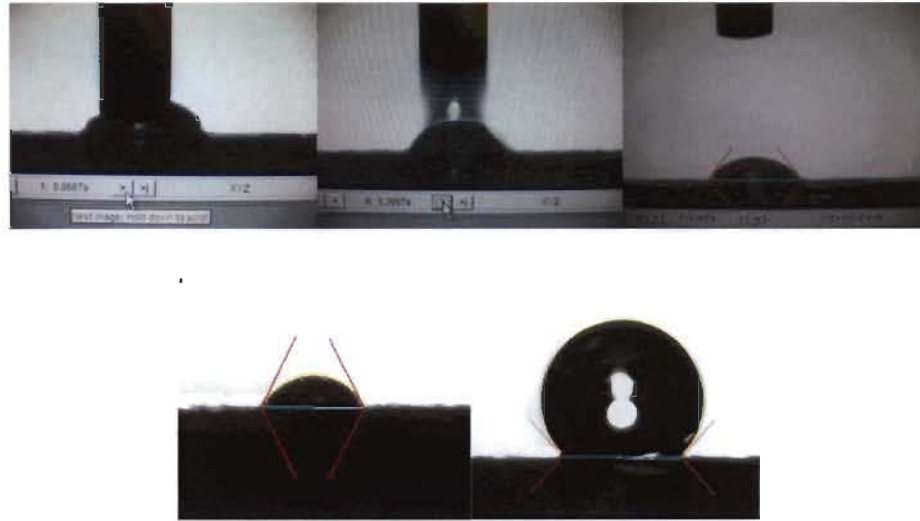


Figure 3-5 Droplet deposit, measurement and final results for angle lower (left) and greater (right) than 90°

3.3 Mercury intrusion

The mercury intrusion method is based on the principle of the penetration of a porous substrate by a non-wetting liquid under pressure and the pressure needed to penetrate a pore of a given size. The phenomena are essentially described by two laws: the Darcy law that relates the penetration rate as a function of pressure and permeability, and the Washburn equation that links the pore size to the pressure.

3.3.1 Darcy's Law

Darcy law is widely used and accepted to measure the permeability of a medium. The permeability (k) is a physical characteristic of a substrate that describes how a fluid passes through a porous network [84]. The Darcy law as defined by the equation 3-4 [84, 85] relates the penetration flow rate to the differential pressure; the differential pressure is generated by the characteristics of the skeletal element crossed (or permeated) which resist the fluid penetration:

$$Q = \frac{k}{\eta} \frac{\Delta P}{L} A \quad \text{Equation 3-4}$$

Where Q is the flow rate, A is the element area of the porous medium being penetrated, k is the permeability, η is the fluid dynamic viscosity, and ΔP is the pressure drop across the sample thickness or length (L). From equation 3-4 the permeability is calculated as follows (equation 3-5):

$$k = \frac{Q}{A} \frac{L}{\Delta P} \eta \text{ (with unit m}^2\text{)} \quad \text{Equation 3-5}$$

It is important to understand the difference between the permeability (k) and the coefficient of permeability (K) or hydraulic conductivity. The permeability (k) is a characteristic of the porous medium and highly dependant on the porosity which it is itself directly related to the physical characteristic of the layer, such as density, pore size, and tortuosity in the medium [86].

The coefficient of permeability (K) is a characteristic of the flow through a material for a specific fluid. The coefficient of permeability is defined by equation 3-6 [87]:

$$K = \frac{k}{\eta} \quad \text{Equation 3-6}$$

Due to the fact that Darcy law does not fully explain all the results obtained from many research studies, it has been modified to consider additional parameters. The most famous modification is the known as the Carman-Kozeny law [88], only valid for laminar flows, which takes into consideration specific surface area, hydraulic radius, and tortuosity.

3.3.2 Washburn Equation

The penetration of a capillary by a liquid can be described as follows: along the boundary defined by the solid-vapour-liquid interface, all the forces involved are at equilibrium. The forces contributing to the formation of the meniscus inside the capillary are the cohesion of the fluid and the fluid adhesion to the capillary wall. The meniscus is concave for a wetting fluid and convex for a non-wetting fluid (Figure 3-6).

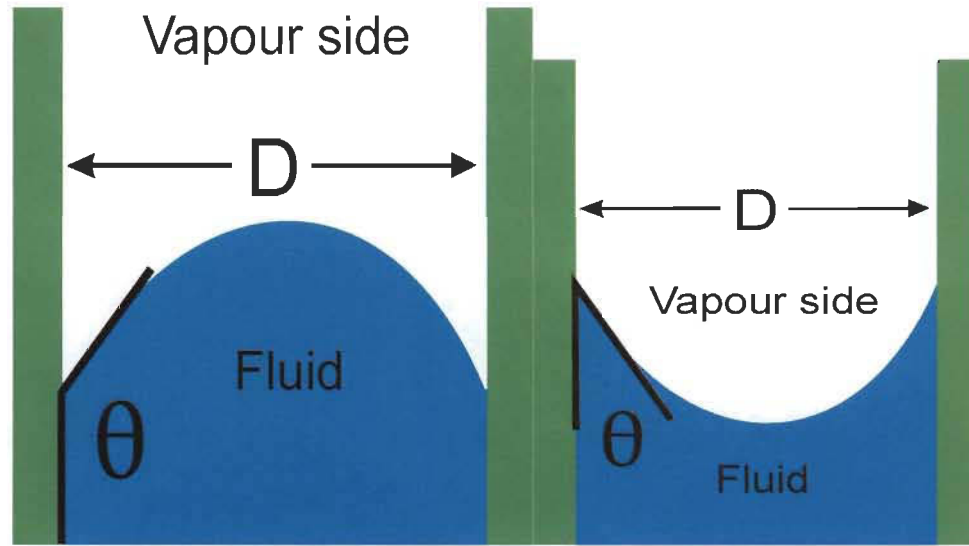


Figure 3-6 Wetting and non-wetting fluid in a capillary

In 1921 Washburn [89] derived an equation relating internal, tension surface, and external forces, applied pressure, acting on a non-wetting fluid penetrating a circular capillary. Washburn demonstrated that the pressure to force a non wetting fluid to enter a pore is directly proportional to the surface tension of the fluid and the contact angle of the liquid with the solid surface. The internal force acting against the non-wetting fluid penetration is related to the cosine of the fluid contact angle θ (Figure 3-6) around the circumference of the capillary ($2\pi r$, r being the capillary radius) as described in equation 3-1:

$$F_{out} = 2 \pi r \gamma \cos \theta \quad \text{Equation 3-1}$$

In essence F_{out} is the external force needed to force the non-wetting fluid to penetrate the capillary, γ is the surface tension of the non-wetting fluid. Therefore to make the non-wetting fluid to penetrate the capillary we need a pressure P as (equation 3-2):

$$P = \frac{F_{out}}{\pi r^2} \quad \text{Equation 3-2}$$

From equations 3-1 and 3-2 we may derive the well-known Washburn relation as described in equation 3-3.

$$P = \frac{-2 \pi r \gamma \cos \theta}{\pi r^2} \quad \text{Equation 3-3}$$

or, considering the pore diameter (equation 3-4):

$$P = \frac{-4 \gamma \cos \theta}{D} \quad \text{Equation 3-4}$$

3.3.3 Mercury porosimetry

The measurement of the porous structure with mercury as a non-wetting fluid was introduced by Ritter and Drake in 1945 [90]. Mercury porosimetry is based on the characteristic of mercury being a high surface tension liquid, strongly non-wetting for most substrates [91]. Mercury intrusion provides a complete pore size distribution spectrum as a function of applied pressure. At low applied pressures, the largest capillaries are filled by mercury while the smallest pores require very high pressures, up to 60 000 psi or 415 mPa [92]. From the Lucas-Washburn equation seen before section (3.3.2), the authors calculate the pore size distribution, the total pore volume, and the pore diameter calculate from capillary pressure-intrusion curves. The pore size distribution provided by mercury porosimetry is a physical characteristic of a porous medium.

The volume of mercury penetrating the substrate pores is measured directly as a function of the applied pressure P which is then converted to a plot of cumulative intrusion volume versus the pore diameter D as calculated from (equation 3-4) [92]. The method of calculation may nevertheless result in some inaccuracy because of the capillary penetration lag with large pores. Further measurement error may arise when a pore with a narrow entry or capillary (also called a bottleneck) is not filled until the pressure applied is high enough to overcome the capillary pressure. The result is that a large pore may actually be identified as a small pore. Although some studies show that small pores

could prevent the filling-in of larger connected pores, Yamazaki and Munakata [93] find results which are not in agreement with the results explained above.

Ridgway and Gane [94] explain how some lack of experimental reproducibility may be associated with large void features. The lack of reproducibility is however confined to the low pressure intrusion region. It is a combination of variations in the samples preparation, the introduction of the sample in the measuring chamber of the mercury intrusion penetrometer, and even the filling-in by mercury of surface and edge features that are not an integral part of the porous structure under analysis.

3.3.4 Further considerations on liquid penetration of complex structures

In applying mercury intrusion technique and results to paper and paper coating, one should consider some limitations and specific aspects of the technique. Indeed, Gane [82] showed that liquid penetration into pores is driven by the liquid viscosity, surface tension, liquid density, and of course the liquid vapour pressure.

Gane [82] shows that viscosity acts to slow flow in small dimension capillaries, but only after a sufficient quantity of liquid has partially saturated the porous system. Consequently, the effect is mainly influenced by the substrate permeability as defined in the Darcy law (i.e. an average measure of a liquid flowing through a saturated medium under external pressure).

Mercury intrusion is related to surface tension which interacts with the surface energy of the material making up the substrate. In paper coating, materials may be minerals, surfactant/dispersant attached to the mineral surface, and the binder system. It should also be reminded that both polar and non-polar liquids wet most coatings; the wetting thus provides the force which drives absorption.

Liquid density is important when considering short timescale effects and interactions within the substrate. The consideration does not necessarily apply at time zero (beginning of the mercury intrusion) but whenever a liquid is facing the choice between penetrating a fine pore or a large pore. On the one hand, the large pore will absorb more mass

of liquid and so inertia will counter and delay the absorption. On the other hand, the fine pore will absorb liquid rapidly for about 10 ns ($\sim 0.1 \mu\text{m}$) before viscosity will slow down the flow. However, due to the small pore size, by the time penetration lag should occur, the coating pore will most probably be already full of liquid.

Therefore, to understand liquid (here mercury) absorption into paper coatings, one needs to reason in terms of complex networks and not simple capillaries. In order to consider the effect of inertial wetting, two parameters should always be taken into account: first, how big are the pores in comparison with the substrate (for coating it will be the base paper structure), and second what is the substrate permeability that will be lost due to liquid absorption (liquid phase of the coating colour)?

Consequently and besides mercury intrusion, when analyzing a coated paper grade with a precoat layer, three types of structures should be considered: a very open pore structure formed by the base paper, a less open structure represented by the precoat, and a very fine pore structure constituted by the top coat layer.

In essence, it is only after a given time delay (sufficient to allow large pores to be saturated) that the network with the finest pores (in contact with the larger pore network) will be able to uptake liquid. For instance, a gloss topcoat will withhold liquid in its finest pores and allow liquid to penetrate the coarser precoat network by surface wetting the larger precoat pores thus the saturated top coated structure will act as a barrier to further liquid penetration. It implies that the precoat pores will not be filled by sole capillary forces but only when some external force will be applied.

Similarly, the same rule is applicable between the coating and the base paper structures. The base pores will not and cannot draw liquid out of the coating by capillarity as the coating pores are finer than the base paper pores. The reason for a base paper to draw liquid from the top coating layer does necessarily require another mechanism. It is proposed here, from our discussions with P. Gane [82], that a mechanism based on fibre surface wetting combined with fibre wall and lumen wall nanopore filling which may further be related to vapour pressure, and subsequent condensation of the vapour, may provide a better explanation than mere capillarity.

3.4 Equipment and methods – Mercury intrusion

To simplify the Lucas-Washburn equation [89] used as a basis for mercury intrusion, let us consider that the surface tension of mercury is 485 dynes/cm and the contact angle between mercury and most papers (including coated grades) is 130°, i.e. a cosine value of minus 0.36729133. Therefore the basic mercury intrusion equation that relates pore diameter to pressure becomes (equation 3-5) below:

$$D = \frac{712,54}{P} \quad \text{Equation}^1 \text{ 3-5}$$

As the intrusion volume is measured with increasing pressures, each pressure applied corresponds to the measurement of pores of an exact pore size (given by above equation 3-5) which are filled with mercury. By measuring the volume of mercury penetrating a pore structure with increasing pressures, it is possible to calculate the pore volume and the pores size distribution.

The mercury intrusion is performed with a Micromeritics Autopore III that allows a maximum pressure to be applied of 414 MegaPascal (MPa) corresponding to about a 0.004 µm Laplace throat diameter (minimum pore dimension that can be measured). The equilibrium pressure time is set to 60 seconds. The mercury intrusion volume is obtained by measuring the variation inside a calibrated capillary tube (stem) that prolongs a bulb or sample holder.

All mercury intrusion data are normalised with a measure of the empty penetrometer, with no sample inside the penetrometer bulb (or blank), to allow for the penetrometer chamber deformation under pressure, mercury compression, and compressibility of the solid phase of the sample. The use of the blank penetrometer correction is explained below in the equation used for the Autopore (equation 3-6) to calculate the true volume intrusion in the sample. It is described in an article by Gane *et al* [95] as:

¹ 712.54 = -4 * cos 130° * 485 = -4 * - 0.36729133 * 485

$$V_{int} = V_{obs} - \delta V_{blank} + \left[0,175(V_{bulk}^i) \log_{10} \left(1 + \frac{P}{1820} \right) \right] - V_{bulk}^i (1 - \Phi^i) \left(1 - \exp \left[\frac{P^i - P}{M_{ss}} \right] \right)$$

Equation 3-6

where

V_{int} volume of mercury intrusion into the sample

V_{obs} intruded mercury volume reading

δV_{blank} blank run volume reading

V_{bulk}^i sample bulk volume at atmospheric pressure

P applied pressure

Φ^i porosity at the atmospheric pressure

P^i atmospheric pressure

M_{ss} bulk modulus of the solid phase of the sample

The Micromeritics Autopore III equipment is built to run the mercury intrusion test in two different sequences as shown in Figure 3-7.



Figure 3-7 Mercury Intrusion equipment

The first sequence corresponds to the test performed at low pressure, followed by a second phase at high pressure. The equipment uses a transducer to detect the mercury volume variation in the stem mounted with the sample holder (Figure 3-8).



Figure 3-8 Sample holder with his stem mounted for the mercury intrusion test

An important experimental procedure point to provide good test accuracy is the method used to set-up the paper sample to be analysed. The method is described by Ridgway and Gane [94]. The sample has to be mounted to ensure an easy flow of the mercury on the entire surface. Furthermore, the paper sample needs to have enough total surface area to ensure that the mercury penetrating the pore structure will use up most of the mercury (around 80%) inside the stem.

To achieve that, a piece of metal wire (stainless steel as to avoid the formation of mercury amalgams) is wound into a spiral together with the paper sample. The outer diameter of the prepared sample should not allow any contact with the penetrometer wall.

For most papers, sample weight around 0.2-0.3 g will fit into a 15 cm³ penetrometer with a 0.392 cm³ stem volume (standard on the Autopore instrument). An example of the sample preparation with the wire and inside the penetrometer is shown in the Figures 3-9 and 3-10.

The Micromeritics Company further explains how the stem and bulb sample function (see Appendix 1). The Appendix 1 also describes the main parameters that can be calculated from the mercury intrusion curves.

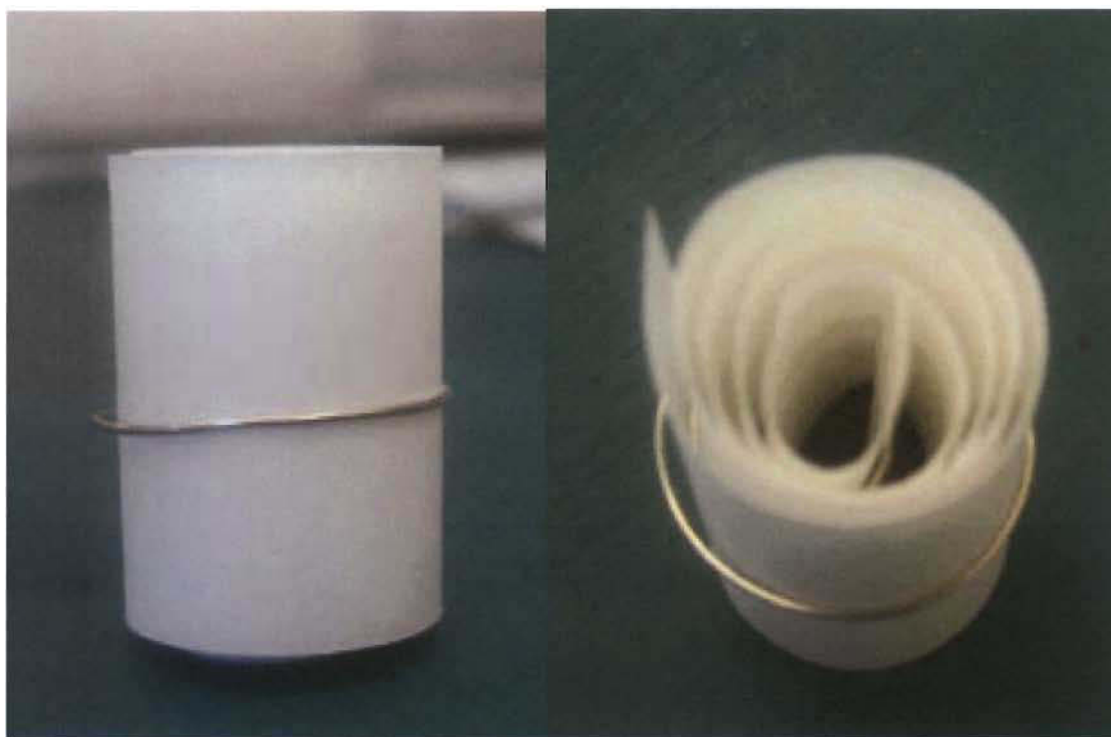


Figure 3-9 Paper sample set up for the mercury intrusion test



Figure 3-10 Paper sample in his penetrometer

3.4.1 Repeatability of the mercury intrusion test

Mercury intrusion testing is a useful tool to analyse any type of structure. However, this test is sample destructive and the repeatability is greatly related to the quality of the sample and the method used to treat the data. A study done by Ridgway [96] clearly shows the mercury intrusion test is highly repetitive. Table 3-1 and Figure 3-11 show the results of this study. The corrected data is acceptable when the hexadecane cut-off is done correctly and applied in the Autopore® program. It has been clearly demonstrated the occurrences and defects present on the surface of the paper, greatly affect mercury intrusion final results. Therefore the variations in the results found come from the paper sample itself instead of method of measurement.

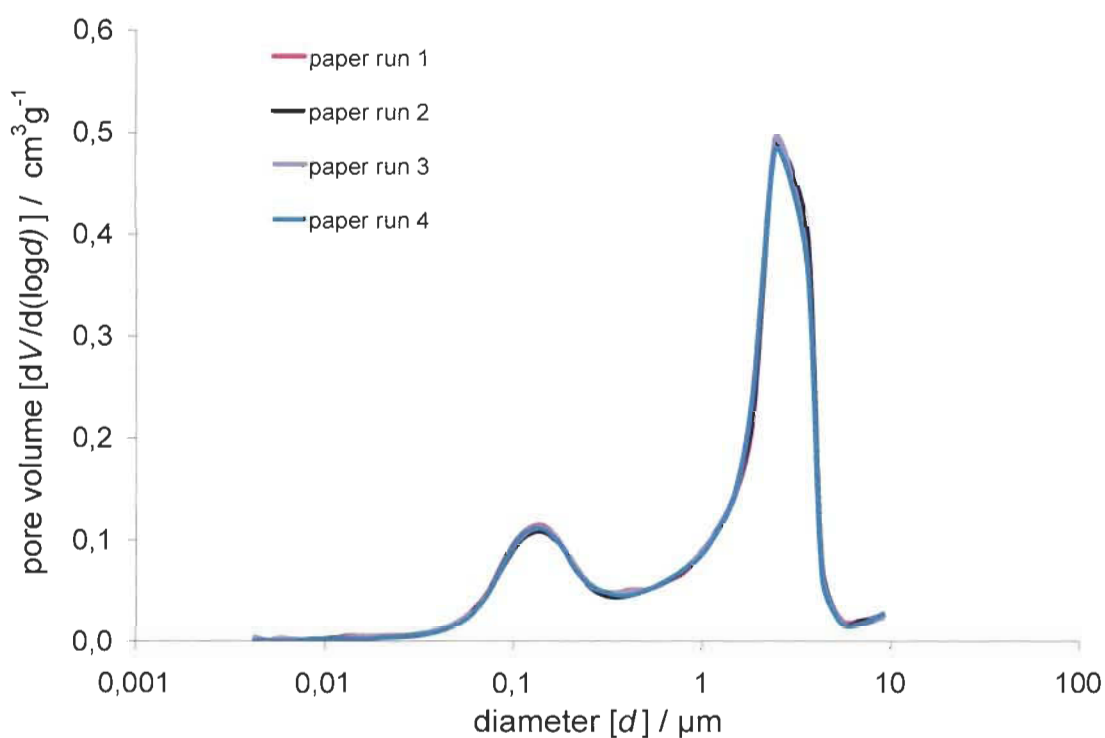
The coefficient of variation (COV) is given by the equation 3-7:

$$(\text{Maximum Value} - \text{Minimum Value}) \div \text{Mean} \times 100$$

Equation 3-7

Table 3-1 Repeatability of the mercury intrusion test

Test	Total pore volume [96]
Paper run #1	0.27759 mL/g
Paper run #2	0.27440 mL/g
Paper run #3	0.27674 mL/g
Paper run #4	0.27190 mL/g
<u>Mean</u>	<u>0.27516 mL/g</u>
<u>Standard Deviation</u>	<u>0.00256</u>
<u>Coefficient of variation (COV)</u>	<u>2.06%</u>

**Figure 3-11 Mercury intrusion curves with samples from the same piece of paper**

3.5 Normalisation and optimization of the mercury intrusion data analysis

The mercury intrusion test generates a data file with a series of results with pressure related to the volume of mercury intruded in the sample, from atmospheric pressure, about 0.1 mPa up to 414 mPa. The data file also contains the desorption data or decrease in volume when the pressure is released. The difference between the upward and downward curves is called hysteresis. As the file contains only raw untreated data, the data may and must be normalised to enable proper analysis of the porous structure being analysed. We propose below a new method to extract pore distribution using successive corrections from either a precoat or a top coat layer, calendered or not, from a correction of the data based on the analysis of the base uncoated or precoated or uncalendered paper and information from the analysis of the hexadecane imbibition technique.

3.5.1 The hexadecane imbibition method and analysis

In the normalization technique, and only for uncoated base stock papers, we use the hexadecane analysis to determine the cut-off points for low mercury intrusion pressures.

In a paper sample, the very large pores, defects or mercury occlusions² [94] generate a high absorption volume of mercury (Figure 3-12) and affect the total pore volume results. The interstices and defects provide artificial information (artefacts) that must be removed from the basic data file to ensure a good reliability and accurate analysis of the test. Such data management or “normalisation” to remove the data artefacts can be achieved by using information from the hexadecane imbibition method. The characteristics of key fluids (mercury, hexadecane, and water) are shown in the table 3-2. Hexadecane is a non polar, aliphatic cyclic, non-wetting fluid that completely fills all void volumes within a paper [76]. The different base uncoated papers used in our work were analysed to find the total pore volume available with hexadecane. Practically, the base

² At very low pressure an “occlusion” first prevents mercury to intrude an artificial surface pore. Such a pore might be created by a raised fibre. When pressure increases, mercury will overcome the occlusion, penetrate the artificial surface pore and create an artefact in the pore distribution curve.

paper samples are cut in small squares (2 cm X 2 cm) which are dried and then weighed. To ensure good repeatability, five tests are performed for each base paper sample. The paper samples are suspended by a thread with only a corner in contact with the hexadecane (Figure 3-13): the samples are not submerged in the fluid due to a risk of air entrapment which would affect the final results.

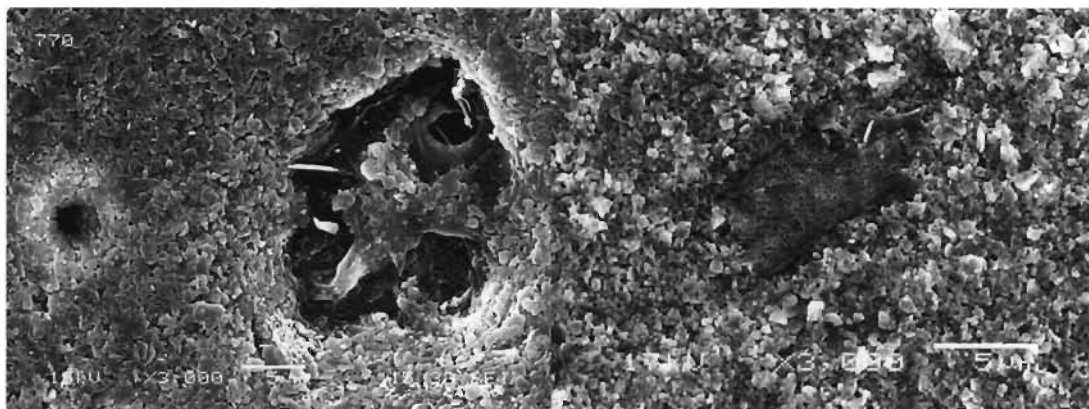


Figure 3-12 Example of surface defect affecting the mercury intrusion volume

Table 3-2 Surface Tension (mN/m) and Contact Angle (°) of the chemicals used in this study

	Surface Tension	Contact Angle
Mercury	485.5	130°
Hexadecane	28.1	1°
Water	71.99	15°

The hexadecane fills up the paper sample pores by capillarity action. Once the samples are saturated by hexadecane, they are weighed and the pore volume is calculated with the following equations 3-8, 3-9, and 3-10. An example of hexadecane calculations (base paper 2007-1-1) are shown in table 3-3.

$$W_{\text{absorbed hexa}} = W_{\text{hexa saturated base paper}} - W_{\text{dry base paper}} \quad \text{Equation 3-8}$$

$$V_{\text{absorbed hexa}} = W_{\text{absorbed hexa}} / 0.77 \quad \text{Equation 3-9}$$

$$\text{Total Pore Volume} = V_{\text{absorbed hexa}} / W_{\text{dry base paper}} \quad \text{Equation 3-10}$$



Figure 3-13 Hexadecane absorption by a base paper sample

Table 3-3 Hexadecane test results BS 2007-1-1

Sample	1	2	3	4	5
sample dry weight (g)	0.0406	0.0394	0.0333	0.0357	0.0332
saturated sample weight (g)	0.056	0.0516	0.0468	0.049	0.0456
Hexadecane weight (g)	0.0154	0.0122	0.0135	0.0133	0.0124
Total pore volume (mL/g)	0.493	0.402	0.527	0.484	0.485

Once the total pore volume per gram of sample is determined from the hexadecane analysis, it is used to normalise the mercury intrusion curve. To obtain a normalised mercury intrusion curve, the hexadecane total pore volume is subtracted from the total pore volume results obtained with the base paper mercury intrusion analysis. Considering that the hexadecane total pore volume mainly represents very large pores, defects, and occlusions at low pressure, the volume is subtracted from the mercury total pore volume of the base paper. The difference between both values then represents the actual pore volume in the base paper, without the defects, large pores, and occlusions. The difference value is subtracted from all the intrusion results in the data file. The point where the normalised curve crosses the x-axis becomes the cut off point for low pressure. The corresponding pressure (MPa) indicates the pore diameter corresponding to the cut off value. The cut off pore diameter represents the upper limit (large pores) used in the Micromeritics® Autopore III analysis for all samples (precoat, topcoat and calendered) derived from the uncoated base paper cut-off determination: i.e. data below the

cut-off limit are not considered for comparisons of the pore distributions. It also implies that data above the cut-off limit may be used to compare the actual effect of precoat, top coat, and calendering. Table 3-4 shows the hexadecane results and the pore diameter cut off point for each base paper used in the study.

Table 3-4 Base paper hexadecane and pore diameter cut off points

HEXADECANE TOTAL PORE VOLUME		Cut off point Pore diameter
BS 2007-1-1	0.478026900	53.8812
BS 2007-1-13	0.450303008	20.5708
BS 2007-1-15	0.453890373	39.2400
BS 2007-2-5	0.482528496	71.9300
BS 2007-10-5	0.500011513	72.0020
BS 2007-10-6	0.489464528	71.9236
BS 2007-10-7	0.511460924	71.9240
BS 2007-10-9	0.460735167	28.7859
BS 2007-10-12	0.466694138	71.9728
BS 2007-10-13	0.500236412	71.9728

3.5.2 Coating layer cut off point

The total mercury intrusion curves represent the total pore structure of the paper: fibre network and coatings included. However, for our study, only the portion of the intrusion curve representing the coating(s) is of interest. To do so, we first removed the portion of all mercury intrusion curves corresponding to the hexadecane pore volume as represented by the “hexadecane cut-off point pore diameter” (as listed in Table 3-4 for all 10 base papers used in the study).

An example of a series of pore distribution curves consisting of a base paper, the same base-paper with precoat, then with top coat, then calendered but with the pore section corresponding to the hexadecane cut-off removal is illustrated in Figure 3-14. To further the analysis and extract the sole information from the coating(s), the base paper was first

subtracted from the precoat, topcoat, and calendered intrusion results. To do so we used the “blank”³ file capability available in the Micromeritics® Autopore III program [97, 98]. As illustrated in Figure 3-15 for a given base paper used for demonstration purposes, the intrusion curves for the precoat, topcoat, and calendered samples all cross the x axis in the same area, around 0.65 μm : i.e. the difference for the corresponding pore volume between the base paper and the other 3 curves (precoat, top coat, calendered) becomes negative. By analysing the graph and the intrusion curves before subtracting the base paper, we conclude that the coating layer(s) begins where the curves cross the X-axis. Therefore, all the pore size values higher than 0.65 μm have been removed as they are not related to pores corresponding to the coating layers. Therefore, for this example, the values above are not significant for the analysis of the coating layers.

To further clean-up the data and truly isolate the pore distribution of the coating layers of interest, we established another cut-off point for the pores smaller than 0.01 μm . The 0.01 μm value is chosen because the corresponding intrusion pressure is 148 MPa (around 21 500 psi). Practically, such a pressure is much higher than any pressure encountered in a commercial press. We also know that very small pores affect the results due to their impact on the final total pore volume. Last but not least, very high intrusion pressures dilate the volume of the penetrometer bulb, thus creating a measure artefact.

According to the limits we just established for the high and low value in pore distribution, the pore interval used for the comparison and analysis of the coating layers (up to calendering) lies between values established in table 3-5 and 0.01 μm . Pores outside the interval are considered to be irrelevant for our analysis.

In the interval analysis defined above, the mercury intrusion curves still include the pores from the base paper. The base paper pores also affect the final total pore volume of the coating layers: they also need to be removed to obtain an accurate, base-paper independent, coating layer pore volume.

³ The complete normalisation method is explained in section 3.6 of this document

As shown in Figure 3-17 for the same sample as Figure 3-16, removing the corresponding base paper pores, we obtain normalized values corresponding exclusively to the coating structure itself.

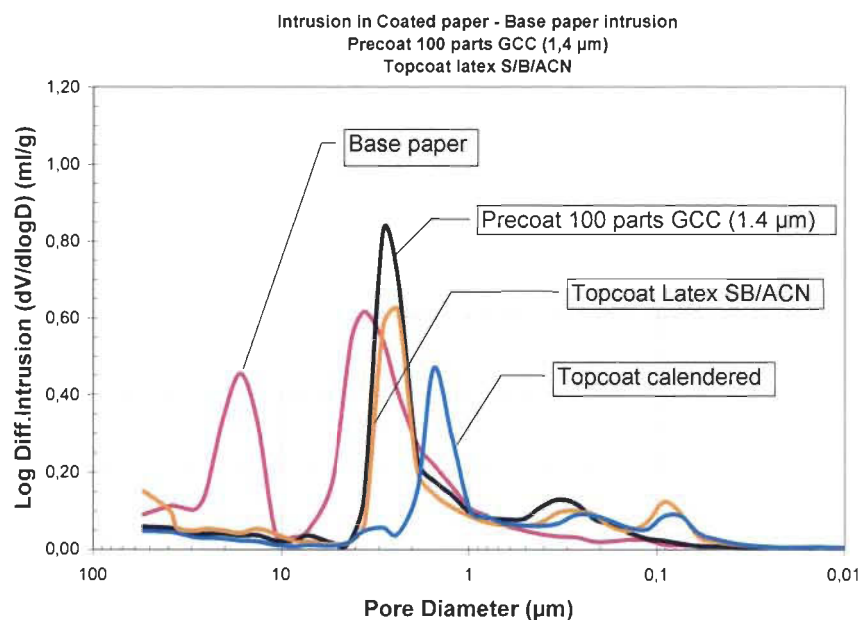


Figure 3-14 Mercury intrusion curves without normalization

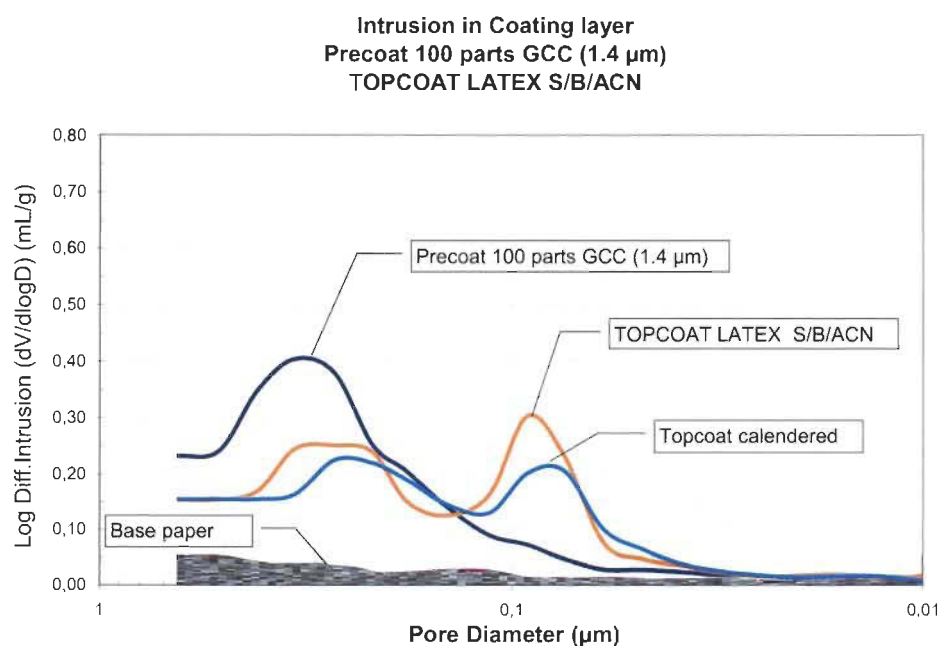


Figure 3-15 Base paper pore structure with coating structure

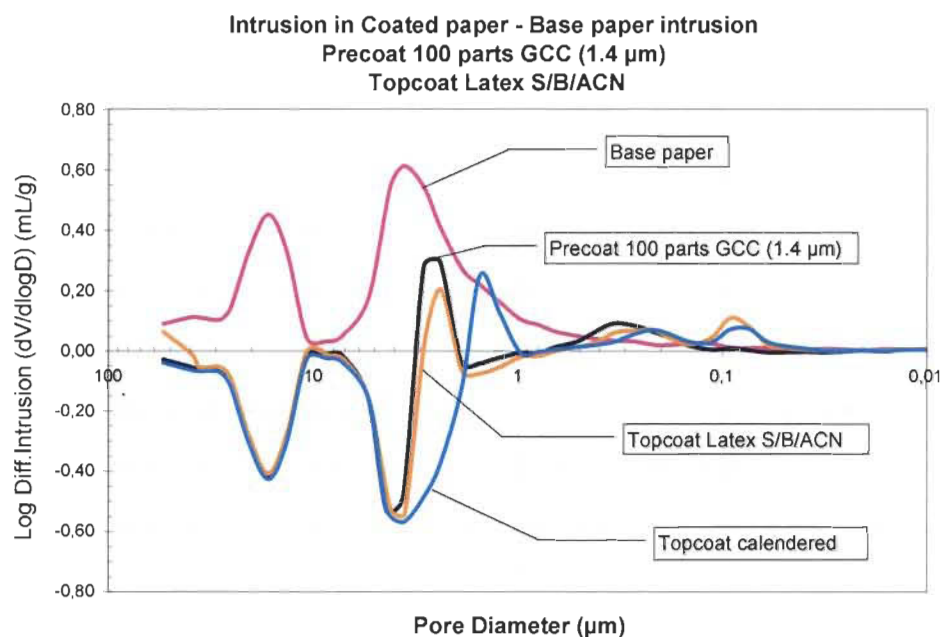


Figure 3-16 Mercury intrusion curves with base paper blank – cut off point for coating

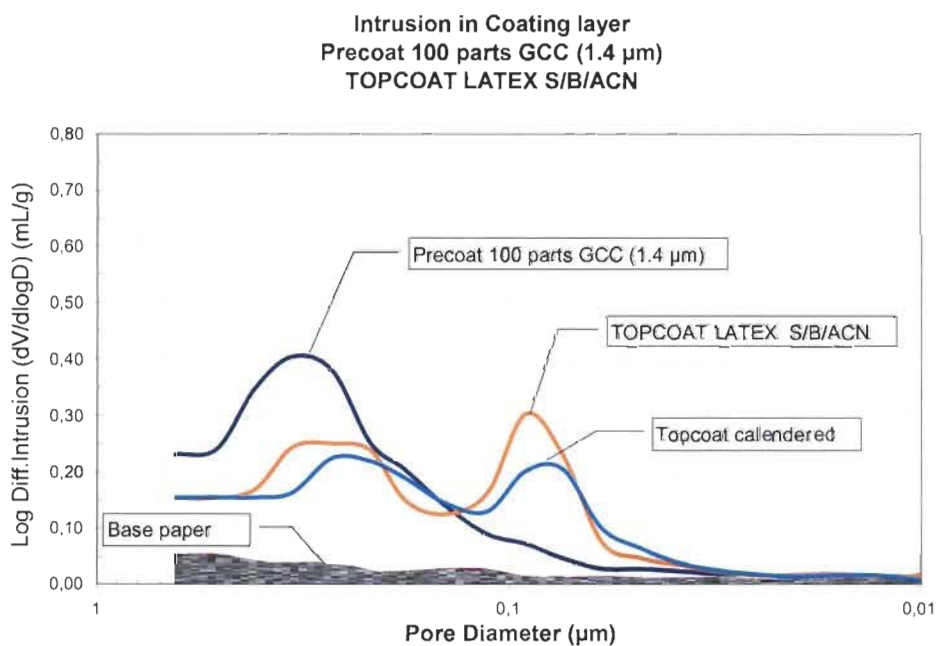


Figure 3-17 Base paper pore structure with coating structure

Table 3-5 Coating layers cut off points (larger pores)

Precoat condition	Pore diameter (μm)
1 to 10	0.65
11 to 14	0.80
15 & 16	0.65
17 to 20	0.51

The data obtained for the top coat and calendered top coat structures include both the precoat and the topcoat layers. To understand separately the effect of precoat and topcoat, it is then necessary to separate both precoat and topcoat layer structures.

3.5.3 Separation of the precoat and the topcoat layers

It was important to separate the base paper and the coating layers to be able to analyse correctly the effect of the coating layers themselves. Once this was achieved, the resulting curves of pore distribution for the coating layers present several interesting characteristics. As a case in point, using different latexes for the topcoat and different pigments in the precoat but with the same proportion (for example 20 parts/clay substitution) may affect the topcoat pore distribution. It then appears necessary to be able to separate the pore structures from the precoat and the topcoat layers. Therefore the same principle used to separate the coating structure from the base paper is applied to separate the pore structures from the precoat and the topcoat (Figure 3-18) layers. The procedure is similar to that of the base paper pore structure removal.

The procedure generates curves similar to the one shown in Figure 3-19. The cut-off point between the topcoat and precoat layer is readily identified and is applied to obtain the final topcoat pore distribution curves of interest. Indeed, the topcoat is the layer eventually printed. We are proposing here a method that allows a measure of the topcoat pore distribution *in situ*: i.e. the topcoat on top of a precoat applied on a base paper in realistic commercial conditions.

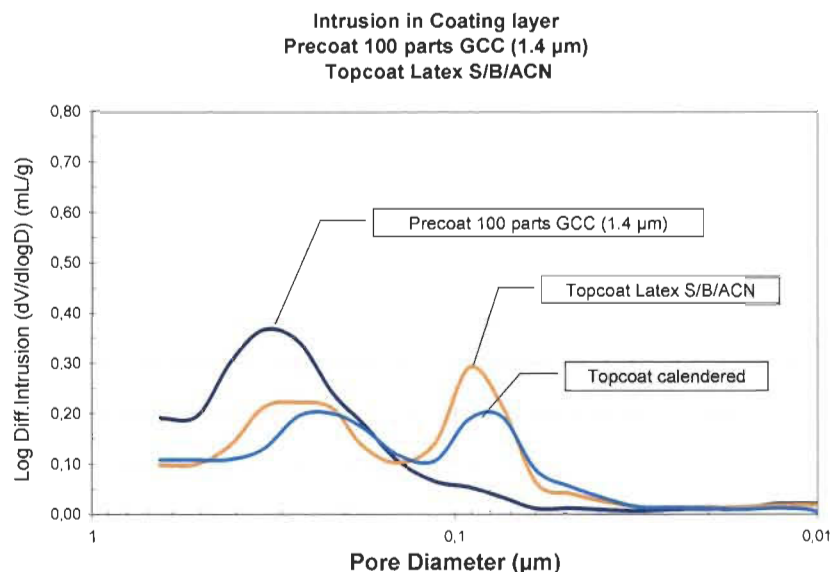


Figure 3-18 Precoated subtraction for the coating structure

Figures 3-20 and 3-21 show the final result obtained with the proposed method: *the pore distribution curves of the topcoat only*. Figure 3-20 presents the topcoat pore structure for double coated papers having the same base paper, the same precoat with 3 different latexes using the same topcoat pigment system: i.e. pigments are the same, only latexes vary. In this case, the low end for pore size is changed from 0.01 μm to 0.03 μm as pore sizes smaller than 0.03 μm result in negative pore values. The topcoat pores falls in the 0.15 to 0.03 μm interval. Figure 3-21 presents the topcoat pore structure for double coated papers having the same base paper, different precoat, and the same topcoat layer composition. As we surmised and as we will further detail in Chapter 5 - Results and Analysis, we see here that the topcoat layer latex and even precoat layer structure have a significant impact on the topcoat layer structure. It would not have been possible to see these differences without our method for mercury intrusion data treatment.

Finally, the values such as total pore volume (TPV), average pore diameter (APD), average pore area (APA), skeletal density, and total pore area (TPA) are also going to be more accurate and representative when using our proposed method of mercury intrusion data treatment. In conclusion, proper management and accurate analysis of mercury intrusion raw data have been shown here to be a key component for an in-depth interpretation of the pore distributions and hence the coating layer structures.

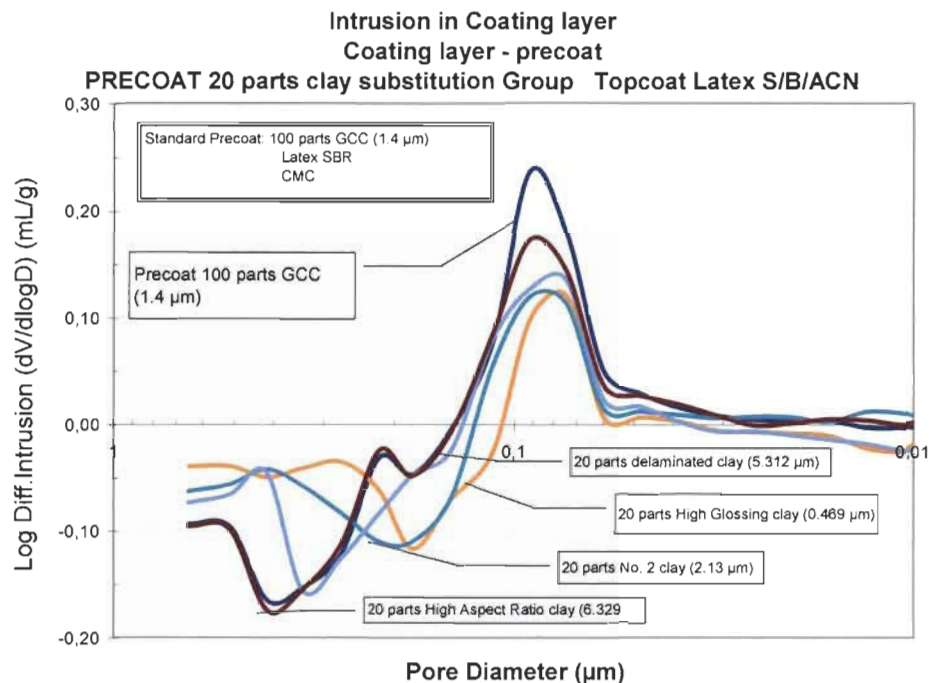


Figure 3-19 Example of curves with the precoat used as blank in the Autopore program

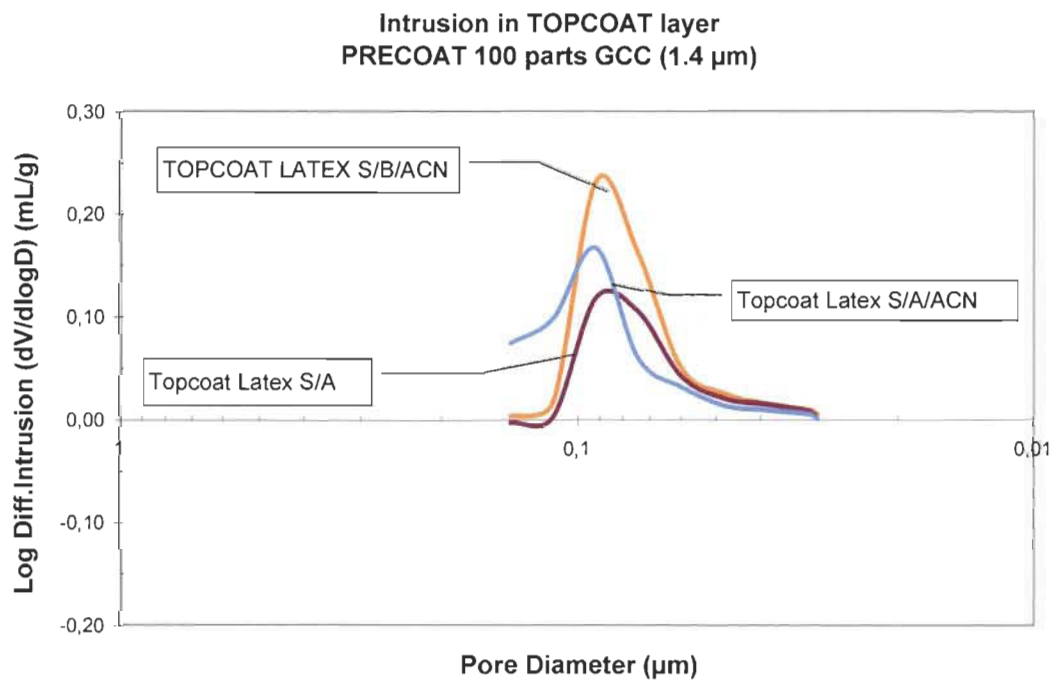


Figure 3-20 Top coating layers for the 3 different latexes with condition 1

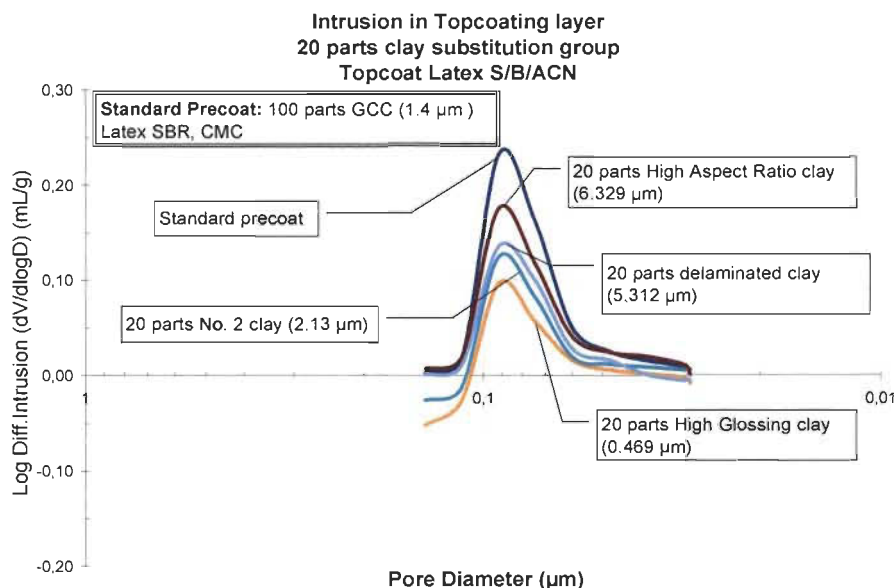


Figure 3-21 Top coating layers for Standard precoat-100 parts GCC (1.4 μm) and 20 parts clay substitution: High Glossing clay (0.469 μm), No. 2 clay (2.13 μm), delaminated clay (5.312 μm), and High Aspect Ratio clay (6.329 μm)

3.6 Mercury Intrusion normalisation method

The method explains how the mercury intrusion results can be normalised to separate the different coating layers one from other and from the base paper. The method refers to the section 3.5 of the thesis. The table 3-6 shows the condition numbers of the study related to the Autopore® test number (highlight in yellow). They are the numbers used for the normalisation and to convert everything in an excel file.

Table 3-6 Autopore® files use to explain the mercury intrusion method. Related to BS1Latex1

Mercury intrusion results – Standard precoat							
Base Paper CLC	Base Paper Intrusion no.	Precoat Intrusion no.	CLC Trial Point	Intrusion no.	Calendred Intrusion no.	Intrusion no.	Hg Intrusion Condition Excel file
BS 2007-599-1	001-535	011-539	501	001-691	551	001-665	BS1 LATEX 1

The files numbers for the penetrometer blank runs are 000-140.SMP (blank run for penetrometer number 500) and 000-171.SMP (blank run for penetrometer number 181). For each coating condition, a file must be created to store the generated files and data. In our example the file is named BS1-Latex1. The file refers to the condition 1 with the latex 1 or named the standard or control made with 100 parts GCC (1,4 μm) and latex S/B/ACN. The following steps refer to the figure 3-22.

Open Autopore® program

Click “File”

Click “Open”

Choose “sample information” (see figure 3-23)

Select the file you want to normalise (see figure 3-24)

Click “OK” to open the file

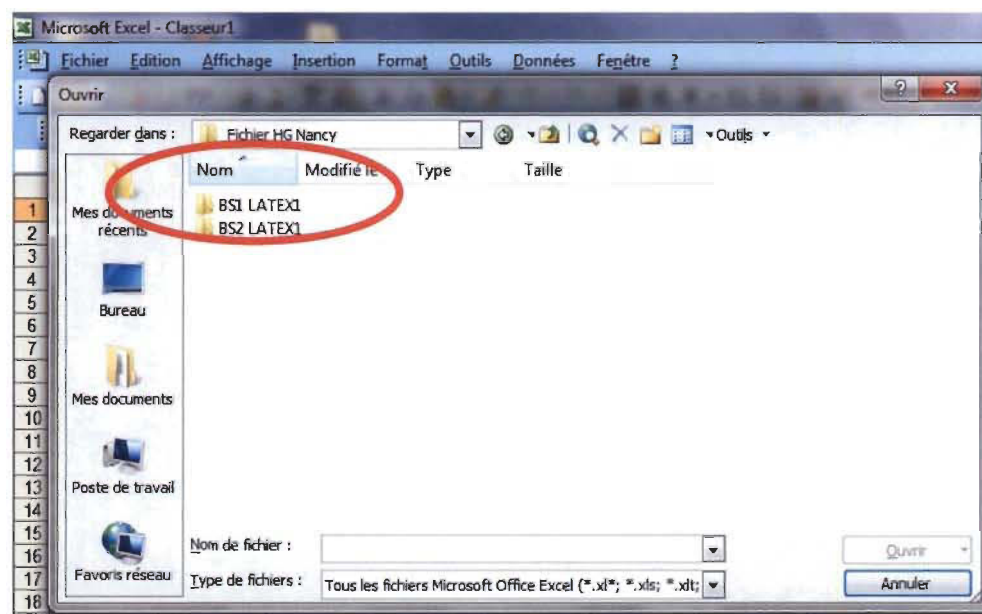


Figure 3-22 Reference file to store the results related to a condition

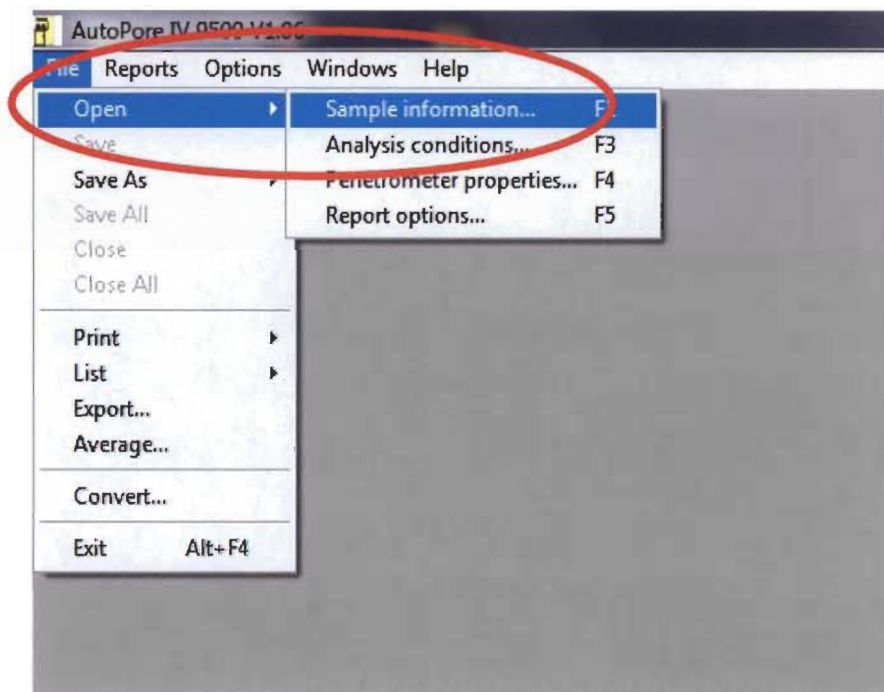


Figure 3-23 Screen to open the mercury intrusion file with the Autopore® program

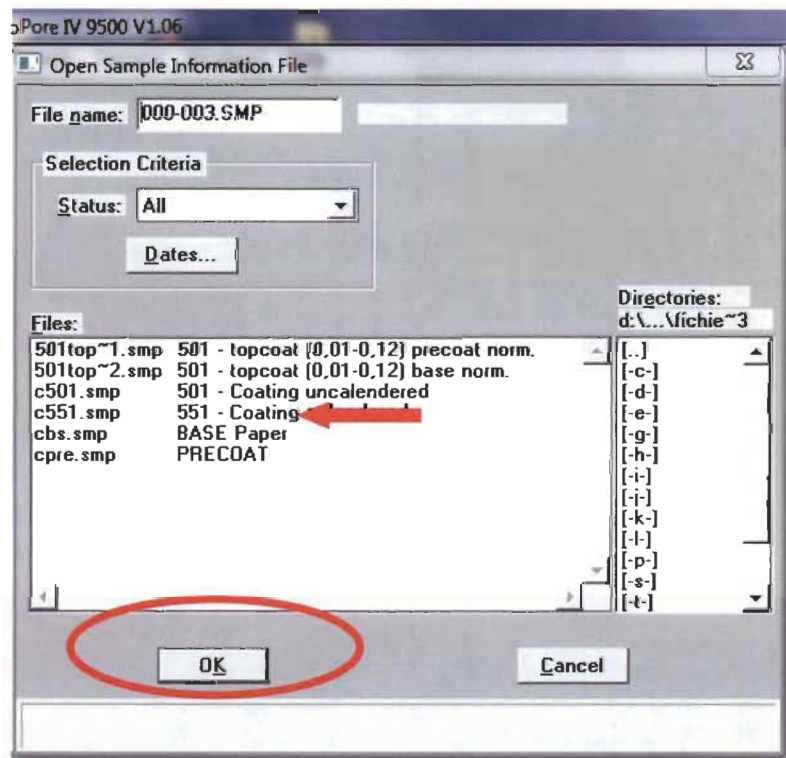


Figure 3-24 Dialog box to choose the desired file to analyse

Once the file is open, the window presented in the figure 3-25 appears on the screen. The top of the dialog box shows a line called “sample”. You will find the name of the file you open or, if you wish, you can modify the name to reflect more what you want to do with the file. After, you have to specify if a blank will be used to correct the data measured when the test is done. You have to click your chosen option on the line “correction method”. If you use a blank file, you have to specify which one you want to use and write the name to the line “Blank correction sample”. The correction file can also be found by using the browse button. In figure 3-25, the correction file used is the blank run of the penetrometer is the 181 5cc 0,366cc. Finally you click on the “advanced” button at the bottom of the screen to have access to the other information available.

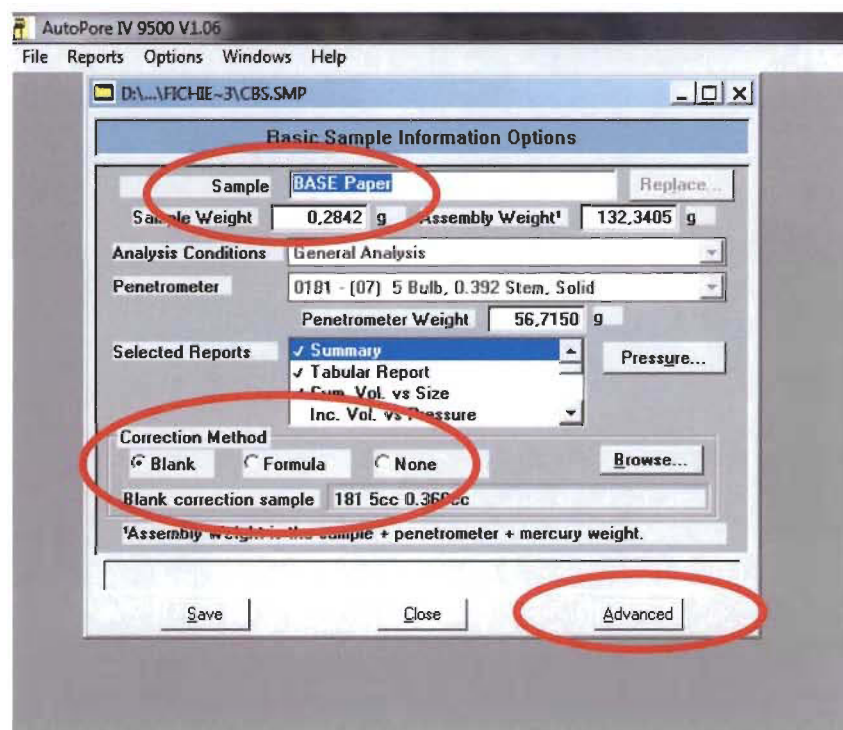


Figure 3-25 Mercury intrusion file while open with Autopore®

After clicking the “advanced” button, a dialog box opens as showed in figure 3-26. You have to choose the tab “report options” located on the top of the dialog box. After, you choose the range of pores you want to analyse. The choice is done in the section “calculation range” and you select pore size. Finally, you let know to the system which range

of pore you want. In our example, the pore range is between 10 nm à 650 nm (0,01 μm à 0,65 μm). This range is the one establish by the analysing done for the complete paper (base, precoat, and topcoat) with the negatives curves presented earlier in the text. The analysis shows the coating part begin with pores to 0,65 μm and finer. The finer limit has been establish arbitrary to 0,01 μm because, in printing, pores finer than this diameter are considered like non relevant. For information, the entire study does not consider the pores higher than 54 μm because, the bigger pores are eliminated by the hexadecane method.

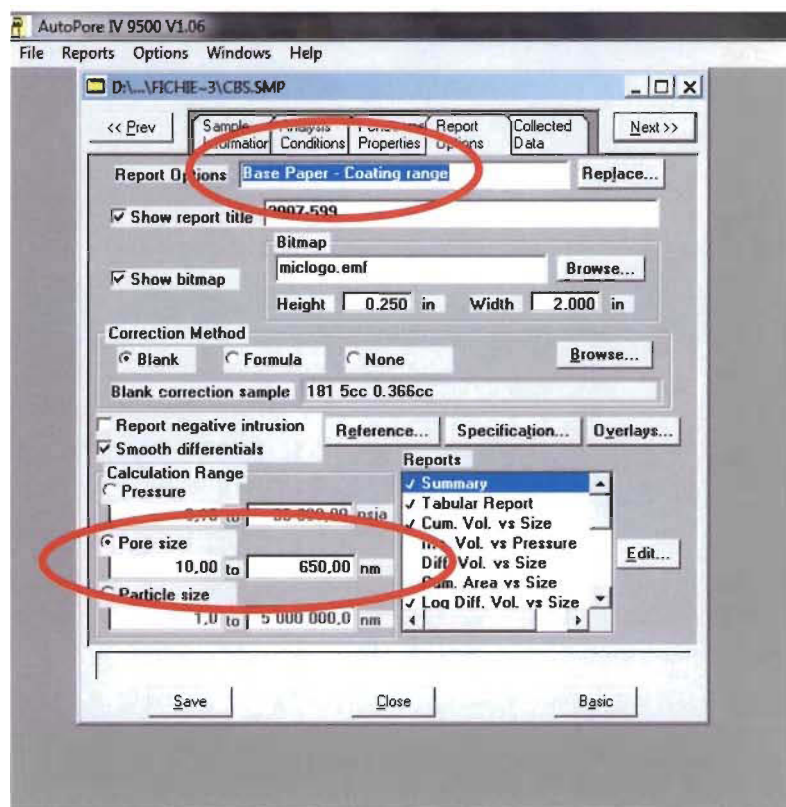


Figure 3-26 Mercury intrusion file after clicking on advanced button

Therefore, the mercury file from this study can be separated in 3 areas defined by:

Coating plus fiber	54 μm à 0,01 μm
Coating	0,65 μm à 0,01 μm
Fiber	54 μm à 0,65 μm

Please note that each study must establish its own range for the three areas. For the normalisation of the coating layers, the pores between 0,01 μm and 0,65 μm have been

used. This section refers to the coating and all pores related to the base stock have been eliminated because they have no effect on the desired results. It is important to remember that some pores from the base stock are still in the coating range analysis and this is the reason why we have to begin the normalisation method by removing those pores. Figure 3-27 shows the 2 dialog boxes we have to open in Autopore®.

On the right, we see the file for the base paper and the blank used for the correction. The blank use is the penetrometer run without paper sample. The left dialog box is to choose the pore size range for the analysis. In the example the range is between 10 nm à 650 nm (0,01 μm à 0,65 μm). Figure 3-28 show the dialog boxes for the normalisation of the precoated layer. The base paper has been used as the blank to remove the base paper pores in the precoated layer. The same logic is used for the double coated paper *i.e.* precoat and topcoat. The figure 3-29 shows the dialog boxes used to do the normalisation for the uncalendered double coated paper. Same thing is done for the calendered paper but it is not shown in the method here.

Finally, the topcoat must be separated from the precoat. The same path is followed and the figure 3-30 shows the dialog boxes found by opening the file in the Autopore® program. The file used as a blank is the precoated layer and the range chosen in our example is 10 nm à 150 nm (0,01 μm à 0,15 μm). After the .smp files has been generated, the files need to be converted in the excel format to be able to do the mathematical treatment of the mercury intrusion results requested by the user. The conversion to an excel file also provided the option to easily draw graphics of these results. The figure 3-31 shows the .smp files and their corresponding excel file.

To generate the excel spreadsheet, you have to click on the “report” on the bar menu on the top of the dialog box. Figure 3-32 shows how to create the excel spreadsheet. First, you click on “report” in the bar menu and you select “start report”. The selection of “start report” opens another dialog box to let the user choose which file he wants convert in excel file. The figure 3-33 shows the screen with the new dialog box after clicking “start report”.

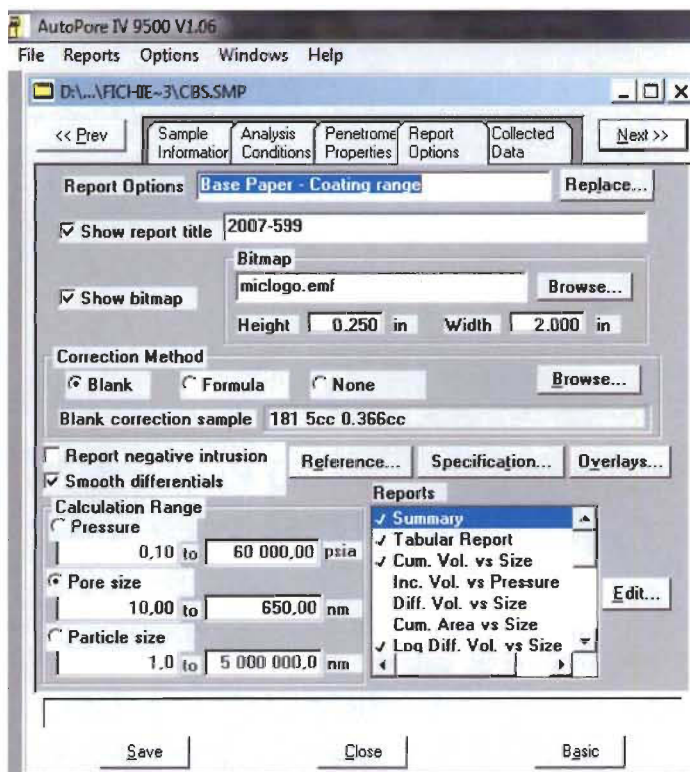
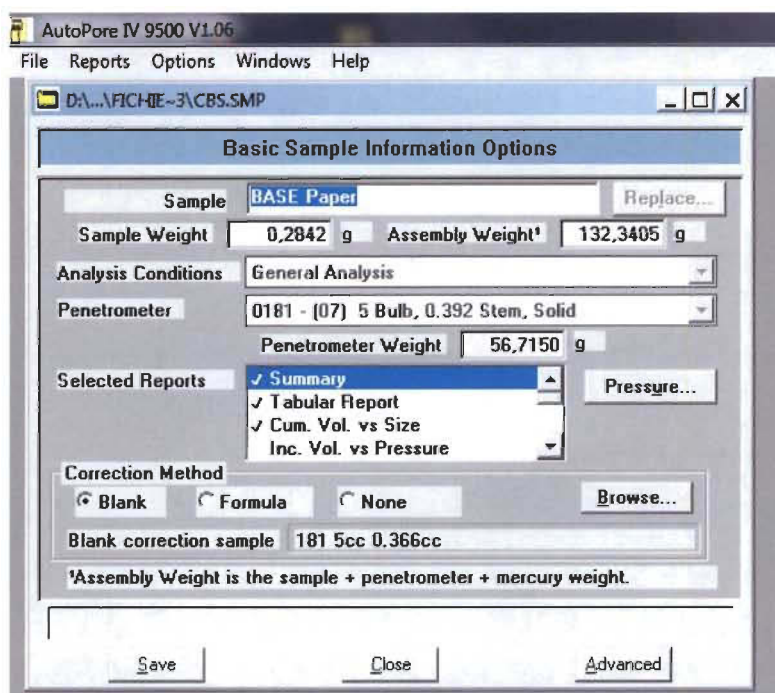


Figure 3-27 Dialog boxes to obtain the results normalised for the base paper

AutoPore IV 9500 V1.06

File Reports Options Windows Help

D:\... \FICHE-3\CPRE.SMP

Basic Sample Information Options

Sample: **PRECOAT** Replace...

Sample Weight: **0,1130 g** Assembly Weight¹: **132,4800 g**

Analysis Conditions: **General Analysis**

Penetrometer: **0181 - (07) 5 Bulb, 0.392 Stem, Solid**

Penetrometer Weight: **56,7181 g**

Selected Reports:

- ☒ Summary
- ☒ Tabular Report
- ☒ Cum. Vol. vs Size
- ☒ Inc. Vol. vs Pressure

Pressure...

Correction Method:

☒ Blank ☐ Formula ☐ None Browse...

Blank correction sample: **BASE**

¹Assembly Weight is the sample + penetrometer + mercury weight.

Save Close Advanced

AutoPore IV 9500 V1.06

File Reports Options Windows Help

D:\... \FICHE-3\CPRE.SMP

<< Prev Sample Information Analysis Conditions Penetrometer Properties Report Options Collected Data Next >>

Report Options

Precoat - Coating range Replace...

☒ Show report title: **2007-599**

☒ Show bitmap:

Bitmap: **miclogo.emf** Browse...

Height: **0.250 in** Width: **2.000 in**

Correction Method:

☒ Blank ☐ Formula ☐ None Browse...

Blank correction sample: **BASE**

☐ Report negative intrusion Reference... Specification... Overlays...

☒ Smooth differentials

Calculation Range:

☐ Pressure: **0.10** to **60 000,00 psia**

☒ Pore size: **10,00** to **650,00 nm**

☐ Particle size: **1,0** to **5 000 000,0 nm**

Reports:

- ☒ Summary
- ☒ Tabular Report
- ☒ Cum. Vol. vs Size
- ☒ Inc. Vol. vs Pressure
- ☒ Diff. Vol. vs Size
- ☒ Cum. Area vs Size
- ☒ Log Diff. Vol. vs Size

Edit...

Save Close Basic

Figure 3-28 Dialog boxes to obtain the results normalised for the precoated layer

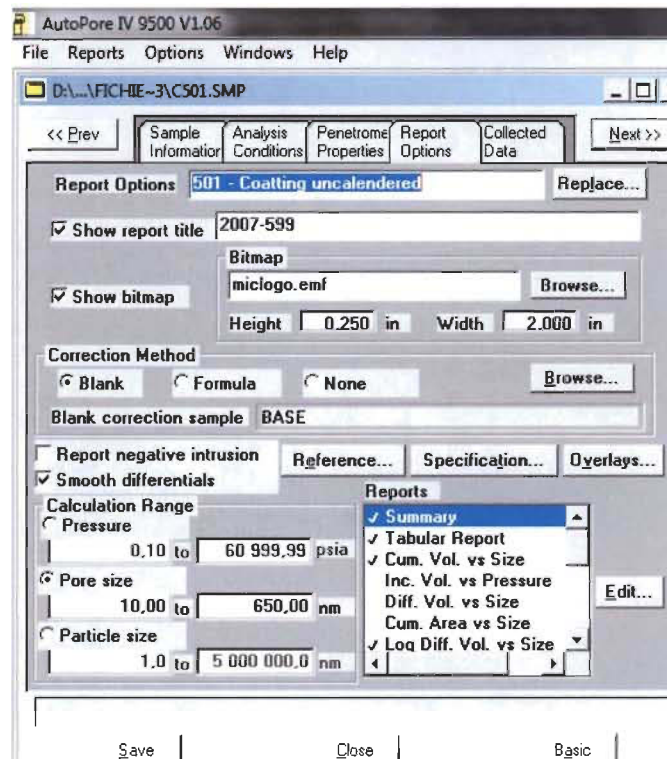
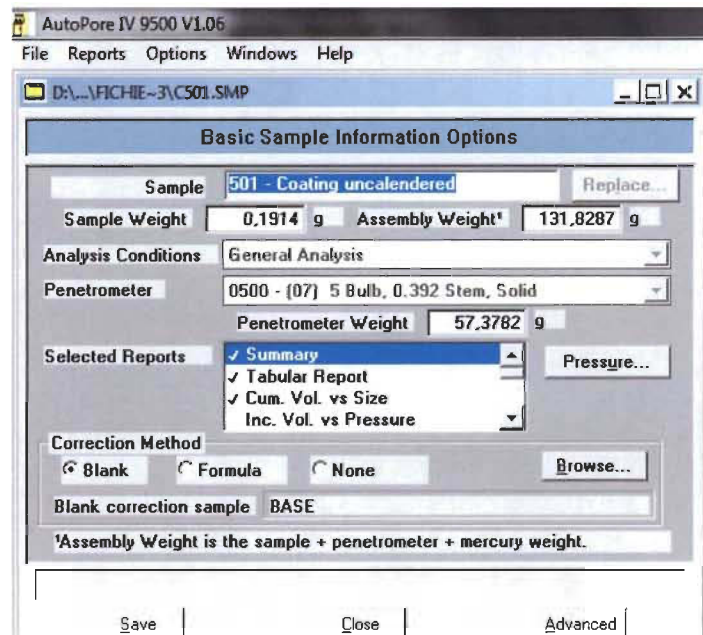


Figure 3-29 Dialog boxes to obtain the results normalised for the uncalendered double coated paper

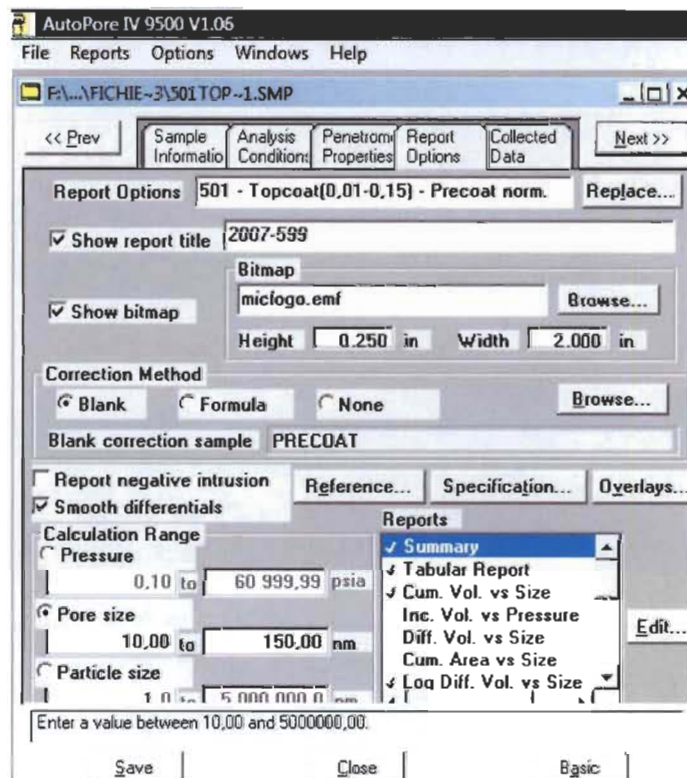
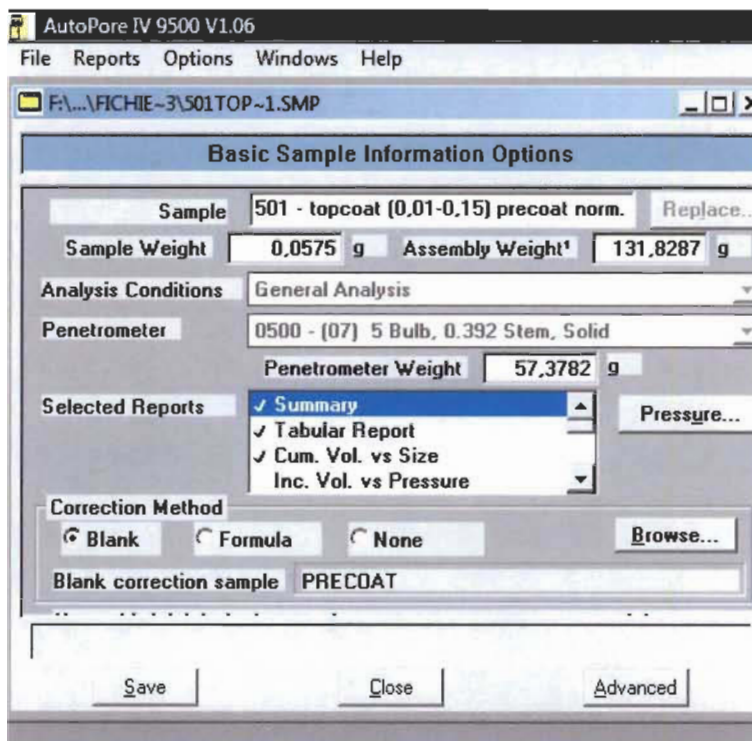


Figure 3-30 Dialog boxes to obtain the results normalised for the calendered double coated paper

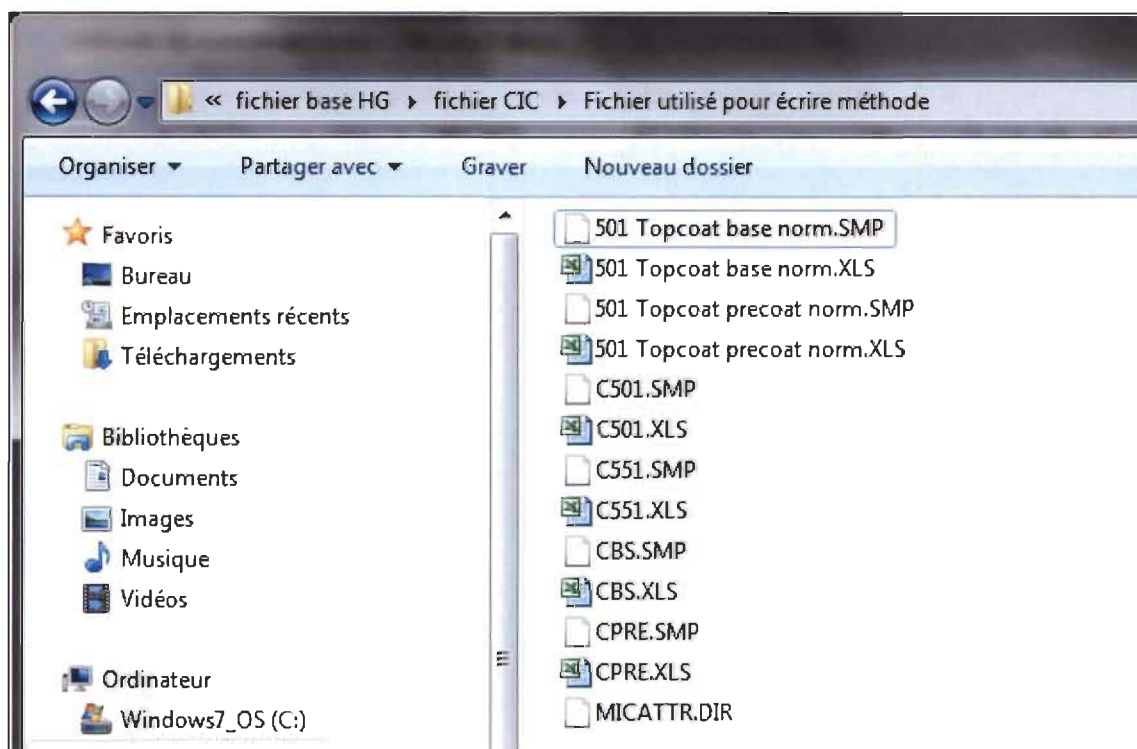


Figure 3-31 .SMP files and their corresponding excel files

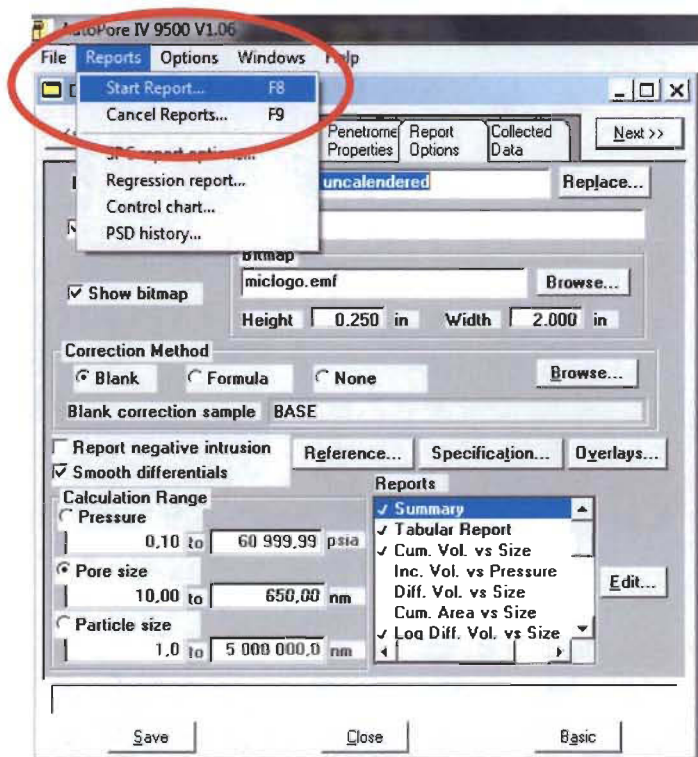


Figure 3-32 Dialog box to start to generate excel spreadsheet with Autopore® program

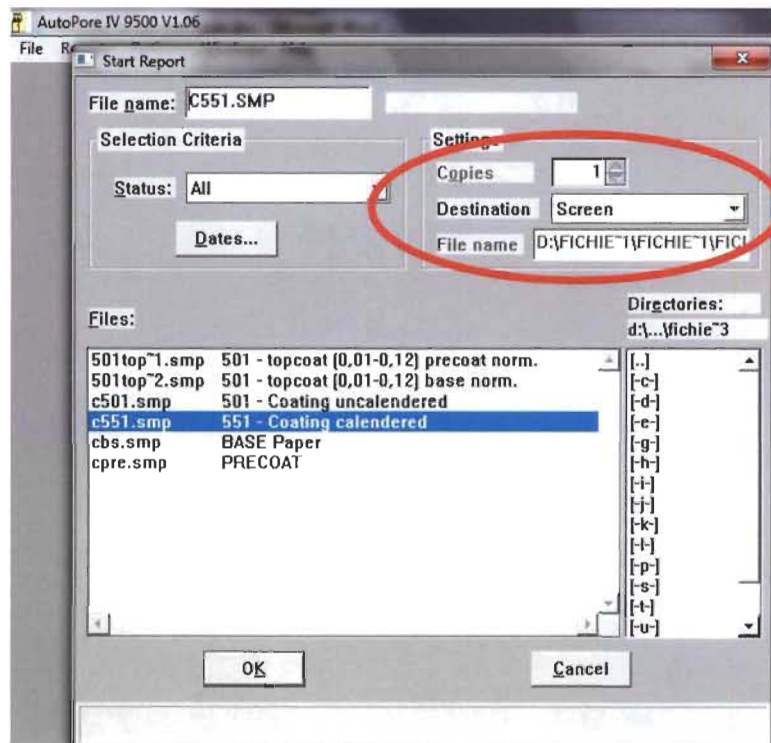


Figure 3-33 Dialog box used to choose the .smp file to convert in excel spreadsheet

It is very important to select “screen” in the destination line (see figure 3-33). The selection of “screen” in the destination line will generate the document on the computer screen and this is the only way to get the document and be able to convert in excel spreadsheet. After the option “screen” is selected, the user chooses the file (or files) which need to be converted in excel spreadsheet and then, click “OK”. By clicking “OK”, another dialog box opens and the user sees the initial selection of reports needed to be generated. The user can change something if necessary. Figure 3-34 shows the dialog box with the selection done for the study. If all the selected documents are okay, click “OK”. A new document appears on the computer screen and the figure 3-35 shows what type of document it is. The document can be printed as shown in figure 3-35 or can be converted in an excel spreadsheet file. The tool menu is located in the right side of the document. The user selects “save as” and the dialog box showed in figure 3-36 appears on the computer screen. The user selects the destination file to “save as” (Enregistrer dans) and also defines the type of the document. The type chooses is “spreadsheet .xls”. Then click save (Enregistrer) and the document is convert in excel spread-

sheet file in the destination the user has selected earlier in the procedure. From this point all the treatments of the results are done with the excel program.

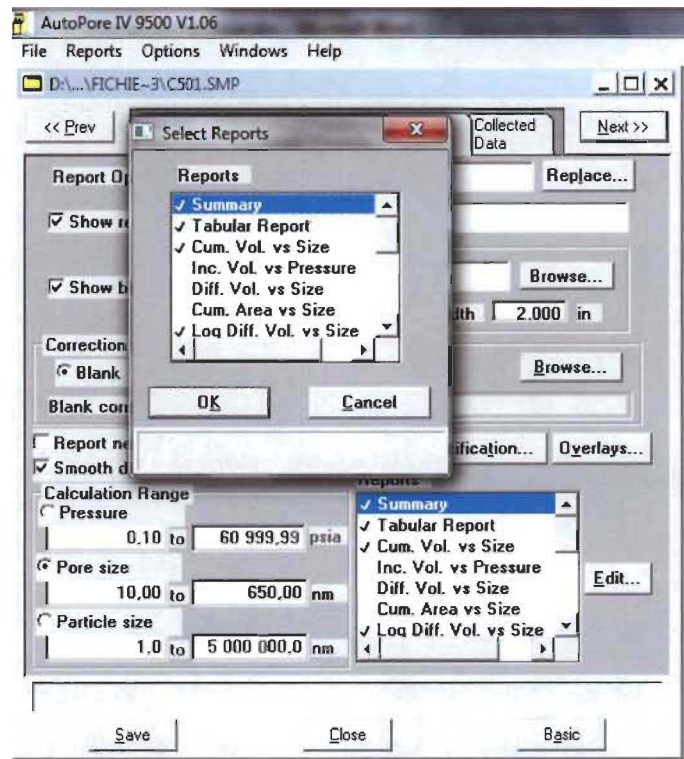


Figure 3-34 Dialog box to choose the reports to convert in excel file

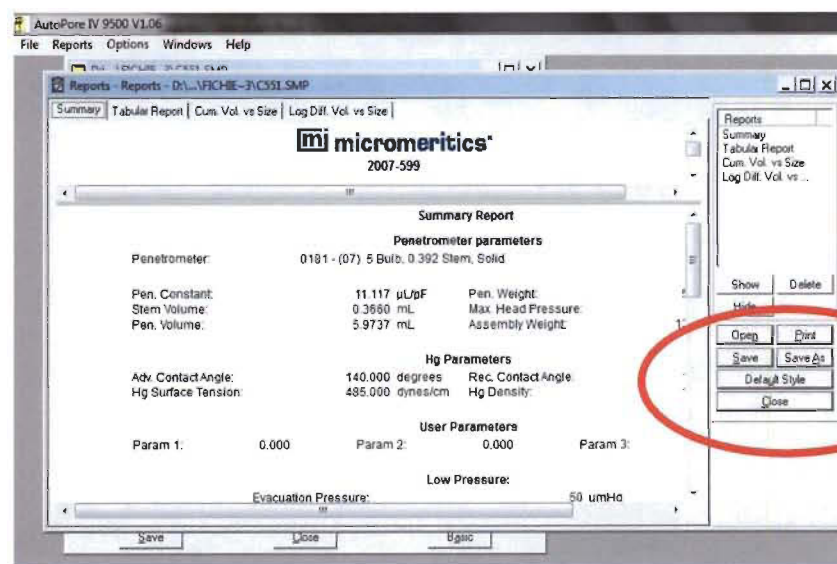


Figure 3-35 Converted file

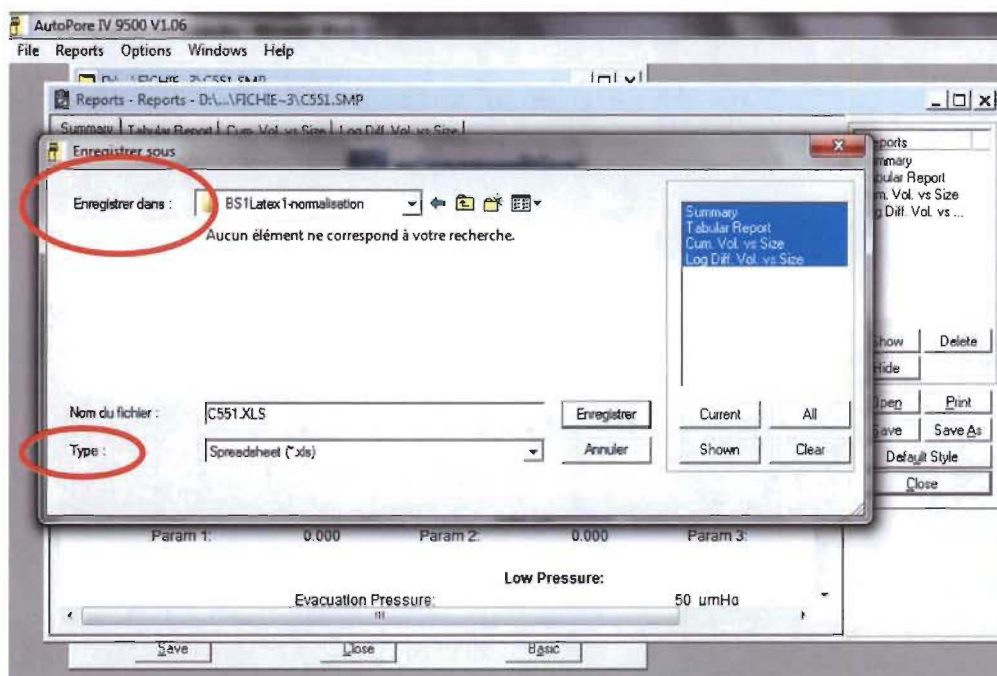


Figure 3-36 Save the document on excel spreadsheet form

3.7 Scanning Electron Microscopy (SEM)

Scanning Electron Microscopy or SEM is used to visually analyse the paper surface. It is a very efficient technique to analyse the irregularities, defects, and the structure of the surface. We found the observations very useful to explain and/or understand any problem that may occur while the coated paper is printed.

Therefore, we used SEM pictures to perform a subjective analysis of paper and coating layer surfaces; to study, for instance, how the pigments have been affected after an external treatment like calendaring and potential effects on surface printability. As an example, Figures 3-37 and 3-38 illustrate how defects shown by SEM may become visually apparent after printing.

SEM is also a useful tool in supporting results and conclusions obtained with other measurement methods.

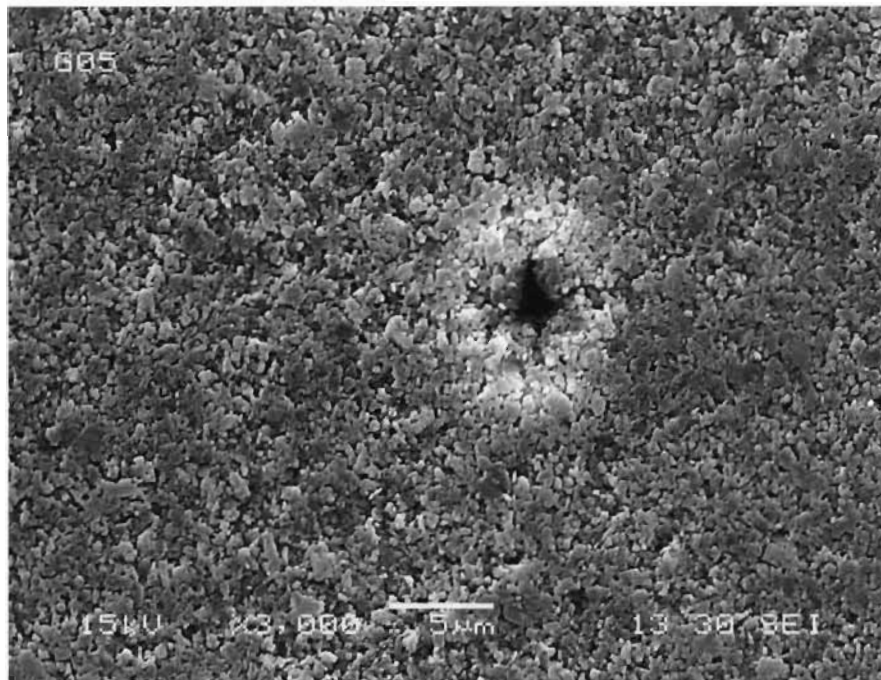


Figure 3-37 Defect in the calendared coating layer

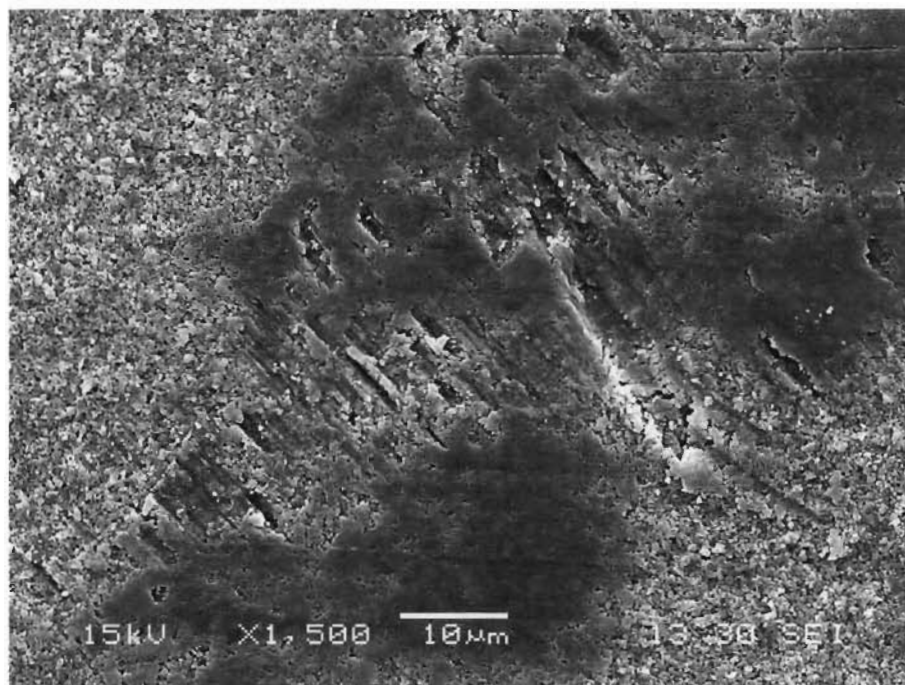


Figure 3-38 Defect generated by blade coating.

Indeed, as previously said, SEM allows the identification of very small defects, poor coating application, pigment agglomeration etc. It may help in explaining some odd results related to any other measurement. The SEM used in this study is a scanning electronic microscope model Jeol JSM-5500 as seen in Figure 3-39.



Figure 3-39 SEM measurement equipment

3.8 Prüfbau DELTACK method

3.8.1 Description of the method

The Prüfbau DELTACK method has been developed to simulate conditions occurring during commercial printing, mainly to appraise ink film splitting forces. It should be emphasized that the Prüfbau DELTACK results are dependent on the printing speed, the printing temperature, the printing tension, the substrates, and of course mainly the substrate surface properties. The instrument used in our study is a Multipurpose Ink Tack Measurement System DELTACK from the company Prüfbau, Munich, Germany. The instrument settings are described in table 3-7; the setting we used is “Web Offset”. The instrument used is shown in Figure 3-40. The paper strip used had a dimension of 5.4 cm width by 30 cm length. The ink used is a heat-set printing ink 40 8020 (Michael Huber, Munich, Germany). The ink set-up for the test is shown in table 3-8.

Table 3-7 Prüfbau Instrument Settings for Sheet Offset and Web Offset

Instrument Setting	Web Offset
Measuring Mode	Mode X
Measuring Unit	1
Printing Tension	1000 N
Printing Tension for Splitting – Print Unit A	1000 N
Printing Form – Print Unit B	Metal 5 cm Width
Printing Form for Splitting	Rubber Green 5 cm width
Print Sample Carrier	Rubber
Speed for printing and Splitting	1.0 m/sec
Minimum Waiting Time after Printing	3 sec
Measuring Interval	1 sec
Number of Measuring Cycles	30
Mean Value Range	80-170 mm

Table 3-8 Ink Test Settings for DELTACK Prüfbau test

Test Ink		
Instrument Setting	Sheet Offset	Web Offset
Ink Quantity	150 mm³	150 mm³
Ink Time for inking unit	30 sec.	30 sec.
Ink Time for Print Form	30 sec.	30 sec.



Figure 3-40 DELTACK measurement instrument

In present study, we followed the DELTACK procedure used by Omya which can be obtained from reference [99]. However, only 2 tests per side were done (and not 3 as in the Omya procedure) but an extra care was taken to ensure that all measurements were done in exactly the same way. The settings used are listed in table 3-9.

Table 3-9 Prüfbau test settings

Printing Speed	1 m/sec
Printing Force, PU A	1000 N
Printing Force, PU B	810 N
Delay	1 second
Number of measurement	30 per test
Ink	150 mm³ of the Heat-Set ink #40 8020.

3.8.2 DELTACK curve analysis

The ink setting on the calendered samples is evaluated with the DELTACK method. An example of the curve obtained with the method is illustrated in Figure 3-41. The method was developed for testing ink setting on coated paper grades. It measures the tack force as a function of time which is determined by the interactions of the ink with the coating surface, the coating structure, and the ink on the tack disc.

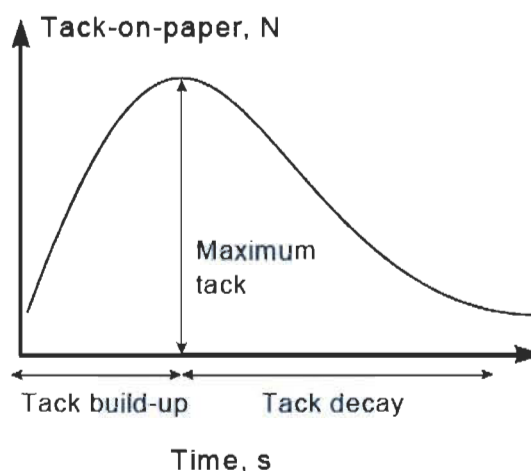


Figure 3-41 Example of tack development from a DELTACK test curve.

An evaluation of the initial ink setting, driven by the solvent loss from the ink to the coating pores, is provided both by the tack build-up slope to the maximum tack, and by the time necessary to reach the maximum in the ink tack force. The tack decay is the start of the final drying process where enough solvent is lost from the ink to provide the dry, non tacky, printed surface.

The porosity, pore size, and total pore volume are known to have a great impact on ink setting [24, 33] [52]. Latex chemistry also affects the ink setting rate. The two considerations mean that ink setting is controlled by capillary absorption in the coating pores as well as ink absorption by the latex [76, 100, 101]. The DELTACK approach is therefore a great tool to relate the printing characteristics of our samples to the structure modification brought about by modifications in the precoat and topcoat formulations.

3.8.3 Maximum in ink tack force

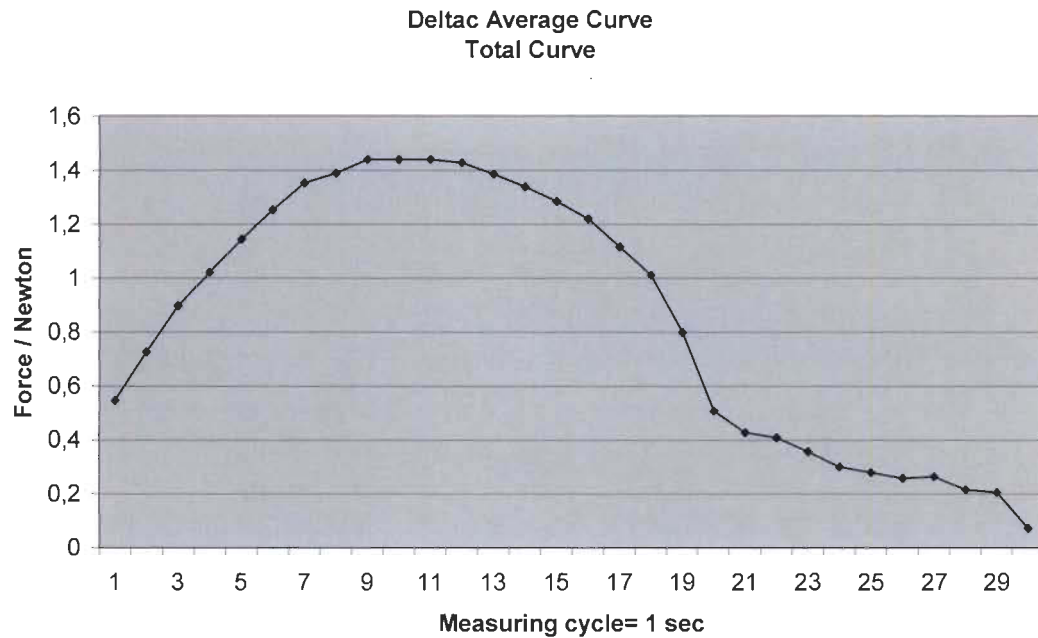


Figure 3-42 Example of a complete DELTACK curve

A standard laboratory DELTACK printing curve as seen in Figure 3-42 shows that the tack force increases to a maximum then decreases. Both the maximum in ink tack force and the time it takes to reach the maximum (as evaluated by the measuring cycles) or “ink setting time” may be used to compare the curves. In our study, we propose to calculate the maximum ink tack and ink setting time for all curves using second degree polynomial equation 3-11:

$$y = ax^2 + bx + c \quad \text{Equation 3-11}$$

with y the tack force value (in Newton) and x the time (in seconds).

It is understood that the equation we are proposing is merely empirical, in order to treat the data as the complete curves found with the DELTACK method do not have an exact second degree polynomial shape. To be able to use a second order polynomial, a part of the curve end could be, upon need, truncated to insure a good fit of the polynomial shape in the corresponding x-interval of the curve. The truncating process is illustrated in Figures 3-42 and 3-43. In these examples, values higher than 21 seconds (x-axis) have been

removed from the data set. The truncation results in a very good correlation between the DELTACK curve and the polynomial fit as demonstrated by the determination coefficient R^2 included in the graphs. It confirms that using a second-order polynomial provides accurate results, meaning the maximum ink tack force and time values calculated with the equation (Figure 3-44) are correct.

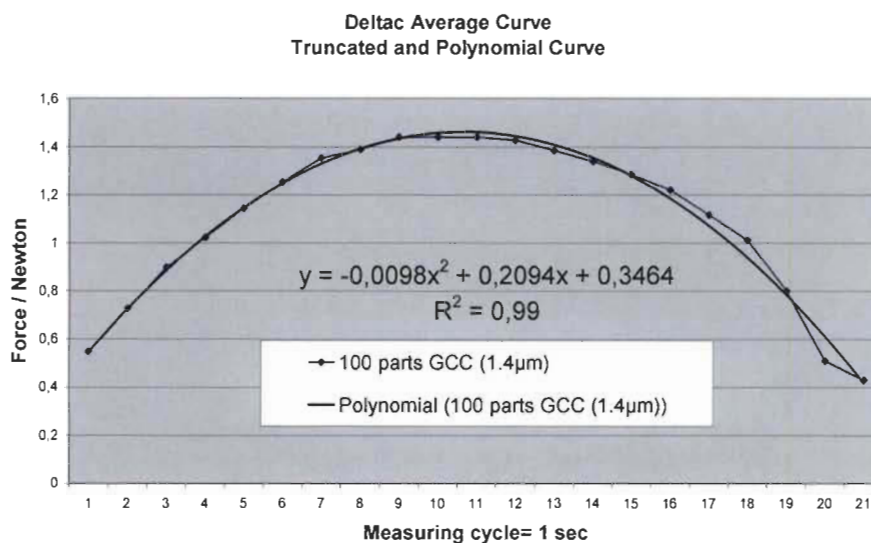


Figure 3-43 Truncated DELTACK Curve to fit the Polynomial Curve

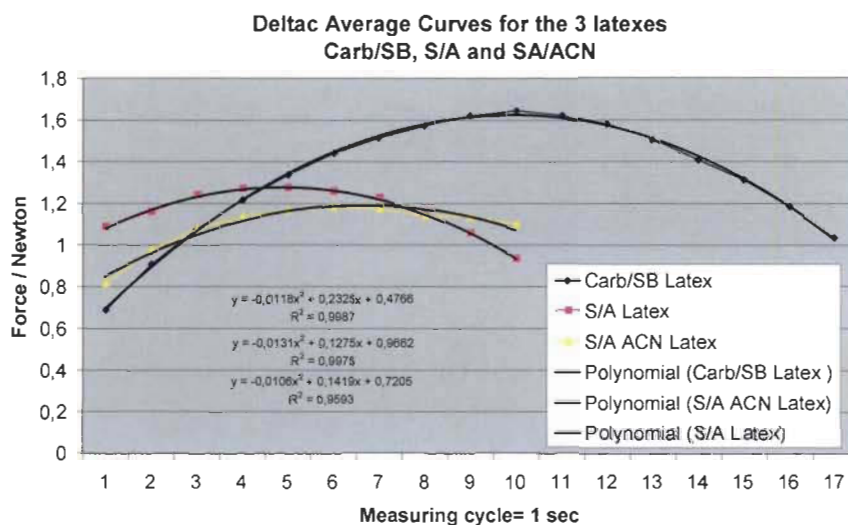


Figure 3-44 DELTACK Curves means and polynomial curves fitting

Chapter 4 - Experimental design

4.1 Experimental levels selection

We learned from the literature study that the precoat has a significant influence on the top coat properties. However, the effect of the different components and parameters of the precoat are yet to be established. Accordingly, we designed the experimental study to analyse the effect of key precoat parameters on the topcoat properties.

From standard precoat composition (initial conditions or Group 0), i.e. a precoat containing 100 parts ground calcium carbonate (GCC) which is the case of about 98% of commercial precoat, we modify the **precoat components/parameters** by:

- replacing 20% of the GCC by clay (later called 20% clay substitution): group samples 1 or Group 1;
- calendering either the base paper or the precoat before precoat and/or top coat application: Group 2.
- substituting the standard precoat latex by an acrylic latex and the carboxy methyl cellulose (CMC) by an amphoteric thickener *i.e.* protein: Group 3.
- replacing 100% of the standard GCC by different GCC or precipitated calcium carbonates (PCC) or Brazilian clay: Group 4.

In practice, above conditions corresponds to a total of 20 “precoat conditions”: 1 for the initial condition (Group 0), 4 for the 20% clay substitution (Group 1), 4 for the calendering of the base paper, the precoat being uncalendered (Group 2A) and 4 when the precoat is calendered but not the base paper (Group 2B), 2 for the latex/CMC substitution (Group 3), and 4 for the 100% pigment substitution (Group 4). On top of all these 20 precoat conditions we have applied 3 different topcoats for a total of 60 conditions (3 x 20). All 60 samples were calendered to a gloss target of 70 [21].

For the 3 topcoats we used 3 different latexes with the same pigments and additives systems. The 3 latexes used are styrene /butadiene /acrylonitrile latex (S/B/ACN), styrene/acrylic latex (S/A), and styrene/acrylic/acrylonitrile latex (S/A/ACN). The experimental design is schematically represented in Figure 4-1.

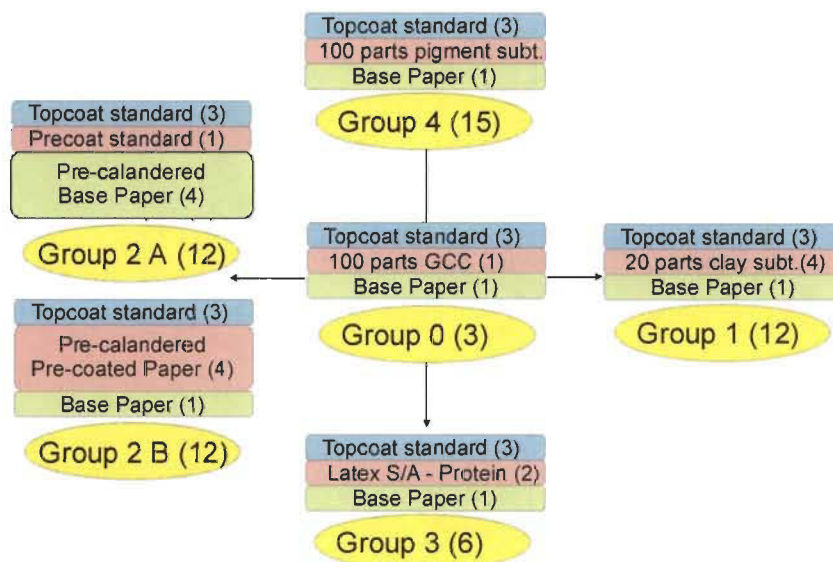


Figure 4-1 Schematic of the experimental design

The technical characteristics of the 3 latexes used for the topcoats are listed in table 4-1. The characteristics of the latex used for the precoat are also included in the same table. The 2 schematics presented in Figure 4-2 and 4-3 [102] showing the latex particle polymerization illustrate the differences between the two latex families (SB and SA).

Table 4-1 Latex characteristics used in the study

Latex	Tg temperature (°C)	Carboxyl ^o	Gel Content	Particle size (Å)
SBR latex	+17	Low	Low	1800
Styrene / Butadiene / Acrylonitrile	+10	medium	Medium	1400
Styrene/Acrylic*	+23	medium	High	1400
Styrene/Acrylic*Acrylonitrile	+40	medium	high	1400

*Acrylic latex use the n-buthyl acrylate like second monomer

The precoat applications were performed on a pilot coater at CIC [103]. The calendaring of the base paper and the precoat were done by soft nip calendaring on the CIC pilot coater. The topcoat applications were done on a CLC 7000 at CIPP. The final 60 top-coated samples were calendered on a laboratory supercalender at CIC. All conditions are detailed below.

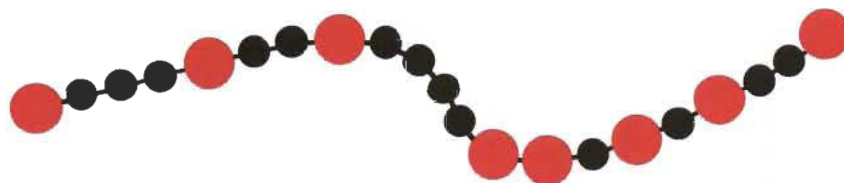


Figure 4-2 Styrene/Acrylic latex molecule

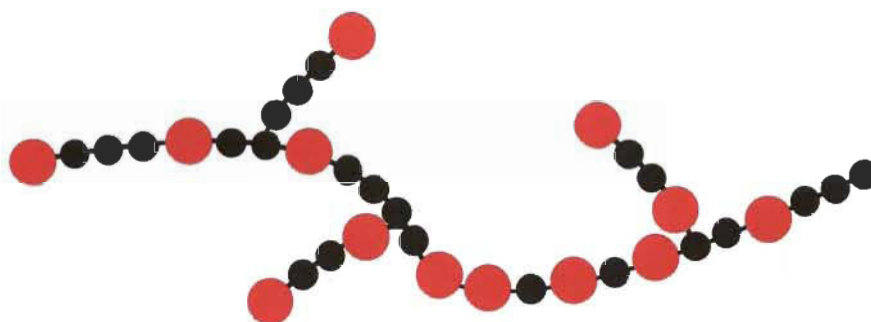


Figure 4-3- Styrene/Butadiene latex molecule

4.2 Precoated paper roll preparation

The precoated samples were coated in a roll form on CIC pilot coater facility [103] using the jet applicator coating head. The complete formulations, calendaring conditions, and coater settings are indicated in the table 4-2, 4-3, 4-4, and 4-5.

The coater operation parameters are listed in table 4-6. Although twelve different rolls from the same base stock were used to make the 20 precoated conditions, the results proved that the base stock paper is very consistent and stable. All the precoated rolls were coated both sides on the pilot coater (as a control for curl). The rougher side was coated first.

Table 4-2 Precoated standard formulations and 20 parts substitution

	Cond. 1	Cond. 2	Cond. 3	Cond. 4	Cond. 5
GCC (1.4 μ m)	100	80	80	80	80
High glossing clay (0.469 μ m)		20			
No. 2 clay (2.13 μ m)			20		
Delaminated clay (5.312 μ m)				20	
High Aspect Ratio clay (6.329 μ m)					20
Latex SBR	10	10	10	10	10
Optical Brightener Hexa.	0.5	0.5	0.5	0.5	0.5
Calcium Stearate	0.4	0.4	0.4	0.4	0.4
Carboxy Methyl Cellulose(CMC)	0.7	0.7	0.7	0.7	0.7
Solids	66%	66%	66%	66%	66%

Table 4-3 Calendering and Soft Nips Settings

	Cond. 7	Cond. 8	Cond. 9	Cond. 10
	Base paper	Base paper	Precoated	Precoated
Temperature Soft Nips #1 and #2	100°C	100°C	100°C	100°C
Pressure Soft Nips #1 and #2	50 kN/m	200 kN/m	50 kN/m	200 kN/m
	Cond. 11	Cond. 12	Cond. 13	Cond. 14
	Base paper	Base paper	Precoated	Precoated
Temperature Soft Nips #1 and #2	200°C	200°C	200°C	200°C
Pressure Soft Nips #1 and #2	50 kN/m	200 kN/m	50 kN/m	200 kN/m

Table 4-4 Precoat formulations – Latex and Amphoteric thickener

	Cond. 15	Cond. 16
GCC (1.4 μ m)	100	100
Latex SBR		10
S/A latex	10	
Optical Brightener Hexa.	0.5	0.5
Calcium Stearate	0.4	0.4
Carboxy Methyl Cellulose(CMC)	0.7	
Protein		2
Solids	66%	66%

Table 4-5 Precoat formulations – 100 parts substitution

	Cond. 17	Cond. 18	Cond. 19	Cond. 20	Cond. 21
BPSD GCC (0.659 μ m)	100				
BPSD GCC (0.3598 μ m)		100			
PCC (0.499 μ m)			100		
Brazilian clay (0.548 μ m)				100	
NPSD GCC (0.6593 μ m)					100
Latex SBR	10	10	10	10	10
Optical Brightener Hexa.	0.5	0.5	0.5	0.5	0.5
Calcium Stearate	0.4	0.4	0.4	0.4	0.4
Carboxy Methyl Cellulose(CMC)	0.7	0.7	0.7	0.7	0.7
Solids	66%	66%	64%	64%	64%

4.3 Top Coated Samples

The 20 precoated rolls in the pilot coater facility have been top coated with a CLC 7000 (Cylindrical Laboratory Coater or CLC for short) because the CLC does not require as much paper as a pilot coater. We needed to do use the CLC as the number of coatings and/or different settings is high and the cost of performing all the conditions on pilot equipment would have been prohibitive.

Table 4-6 Precoat Operation Parameters - Coater

Coating Unit	Jet Applicator
Speed	1400 m/min
First Side to Coat	Rough
Coat Weight Application	12 g/m ²
Moisture	4.5% for the rough side
Blade	0.457 / 84 mm / 45°
Dwell Length	350 mm
Jet Opening	0.9 mm
Jet Angle	34°
Gap – Jet/Baking Roll	10 mm
Beam Angle	45° - Constant Tip angle

The formulations used for the top coat are listed in the table 4-7. The CLC conditions for the coating are as follows: speed of 800 m/min, pre-heating of 10 seconds at 80% intensity, drying time of 30 seconds at 100% intensity, and coating length of 5 meters (on a 760 mm width).

The coating blade is 0.457 mm thick with a 50° tip angle. Remembering that the precoat was applied on both sides of the base stock paper, the top coating was always applied on the same precoat side: the one corresponding to the smooth side of the base paper as seen in Figure 4-4.

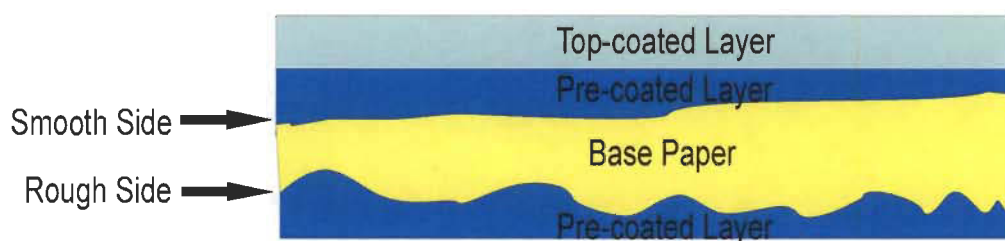


Figure 4-4 Schematic representation of the cross section of the final paper samples produced for the study

4.3.1 Control of the top coat weight for the CLC samples

When adding the top coat layer, each CLC coating run provides a 14 cm wide coated strip in a helicoidal form. Twelve samples are cut out of the 14 cm wide trip using a template 12.5 cm by 40 cm for a total area of 500 cm² per sample. In parallel, a sample with the same size (500 cm²) is cut out from the “uncoated paper” (it is actually the pilot precoat samples) portion from each CLC run. The “uncoated paper” sample serves as the reference to calculate precisely the coat weight applied with the CLC.

The target coat weight is 12 ± 0.5 g/m². All 500 cm² top coated samples are weighed and only the samples within a ± 0.5 g/m² tolerance are kept for the study. A minimum of 15 CLC samples at the correct coat weight are needed for each precoat/topcoat combination.

Table 4-7 Topcoat Formulations used with the CLC

	solids	1	2	3
BPSD GCC (0.659 μm)	76%	70	70	70
High glossing clay (0.469μm)	70%	30	30	30
Polyacrylate salt dispersant	40%	0.15	0.15	0.15
S/B/ACN	50	12		
SA	50		12	
S/A/ACN	50			12
Optical Brightener Hexsulpho-	100	0.7	0.7	0.7
Calcium Stearate	50	0.7	0.7	0.7
Ammonium zirconium carbonate	32	0.3	0.3	0.3
Carboxy Methyl Cellulose(CMC)	90	0.5	0.5	0.5
Solids		65%	65%	65%

4.4 Calendering the top coated samples

All CLC top coated samples have been calendered. The calender used is a laboratory supercalender with 2 nips formed by 2 cotton rolls and one steel roll. The calendering is performed to obtain a gloss target of 70 [21] for the control condition (Group 0) for each latex used in the study: i.e. S/B/ACN latex, S/A latex, and S/A/CAN latex. Once the calendering conditions were found for each latex, all other group samples containing the same latex were done using the same latex calendering conditions. The laboratory calendering conditions are listed in the table 4-8.

Table 4-8 Laboratory Calendering Conditions

Speed	14.7 m/min
Sample side on steel	Smooth
Number of passes	1
Steel Temperature	60°C
Nips Pressure - S/B/ACN latex	34.46 bar
Nips Pressure - SA latex	34.46 bar
Nips Pressure - S/A/ACN latex	20.68 bar

Chapter 5 - Results and Analysis

5.1 Introduction

As a reminder, the purpose of present work is to understand the effects of precoat components/parameters on the structure, both of the precoat and of the final double-coated paper, and on the printability of double-coated paper grades.

In order to achieve that, from a standard precoat containing 100% GCC and coated with 3 different latexes, we have modify the double-coated papers by replacing 20% of the GCC by clay in the precoat (also called 20% clay substitution or Group 1), calendaring either the base paper or the precoat before precoat and/or top coat application (Group 2), substituting the standard precoat latex by an acrylic latex and the carboxy methyl cellulose (CMC) by an amphoteric thickener *i.e.* protein: (Group 3), and finally replacing 100% of the standard GCC by different GCC or precipitated calcium carbonates (PCC) or Brazilian clay (Group 4).

To facilitate the analysis of results, we have summarized the experimental design conditions in Table 5-1 which outlines the overall approach of our study: *i.e.* the 20 different precoated conditions. It should also be reminded that the same pigments and additives systems are applied as topcoat but with 3 different latexes within each of the 20 precoat conditions (*i.e.* for a grand total of 60 conditions).

The three latex chemistries examined are styrene/butadiene/acrylonitrile (S/B/ACN), a styrene/acrylic (S/A), and a styrene/acrylic/acrylonitrile (S/A/ACN) as these are the most commonly used in the industry for the considered coating applications.

The variations within the various coating structures brought about by above modifications are analysed by mercury intrusion as explained in Chapter 4.

Table 5-1 Precoated formulations related with the group and the condition number

Precoated formulation	Group	Samples
100 parts GCC (1.4 μm)	Control	3 topcoat = 3 samples
20 parts High glossing clay (0.469 μm)	Group 1 20 parts clay substitution	3 topcoat x 4 precoat = 12 conditions
20 parts No.2 clay (2.13 μm)		
20 parts delaminated clay (5.312 μm)		
20 parts High aspect ratio clay (6.329 μm)		
Base paper calendered 100°C - 50 kN/m	Group 2 Base paper & Precoat calendering group	3 topcoat x 4 calendered base paper and 4 calendered precoat = 24 conditions
Base paper calendered 100°C - 200 kN/m		
Precoat calendered 100°C - 50 kN/m		
Precoat calendered 100°C - 200 kN/m		
Base paper calendered 200°C - 50 kN/m		
Base paper calendered 200°C - 200 kN/m		
Precoat calendered 200°C - 50 kN/m		
Precoat calendered 200°C - 200 kN/m		
Precoat 100 parts GCC (1.4 μm) + Acrylic Latex	Group 3 SA + Protein substitution group	3 topcoat x 2 precoat 6 = conditions
Precoat 100 parts GCC (1.4 μm) + Protein		
100 parts BPSD GCC (0.659 μm)	Group 4 100 parts pigment substitution	3 topcoat x 5 precoat = 15 conditions
100 parts BPSD GCC (0.3598 μm)		
100 parts PCC (0.499 μm)		
100 parts Brazilian clay (0.548 μm)		
100 parts NPSD GCC (0.6593 μm)		

Similarly, the effect of the structure variations brought about by above modifications on printability can be explained by contact angle analysis and DELTACK curves. For the DELTACK curves we are focusing on the comparison of the actual curves, namely through average values for total condition, and maximum tack force and time. The link between surface structure modification and printability is also supported by the analysis of SEM pictures.

All results have been further validated through statistical analysis using the projection on latent structure method.

5.2 Effects of 20 parts clay substitution in the precoat layer (Group 1)

The Group 1 includes 5 different conditions. The first condition has a precoat formulation that includes 100 parts GCC (1.4 μm) and is considered as the reference comparison point. The 4 other conditions are 80 parts GCC (1.4 μm) as in the reference but now with 20 parts clay having a different particle size distribution, and aspect ratio, as listed in table 5-2. In essence, the 20% clay substitution is the variable between each formulation. The aspect ratio of the clay has not here been considered as a key variable (as it will be seen from our results).

Table 5-2 Conditions for the 20 parts clay substitution - Group 1

Precoated formulation	Group	Formulation number
100 parts GCC (1.4 μm)	Control	3 topcoat = 3 samples
20 parts High glossing clay (0.469 μm)	Group 1 20 parts clay substitution	3 topcoat x 4 precoat = 12 conditions
20 parts No.2 clay (2.13 μm)		
20 parts delaminated clay (5.312 μm)		
20 parts High aspect ratio clay (6.329 μm)		

5.2.1 Analysis of the precoat and topcoat structures: 20 parts clay substitution (Group 1)

5.2.1.1 Analysis of the precoat and topcoat structure through pore size distribution

Figure 5-1 presents the pore size distribution of the precoat for the reference paper (in blue, average particle size 1.4 μm) and the 4 samples with 20 parts clay substitution by clays of increasing average particle size from 0.469 μm to 6.329 μm . We can conclude that the pore diameter increases and the volume slightly increases with the increasing of the average particle diameter and the aspect ratio (high aspect ratio). As all precoats contain the same latex (S/B), the structure modification is due to the network of pigments, the way they arrange in the matrix. The smaller the particle size, the easier it is for the particle to fill-in existing pores.

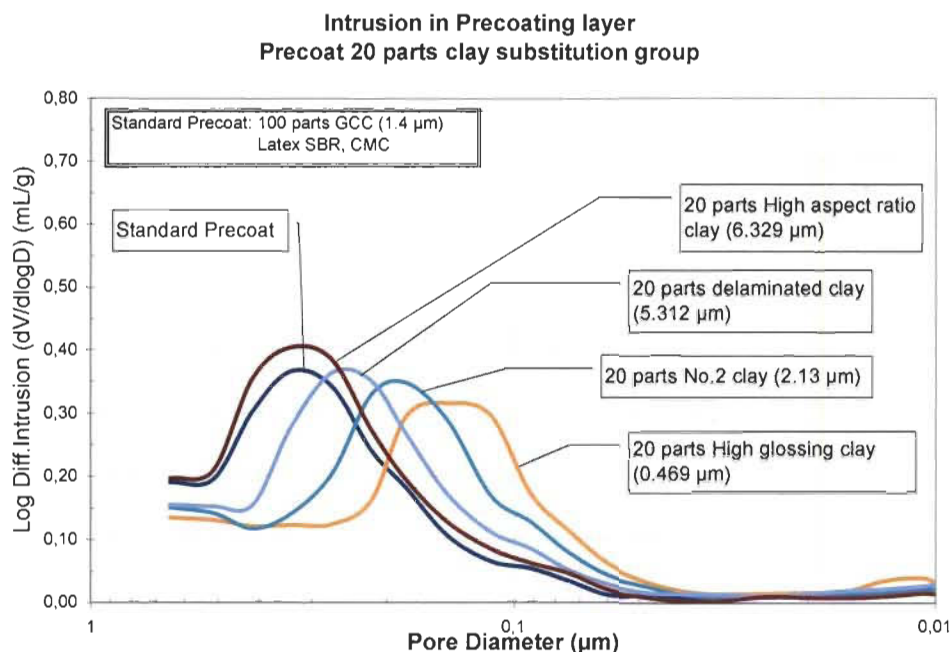


Figure 5-1 Mercury Intrusion in Precoated layer – Precoat 20 parts clay substitution Group

Figure 5.2 presents the pore distribution for the precoat (standard or reference condition) and the pore distribution of the topcoat for the 3 latexes used in the study. It appears clearly that applying a topcoat on a precoat has a direct influence on the pore distribution of the precoat. The pore volume decreases for all precoat structure once the topcoat is applied. However, using different latexes does not change the resulting structure of the precoat. Indeed, by analysing the 3 curves corresponding to the 3 latexes on Figure 5-2, it is apparent that the precoat structure is exactly the same with the 3 different topcoat conditions.

Important remark on the analysis of the mercury intrusion graphs. It is here worthy to note that the curves in Figure 5-2 originate from 3 different mercury intrusion tests but that the curves are quite coherent: *i.e.* the apex in the precoat in pore size distribution occurs at the same pore diameter for all 3 samples. The comment we are making here for Figure 5-2 is true for all curves we have analysed in our study. We consider that such an accurate location of the apexes and curves is a confirmation that our technique of data treatment is valid. It is also why we are able to perform a fine and detailed comparison of mercury intrusion curves and isolate the various effects of pigment,

latexes, and of the all conditions of our study. Subsequently, the “subtraction” of the precoat data becomes feasible to allow for the sole top coat analysis. The analysis of the topcoat distribution is done below for the 3 latexes, using the data “subtraction” method.

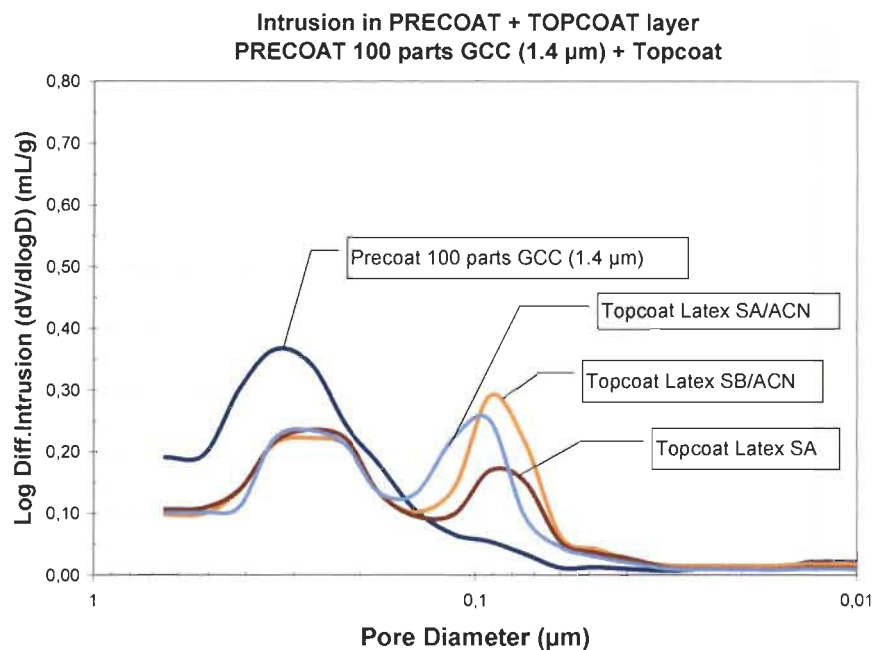


Figure 5-2 Mercury Intrusion in Coating structure for condition with Standard Precoat - 100 parts GCC (1.4 μm) - uncalendered

Figures 5-3, 5-4, and 5-5 present the topcoat pore distribution for the calendered samples for the 3 latexes used in the topcoat: *i.e.* S/B/ACN, S/A latex, and S/A/ACN, respectively. Each Figure present 5 different curves: one corresponding to the reference precoat (dark blue), and 4 curves corresponding to the 20 parts clay substitution: *i.e.* high glossing clay (orange), N° 2 clay (pale blue), delaminated clay (grey), and high aspect ratio clay (brick red).

For all topcoat structures, the cut-off gap in pore size is 0.03 μm to 0.14 μm . The cut-off value and the pore interval is selected to correspond to the minimum in the pore size distribution between the precoat and the topcoat for the standard precoat (reference) using the S/B/ACN latex. It is easy to verify in Figure 5-3 that the reference mercury intrusion curve (in dark blue) intersects the x-axis (0 value in mL/g) at 0.14 μm . All the

other conditions within the group in Figure 5-3 cross the x-axis to/or very close to 0.14 μm .

The S/A latex (Figure 5-4) and S/A/ACN (Figure 5-5) present a very different effect on the topcoat structure. For the S/A latex, all the curves below 0.1 μm are under the x-axis (remembering it is an artefact due to the data treatment) indicating that, for this latex, the topcoat has a lower pore volume than the topcoat with the S/B/ACN latex. The opposite is true for the S/A/ACN latex where all curves are above the x-axis, indicating a higher topcoat pore volume compared to the topcoat with the S/B/ACN latex. We conclude that the latexes have an influence on the topcoat pore structure although we do not have, at this time, an explanation to such an effect we surmise that it might be related to the chemical structure and/or gel content of the latexes. The characteristics of the latexes are listed in table 4.1.

The changes in pore volume and diameter observed with the precoat (see Figure 5-1) are transposed on the topcoat: these vary as a function of the clay used for the 20 part clay substitution. The only difference is the change on the coating structure is only in pore volume as related to the clay used: for instance, the high glossing clay always presents the lowest pore volume and the high aspect ration clay always presents the highest pore volume. It is true for the 3 topcoat latexes (S/B/ACN, S/A and S/A/ACN) as it can be verified in Figures 5-3, 5-4 and 5-5. The analysis will be further detailed using the average pigment size as an independent variable.

5.2.1.2 Influence of the precoat (20 parts substitution) on the topcoat/precoat combined structure

Figure 5-6 shows the total pore volume for the combined precoat/topcoat layers structure as a function of the clay average particle size in the 20 part substitution. The precoat only curve (without topcoat) is used as a reference for the initial structure before topcoat application.

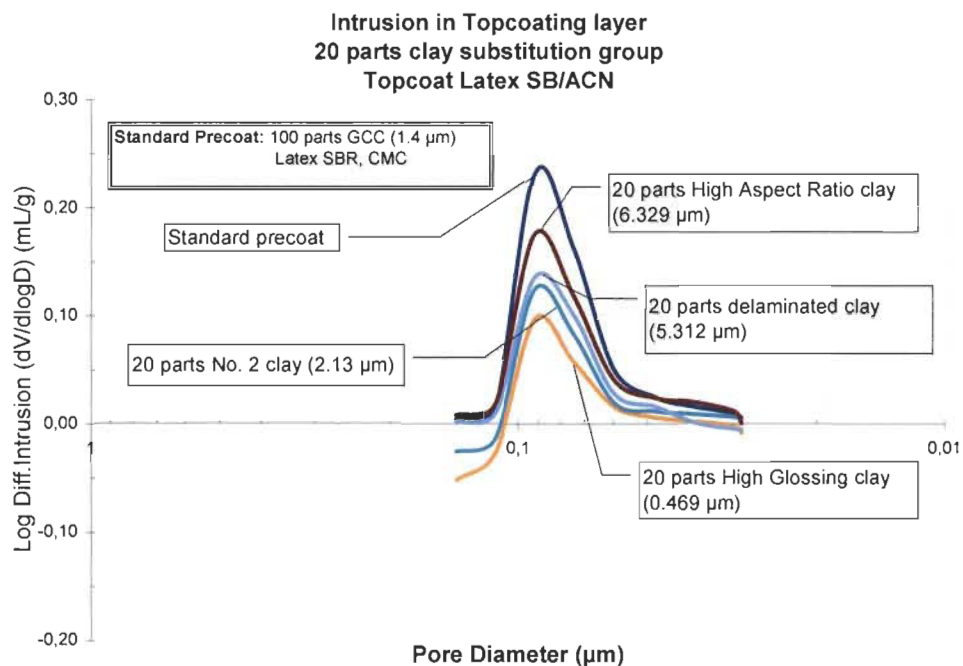


Figure 5-3 Mercury Intrusion in Topcoating Layer - 20 parts clay substitution group - S/B/ACN latex – uncalendered

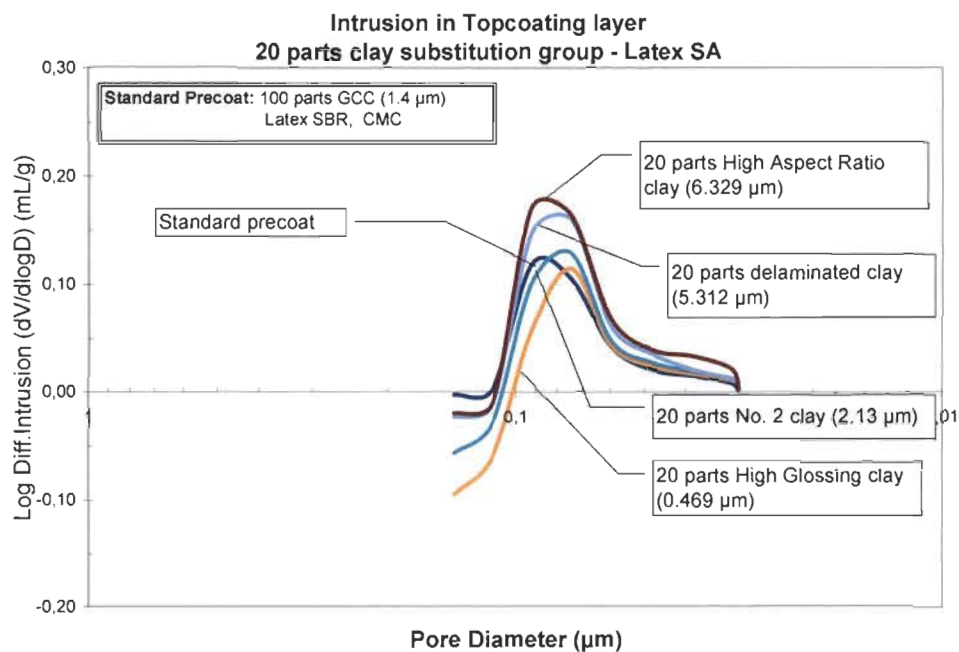


Figure 5-4 Mercury Intrusion in Topcoating Layer - 20 parts clay substitution group - S/A latex – uncalendered

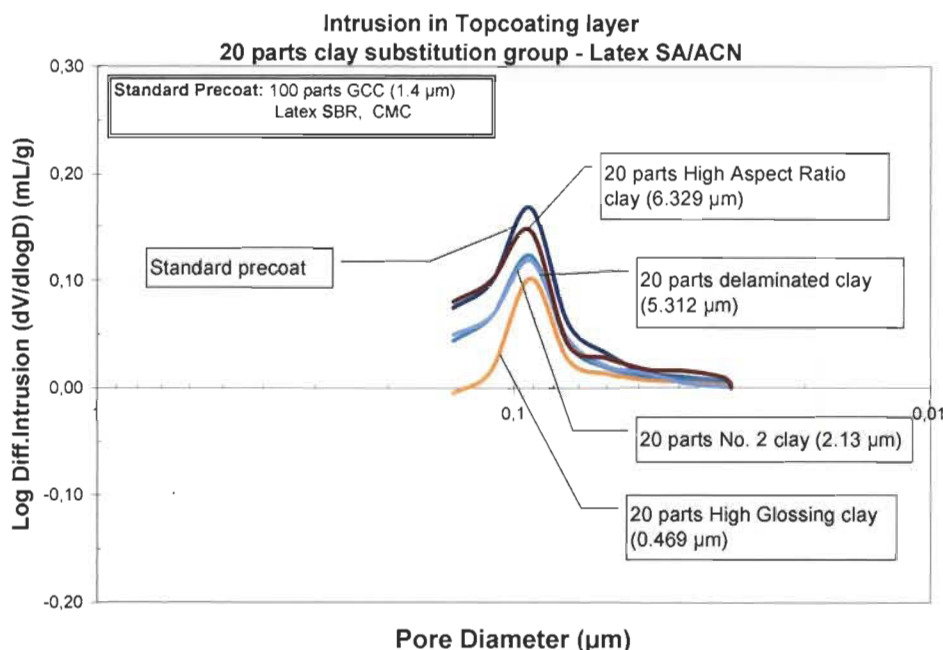


Figure 5-5 Mercury Intrusion in Topcoating Layer - 20 parts clay substitution group - Latex S/A/ACN – uncalendered

Figure 5-7 is identical but after calendering of the topcoat. For both uncalendered and calendered samples, the total pore volume of the precoat/ topcoat layers increases with the pigment size used as the 20 parts replacement in the precoat. We will come back to the physical explanation later when analyzing the topcoat structure variations as a function of the precoat 20 part substitution.

Both for the uncalendered (Figure 5-6) and the calendered samples (Figure 5-7), the latex S/A/ACN shows a higher pore volume than the other latexes (S/B/ACN and SA) notwithstanding the fact that the pressure we use to obtain a target gloss of 70 is about 20.7 bar for the S/A/ACN latex compared to 34.5 bar for the 2 other latexes. The difference in structure, already present in the uncalendered samples, is maintained in the calendered samples.

As far as gloss development is concerned, the acrylonitrile (ACN) is known to improve gloss development: it is probably the reason why the pressure needed to obtain a 70 gloss is lower for the S/A/ACN latex. However, it does not occur for the S/B/ACN latex. The gel content of the S/B/ACN latex being lower than the S/A/ACN latex might

be the reason why the calendering pressures to obtain a 70 gloss are the same for the S/A and S/B/ACN latexes.

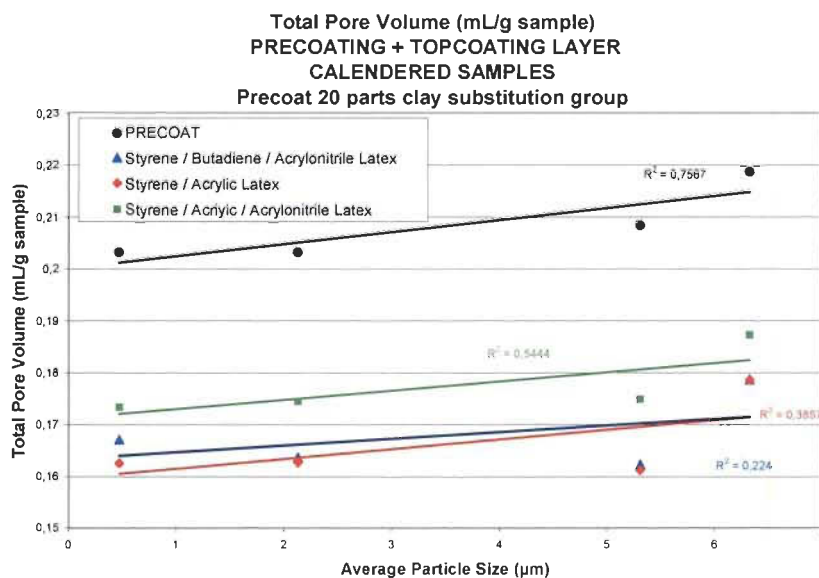
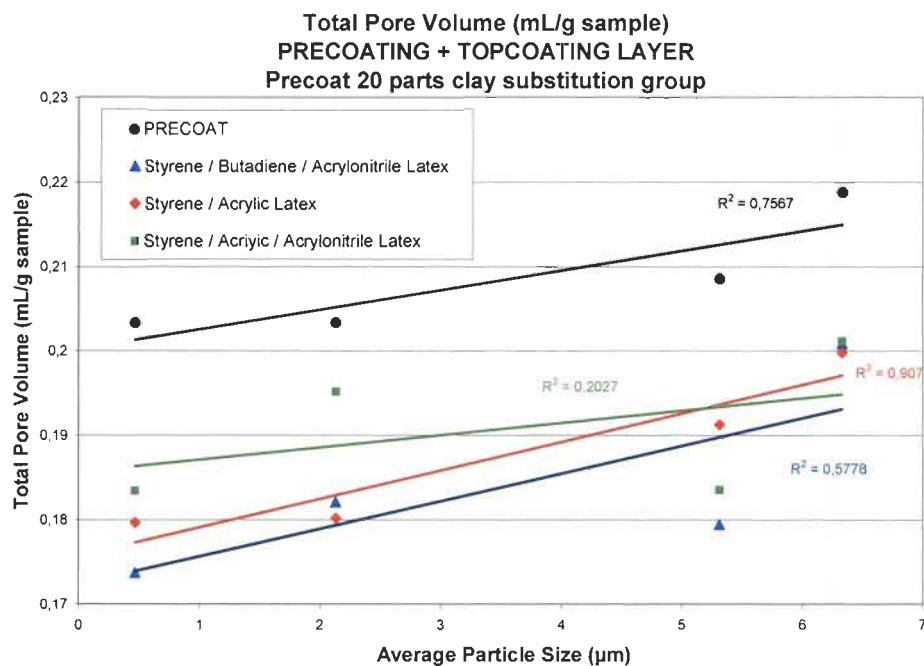


Figure 5-8 presents the average pore diameter of the precoat/topcoat layer structure to increase with the pigment size of the precoat 20 part substitution. It is apparent that the precoat structure is more open with larger particle size pigment than with smaller particle size pigment used in the 20 parts substitution. The effect is less apparent for the precoat/topcoat combined structure, whatever the latex used. Therefore, we should look at the topcoat structure only to analyse the influence of the precoat 20 part pigment substitution.

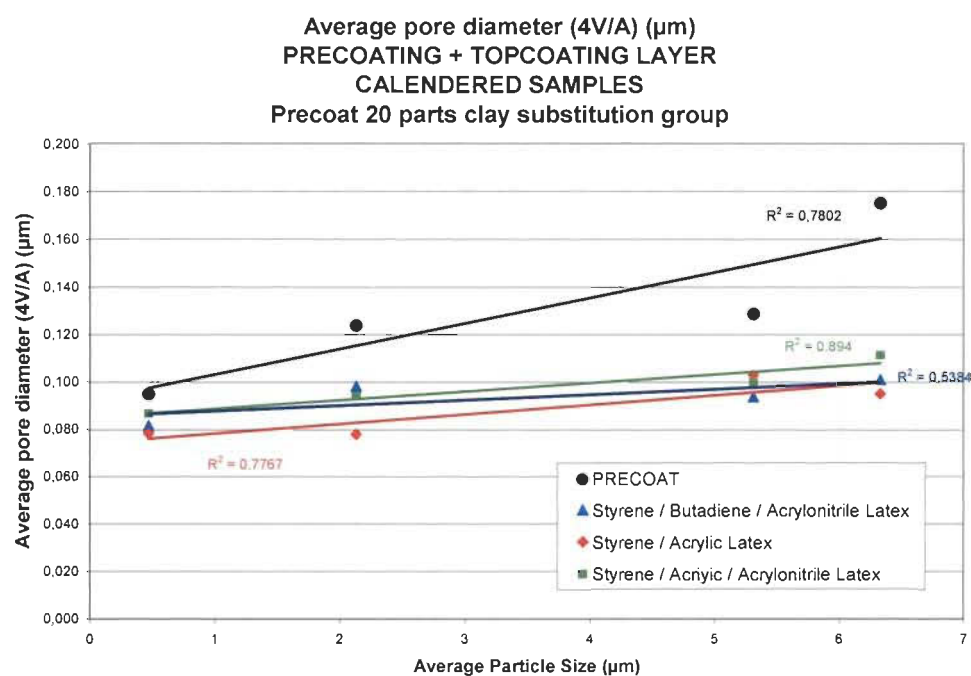


Figure 5-8 Average Pore Diameter (APD) Calendered Paper for Group 1 - Comparing the 3 latexes

5.2.1.3 Influence of the precoat structure (20 parts substitution) on the topcoat structure

As said previously, the increase in total pore volume as a function of the pigment particle size in the precoat layer (Figures 5-6 and 5-7) needs further explanation. Due to the fact that both Figures show that the precoat total pore volume increases with the particle size, we may surmise that it is solely due to the increase in the precoat. However Figure 5-9 shows that the topcoat total pore volume increases with the pigment average particle

size in the precoat. It is true for the 3 different latexes used in the topcoat although the topcoat layers have all the same pigment system (70 parts GCC and 30 parts N°1 glossing clay). It can then be concluded that the precoat structure has a direct effect on the structure of the topcoat. We propose that three physical principles may explain such an effect:

1. forced penetration of the topcoat coating color in the precoat structure: an open structure with large pores (as defined by pore diameter) bringing about more penetration than a closed structure with small pores,
2. capillary penetration within the precoat structure: smaller pores favouring capillary penetration,
3. preferential topcoat pigment penetration within the precoat structure: smaller pigments (N°1 high glossing clay) penetrating more easily the precoat structure than larger size pigment (GCC).

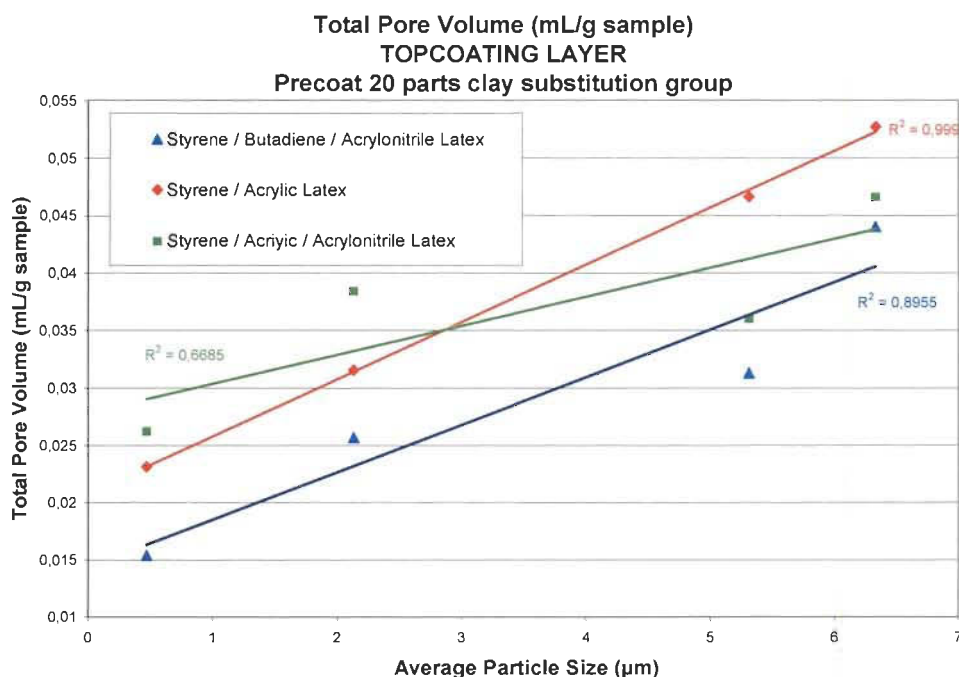


Figure 5-9 Total Pore Volume (TPV) Topcoated layer for Group 1 as a function of the particle size of the precoat layer - Comparing the 3 latexes

Forced penetration implies that larger pores lead to more penetration of the topcoat layer within the precoat layer: i.e. leaving less coating layer on top and subsequently a smaller pore volume. According to the fact that the topcoat pore volume increases (linearly, Figure 5-9) with the precoat average particle size, this hypothesis can be ruled out: the forced penetration is not the right explanation.

The effect of capillary penetration can be further analysed by looking at the average pore diameter of the topcoat layer. For instance, analyzing the average pore diameter in Figure 5-10 of the topcoat structure with the S/A/ACN latex, the pore size of the topcoat is independent of the pigment average particle size in the precoat. The increase in pore volume can then only be accounted for by a large number of pores of the same diameter. In other words, for a close structure in the precoat, there is less pores remaining than in the open structure. It means that more coating color penetrates the precoat structure when pores are smaller: it can only be explained by capillary penetration that is favoured by smaller capillaries, here smaller pore sizes (in the precoat structure). We concluded that capillary penetration should be considered as an acting force as can be seen in Figure 5-11.

However, when analyzing the topcoat structures related to the S/A and S/B/ACN latexes, we see that the average pore diameter increases slightly, but significantly, with the pigment average particle size in the precoat. It means that another phenomenon is taking place.

We propose “preferential topcoat pigment penetration” in the precoat as the solid phase of the topcoat coating color contains two pigments of different sizes (around 0.15 - 0.20 μm for the clay and around 0.66 μm for the GCC) as can be seen in Figure 5-12. Large pores in the precoat may absorb smaller pigments from the topcoat, whereas leaving a larger pore structure in the topcoat. For these two latexes, we surmise that there is a combination of the two phenomena: capillary penetration and preferential pigment penetration.

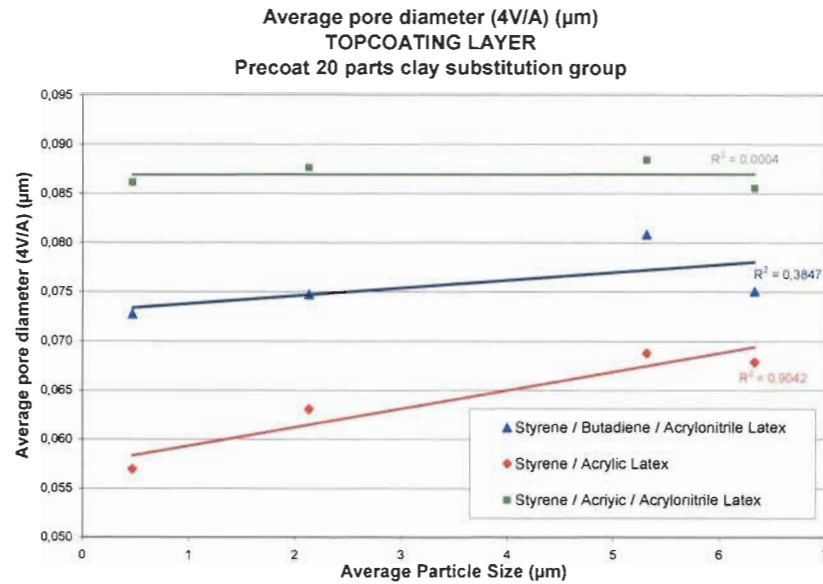


Figure 5-10 Average Pore Diameter (APD) Topcoated layer for Group 1 as a function of the particle size of the precoat layer - Comparing the 3 latexes

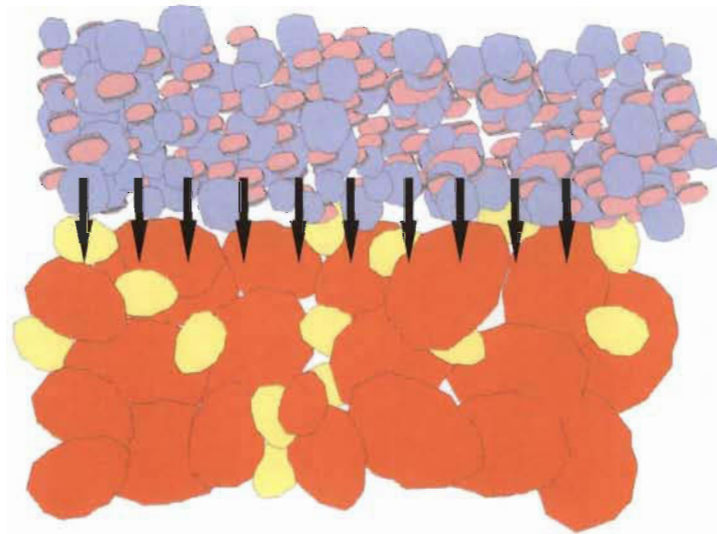


Figure 5-11 Capillary theory related to smaller pores in the precoat. Top-coat: GCC is in purple-blue, clay in light red. Precoat: GCC is in orange and N°1 fine clay is in yellow.

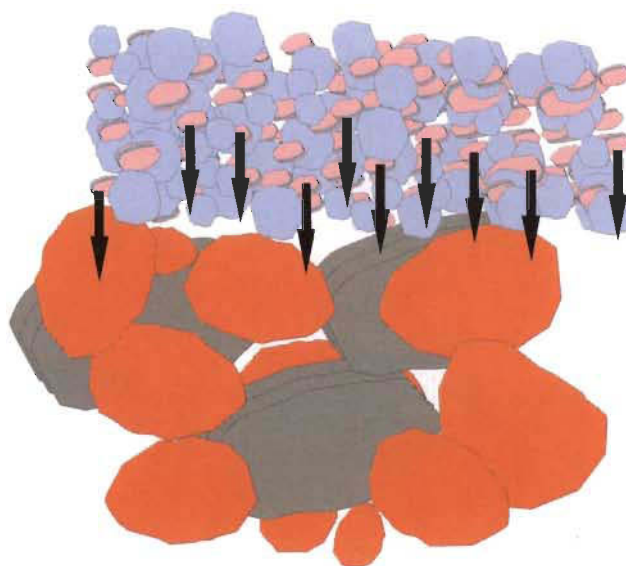


Figure 5-12 Preferential movement theory related to bigger pores in the pre-coat. Topcoat: GCC is in purple-blue, clay in light red. Precoat: GCC is in orange and high aspect ratio clay is in grey.

5.2.2 Printability variations related to 20 parts clay substitution in the pre-coat (Group 1)

As presented in Section 3.8, the printability of the double coated samples is evaluated by the DELTACK method for each latex. A typical graph is shown in Figure 5-13 for latex S/B/ACN and the 4 samples of the 20 parts clay substitution group. For all 3 latexes, the shape of the curves is somehow similar.

The same comment is valid for the remaining groups. Consequently, and for clarity sake, all the remaining graphs are presented in Appendix **2**. As explained in Section 3.8.2, the key information deduced from the DELTACK Method are the time to reach maximum tack and the maximum tack value as these two parameters can be related to the topcoat/precoat layer structure and the composition, mainly latex type, of the topcoat layer.

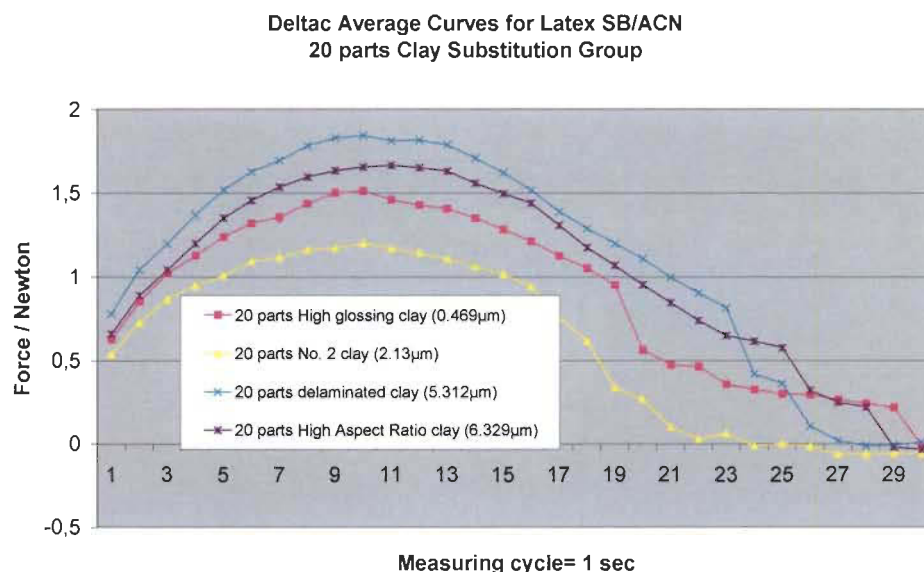


Figure 5-13 DELTACK – 20% clay substitution Group, S/B/ACN latex

Figure 5-14 shows the maximum tack force (maximum force, in N) as a function of the time (in sec) to reach the maximum force. The S/A and S/A/ACN latexes are regrouped and there seems to be no relationship relating time and force. However, for the S/B/ACN, the maximum force increases linearly with time; in other words, when the ink tack force is reached sooner, it is also lower in force value. We surmised that it might be due to the structure of the topcoat. Figure 5-15 shows the time to reach the maximum force as a function of the pore volume of the topcoat/precoat structure. Again, the data are grouped as a function of the latexes. When analysing the S/B/CAN values, it can be seen that the low times (to reach maximum force) correspond to small pore volumes and that the high times correspond to high pore volume. Consequently, going back to Figure 5-14, we conclude that, for the S/B/ACN latex, the minimum tack force correspond to a low pore volume, and that the maximum tack forces correspond to large pore volume. From an ink transfer standpoint, large volume allow for more ink to penetrate the structure than small volume. In essence, a large pore volume in the topcoat/precoat structure will lead to a thinner ink film, after multiple transfers as it occurs in the DELTACK method and by consequence to a higher tack force. The phenomenon can be further modulated by solvent penetration within the topcoat structure, according to the average pore diameter of the topcoat/precoat structure.

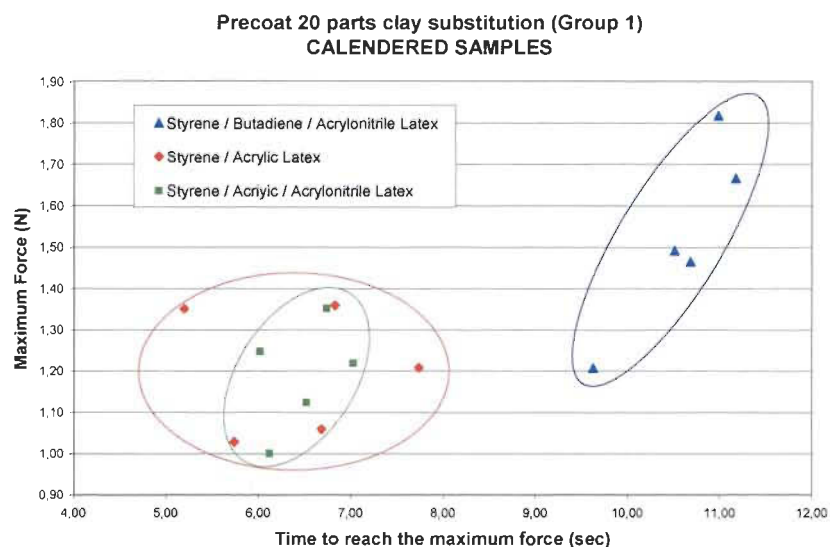


Figure 5-14 Time to reach the maximum force function of the maximum force

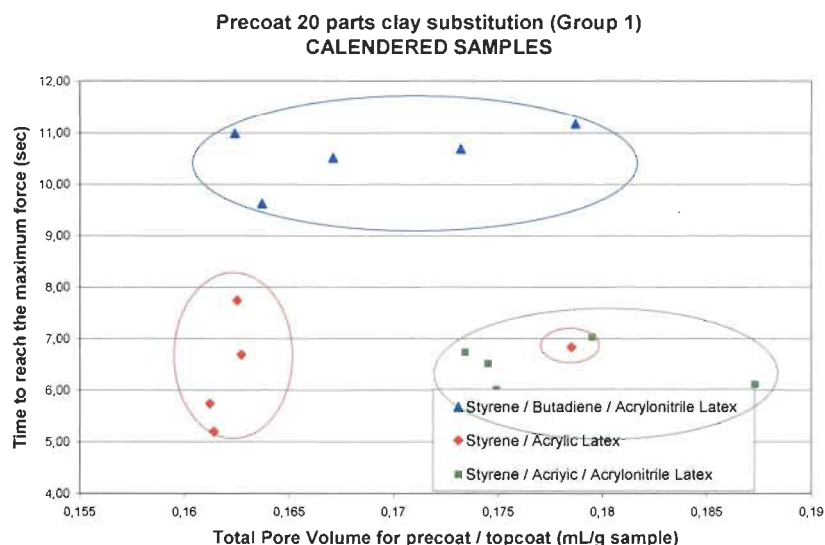


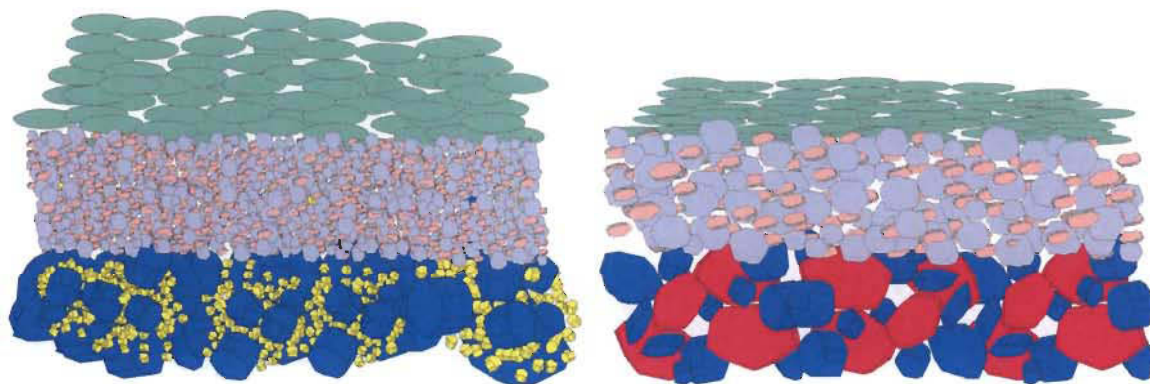
Figure 5-15 Total Pore Volume function Time to reach the maximum force

Another conclusion from the analysis of Figures 5-14 and 5-15, is that the key information relating the structure of the topcoat/precoat layer will be deduced from the analysis of the maximum tack force as a function of both the pore volume, allowing for the capacity to absorb a given volume of ink, and the average pore diameter, to take into account the capillary phenomenon. Figures 5-17 and 5-18 show the maximum (tack) force

as a function of the pore volume and the average pore diameter of the topcoat/precoat structure, accordingly. In addition to the grouping related to the 3 latexes, we find that a apex (minimum for the volume, maximum for the average pore size) occurs for both, the S/B/ACN and S/A latexes. The fact that no apex occurs with the S/A/ACN latex might simply be due to the lack of data at low values in either pore volume or diameter. Considering, for instance, the curves (in red) corresponding to the S/A latex, two different situations occur. On the one hand, the same maximum tack force originates from structure having two largely different pore volumes (Figure 5-17) but the same average pore diameter (Figure 5-18), as seen from data points corresponding to the downward arrows. On the other hand, the same maximum tack force originates from structure having the same pore volume (Figure 5-17) but two largely different average pore diameters (Figure 5-18), as seen from data points corresponding to the upward arrows.

Obviously to explain such behaviour of the topcoat/precoat structure, at least two phenomena must occur and have opposite effects. Let us consider the case where we obtain the same maximum tack force with a) the same pore volume (upwards arrows, Figure 5-17) and b) largely different pore diameters (upward arrows, Figure 5-18). To understand the phenomenon that we know to be related to the topcoat/precoat structure as we have illustrated in Figures 5-11 and 5-12, we need to have some information on the topcoat structure only. Such information is provided by the Figures 5-9 and 5-10 which show both the average pore size and the pore volume of the topcoat to increase linearly with the pigment size of the precoat structure (20 parts substitution). In Figure 5-17, the available volume for ink penetration provided by the topcoat/precoat structure is the same, and we could conclude that the ink transfer is the same and that the remaining ink layer on top of the topcoat structure is the same, providing the same maximum tack force. We propose here that the maximum tack force is due to a more complex phenomena as the average pore size of the two structures is widely different: *i.e.* the ink transfer should not be the same (ref. work by [104, 105]). In essence, we propose and surmise that ink transfer is different because the topcoat structures are different. In effect, the arrow (case a) corresponding to the low pore size in precoat/topcoat structure corresponds to very fine pores and a very small volume in the topcoat structure (see Figures 5-9 and 5-10). In parallel, the arrow (case b) corresponding to the high pore size (in pre-

coat/topcoat structure) corresponds to a larger pores and larger volume in the topcoat structure. Practically, it means that ink layer remaining of the surface in case ‘‘a’’ will be thicker than in case ‘‘b’’ (smaller pores and smaller available volume). However, considering the actual sizes of these pores, it also means that the structure with very small pores will favour, due to capillary penetration, the preferential absorption of ink solvent. In essence we will end up with a thicker ink film but with less solvent, *i.e.* a tackier ink. In the case of the larger pores, there will be no or less penetration of ink solvent. It is therefore quite feasible that the two effects being opposite, we will end up with the same maximum tack force. The phenomenon is illustrated in Figure 5-16.



Bottom = precoat layer / middle = topcoat layer / top = ink film (green)

Figure 5-16 Ink film thickness related to an equal ink tack force and the precoat structure: close precoat structure (left) and open precoat structure (right)

Furthermore, we also know that some precoat formulations containing high glossing clay ($0.469\text{ }\mu\text{m}$) and No. 2 clay ($2.13\text{ }\mu\text{m}$) produce a larger amount of small sized pores in the final pore size distribution after topcoat application and calendering than the pre-coats containing delaminated clay ($5.312\text{ }\mu\text{m}$) and high aspect ratio clay ($6.329\text{ }\mu\text{m}$). It is also known that for coatings of equal pore density (number of pores per unit area), the ink sets faster due to the larger pores. Compared at equal pore volume which is a function of size and pore density, coatings with smaller pores set ink faster because of the larger number of sites available for ink penetration by capillarity [9].

When analyzing the situation where a) the available pore volume of the topcoat/precoat structure is widely different (downwards arrows, Figure 5-17) but b) the average pore diameter of the topcoat/precoat structure is the same (downwards arrows, Figure 5-18), then, a similar analysis can be performed. In essence, we will end up with two different ink layers because the topcoat structure is modulated by the precoat structure. Therefore, due to the preferential solvent penetration, the maximum tack force will still approximately be the same. One should note that we have taken two extreme cases and that this compensation effect of solvent penetration controlling the ink tack and ink transfer controlling the ink thickness (and therefore also the tack force) is valid for all intermediary cases.

Although we understand that the proposed mechanism could be modeled (ref. work by [106]), it is outside the scope of present work. It should also be noted that the mechanism that we are here proposing is complementary to previous works and models proposed by [76, 107, 108] as is explained below.

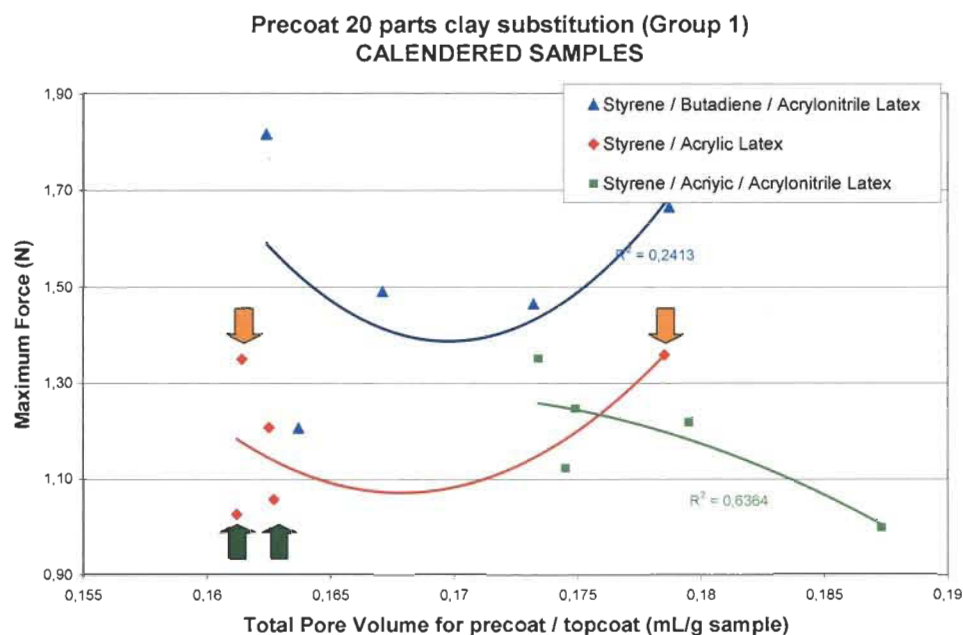


Figure 5-17 DELTACK maximum force versus total pore volume for 20 parts clay substitution group

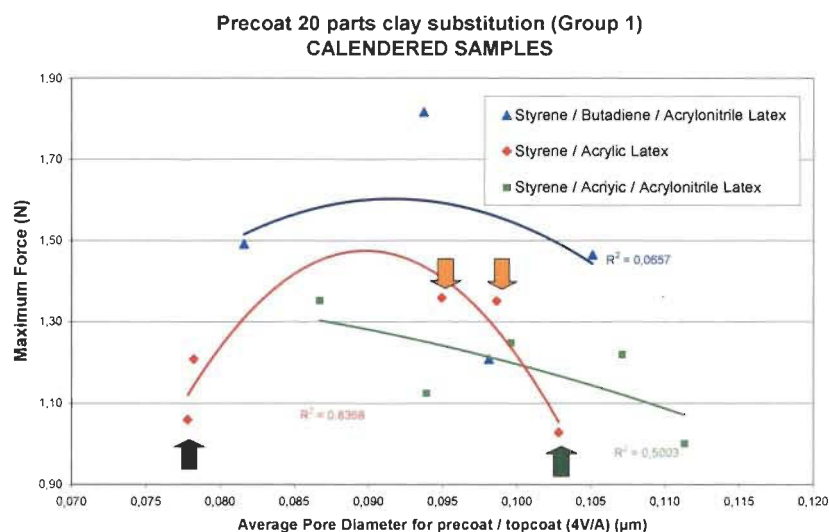


Figure 5-18 DELTACK maximum force versus average pore diameter for 20 parts clay substitution group

The slow ink setting trend containing latex with low T_g and acrylonitrile is seen for all the precoat and topcoat combinations. Latexes S/B/ACN has an ink setting behaviour that follow the coating porosity while latex S/A and S/A/ACN have a slower ink setting than could be predicted from the sole topcoat/precoat porosity.

The slow ink setting trends for topcoats with the latex containing acrylonitrile could be explained by the slowing effect of acrylonitrile and the well-known rule in coating formulation and physics: latex is about 10% of the coat weight, 20% of the coating volume, and 50% of the coating surface. Indeed, Rousu *et al.* [101] showed that low latex solubility parameter (butadiene < styrene = acrylate < acrylonitrile) leads to a large effect of oil interaction. Furthermore, latexes with low glass transition temperature (T_g) and percentage of gel (gel-%) show an increased interactivity with ink oils [109].

It also means that the setting of the ink can also be adjusted to be faster or slower according to the choice of ink. It implies that the differences we have analysed could be greater or smaller depending on the ink used in the printing operation.

Finally, we used a lower calendering pressure for the S/A/ACN latex coatings to achieve the same gloss target than all other coatings. The difference in calendering probably

produces a slightly different connectivity for the coating pores compared to the other coatings. We have not further analysed such a probability.

Last but not least, the DELTACK method is performed without fountain solution. The acceptance of different liquids (solvent, fountain solution, ink oils, etc.) to the pores will further complicate how the pore-to-throat diameter ratio, and the available volume of the small voids will influence the ink setting (and therefore the maximum tack force from the DELTACK method). It is still unclear how the latex with the increased solvent absorption (lower solubility parameter) shows a faster ink setting, and the question remains if the latex swelling may partly close or not surface pores. Consequently, the latex swelling effect may further reduce the coating porosity and capillary absorption [110-111]-112].

The last comment pertains to the solubility parameter of the solvent within the ink. As the difference between the solubility parameter of the solvent within the ink and the chemistry of the latex increases, the rate of solvent absorption decreases. The addition of acrylonitrile to a latex polymer decreases the solubility parameter compared to styrene butadiene latex. The result is that the difference between the solubility parameter of the solvent and the acrylonitrile latex that of the styrene butadiene latex, results in a decreased ink set rate for the acrylonitrile containing latex [113, 114].

5.2.3 Contact Angle results comparison from Group 1 (20 parts clay substitution)

The contact angle measurements as a function of the average particle size of the precoat layer for the group 1 (20 parts clay substitution) are represented in Figures 5-19 and 5-20 for the uncalendered and calendered samples, respectively. It can be seen that the contact angle for the S/B/ACN is always higher than for the S/A/ACN and the S/A latexes, the effect being more pronounced for the uncalendered samples. It is confirmed by looking at the contact angle mean shown in table 5-3.

We surmised that it might be due to either to the non polar component of the S/B/ACN being higher than for the other two latexes or to differences in the film forming proper-

ties. In addition, for the S/B/ACN latex, the contact angle decreases as a function of the average particle size of the precoat layer whereas it is independent of the average particle size for the other two latexes. In addition, the calendering has a greater effect on the contact angle for the pigment with a higher PSD as the particles with the highest average particle size have also the highest aspect ratio.

It is important to remember here, the S/A/ACN latex has been calendered with a lower pressure than the two other one. In effect, the S/B/ACN seems to be more affected by the calendering than either the S/A latex or the S/A/ACN latex. In this particular case, the S/B/ACN latex shows an important reduction in contact angle between the coated paper and calendered paper. For the two other latexes, the contact angle increases upon calendering. The effect of calendaring is classical and related to the reduction in surface roughness.

From above analysis, we can conclude that also the contact angle provides some information on the effect of the precoat, it is not sufficient to deduce useful in-depth information on the effect of precoat layer on the final surface properties of the paper. The results obtained in the other groups confirmed this analysis and therefore, we will not repeat it.

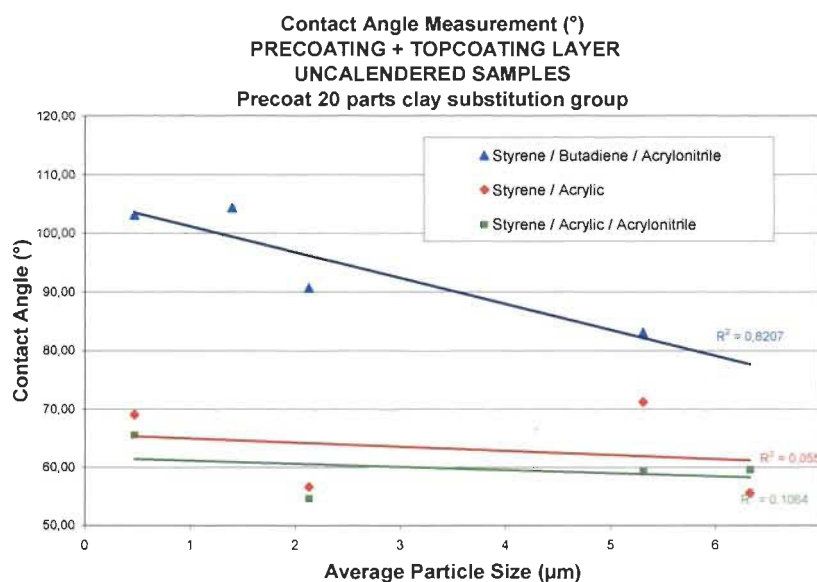


Figure 5-19 Contact angle for Coated Paper– 20% clay substitution Group

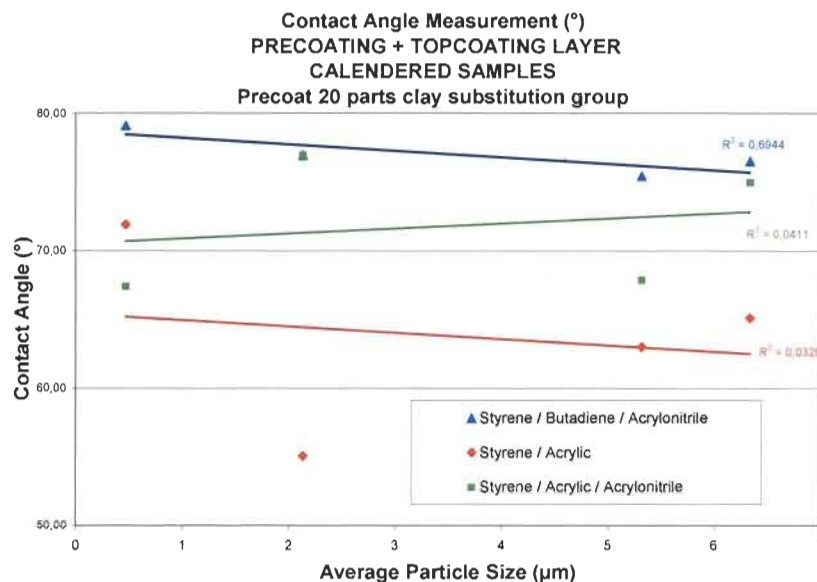


Figure 5-20 Contact angle for calendered Paper– 20% clay substitution Group

Table 5-3 Mean Contact Angle (°) values for Group 1 – Coated and Calendered Paper

	S/B/ACN latex	S/A Latex	S/A/ACN latex
Coated Paper	94.66°	60.56°	58.81°
Calendered Paper	75.31°	64.29°	70.85°

5.2.4 Summary: 20 parts substitution in the precoat layer (Group 1)

Present work has clearly demonstrated that substituting 20 parts of clay in 100 parts GCC precoat formulation permits a modulation of the coating structure to obtain the desired structural and printing properties. Similarly, we have shown that the topcoat structure is affected by the precoat and that a possible is capillary penetration, a preferential movement, or a forced penetration into the precoat structure by the topcoat. The forced penetration, or a part of it, probably originates from the rewetting of the precoat layer upon topcoat application.

Another key conclusion is that differences in printing properties as described by the DELTACK analysis are mainly related to the type of latex used in the topcoat layer.

The butadiene base latex is always higher in maximum tack force and time to get the maximum tack force compared to the styrene acrylic. The topcoat containing styrene acrylic present similar behaviour when comparing DELTACK curve shapes. Finally, we found that it is possible to have the same ink tack with very different pore structures, either with an equal pore volume and a very different average pore size of the structure or, in the opposite way, a very different pore volume with the same average pore size. We have proposed a fundamental mechanistic approach to explain this particular phenomenon. The phenomenon is related to the changes in topcoat structure coming from the different precoat structures. Overall, the structural changes in the complex two layer structure provided by the precoat/topcoat are able to modify how the ink and/or the ink solvent penetrate preferentially into the two layer structure resulting in a thick or thin ink layer with different final compositions but providing the same tack force.

5.3 Effect of calendering the base stock or the precoat layer (Group 2)

The group has been created to verify if calendering the base paper or the precoated layer could improve the final properties of the double coated paper sheet. As seen in table 5-4, the group comprises 8 conditions: 4 conditions are used to check the effect of calendering of the base paper before precoat/topcoat application and 4 conditions serve to check the effect of calendering the precoated layer before topcoat application. Two temperatures and two pressures are used for calendering, resulting in 4 different conditions. The 4 different conditions of temperature and pressure applied on the base stock or the precoated layer are the same to be able to verify if calendering temperature and pressure would have cumulative or opposite effects on the final double coated paper structure and properties.

The precoat and topcoat layers are identical for all 8 conditions. The precoated layer is 100 parts of GCC (1.4 μm) with a S/B latex. The complete formulation is described in table 4-2. The topcoat layer is a mix of 70 part of BPSD GCC (0.659 μm) and High glossing clay (0.469 μm). Due to the primordial importance of the latex effect seen previously, we still use 3 different latexes (i.e. 3 different samples), namely S/B/ACN, S/A, and S/A/ACN. The formulations are shown in table 4-7.

Table 5-4 Conditions for the calendering group - Group 2

Precoated formulation	Group	Formulation number
Base paper calendered 100°C - 50 kN/m	Group 2	
Base paper calendered 100°C - 200 kN/m		
Precoat calendered 100°C - 50 kN/m	Base paper &	3 topcoat x
Precoat calendered 100°C - 200 kN/m		4 calendered base paper
Base paper calendered 200°C - 50 kN/m	Precoat	And
Base paper calendered 200°C - 200 kN/m		4 calendered precoat
Precoat calendered 200°C - 50 kN/m	calendering group	= 24 conditions
Precoat calendered 200°C - 200 kN/m		

5.3.1 Analysis of the precoat and topcoat structures: calendering base paper and precoated layer (Group 2)

In order to analyse the effect of precalendering either the base paper or the precoat on the double coated papers structure, it is necessary to detail how it affects the precoat and topcoat structures separately, then the total structure of the complex double coating layer. Indeed, it was shown previously that the two layers interact through capillary penetration during manufacturing. Figure 5-21 is a good example of the base paper while a calendering has been done. The Figure shows the calendering treatment of the base paper for group 2 when 200°C and 200 kN/m were applied to the paper.

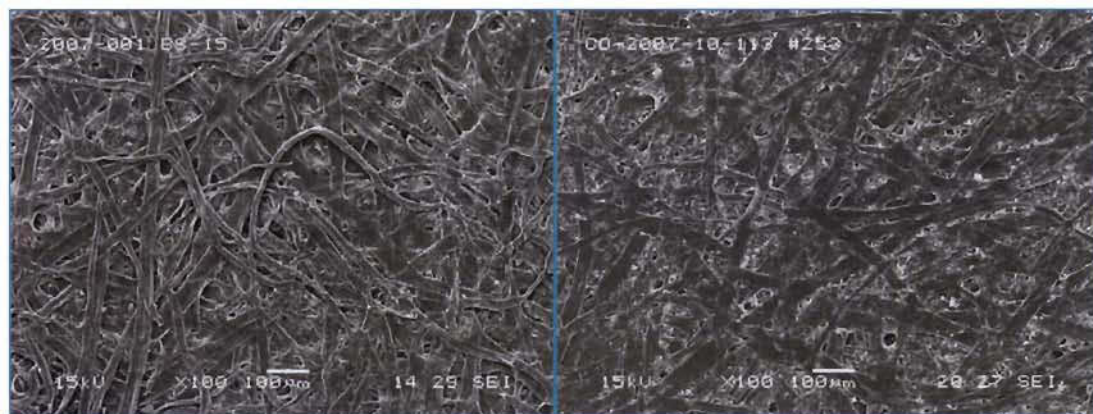


Figure 5-21 Uncalendered (left) and calendered (right) base stock use in this study

5.3.1.1 Analysis of the precoat and topcoat structure through pore size distribution

The various structures have been analysed using mercury intrusion and the normalization technique that has been described previously (Separation of the precoat and the topcoat layers).

Analysis of the precoat layer structure.

Figure 5-22 shows the pore size distribution of the precoat layer only for the precalendering of the base paper (4 conditions: see Table 5-4) and for the precalendering of the precoat layer (4 conditions: see Table 5-4). For these samples no top coat layer has yet been applied.

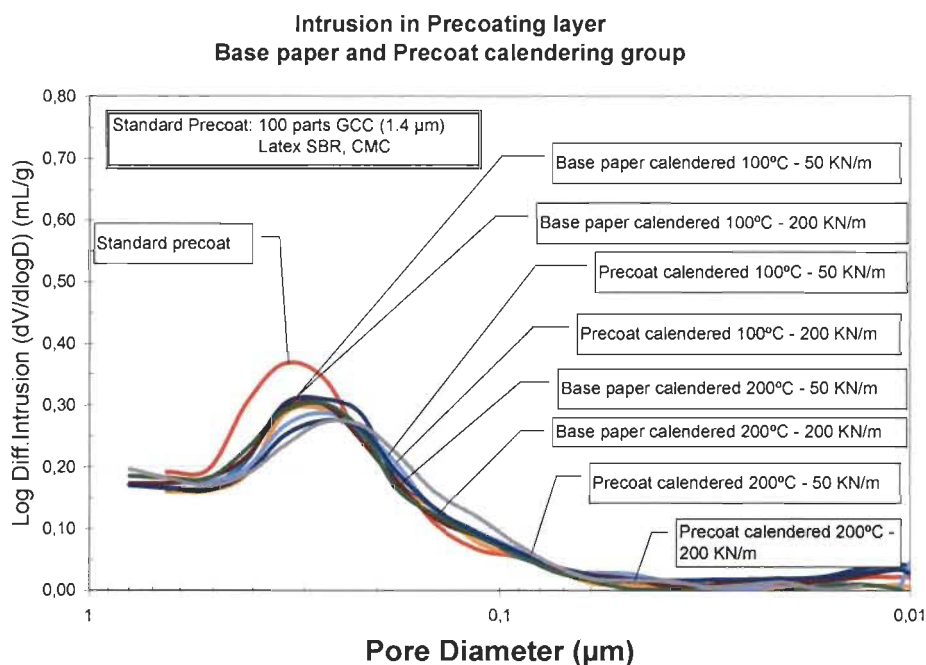


Figure 5-22 Mercury Intrusion in Precoated layer – Base Paper and Precoat Calendered Group

At the planning stages of present work, we made the hypothesis that precalendering either the base stock or the precoat layer would result in a lower mercury intrusion volume while increasing the calendering temperature and/or the pressure applied. Upon precalendering of either the base paper or the precoat, the pore size distribution of the sole

precoat layer (Figure 5-22) is always lower than the pore distribution of the reference paper. Such is to be expected from the physics of calendering as soft nip calendering somehow reduces the pore size and pore volume. However, no measurable difference can be seen in Figure 5-22 between the pore size distributions corresponding to the 8 calendered conditions as far as precalendering in a first operation either the base paper or the precoat layer. The effect of the calendering conditions, even if minor, becomes clear when analyzing the total pore volume; it is due to the fact that calculating the total pore volume integrates the pore volume at all sizes.

Table 5-5 shows, as expected, that calendering at 200 kN/m results in a lower total pore volume than calendering at 50 kN/m. However, calendering at 100°C generates a larger total pore volume than calendering at 200°C. We will come back to this apparently surprising result when analyzing the combined precoat/top coat layer structure.

Table 5-5 Average volume structure (mL/g) for the precoat layer (Group 2)

Soft Nips Pressures and Temperatures			
	100°C	200°C	
Base paper calendered - 50 kN/m	0.1909	0.2000	Average 50 kN/m
Precoat calendered - 50 kN/m	0.1869	0.1957	<u>0.1934</u>
Base paper calendered - 200 kN/m	0.1661	0.1895	Average 200 kN/m
Precoat calendered - 200 kN/m	0.1772	0.1972	<u>0.1825</u>

Analysis of the topcoat layer structure.

Figure 5-23 shows the pore size distribution for the top coat layer only for the S/B/ACN latex (used in the top coat layer mix) for the precalendered base paper (top graph) and the precalendered precoat layer (bottom graph). The reference (standard) top coat layer has been added to both graphs; it corresponds to the case where neither the base paper nor the precoat layer has been calendered. Similar graphs, not shown here, were obtained for the S/A and the S/A/ACN latexes used in the top coat.

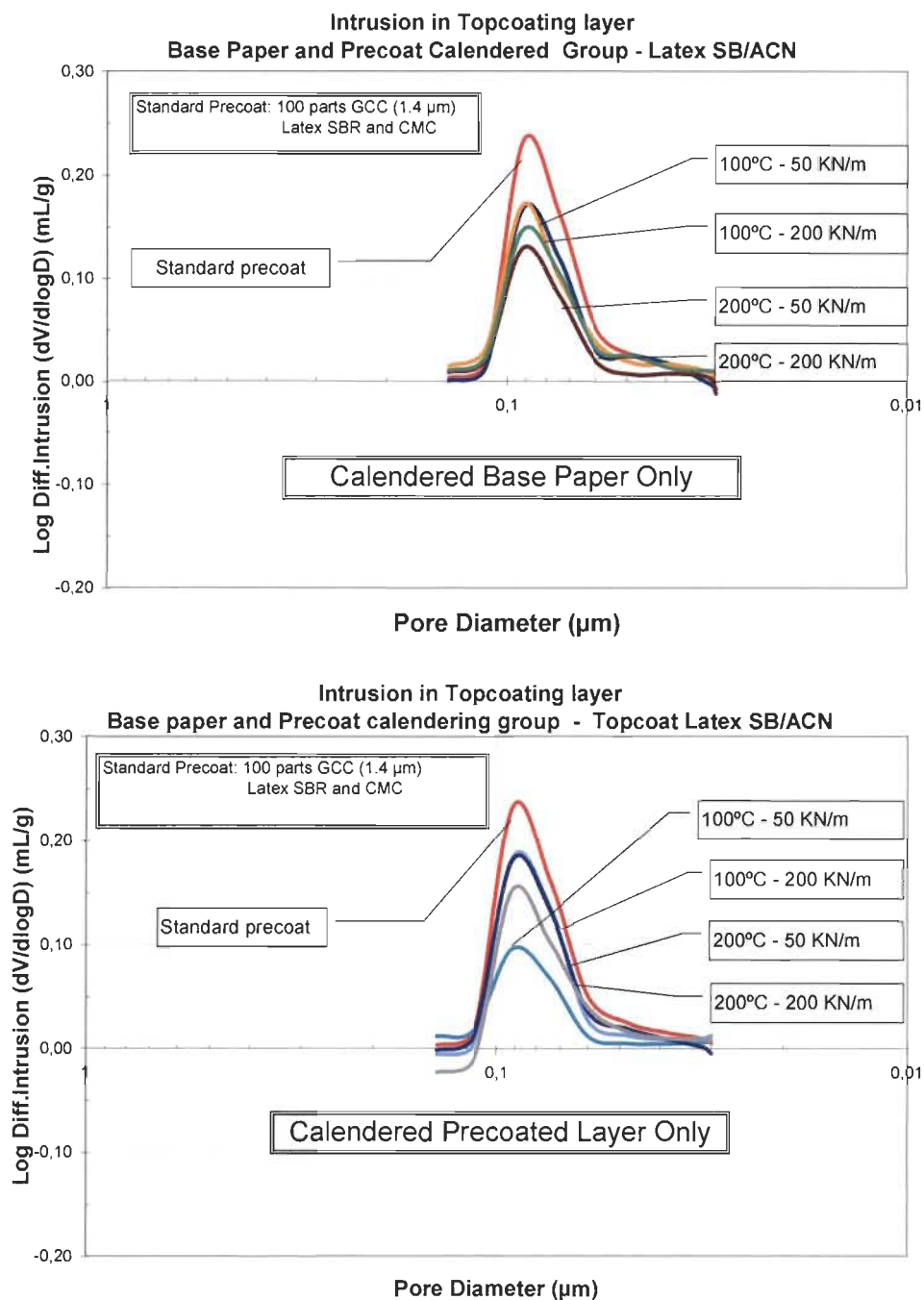


Figure 5-23 Mercury Intrusion in Topcoated layer – Base Paper and Precoat Calendered Group Separated – S/B/ACN latex

As for the precoat analysis, the top coat structure corresponding to the reference paper, with no calendering of either base paper or precoat, show a more open structure than the samples precalendered (base paper or precoat) before top coat application. When the base paper is precalendered, the pore size distribution curve is higher for the 200°C cal-

endering temperature than for the 100°C temperature. The effect on the pore distribution curves is not as clear when dealing with the precalendering of the precoat layer. However, as shown previously, we surmise that the total pore volume which integrates the incremental volumes along the pore sizes might render the calendering temperature and pressure effects more apparent. The total pore volume of the top coat layer applied to precalendered base paper and precalendered precoat is shown in Table 5-6 for the 3 latexes.

When precalendering the precoat which contains styrene butadiene (SB) latex, the SB latex tends to plasticize with temperature. The effect being more pronounced at 200°C than at 100°C, we propose that at 100°C the precalendered precoat surface will be more open than at 200°C. We propose that a filtration effect, similar to the one already proposed to explain the filler substitution effect in the precoat (Printability variations related to 20 parts clay substitution in the precoat (Group 1)), applies here. In essence, coating colour filtration and segregation through an open structure, as represented by the surface of the precoat calendered at 100°C, should create a denser top coat structure, i.e. a smaller total pore volume, than filtration through a close structure, as represented by the surface of the precoat calendered at 200°C. It also means that the top coat layer packing is improved at 100°C.

Similarly, on the basis of our proposed mechanism, precalendering the base paper has an effect on the packing of the precoat: i.e. the total pore volume of the precoat layer, when applied on the base paper precalendered at 100°C should be smaller than at 200°C. This is confirmed from Table 5-5 results showing the total pore volume of the precoat layers. As the top coat layer is now applied to a denser precoat (when base paper is precalendered at 100°C), less filtration effect occurs than when the base paper is precalendered at 200°C. As before, the packing of the top coat layer on dense precoat structures provides an open structure: i.e. the total pore volume of the top coat layer when precalendering the base paper at 100°C should be higher than the total pore volume of the top coat layer when the base paper is precalendered at 200°C. This is confirmed in Table 5-6 showing the total pore volume of the top coat layers. The effect of precalen-

dering pressure, either on the base paper or on the precoat layer, although less apparent, confirms present filtration and packing mechanism.

Table 5-6 Average pore volume (mL/g) for the topcoat layer for each latex (Group 2)

Soft Nips Pressures and Temperatures			
	Topcoat latex		
	S/B/ACN	S/A	S/A/ACN
Base paper calendered 100°C - 50 KN/m	0.0396	0.0384	0.0442
Base paper calendered 100°C - 200 KN/m	0.0434	0.0329	0.0325
Top coat average value corresponding of base paper at 100°C	<u>0.0415</u>	<u>0.03565</u>	<u>0.03835</u>
Base paper calendered 200°C - 50 KN/m	0.0308	0.0232	0.0368
Base paper calendered 200°C - 200 KN/m	0.0383	0.0361	0.0382
Top coat average value corresponding of base paper at 200°C	<u>0.0345</u>	<u>0.02965</u>	<u>0.0375</u>
Precoat calendered 100°C - 50 KN/m	0.0222	0.0361	0.0309
Precoat calendered 100°C – 200 KN/m	0.0422	0.0291	0.0329
Top coat average value corresponding to precoat layer at 100°C	<u>0.0322</u>	<u>0.0326</u>	<u>0.0319</u>
Precoat calendered 200°C - 50 KN/m	0.0422	0.0361	0.0373
Precoat calendered 200°C – 200 KN/m	0.0349	0.0426	0.039
Top coat average value corresponding to precoat layer at 200°C	<u>0.0385</u>	<u>0.03935</u>	<u>0.03815</u>

Analysis of the combined precoat and topcoat layer structure.

Figure 5-24 shows the pore size distribution for the whole precoat/top coat structures for the S/B/ACN latex (used in the precoat). Again, a reference (standard) pore size distribution shown corresponds to no calendering of either base paper or precoat layer. The tendencies for pore size distributions as analysed separately for the precoat and the top coat layer are here combined. It is however important to look at such a combined pore size distribution as we have seen (Printability variations related to 20 parts clay substitu-

tion in the precoat (Group 1)) that both coating layers affects the final printing characteristics of the double-coated paper.

As before, besides the reference paper, Figure 5-24 shows that the differences in pore size distribution among the various conditions are subtle; just the extreme conditions, for instance precalendering at 100°C and 50 kN/m presents the lowest distribution, essentially for the top coat portion of the graph.

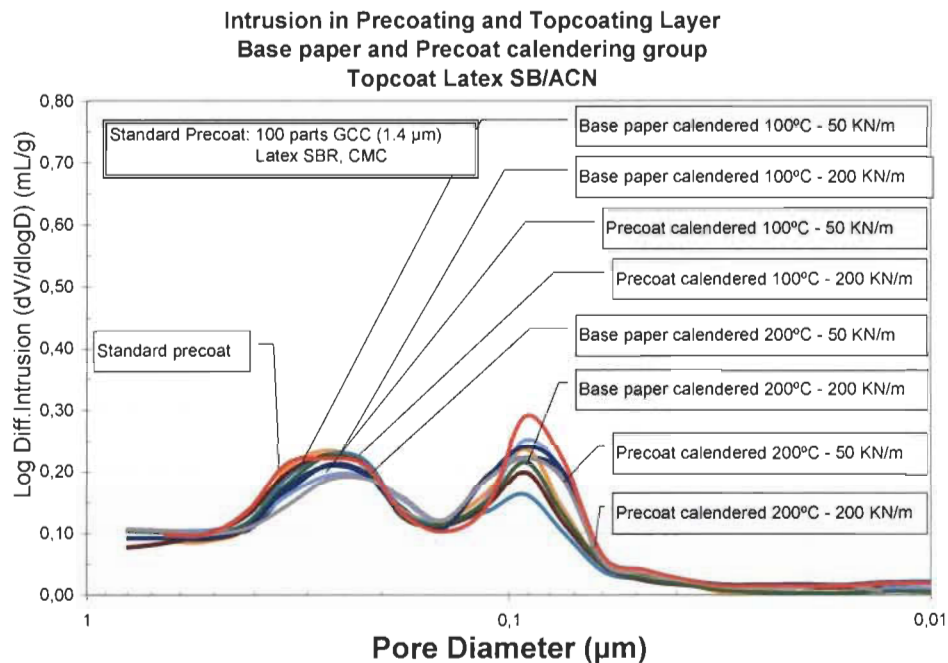


Figure 5-24 Mercury Intrusion in Coating Structure – Base Paper and Precoat Calendered Group

The Figure 5-26 presents the total pore volume of the combined precoat and top coat layer structure for the reference paper (in yellow), the precalendered base paper (in blue), and the precalendered precoat layer (in purple) for the various precalendering temperatures and pressures. It can be seen that the effect of the precalendering temperature is preponderant over the effect of the precalendering pressure. Moreover, the effect of the temperature on the total pore volume of the combined precoat/top coat structure implies that the packing effect due to the surface pore closing is preponderant: i.e. at 100°C the total pore volume is always lower than at 200°C.

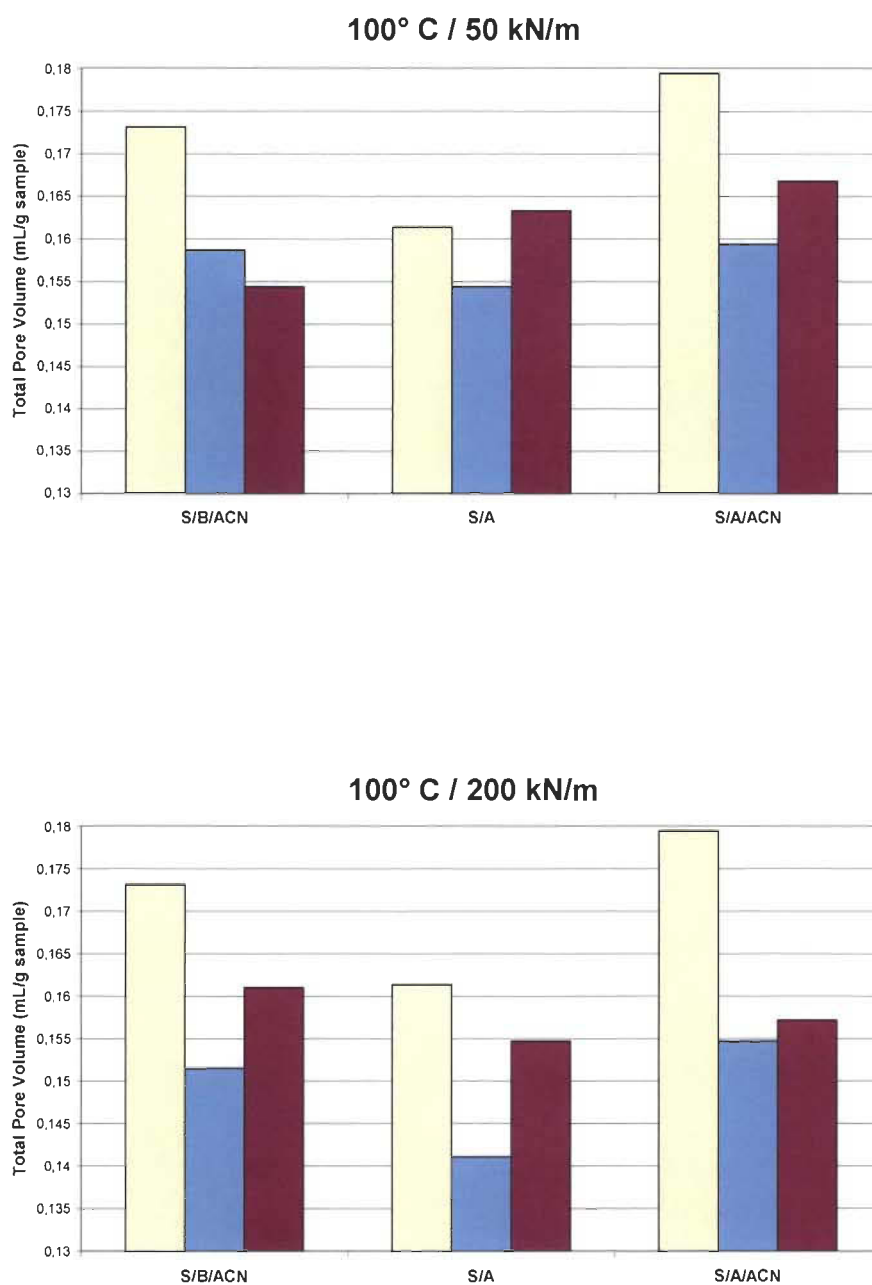


Figure 5-25 Total pore volume (mL/g) for the standard reference (yellow), calendered base paper (blue) and precoat layer (purple) for the different pressures and 100°C used in calendering.

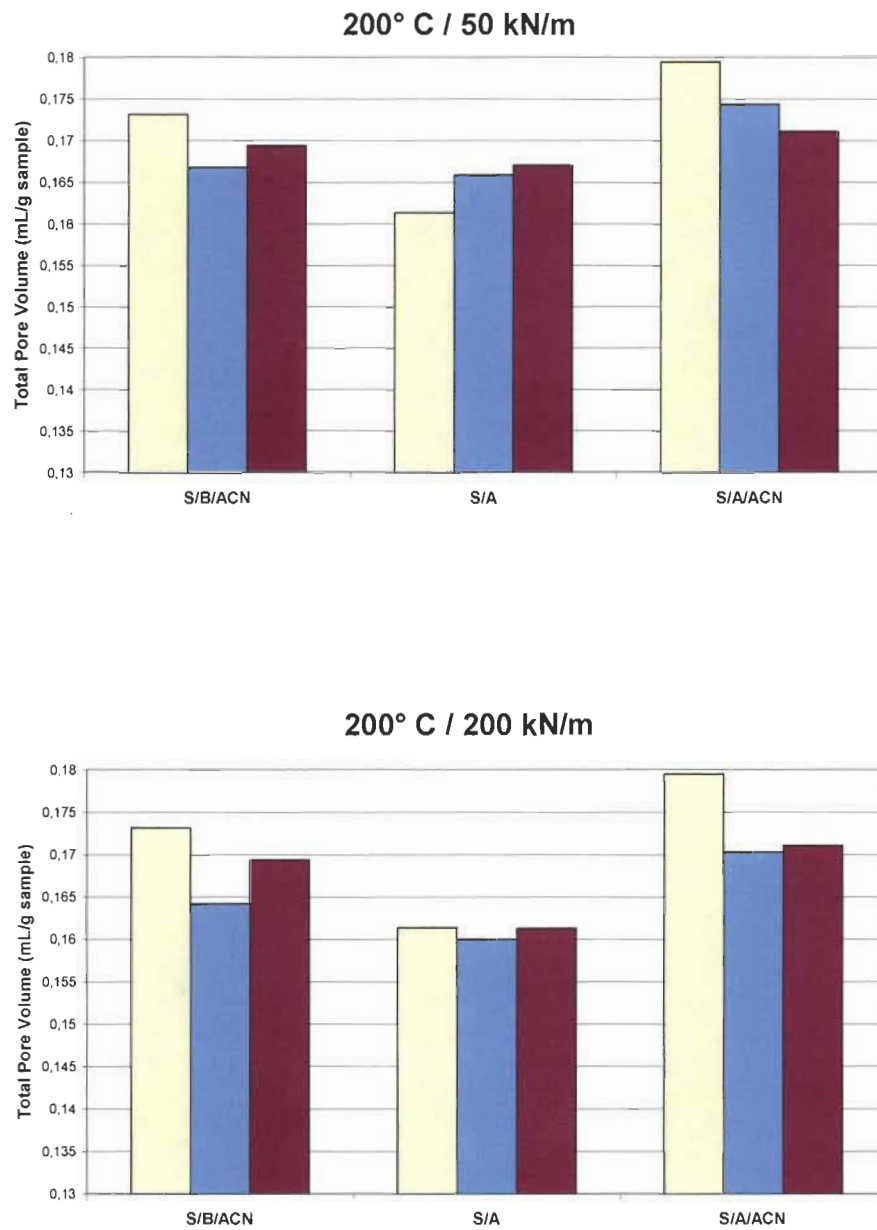


Figure 5-26 Total pore volume (mL/g) for the standard reference (yellow), calendered base paper (blue) and precoat layer (purple) for the different pressures and 200°C used in calendering.

5.3.2 Printability variations related to precalendering the base stock or the precoat layer (group 2)

As for the previous series of experiments (Group 1), the effect of precalendering either the base paper or the precoat layer on printability is analysed through the DELTACK maximum force. Figure 5-27 presents the average value for the 8 precalendering conditions (2 temperatures, 2 pressures, and 2 layers: base stock and precoat) for the 3 latexes included in the top coat layer. The reason for showing average curves is that the curve shapes are similar from one condition to the other: the main difference, as shown in Figure 5-27, is related to the latex type.

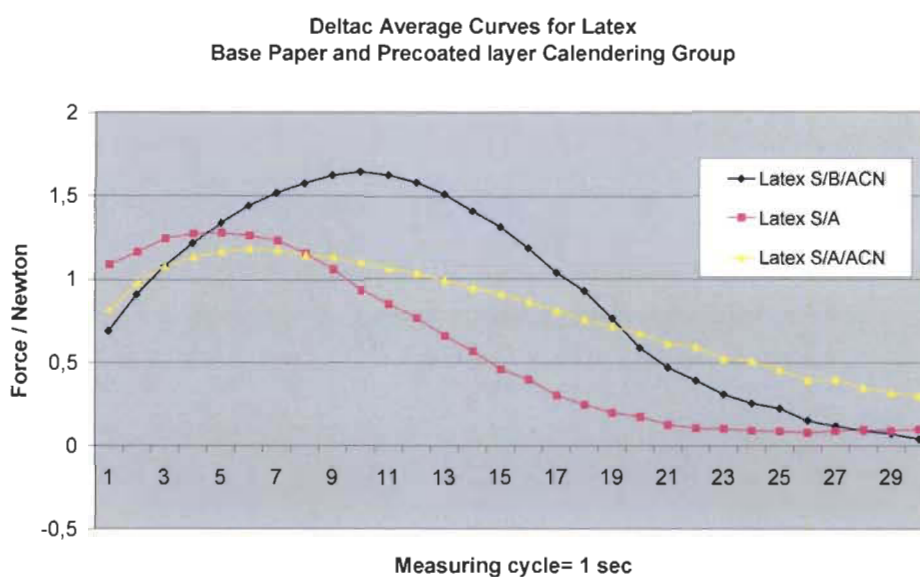


Figure 5-27 DELTACK mean for each latex (8 calendaring conditions)

As we have seen that the total pore volume is the main difference when considering the effect of precalendering, Figure 5-28 presents the maximum DELTACK force obtained for the 8 precalendering conditions for the three latexes as a function of the average total pore volume. Actually, the analysis is somehow similar to the one realized for Group 1 as far as total pore volume is concerned. Considering that the precalendering temperature is the main factor controlling the total pore volume, we have identified on Figure 5-28 the temperature for the data points representing the 8 conditions. Considering the effect of temperature on the structure of the double-coated layer, and separately on each coating layer, the points regroup themselves as a function of the temperature. This is

however not surprising when considering that the total pore volume may originate from two different structures. In essence, there is a preferential filtration of ink components that will provide the same maximum DELTACK force for different structures (corresponding here to different total pore volumes).

We have seen previously that the structure of the precoat, and consequent effect on the structure of the top coat, is different whether the temperature is 100°C or 200°C. We have also explained the phenomena by either plasticization, when precalendering the precoat, or closing the surface pore structure, when precalendering the base paper. It somehow confirms the mechanistic model we have proposed to explain the effect of the structural changes brought about by the 20% substitution of pigments in the precoat for 5.2.1.3.

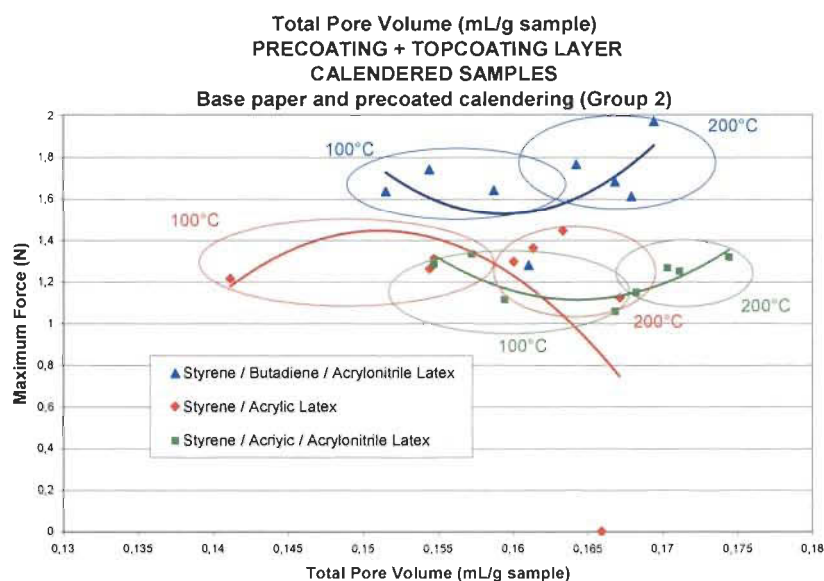


Figure 5-28 Localisation of the dots for the precalendering, both base paper and precoat, at 100°C and 200°C for the S/B/ACN, S/A, and S/A/ACN latex

5.3.3 Summary: base paper and precoated layer calendering group (Group 2)

The group 2 has been created to verify the effect on a double-coated paper of precalendering either the base paper or the precoat layer. In all case, precalendering produces

lower pore size distribution, and consequently a lower total pore volume, than the reference paper, with no precalendering. Although the analysis of the pore distribution curves were difficult and that no clear trend could be easily establish to understand how precalendering specifically affected the structures, they nevertheless led us to the conclusion that the structure thus produced by precalendering are different. The analysis of the total pore volume is found to be a powerful tool to analyse the difference in precalendering.

First we found that precalendering at 100°C results in a higher precoat pore volume than precalendering at 200°C. As expected, calendering at 200 kN/m also produces smaller total pore volume of the precoat than precalendering at 50 kN/m. More surprising are the results obtained for the topcoat structure upon precalendering either the base paper or the precoat. Here, two apparently opposite effects occur:

- when precalendering the base paper, the top coat total pore volume is higher at 100°C than at 200°C, on the opposite
- when precalendering the precoat layer, the top coat total pore volume is higher at 200°C than at 100°C.

The mechanism we propose to explain such apparently contradictory results is related to the filtration and packing of the structure that occurs during the coating operation. It is related to the movement of the water and materials when a wet coating layer is applied over another surface. Indeed, the surface pore structure being more or less open will control filtration and packing. High temperature precalendering of the precoat layer has a direct impact on the top coat structure. Precalendering the base paper has the same effect on the precoat structure but the situation is then necessarily reversed when the top coat is applied in a kind of “domino” effect.

Finally, we explained that is feasible to obtain the same printing characteristics (maximum DELTACK force) with the different structures created by precalendering. Here too, the effect of temperature precalendering is found to be the predominant factor.

As a final conclusion, we show here that it is possible to control the double-coated layer micro-structure and down to nano-structure (30 nm) through precalendering and thus control the printing characteristics of double-coated papers.

5.4 Effect on Styrene/Acrylic and Protein substitution in precoat layer (Group 3)

The group 3 was designed to verify if a change in the chemistry of the precoat layer could have an effect on the final printability or the structure parameters of the coating layers. Groups 3 contains only 2 condition levels related to the chemistry of the components added, besides the pigments, in the coating colors. For the first condition, S/A latex replaces the latex S/B that was used for all other conditions, all groups considered. Latex S/A used in Group 3 is the same latex that is used in the topcoat layer. For the second condition, a protein (Procote 4200-S), i.e. an amphoteric molecule, replaces the CMC which was used as a thickener in all other conditions, all groups considered. A summary of the different conditions included in this group is presented in table 5-7.

Table 5-7 Conditions for the S/A precoat latex and amphoteric thickener - Group 3

Precoated formulation	Group	Formulation number
100 parts GCC (1.4 μm)	Control	3 topcoat = 3 samples
Precoat 100 parts GCC (1.4 μm) + Acrylic Latex	Group 3 SA + Protein substitution group	3 topcoat x 2 precoat 6 = conditions
Precoat 100 parts GCC (1.4 μm) + Protein		

5.4.1 Analysis of the precoat and topcoat structures through pore size distribution: Styrene/Acrylic and Protein substitution (Group 3)

Figure 5-29 shows the pore size distribution of the precoat layer as a function of the pore diameter for the S/A latex and the protein substitution. The curve of the standard precoat is also included as a reference, for comparison. The pore size distributions for the two

conditions present similar effects that were observed in the Group one for the effects of 20 parts clay substitution.

When compared to the standard curve precoat formulation, the pore volumes as a function of pore diameter curves are lower than that of the standard precoat (Figure 5-29). Furthermore, the two curves representing the latex S/A and protein substitution are similar, practically identical.

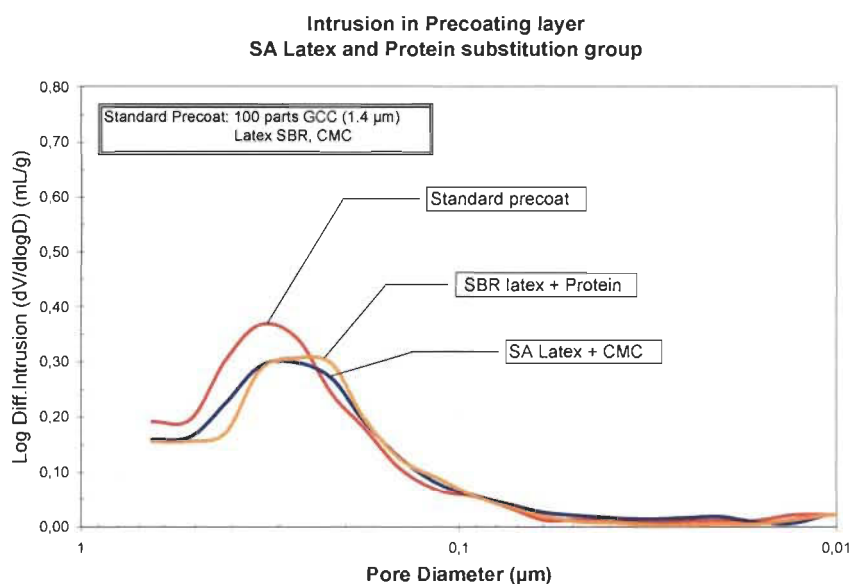


Figure 5-29 Mercury Intrusion in Precoating layer with 100 parts GCC (1.4 µm) –SA Latex and Amphoteric Thickener (protein)

Figure 5-30 and 5-31 present the total pore volume of the whole coating structure, i.e. precoat and topcoat layers, for the 3 different latexes used to make the topcoat layers. The fourth curve in Figure 5-30 represents the precoat with acrylic latex substitution (S/A replacing S/B, GCC, 1.4 µm) and no topcoat applied; for the remaining 3 curves, S/A is used in the precoat layer. The fourth curve in Figure 5-30 represents the precoat with protein substitution (protein replacing CMC, GCC, 1.4 µm) and no topcoat applied; for the remaining 3 curves, protein is used in the precoat layer.

On the one hand, the analysis of each Figure shows that there is no difference in the precoat structure after the application of a topcoat layer. It is true for the curves obtained with the S/A latex substitution and the curves obtained with the protein substitution. On

the other hand, the comparison of the resulting precoat curves after a topcoat application is quite different when comparing the effect of the S/A latex substitution (Figure 5-30) and the effect of protein substitution (Figure 5-31): namely the shape of the curves corresponding to the precoat portion of the curves are quite different in the distribution of the volumes as a function of decreasing pore diameter.

For the protein substitution, the curve has a larger base becoming broad (Figure 5-31) than for the acrylic substitution. Furthermore, for the protein substitution, the maximum pore volume obtained is lower than the S/A latex substitution in the precoat. Indeed, the pore volume corresponding to pores sizes in the 300-500 nm range is greater for the “S/A-CMC” than for the “S/B-protein” substitution. We surmise that the effect is due to a better compaction of the structure brought about by the protein.

When analyzing the pore volume for the topcoat, it is clearly seen that the total pore volume (area under the curves at very low pore diameter, below 150 nm) may be ranked as follows: S/A/ACN > S/B/ACN > S/A. This is true for both the S/A and protein substitution (Figure 5-30 and 5-31). However, for the protein case, the total pore volume is larger, for the 3 latexes than for the acrylic substitution case. This might be due to the filtration effect of the precoat compaction surmised above.

The “compacted” precoat structure for protein substitution has smaller pores that prevent penetration of the topcoat components thus leaving an more open pore structure of the topcoat than for the acrylic substitution. It is in agreement with the mechanisms of structure development of coating layers we proposed in Group 1 and 2.

Figures 5-32, 5-33, and 5-34 present the pore volume as a function of the pore diameter for the final calendered double-coated paper (precoat/topcoat) for the acrylic latex and the protein substitution in the precoat for the 3 latex used in the topcoat, i.e. S/B/ACN (Fig. 5-32), S/A (Fig. 5-33), and S/A/ACN (Fig. 5-34).

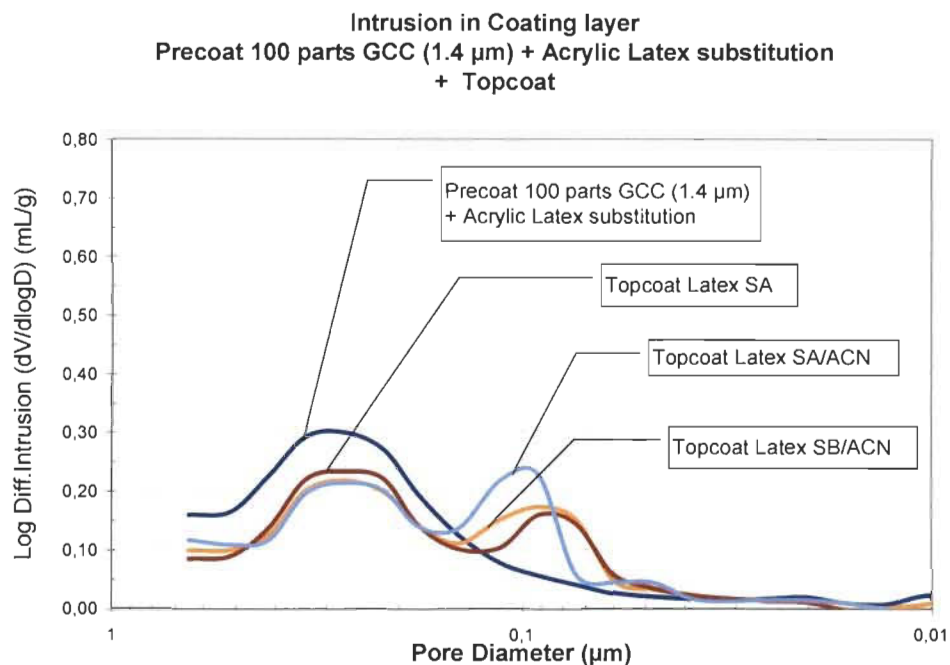


Figure 5-30 Mercury Intrusion in Coating structure for condition with 100 parts GCC (1.4 μm) and Acrylic Latex - uncalendered

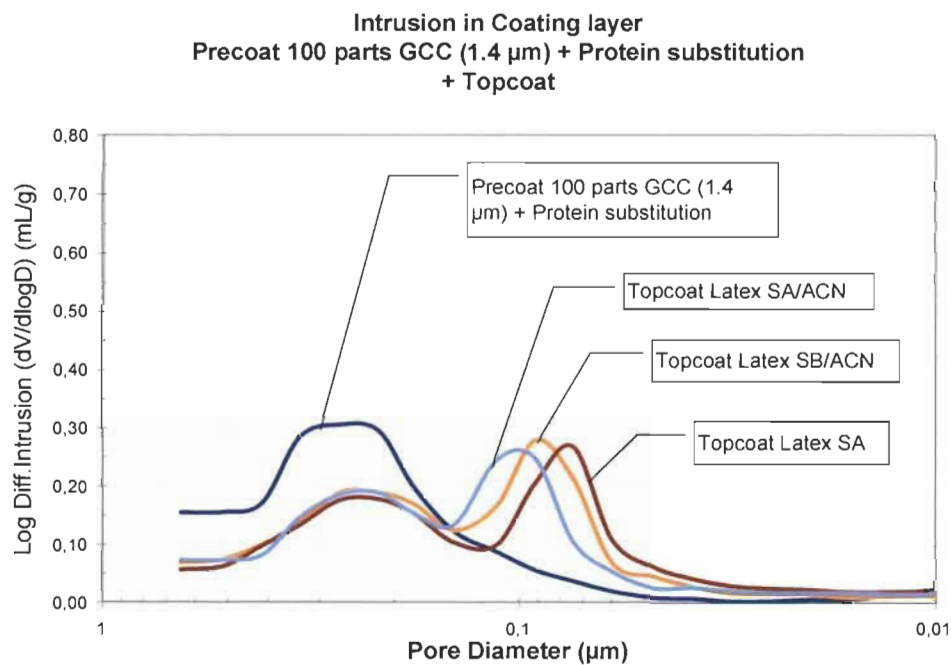


Figure 5-31 Mercury Intrusion in Coating structure for condition with 100 parts GCC (1.4 μm) – Amphoteric Thickener (protein) – Uncalendered

The structures and the differences in the structures of precoat curves shapes are preserved, although the total pore volume (area under the curves) has been reduced, as expected from the calendering process. It is true for the 3 latexes used in the topcoat (Figure 5-33, 5-32 and 5-34). The differences observed in the pore structure of the precoat layer are not directly transferred to the topcoat structure. The total pore volume of the topcoat layer for the S/A/ACN is greater than for the S/A and SB/ACN cases. It might simply be due to the fact that the calendering pressure was lower as we decided early on to calender the samples at the same gloss target (70).

The other minor differences, i.e. the total pore volume of the topcoat (TPV_{top}) ranking as follows: “protein $TPV_{top} > S/A \ TPV_{top}$ ” for the S/B/ACN in the topcoat (Fig. 5-32), “protein $TPV_{top} < S/A \ TPV_{top}$ ” for the S/A latex in the topcoat (Fig. 5-33), and “protein $TPV_{top} = S/A \ TPV_{top}$ ” (curves are on top of one another) for the S/A/ACN latex in the topcoat (Fig. 5-34) might be due to combination of calendering pressure and the glass transition temperature of the various latexes, 10°C, 23°C, and 40°C, respectively.

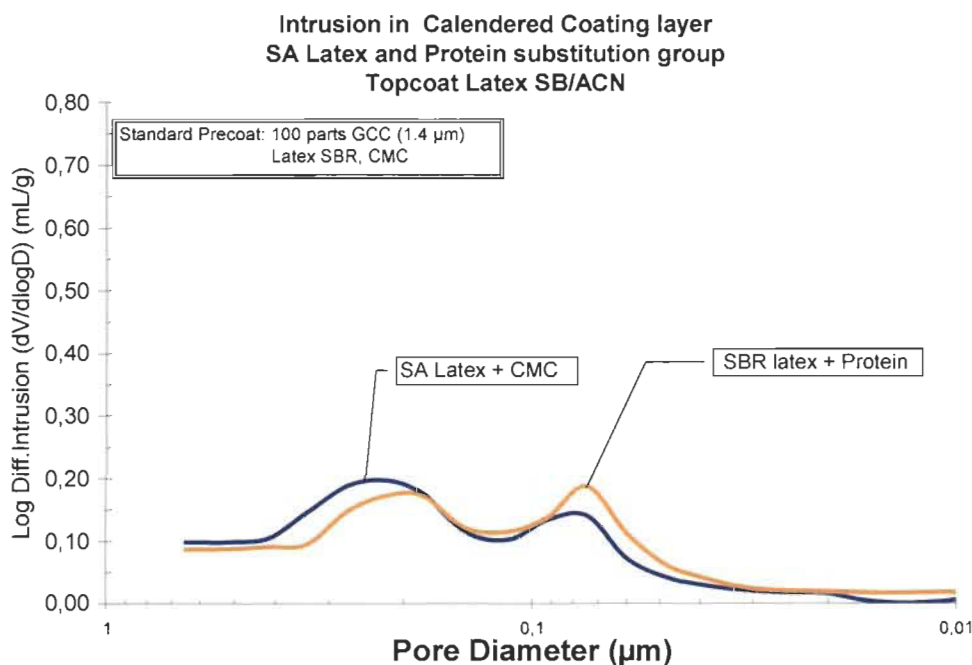


Figure 5-32 Mercury Intrusion in Calendered Structure with 100 parts GCC (1.4 μm) –S/B/ACN Latex and Amphoteric Thickener (protein)

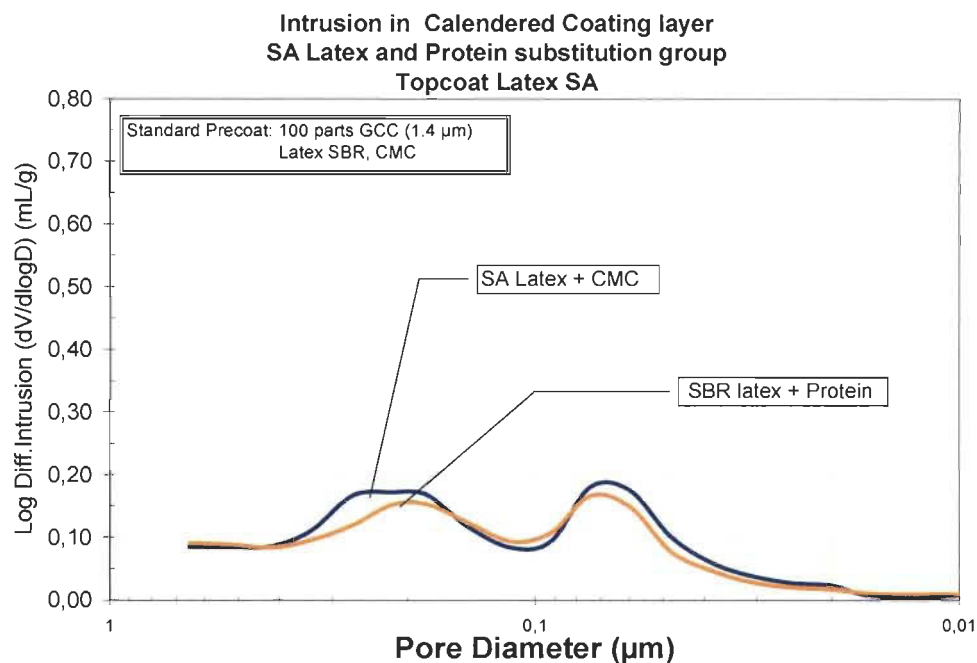


Figure 5-33 Mercury Intrusion in Calendered Structure with 100 parts GCC (1.4 μm) –SA Latex and Amphoteric Thickener (protein)

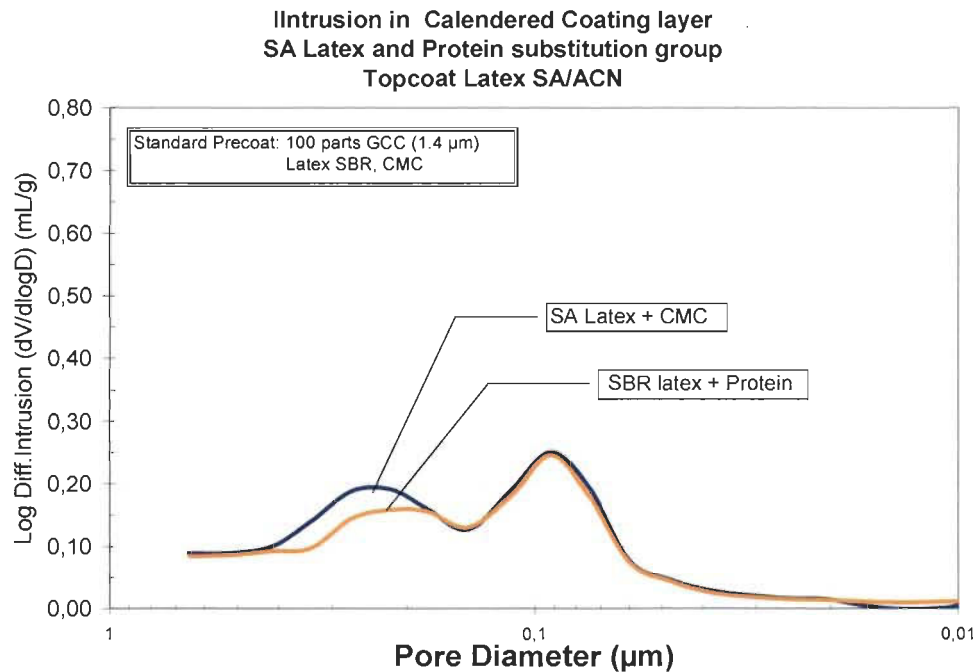


Figure 5-34 Mercury Intrusion in Calendered Structure with 100 parts GCC (1.4 μm) –S/A/ACN Latex and Amphoteric Thickener (protein)

Above observations are confirmed by analyzing Figure 5-35 which show the total pore volume (TPV) for each precoat/topcoat samples of the S/A and protein substitutions in the precoat composition and each latex used in the topcoat coating colour, i.e. S/B/ACN, S/A, and S/A/ACN. The standard precoat i.e. 100 parts GCC (1.4 μm) is also added as reference.

The protein (Procote 4200-S) has a lower TPV for the precoat layer which is maintained or even slightly increased upon topcoated application (Figure 5-35). As the protein is a colloid amphoteric material, it will create a close chemical and physical association with the pigment. On the contrary, the TPV of the precoat layer made with the acrylic latex (S/A) shows smaller values for the 3 latexes used for the topcoat (Figure 5-35). The S/A latex has smaller particle size than the S/B latex used for all other precoat conditions. It is probably the reason why we can observe such an effect.

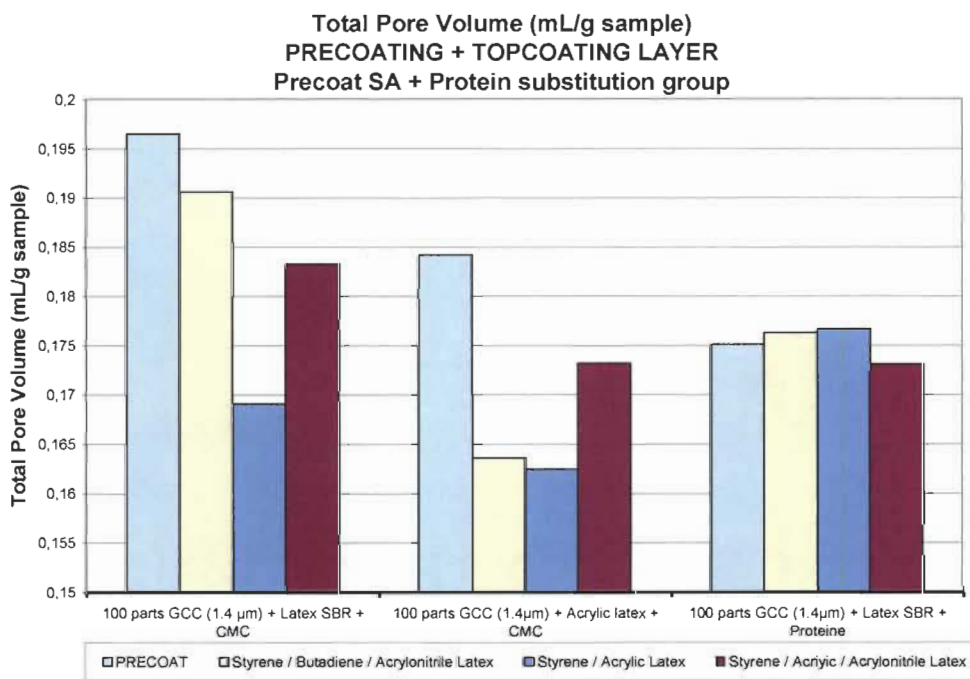


Figure 5-35 Total Pore Volume (TPV) Coated Paper for Group 3 - Comparing the 3 latexes. Precoat: all 3 groups 100 parts GCC (1.4 μm and (A): SBR+CMC, (B): S/A+CMC, and (C) SBR+Protein.

5.4.2 DELTACK results comparison from Group 3 (SA latex and protein substitution)

First we will interest ourselves in comparing the effect of the protein and latex S/A substitution with the 3 different latexes used in the topcoat in order to evaluate the effect of the topcoat latexes among themselves, second we will look at the effect of using the latex S/A and protein substitution when compared to the standard practice of using SBR/CMC combination in the reference (or standard) double coated paper.

First, Figures 5-36, 5-37, and 5-38 present the DELTACK curves for the S/A and protein substitution in the precoat layer, for the latexes used in the topcoat layer, S/B/ACN, S/A, and S/A/ACN, respectively. For the 3 Figures, the curves for the S/A and protein substitution are similar for each top coat composition. The difference seen in Figure 5-36 for the S/B/ACN cannot easily be explained from the various topcoat and topcoat structures as evaluated in Figure 5-32: there could be a combination of pore volume and pore diameter, acting both on the volume availability and capillary absorption. Indeed the times (in seconds) available for absorption are sufficient in the DELTACK experiments for capillary absorption to have some importance when compared to the times occurring upon coating application a commercial coater.

Nevertheless, it appears to be a difference when comparing the various topcoat latexes. Figure 5-39 shows the DELTACK mean curves for the 3 latexes used for the topcoat layers. The shapes of the various curves are similar or equivalent to the ones observed for the previous conditions (Group 1 and 2). Using S/BACN in the topcoat coating colour provides a higher surface resistance than using S/A or S/A/ACN but the tow last latexes provide better printability; which is coherent with commercial practice.

Second, Figure 5-40 shows that the acrylic latex used in the precoat condition may possibly react differently than the S/B-CMC used for the reference precoat layer. The maximum DELTACK force for the reference paper is higher and it occurs later than for the two substitutions cases.

The S/B latex used in the precoat has a bigger particle size than the 3 topcoat latex. It has also a low gel content. These two factors are known to decrease the bond strength and the ink setting [115].

Nevertheless, the results for the DELTACK presented previously show clearly that the application of a wet coating layer over another one modified the structure. Therefore, it confirms that the latex used in a precoat does affect how the topcoat layer applied over it will react, especially if the latex has quite different properties than the one normally used.

It should however be emphasised that we have only looked at two substitution conditions in the precoat layer and that more work should be performed to study these effects. In the course of this work, we may conclude that the substitution of SBR by S/A and CMC by protein is not truly worthy unless specific printing characteristic are targeted.

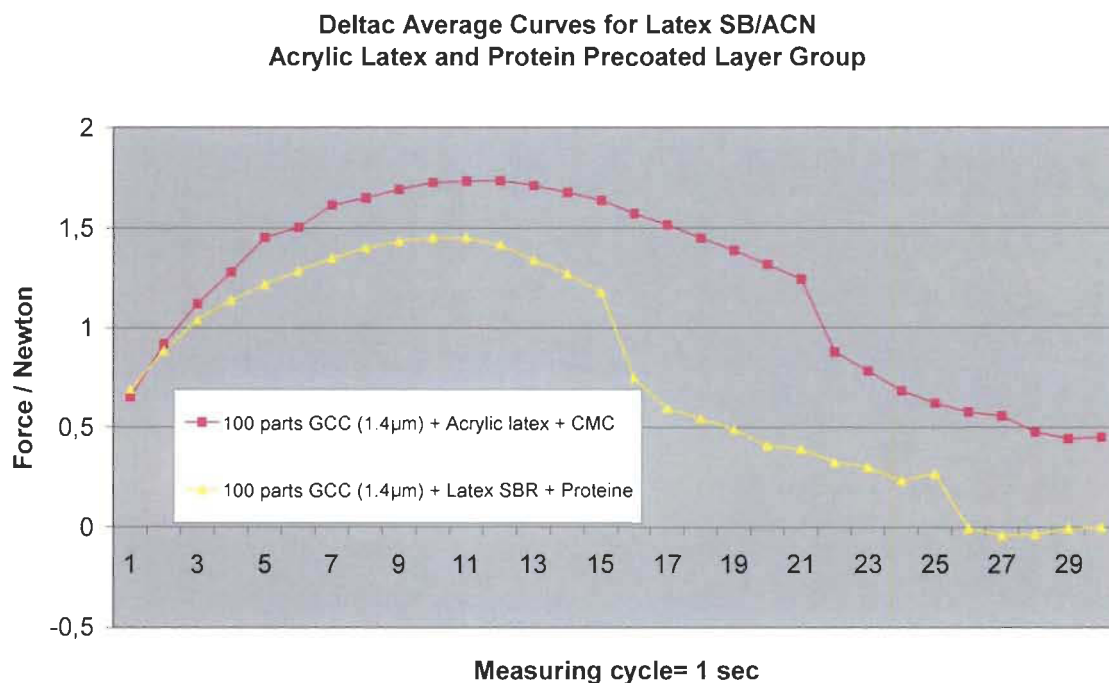


Figure 5-36 DELTACK – S/A Precoating layer and protein Group, latex, S/B/ACN

Deltac Average Curves for Latex S/A
Acrylic Latex and Protein Precoated Layer Group

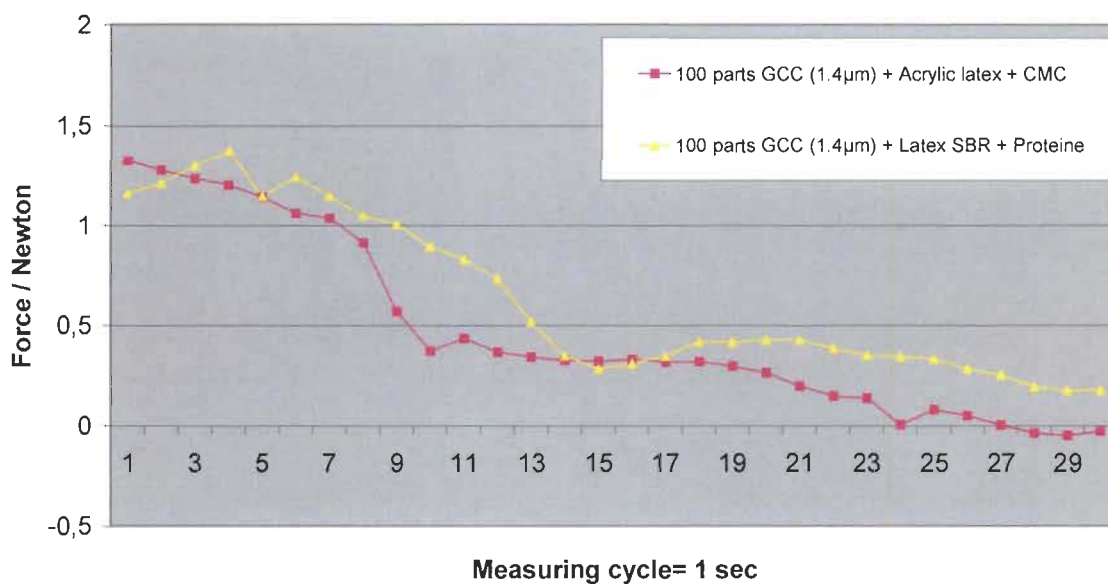


Figure 5-37 DELTACK – S/A Precoating layer and protein Group, S/A latex

Deltac Average Curves for Latex SA/ACN
Acrylic Latex and Protein Precoated Layer Group

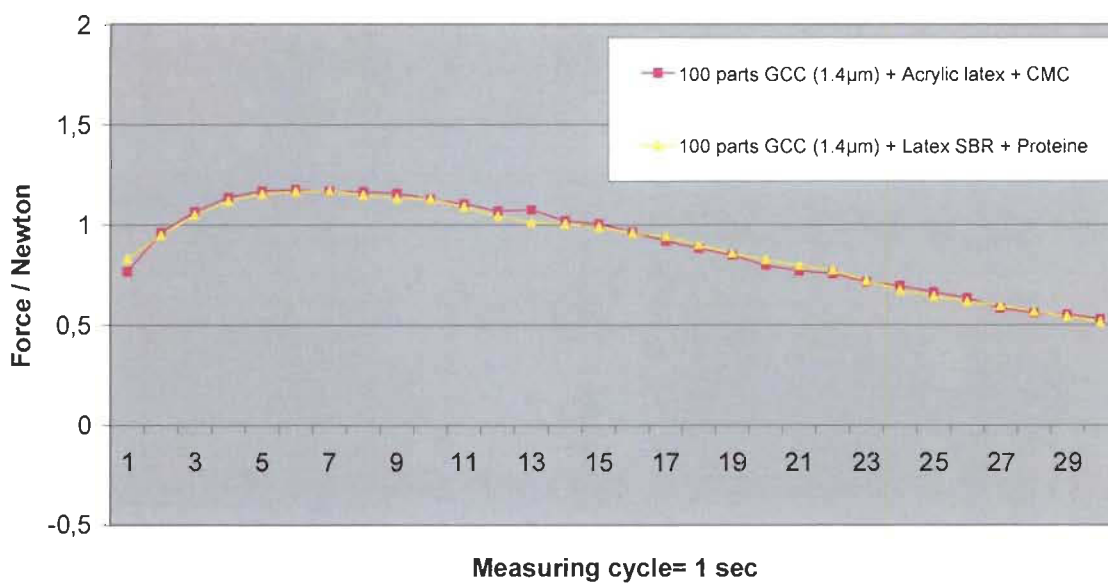


Figure 5-38 DELTACK – S/A Precoating layer and protein Group, latex, S/A/ACN latex

Deltac Average Curves
Acrylic Latex and Protein Precoated Layer (Group 3)

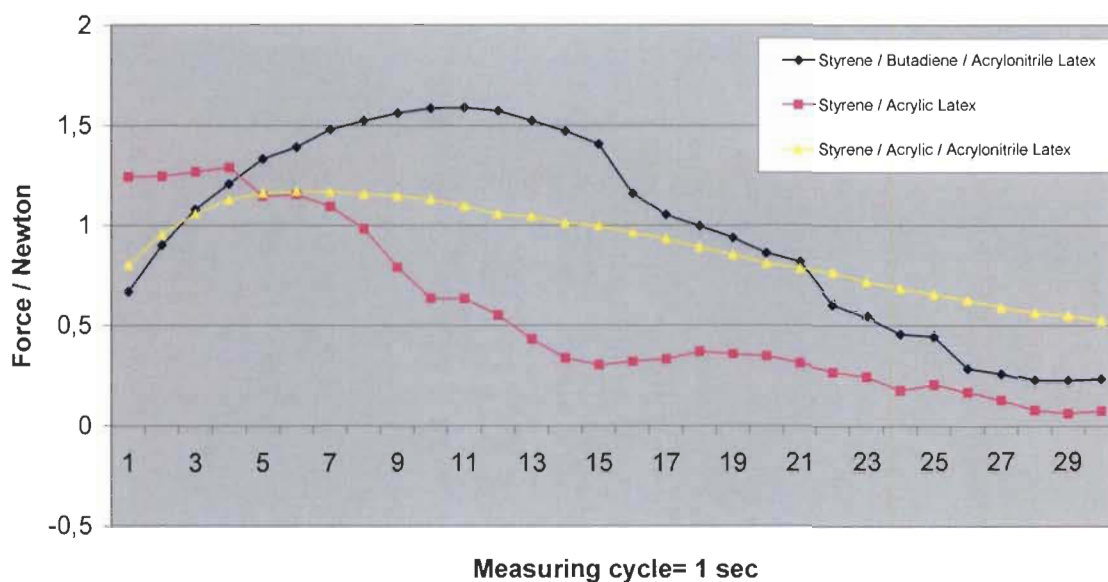


Figure 5-39 DELTACK mean value for the 3 topcoat latex conditions with S/A latex and Protein substitution)

Deltac Average Curves for Latex S/A
Acrylic Latex and Protein Precoated Layer Group

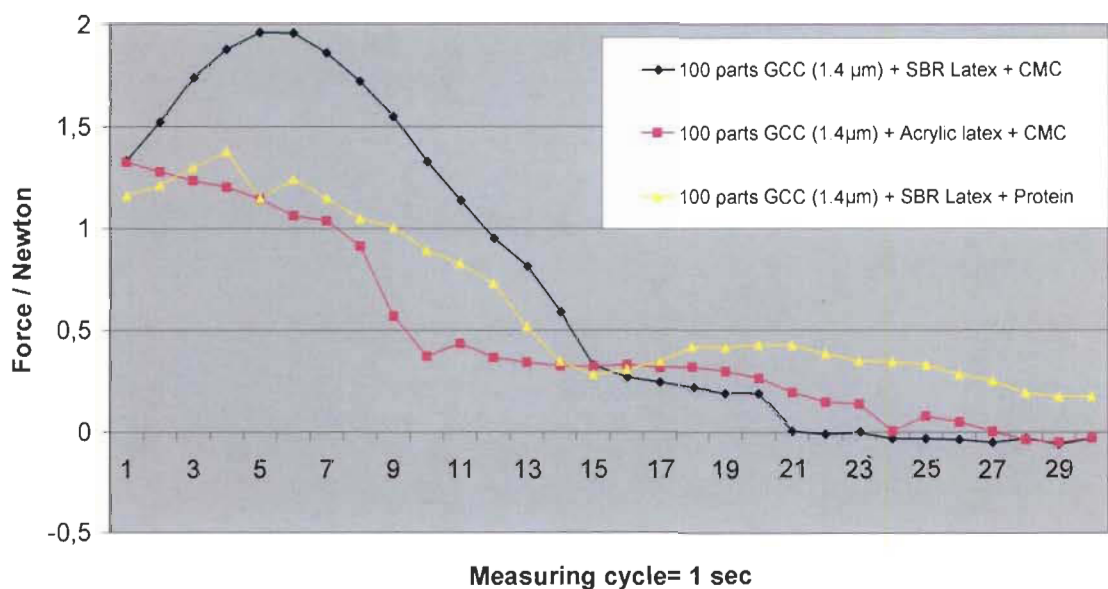


Figure 5-40 DELTACK measurements for the S/A latex topcoat conditions (S/A latex and Protein substitution)

5.4.3 Summary: Latex and thickener substitution in precoat layer (Group 3)

Using either a protein or a S/A latex in the precoat to substitute for an SB+CMC combination does not show significant improvement especially when the S/A latex precoat substitution is concerned. However, the protein substitution case presents an interesting behaviour as we can clearly demonstrate the effect of such a substitution on the structure of the coating layer. The protein definitively results in a broader pore distribution in the precoat layer. Finally, it is difficult to conclude on a general trend as just one condition has been studied. It is an area of coating improvement that could be study specifically to understand as such a product changes the coating structure. It would be of future research interest to study the effect of structure/chemistry of the latexes on printing characteristics as the effect on the DELTACK results seen here are not really different than what we have analysed for the previous conditions.

5.5 Effect on 100 parts substitution in the precoat layer (group 4)

The last 5 conditions of the study of the influence of the precoat layer on the double-coated layer structures are the complete replacement (100 parts) of the pigment used in the precoat layer. All the pigments selected for such a replacement are representative of the pigments used commercially and extensively in the coated paper industry. A summary of the different conditions are listed in table 5-8.

Table 5-8 Conditions for 100 parts substitution - Group 4

Precoated formulation	Group	Formulation number
100 parts GCC (1.4 μm)	Control	3 topcoat = 3 samples
100 parts BPSD GCC (0.659 μm)	Group 4 100 parts pigment substitution	3 topcoat x 5 precoat = 15 conditions
100 parts BPSD GCC (0.3598 μm)		
100 parts PCC (0.499 μm)		
100 parts Brazilian clay (0.548 μm)		
100 parts NPSD GCC (0.6593 μm)		

BPSD: broad particle size distribution

NPSD: narrow particle size distribution.

5.5.1 Analysis of the uncalendered precoat and topcoat structures, pore size distribution: 100 parts precoat pigment substitution (group 4).

Figure 5-41 presents the pore volume distribution as a function of the pore diameter for the 5 pigments used in the precoat layer, *i.e.* GCC NPSD (0.6593 μm), PCC (0.499 μm), Brazilian clay (0.548 μm), GCC BPSD (0.659 μm), and GCC BPSD (0.3598 μm). The curve representing the standard precoat (100 parts GCC, 1.4 μm) structure is included for comparison. The curves clearly illustrate the difference in the structures obtained between a pigment with narrow particle size distribution (NPSD) and a pigment with a broad particle size distribution (BPSD). The NPSD pigment reaches a higher value in pore volume with a narrow pore size distribution.

It is interesting to note that the PCC which has the narrowest particle size distribution also presents the highest volume value (at 180 nm). We will see later that the analysis is confirmed when considering the total pore volume. Figure 5-42 shows the total precoat-top coat structure after the application of the topcoat. We have only illustrated here the tendencies for the latex S/B/ACN in Figure 5-42 although similar curves with similar characteristics were obtained with S/A latex and S/A/ACN latex. The part of the curves representing the precoat structure after topcoat application is always lower in volume than for the precoat structure before application of the topcoat layer. It was expected as it is exactly what occurred for all other conditions upon topcoat application. There are at least two effects occurring. First, application of the topcoat rewets the precoat structure thus disturbing and partly rearranging the precoat structure. Second, depending on the initial precoat structure, some topcoat components penetrate the precoat structure thus reducing the precoat total volume.

Another effect might be due to the shape of the pigment as they directly affect the pore shape and the related pore volume (packing efficiency, Figure 2-4 to Figure 2-9). Although Figure 5-42 represents the structures obtained for the S/B/ACN latex, the last assertion is true for the S/A and S/A/ACN latexes. Therefore, present analysis confirms previous findings on the influence of the precoat structure. It is possible to conclude that the precoat structure greatly impact the final structure of coated paper.

Figures 5-43, 5-44, and 5-45 present the pore volume for the 100 part substitution group as a function of the pore diameter for the 3 topcoat latexes used in this study, *i.e.* S/B/ACN, S/A, and S/A/ACN, respectively. It should be reminded here that the negative values for the mercury intrusion appearing at the beginning of each curve is a calculation artefact related to the data treatment that allows us to compare each graph one to another. The curves for each latex present similar characteristics, almost identical, to the ones found for group 1 (5.2.1.1) corresponding to 20 parts substitution.

It is important to remember that the pigments/binder/chemicals system used for the topcoat in group 1 (20 parts substitution) and group 4 (100 parts substitution) is the same. Therefore, we may conclude that, due to the predominant influence of the precoat, all topcoats used in this study results in a certain type of structure pattern.

In addition, it should be emphasized that the pattern structure of the topcoat remains the same even with very different precoat pigments. Last but not least, it will nevertheless result in various precoat – topcoat structure combinations.

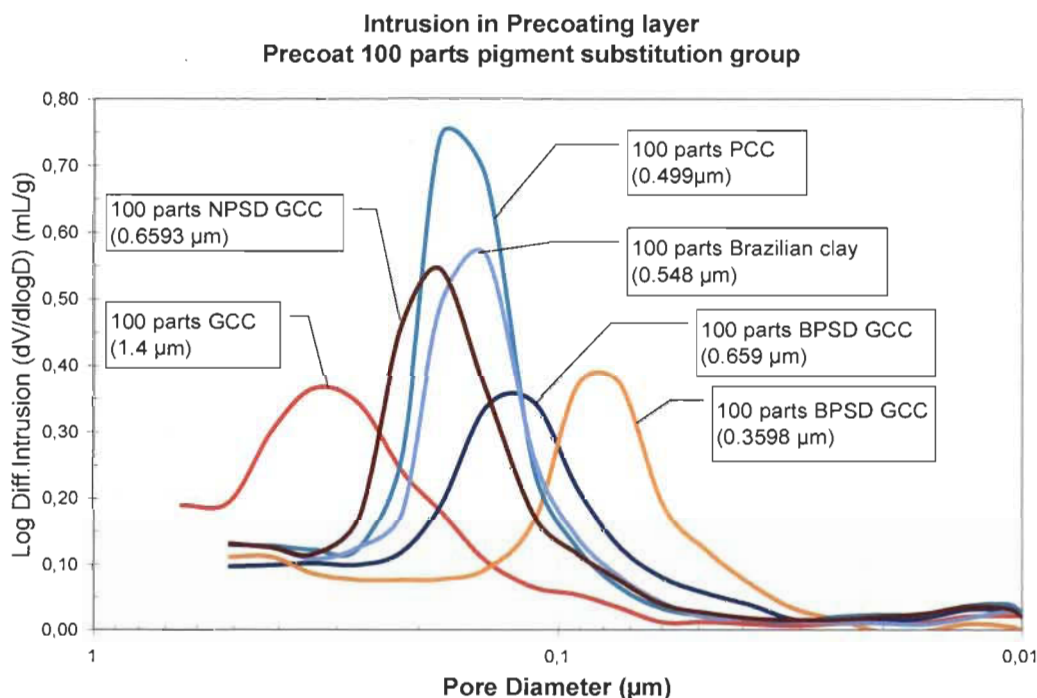


Figure 5-41 Mercury Intrusion in precoat layer – 100 parts substitution Group. The reference curve GCC is in red.

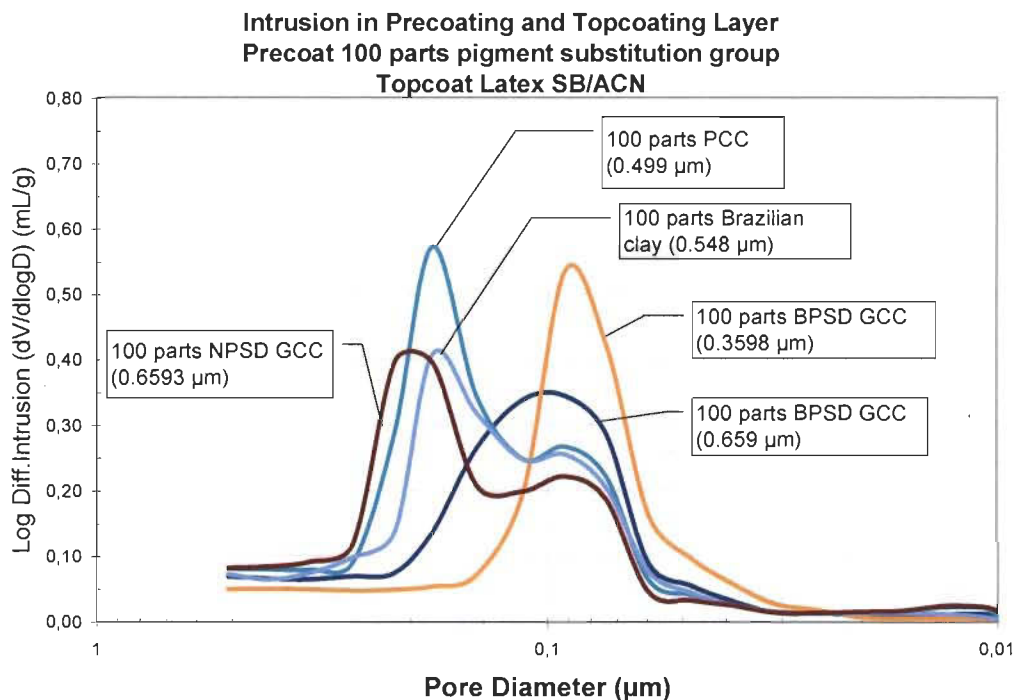


Figure 5-42 Mercury Intrusion in Coating Structure layer – 100 parts substitution Group. Uncalendered samples.

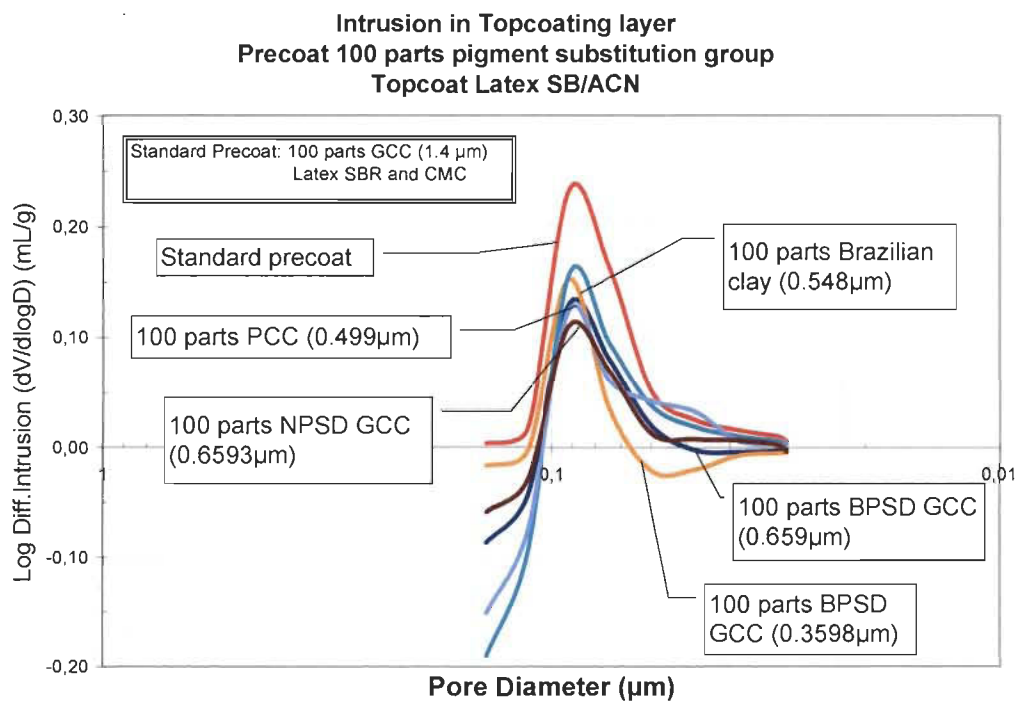


Figure 5-43 Mercury Intrusion in Topcoat Structure – 100 parts substitution Group – S/B/ACN latex. Uncalendered samples.

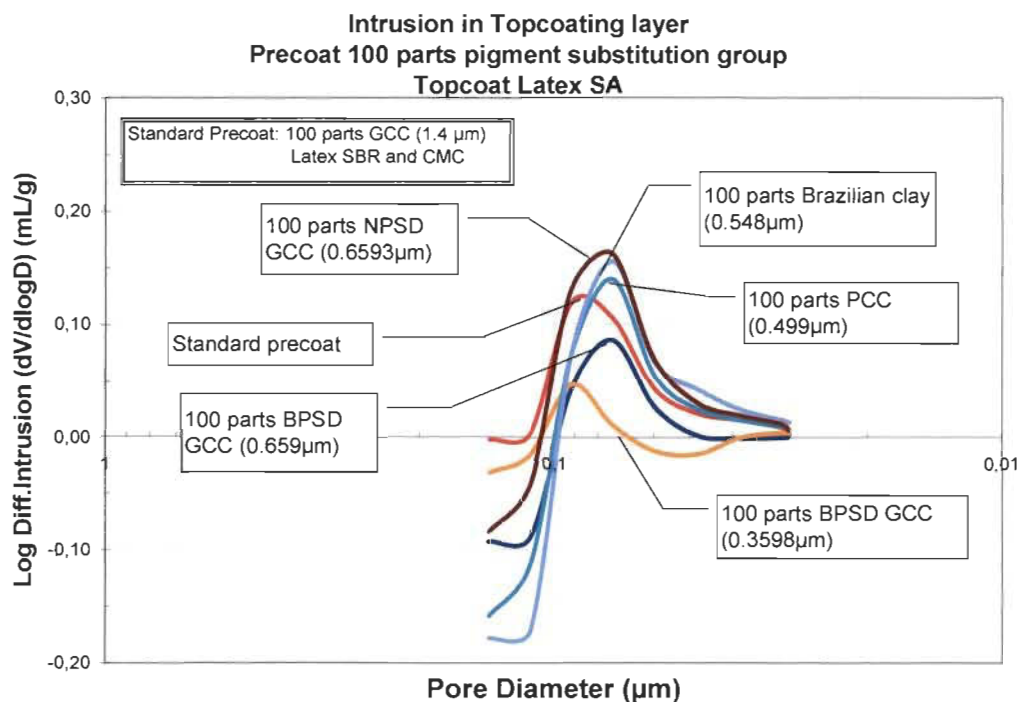


Figure 5-44 Mercury Intrusion in Topcoat Structure – 100 parts substitution Group – SA latex. Uncalendered samples.

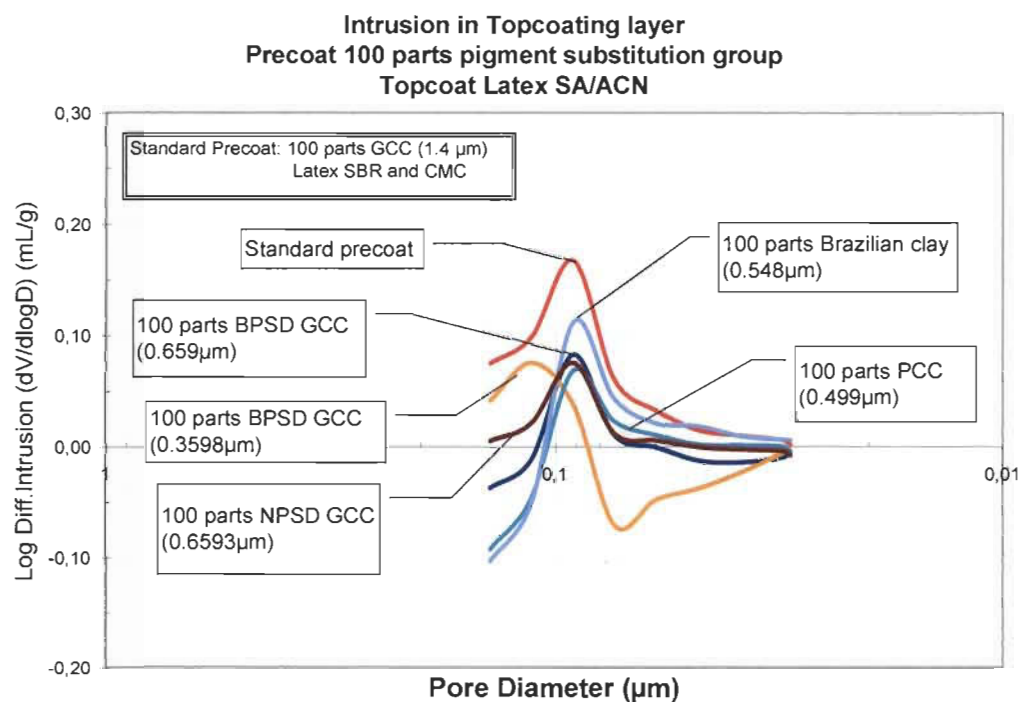


Figure 5-45 Mercury Intrusion in Topcoat Structure – 100 parts substitution Group – S/A/ACN latex. Uncalendered samples.

5.5.2 Analysis of the calendered precoat and topcoat structures total pore volume, total pore area, and average pore diameter: 100 parts precoat pigment substitution (group 4).

As the pore distributions for the calendered and uncalendered samples present the same pattern, we surmised that it was possible to obtain additional information when comparing global values for the 100 part substitution group and for each latex used in the topcoat; *i.e.* total pore volume, total pore area, and average pore diameter as characterizing both the calendering and the substitution effects.

In order to compare the effect of the 3 latexes, the total pore volume (TPV) is presented in Figure 5-46, the total pore area (TPA) in Figure 5-47, and the average pore diameter (APD) in Figure 5-48 as a function of the particle size of each pigment used in the precoat. The standard precoat (GCC 1.4 μm) is added as a reference. The parameters TPV, TPA, and APD are for the precoat/topcoat layers and for the calendered coated paper. The total pore volumes shown in Figure 5-46 clearly indicate that the 3 pigments with a broad distribution (BPSD) have the same volume. As seen for Figure 5-41, the volume increases for pigments with narrow particle size distribution. Then, it is possible to conclude that the total pore volume is somehow inversely proportional to the particle size distribution. Figure 5-46 also shows the latex type has no effect on the total pore volume of the structure.

The fact that the latex has no influence on the total structure is coherent with the analysis performed for all other groups. In Figure 5-47, the total pore area for the broad particle size distribution pigment (BPSD-GCC) is inversely proportional to the particle size. The other pigments do not necessarily follow the same rule as it is especially seen for the PCC pigment. However, we do not have any other particle size for comparison.

Finally, as could be expected from the packing of the pigments, Figure 5-48 shows that the average pore diameter is directly related to the particle size of pigments used in the precoat.

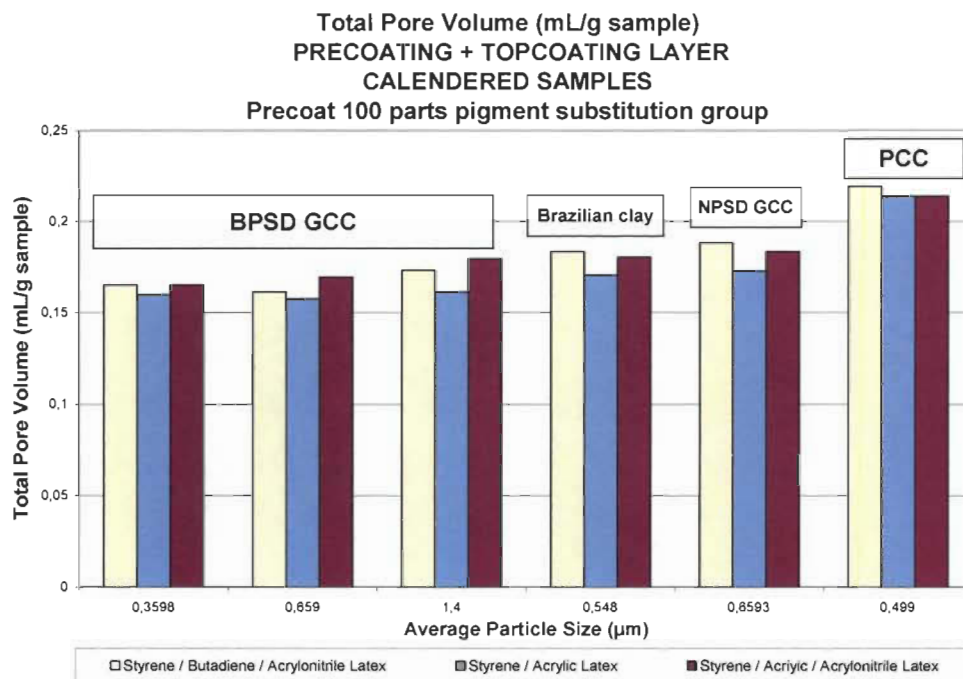


Figure 5-46 Total Pore Volume (TPV) of the calendered precoat/topcoat structure for Group 4 - Comparing the 3 latexes. The samples are ordered in decreasing particle size distribution.

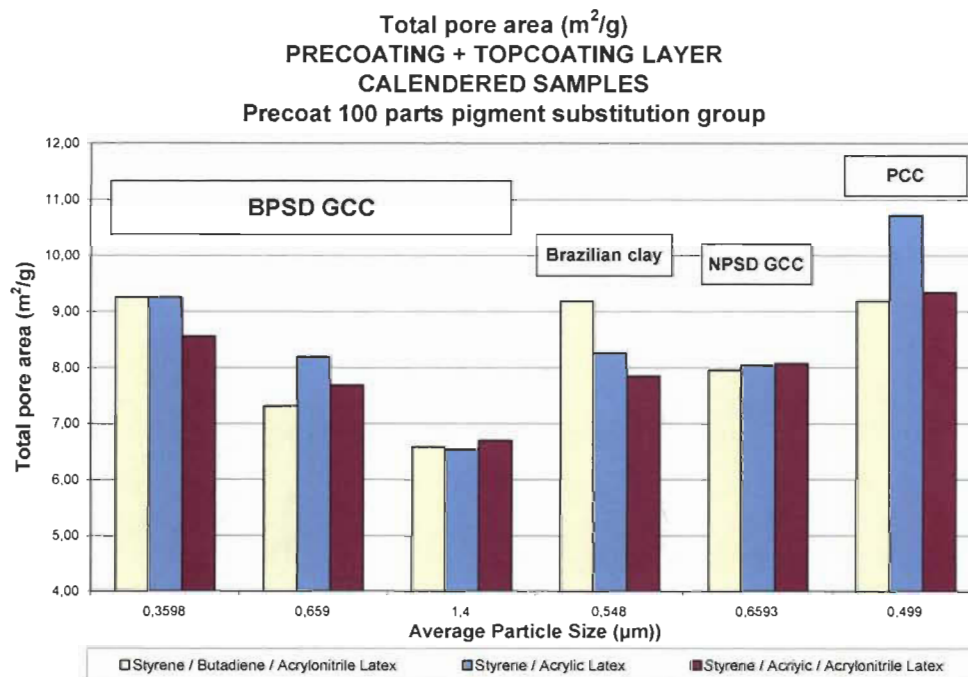


Figure 5-47 Total Pore Area (TPA) Coated Paper for Group 4 - Comparing the 3 latexes. The samples are ordered in decreasing particle size distribution.

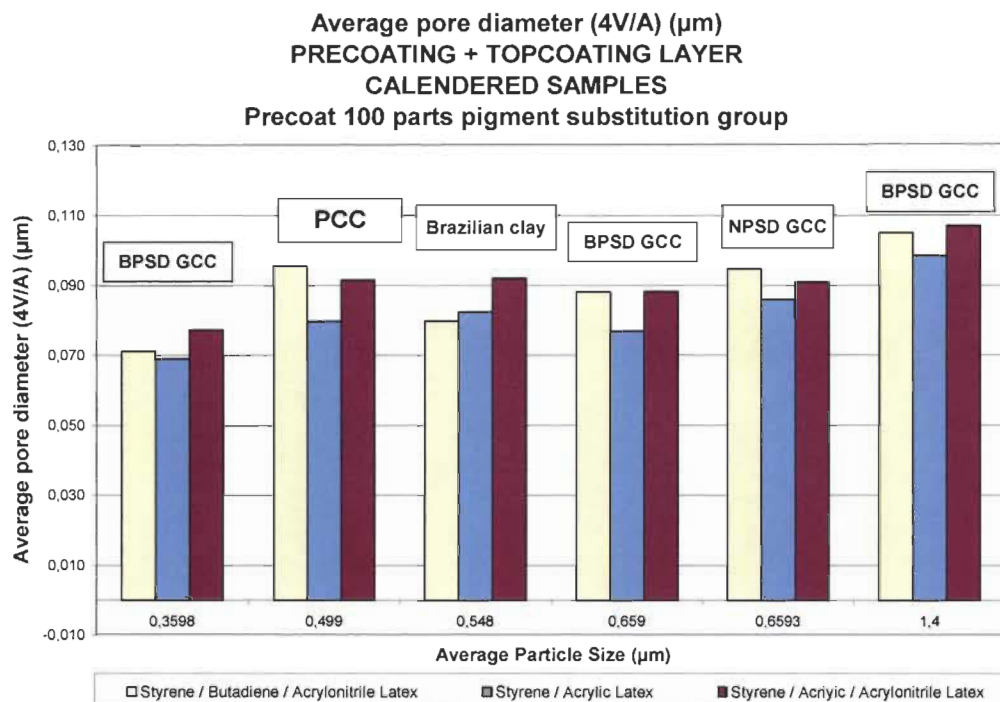


Figure 5-48 Average Pore Diameter (APD) Coated Paper for Group 4 - Comparing the 3 latexes. Samples are ordered as a function of the particle size.

5.5.3 DELTACK results comparison from Group 4 (100 parts pigments substitution)

As it will be seen in further details later (5.6), the shapes of the DELTACK curves are somehow similar for all conditions in present group 4 (100 parts substitution). Accordingly, Figure 5-49 show the DELTACK curves force as a function of time (measuring cycle) for the mean of all 5 pigment substitutions; i.e. BPSD-GCC, PCC, Brazilian clay, and NPSD-GCC, with one curve for each latex used in the topcoat, S/B/ACN, S/A, and S/A/ACN, respectively. As previously found for the other groups, the latex is the major factor influencing the DELTACK measurement.

Figures 5-50 and 5-51 correspond to the maximum force obtained for the DELTACK test in function of the total pore volume (5-50) and the average pore diameter (5-51) for each conditions of the group 4 and for each topcoat latex.

The arrows presented in both Figures are for matched data pairs: for instance, the data points corresponding to the green arrows in Figure 5-50, for pore volume, correspond to the same data in Figure 5-51 but for pore diameter. Furthermore, the colours are dark green and orange for S/B/ACN latex, lavender and pink for the S/A latex, and blue and black for the S/A/ACN latex. It is interesting by the observation of the graphics from Figure 5-50 and 5-51. When comparing the upwards and downwards arrows in both Figures, we immediately see that the pairs can be directly related and are fully coherent to the theory developed for group 1 (Figure 5-17) when only 20 parts substitution was concerned.

As seen previously for Group 1 (20 parts substitution), Figures 5-50 and 5-51 present two different opposite configurations. Indeed, a given maximum DELTACK force can be obtained with two configurations of pore volume and average pore diameter, namely: a) the same (or almost identical) pore volume (upwards arrows, Figure 5-50) but largely different average pore diameters (upward arrows, Figure 5-51), and b) largely different pore volumes (downward arrows, Figure 5-50 and same (or almost identical) pore diameter (downward arrows, Figure 5-51).

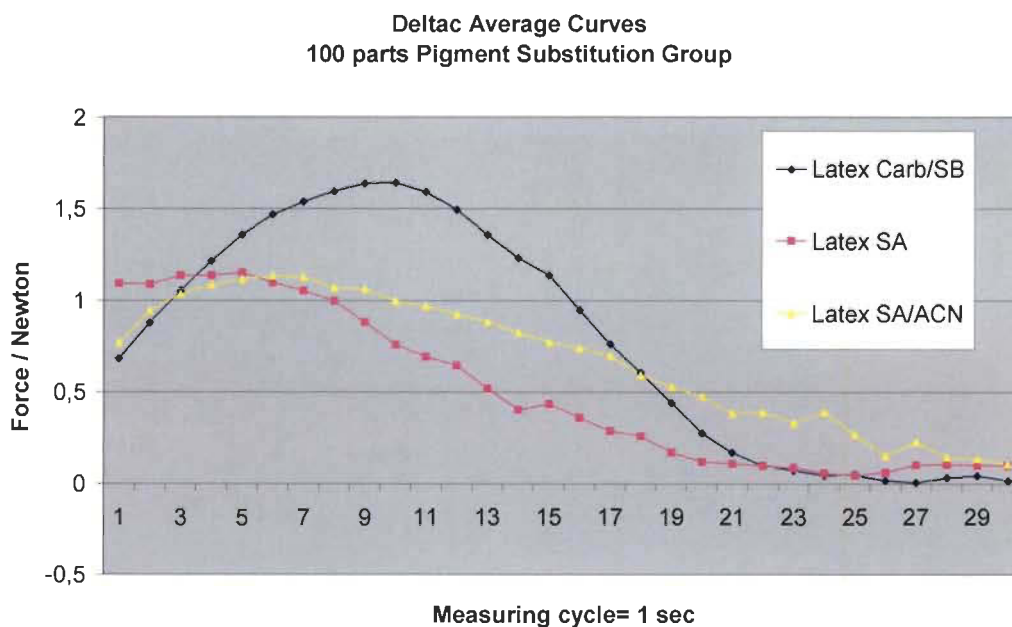


Figure 5-49 DELTACK mean for each latex (5 conditions – 100 parts substitution)

As we proposed earlier, the maximum tack force is due to a complex phenomenon of preferential filtration and ink transfer build-up. As the average pore size of the two structures (case a and case b) is widely different, the ink transfer cannot be the same (ref. work by [104, 105]).

We proposed, and it is confirmed here, that ink transfer is different because the topcoat structures are different and that the filtration mechanisms of ink components is necessarily different for such different combinations of precoat/topcoat structures.

Practically, the thickness of the ink layer remaining on the surface might be different and still produce similar tack forces as very small pores will favour, due to capillary penetration, the preferential absorption of ink solvent.

We will then end up with a thicker ink film but with less solvent, *i.e.* a tackier ink. In the case of the larger pores, there will be no or less preferential penetration of ink solvent. It is therefore quite feasible that the two effects being opposite, we will end up with the same maximum tack force. Furthermore, we concluded that ink layer thicknesses on the topcoat structure are modulated by the underlying precoat structure.

Although we had taken two extreme cases in Group 1, we can now generalize our proposed mechanism as the compensation effect of solvent penetration controlling the ink tack, and the effect of ink transfer controlling the ink thickness, and therefore also the tack force, is valid for all double-coated structure cases.

Finally, the analysis being valid for all 3 latexes used in the topcoat structure, we further conclude that the maximum DELTACK force is a combination of latex type, as the predominant factor, and overall structure of the precoat/topcoat layer for the second factor explaining the mechanisms of force build-up through preferential filtration occurring during the sequential transfer cycles.

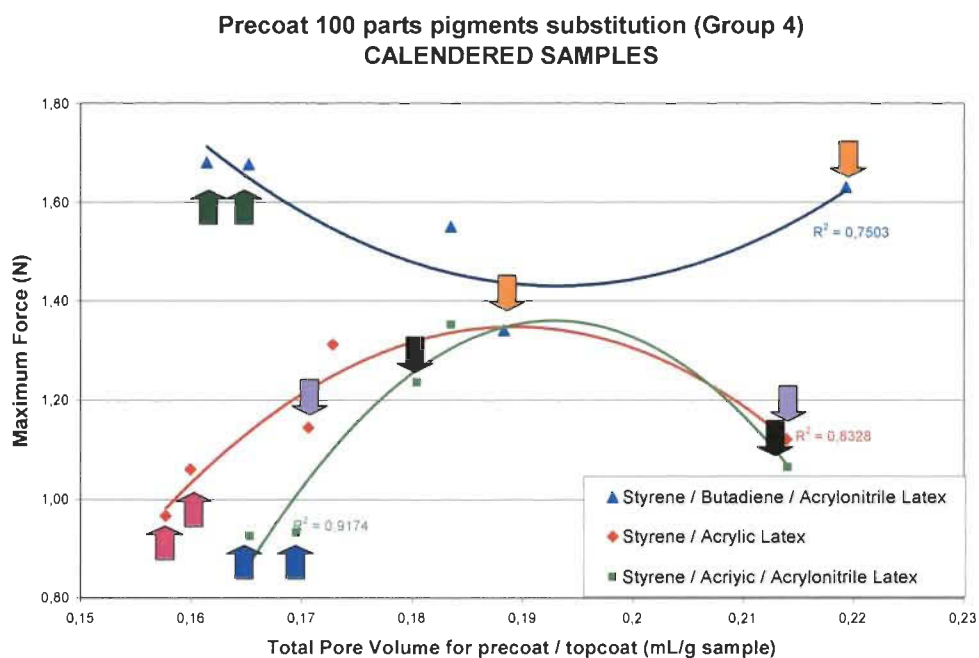


Figure 5-50 DELTACK maximum force versus total pore volume for 100 parts pigments substitution group- all conditions

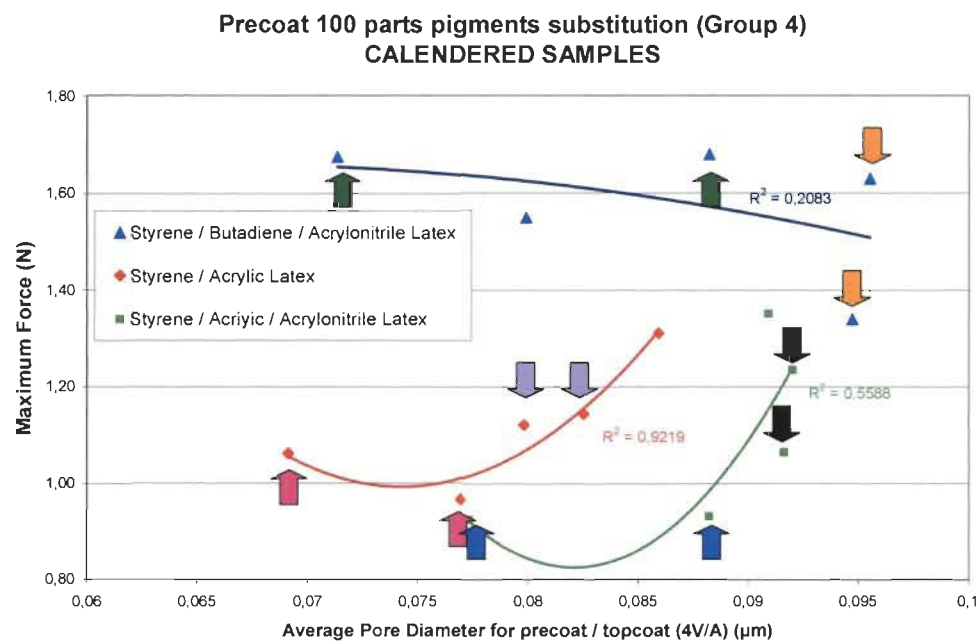


Figure 5-51 DELTACK maximum force versus average pore diameter for 100 parts pigments substitution group – all conditions

5.5.4 Summary: 100 parts substitution in the precoat layer (Group 4)

The analysis of the structures of the samples obtained when substituting 100 part pigments for different pigments in the precoat layer structure allows us to confirm that the precoat structure greatly impact the final structure of coated paper. We have seen here the key importance of the particle size distribution and of the average particle size, and how they impact the precoat/topcoat structure. More specifically, we found, and explained how, the total pore volume is somehow inversely proportional to the particle size distribution. We also found that the total pore area decreases with particle size but, in the case of the broad particle size distribution pigment, it is inversely proportional to the particle size. Finally, as expected from pigment packing and influence on the coated layer pores, we confirmed that the average pore diameter is directly related to the particle size of pigments used in the precoat.

Last but not least, the mechanism we proposed to explain similar maximum ink tack force, as measured with the DELTACK, with widely different pore structures, namely similar total pore volumes obtained with widely different average pore diameters, and largely different total pore volumes obtained with similar average pore diameters, has been validated and confirmed. As a reminder, the theory is based on the effect of preferential solvent penetration controlling the ink tack, and the effect of ink transfer controlling the ink thickness.

5.6 DELTACK and ink tack comparison of Groups and latex – Average Curves

Along the analysis of the various modifications of the precoat layer: 20 parts of clay substitution (Group 1), precalendering of base stock paper and precoat layer (Group 2), latex and thickener substitution in the precoat (Group 3), and 100 part substitution of pigment in the precoat (Group 4), we mentioned many times that the DELTACK curves used to analyse the printing characteristic of the double-coated paper were somehow similar in shape and that the effect of the latex was the predominant factor for tack force build-up notwithstanding the fact that the maximum values were mainly structure dependent. Accordingly, we intend to show here that it is indeed the case by the compari-

son of average curves calculated for each group; *i.e.* modification of the precoat structure.

Table 5-9 shows the average maximum ink tack, in force (N) and time to reach the maximum force (in seconds) for the average of all 20 various modifications of the precoat for the each of the 3 latexes used in the topcoat (20 conditions per latex). The Table also show the average determination coefficient (R^2) obtained when fitting the 20 DELTAC curves with a second order polynomial (excluding the data corresponding to the levelling out of the curve at high time cycle values). The average total pore volume and average total pore area are provided for information only.

Figure 5-52 provides the general curve shapes obtained for all 20 precoat conditions, for each topcoat latex used in the study. The differences obtained among the 3 latexes while printing are here clearly illustrated. The S/B/ACN latex takes a longer time to get to the maximum pick force (Table 5-9 and Figure 5-52), *i.e.* a longer time for ink setting. It takes 50 % less for the S/A latex and 32 % less for the S/A/ACN latex. As previously explained, the gel content is a key factor that may explain such differences. The acrylic content (S/A and S/A/ACN) reduces the ink setting time but also the coating strength. Figures 5-53, 5-54, 5-55, 5-56, 5-57, and 5-58 show the results for each different group and specific precoat conditions: the control or reference (5-53), the 20 parts clay substitution (5-54), the precalendering effect (5-55), the latex and thickener substitution (5-56), and the 100 parts pigment substitution for the carbonates (5-57) and for the Brazilian clay (5-58).

It is evident that the 3 latexes present a similar behaviour within each single group with only the S/A latex for a 20 parts clay substitution having a different curve shape (Figure 5-54).

A major conclusion from above considerations is that, as detailed in our proposed mechanisms, is that ink transfer is mainly controlled by the topcoat layer as the 3 different latexes are used in the topcoat, while the tack force is further controlled by the whole precoat/topcoat structures induced by the precoat structure.

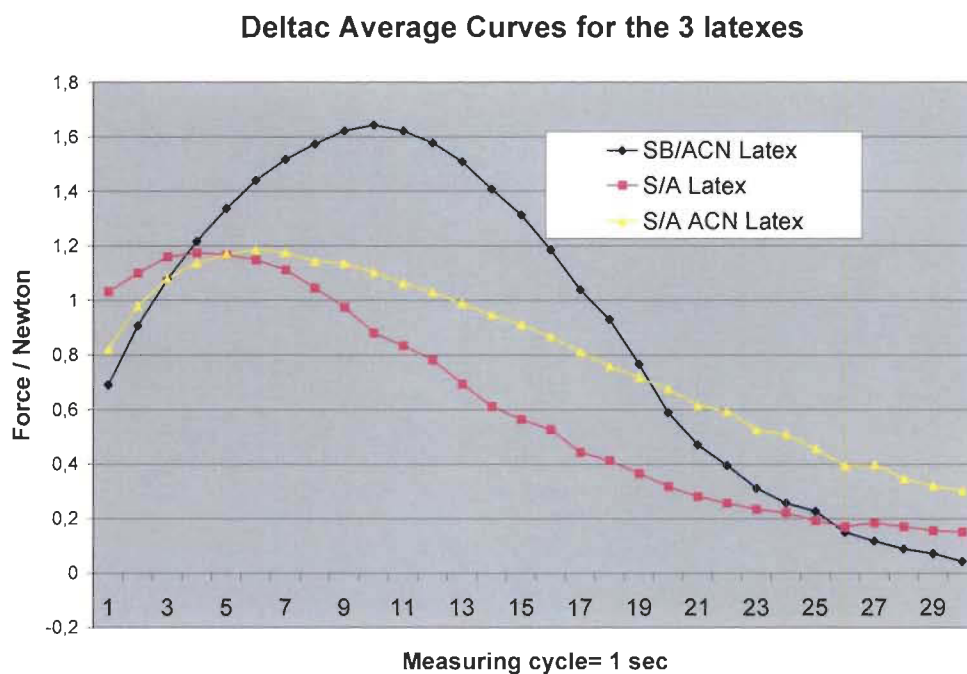


Figure 5-52 General DELTACK Comparison curves for the 3 latex

Table 5-9 Maximum ink tack force and time for all conditions for the 3 latexes used in this study

Condition	Max Ink Tack		R ²	TPV mL/g	TPA 4V/A (μ m)
	Time	Force			
	(second)	(Newton)			
S/B/ACN	10.16	1.56	0.9679	0.1686	0.098
S/A	4.37	1.23	0.9474	0.1641	0.092
S/A/ACN	6.72	1.17	0.9163	0.1731	0.103

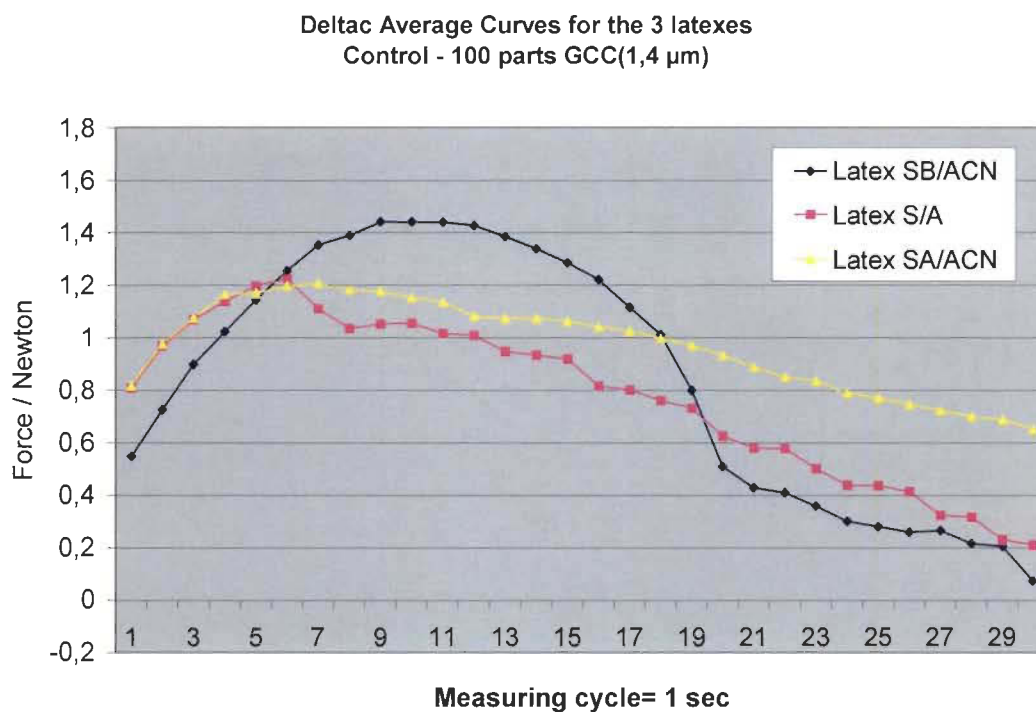


Figure 5-53 DELTACK Curve for the control precoating layer – 100 parts GCC (1.4 μ m)

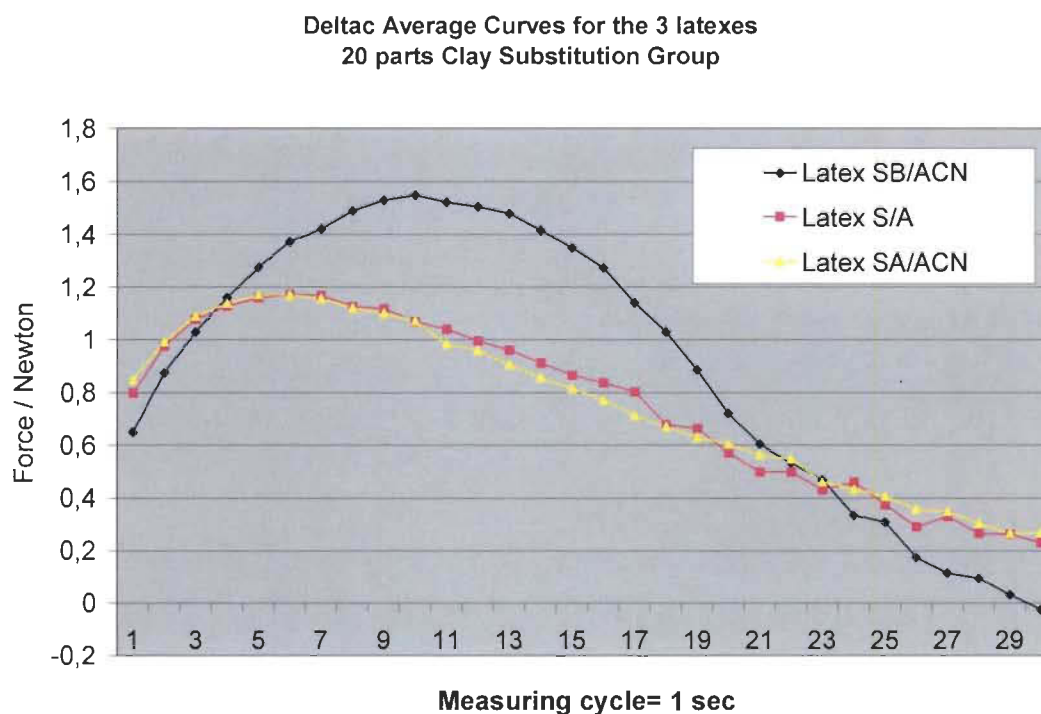


Figure 5-54 DELTACK Average Curves for the 3 latexes for the 20 parts substitution Group

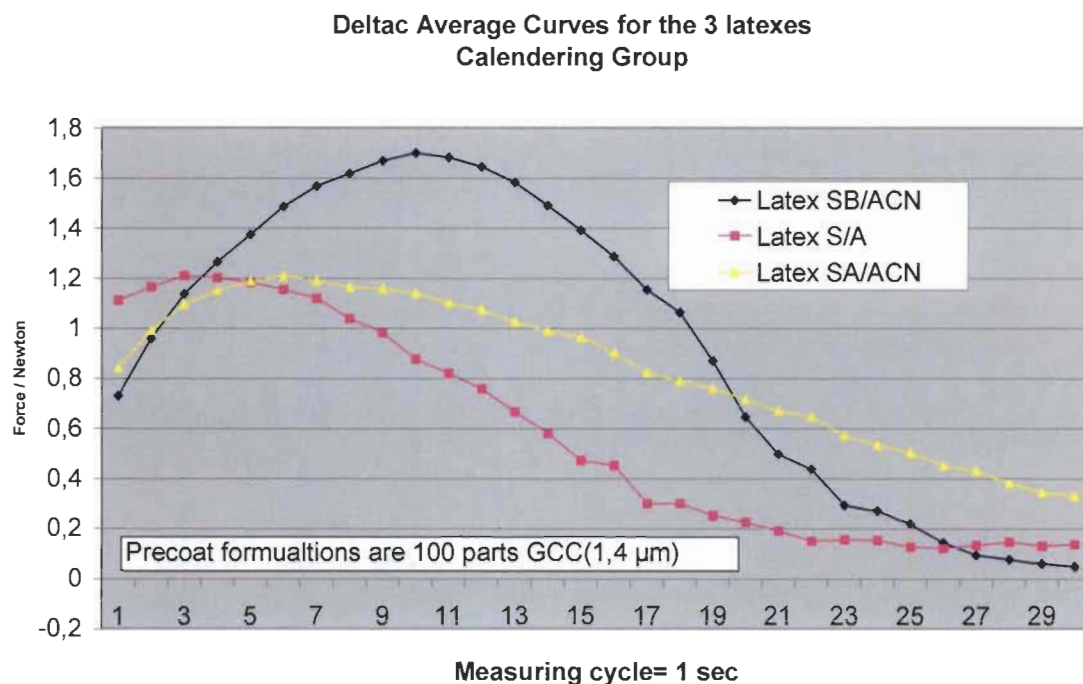


Figure 5-55 DELTACK Average Curves for the 3 latexes for the base paper and precoating layer calendering Group

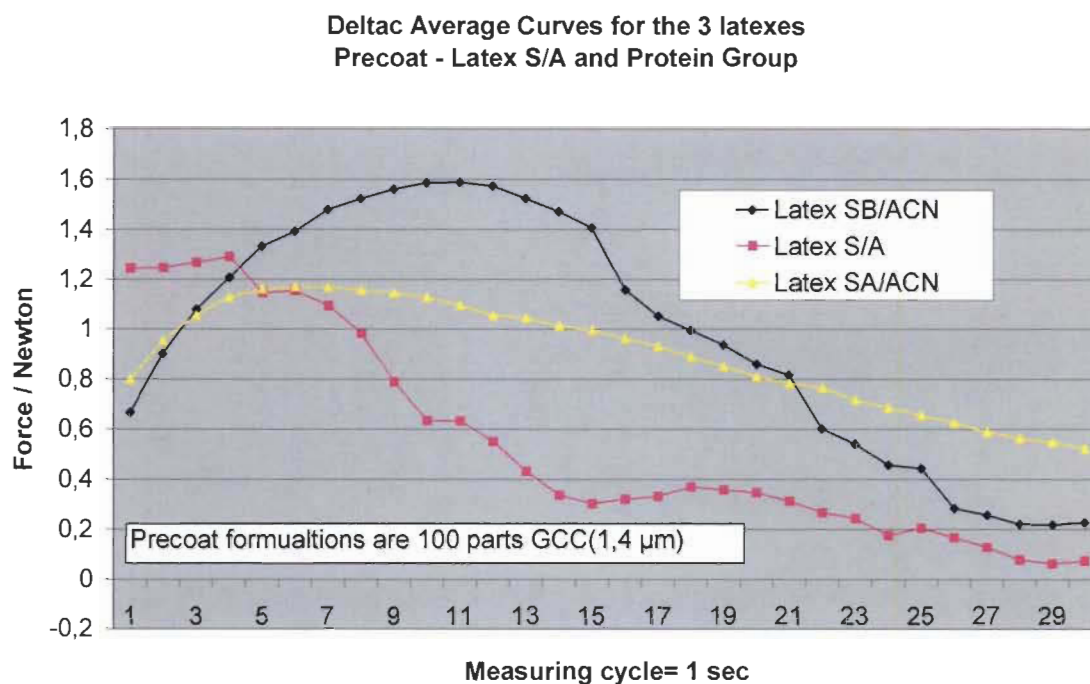


Figure 5-56 DELTACK Average Curves for the 3 latexes for the Acrylic latex and Protein substitution Group

Deltac Average Curves for the 3 latexes
100 parts Pigment Substitution Group - Carbonates

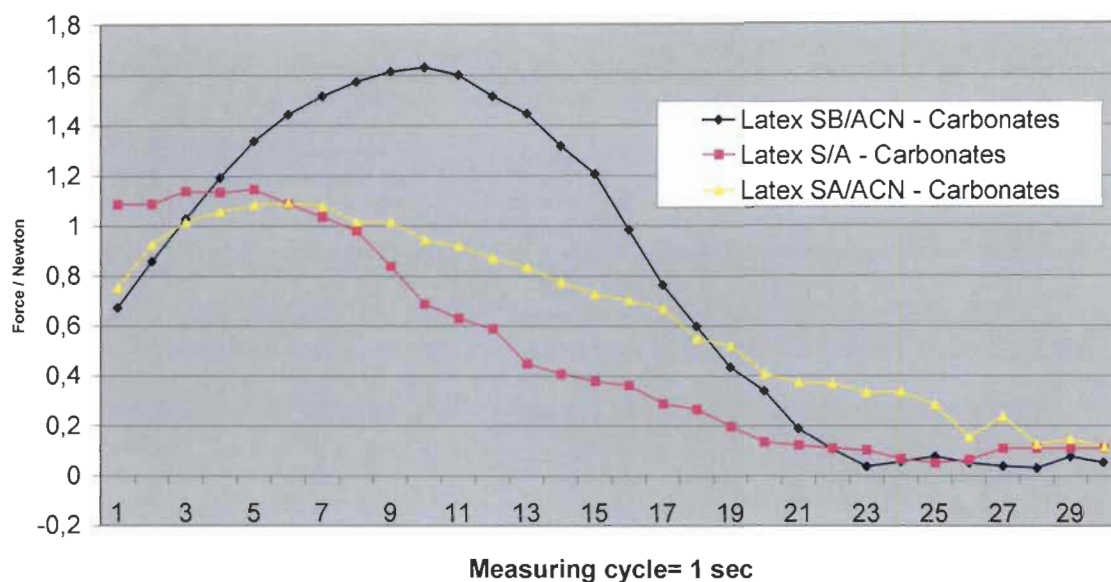


Figure 5-57 DELTACK Average Curves for the 3 latexes for the 100 parts substitution Groups – Carbonates

Deltac Average Curves for the 3 latexes
100 parts Pigment Substitution Group - Brazilian Clay

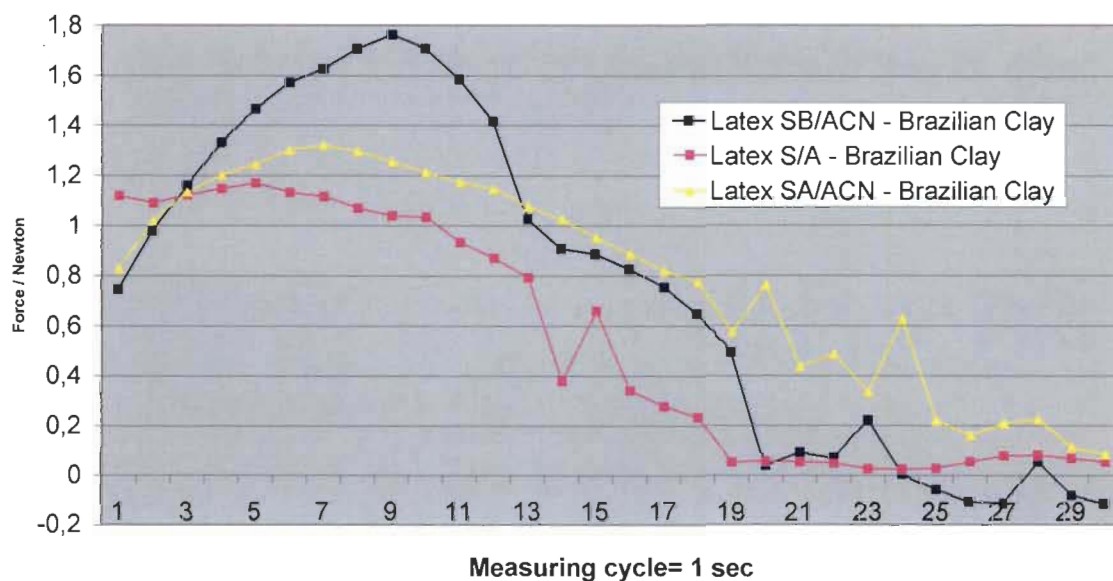


Figure 5-58 DELTACK average curves for the 3 latex – Brazilian clay

5.7 Projection on a Latent Structure (Partial least Square) Study

In the analysis of the effect of the precoat variables such as pigment type, precalendering of the precoat layer and/or base paper, substitution of pigment, either 20 parts or 100 parts, latex and thickener substitution, we have seen that parameters such as pigment type, size, etc. had a significant influence on the double-coated paper structure. We have demonstrated that the latex type in the topcoat was the predominant factor for tack build-up (DELTACK force). We have also seen that the structural parameters, as induced by above variables, would have a complementary effect that explained the maximum tack force. In order to verify that the main parameters we proposed to explain the various effects on the structure and the printing characteristics (DELTACK) are indeed justified and that there are no other second order effect, we performed a partial least square analysis of the set of data developed in the course of present study. It should already be emphasized that this additional step is a mathematical verification step as it is not a first time analysis. For instance, we already know that latex is the key component from a printability standpoint.

5.7.1 General presentation of the PLS method

Basically PLS is a sort of Principal Component Analysis (PCA). PCA is a powerful and common tool in the analysis of study phenomena. Multivariate projection methods represent a useful and versatile mathematical tool in the modeling, monitoring, and prediction of the often complex problems and data structures encountered within data-rich disciplines in Research, Development and Production (RDP) [116]. One type of analysis included in the PCA is the projection on a latent structure (PLS) also known as Partial Least Square.

PLS was first introduced by Wold *et al* ([116-119]) and has continuously grown since. An alternative term for PLS, and a more correct according to Wold [118], is “projection to latent structures”. However, the term “partial least squares” is still dominant in many areas. It is widely applied in the field of chemometrics, in sensory evaluation, and more recently, in the analysis of functional brain imaging data.

Briefly, projection on latent structure regression (PLS-regression) or partial least squares regression (PLS-regression) is a statistical method making relationship between principal components regression. Because both, the X and Y data are projected to new spaces, the PLS family of methods are known as bilinear factor models [117]. PLS method identifies directly X and Y values which allows to establish predictive cause and effects models. These predictions can be between the X values, between the Y values and between X and Y values.

PLS-regression is an important step in PLS path modeling, a multivariate data analysis technique that employs latent variables. The technique is often referred to as a form of variance-based or component-based structural equation modeling. It is used to find the fundamental relations between two matrices (X, above “variables” and Y, above “parameters”), *i.e.* a latent variable approach to modeling the covariance structures in these two spaces.

A PLS model will try to find the multidimensional direction in the X space that explains the maximum multidimensional variance direction in the Y space as illustrated in Figure 5-59 where the dispersion of the dots on the graphic is well explained by the 2 red axes. PLS-regression is particularly suited when the matrix of predictors has more variables than observations, which is our case, and when there is multicollinearity among X values. By contrast, standard regression will fail in these cases [117].

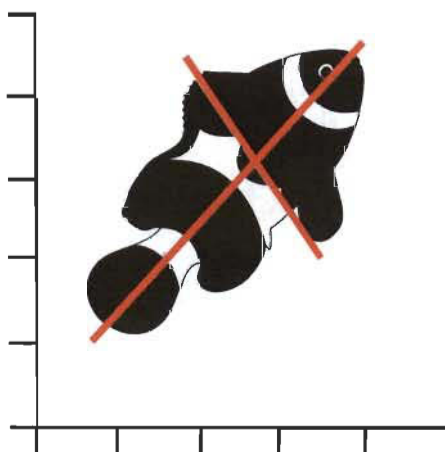


Figure 5-59 2 principal axis on a fish picture

Practically, the program finds the axis in the three dimensional (3D) space giving the best correlation between n random variables as can be seen in Figure 5-60. The method is also known as Karhunen-Loeve transformation or Hotelling transformation (from Harold Hotelling). The results may be graphically displayed in different ways. It works because the methods capture the dominant, latent properties of the system under study.

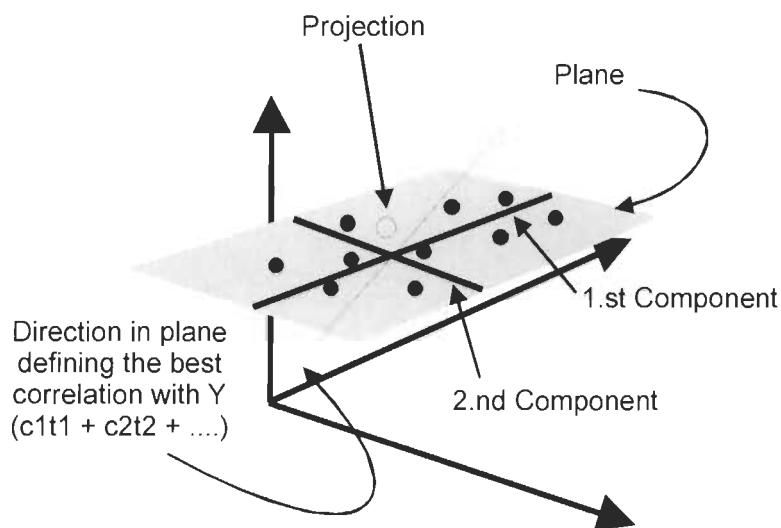


Figure 5-60 Graphic showing 2 principal components, the best correlation with Y and the projection on a surface

By contrast to PCA, PLS regression finds components from X that are also relevant for Y. Specifically, PLS regression searches for a set of components (called latent vectors) that perform a simultaneous decomposition of X and Y with the constraint that these components explain as much as possible of the covariance between X and Y. This step generalizes PCA. It is followed by a regression step where the decomposition of X is used to predict Y. The technique is often referred to as a form of variance-based or component-based structural equation modeling [117, 119].

A more complete explanation of the PLS method is presented in Appendix **3**.

5.7.2 PLS Results

The structure of the PLS analysis represented in table 5-10 was selected upon consideration of the importance we previously found in the variables. Indeed, the 2 component analysis includes latex type, the 3 components analysis adds the particle and pigment size variables, and the 4 component analysis includes all data up to the precalendering variables. However, the order of selection has no importance anymore when the 4 component analysis is concerned.

Before going into detailed analysis, it should be stressed that the determination coefficients R^2 we found are often low, with values between 0.5 and 0.7. Of course, removing the non-significant values would have helped to improve or raise the R^2 value. Indeed, in PLS studies, the variables located inside a given area, limited ± 0.2 value for both axes around 0, are normally less important. An example is presented in Figure 5-61 which shows the projection on a plane of the correlation coefficients for each variable as related to 2 components (one per axis). Such data are sometimes removed from the analysis as they do not have any significant effect on the final results. In our study, the values inside the “ ± 0.2 square area” were intentionally kept into the analysis to consider all available data. This decision has the effect of reducing the R^2 value while keeping the correlations significant.

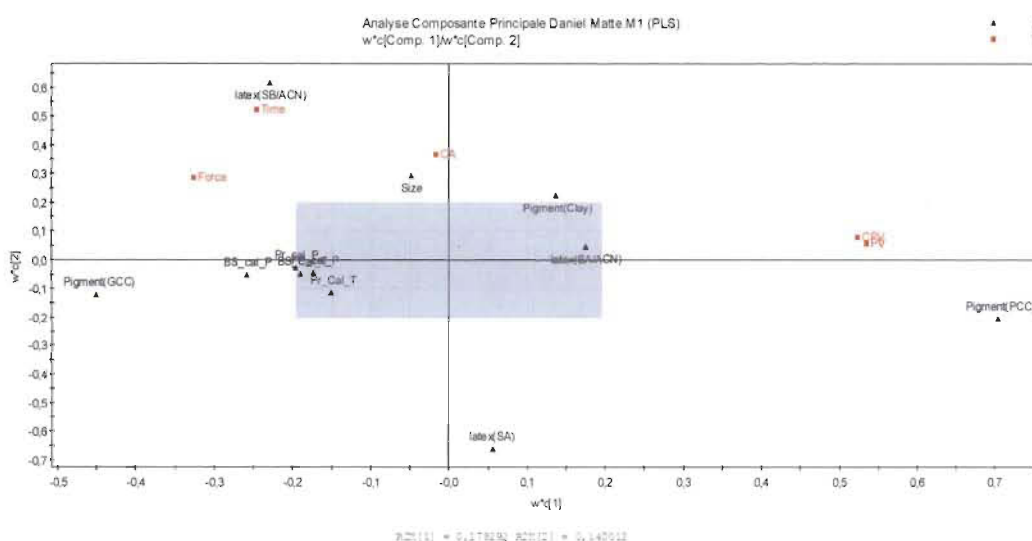


Figure 5-61 PLS Regression – Projection graphic with the ± 0.2 square low correlation area

Table 5-10 Modeling structure related to the components used

	2 components	3 components	4 components
Variables Y			
Time (DELTACK)	√	√	√
Force (DELTACK)	√	√	√
Contact Angle	√	√	√
Total (pre-coat/topcoat) Pore Volume	√	√	√
Precoat Pore Volume	√	√	√
Variables X			
Particle Size		√	√
Pigment Type		√	√
Latex type	√	√	√
Base Stock Temp. Cal.			√
Base Stock Pres. Cal.			√
Precoat Temp. Cal.			√
Precoat Pres. Cal.			√

5.7.3 PLS Study for 2 components - Effect of precoat pore volume on the final results

As our initial hypothesis is to demonstrate if and how the precoat would determine the structure and printing characteristics of a double-coated paper, it is logical to first analyse the effect and importance of precoat volume to explain the data set (results). Consequently, two projection graphics at 4 components are performed and presented in Figures 5-62 and 5-63, one with the precoat pore volume inserted into the PLS study and the second without the precoat pore volume values.

Comparison of the two Figures indicates that the precoat pore volume itself has no (or very little) measurable effect on the other variables. Only a slight variations in the pro-

jection graphs occur by adding the precoat pore volume in the PLS analysis. In fact, as we have seen previously in the mechanistic and physical analysis, the precoat pore volume works in combination with one and/or more other variables to achieve a desired printability level.

5.7.4 Effect of the latex

A key conclusion of the mechanistic study is the predominant importance of the latex type of the topcoat on the maximum tack force value. Although quite not expected, the latex in the topcoat was not part of the initial hypothesis of the thesis focus on the precoat impact. To confirm the point, we have performed the 2 component analysis with the latex type as a variable. According to previous results (0), we could have done the same for the precoat volume. Another reason to use the latex here is to present and understand the PLS analysis with only 2 components. Results would have somehow been similar with the precoat volume and a 2 components analysis.

Table 5-11 which presents the PLS results, determination coefficients and correlation factors, Figure 5-64 which shows the importance factor (or weight on a normalized scale) and Figure 5-65 which presents the projection graphic are used to explain the results of the 2 component analysis. Although the PLS analysis clearly shows, as expected from the previous DETLTACK analysis, that the latex has a part of the variations in the printability characteristics, it does not explain all data variations. The 3 latexes used in the trial are responsible for only 0.19 (19%) in Y of the total variation (table 5-11).

The projection graphic in Figure 5-65 confirms that the 3 latexes behave in total opposition. The same graphic also indicates that the contact angle (CA), the pore volume for the uncalendered paper (VP), the pore volume for the calendered paper (VPC), the maximum DELTACK force (Force) and time (Time) are not very relevant.

Globally, the latex has a key impact but the variations must be explained with some other variables; whereas the need to perform the analysis with more than 2 components.

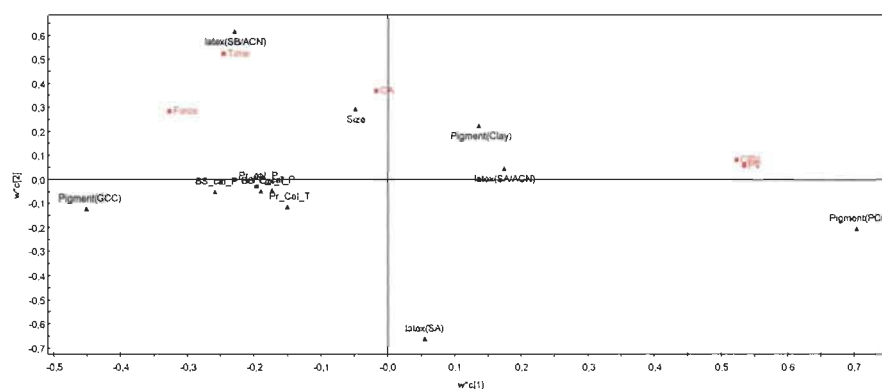


Figure 5-62 Graphic projection for the Component 1 and 2 without pre-coated pore volume variable

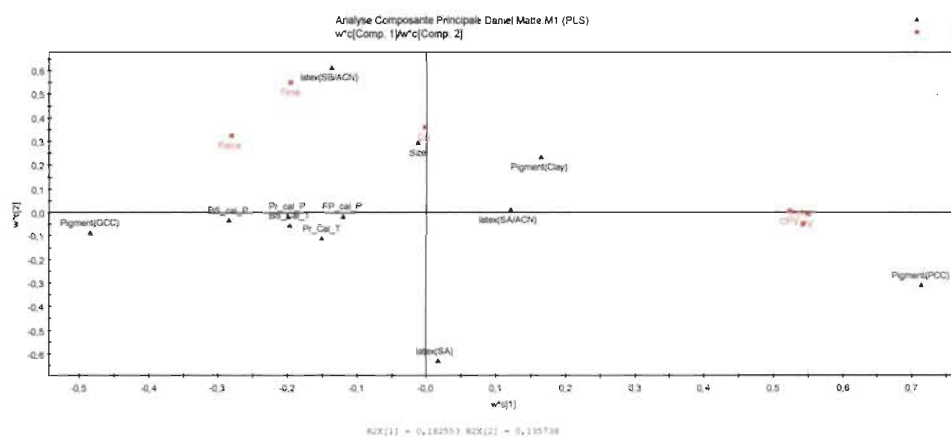


Figure 5-63 Graphic projection for the Component 1 and 2 with pre-coated pore volume variable

Table 5-11 Correlation factor R^2 for 2 components – Results

Correlation factor X and Y for 2 components		
Type: PLS Observations (N)=60. Variables (K)=8 (X=3, Y=5), Qualitative (1. expanded=3)		
A	1	2
R2X – Cent.	0.5	0.5
R2X(cum)	0.5	1
Eigen values	1.5	1.5
R2Y – Cent.	0.157	0.0337
R2Y(cum)	0.157	0.19
Q2	0.12	0.00445
Limit	0.05	0.05
Q2(cum)	0.12	0.124
Significance	R1	R2
Iterations	9	2

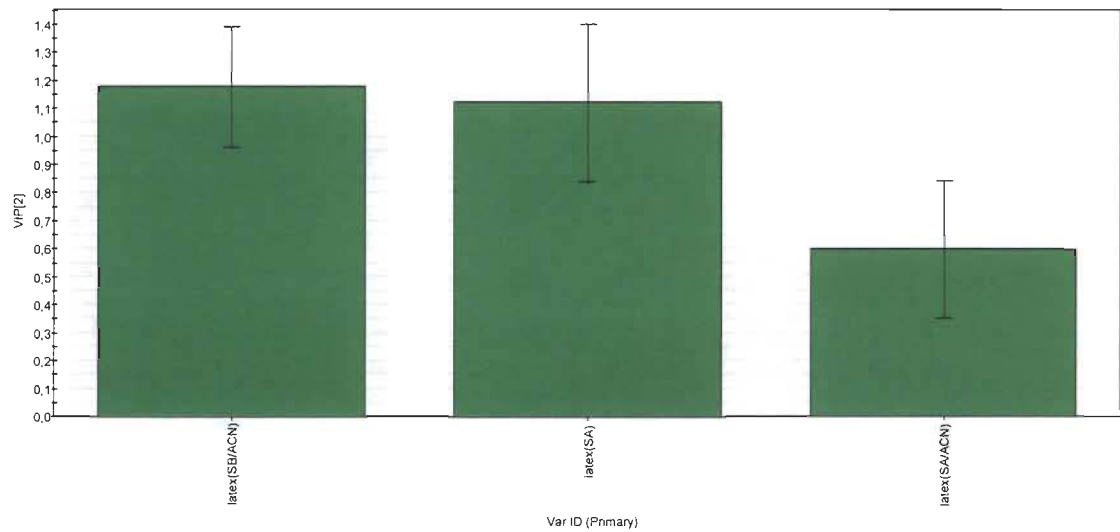


Figure 5-64 PLS Result (2 Components) – Graphic for the 3 latex

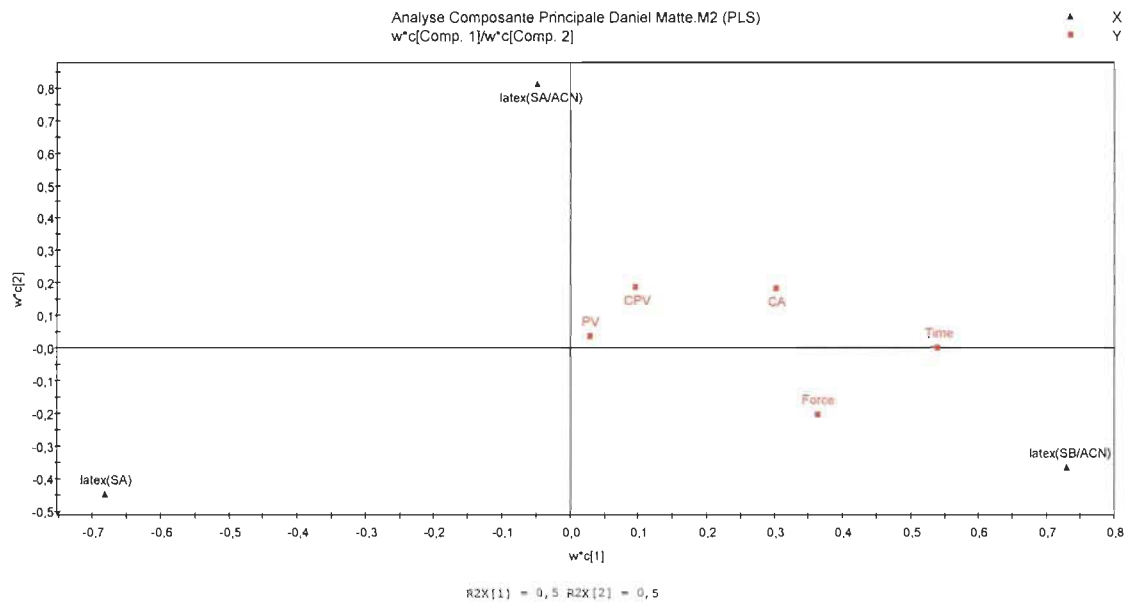


Figure 5-65 PLS Result (2 Components) – Correlation factor R^2 projection graphic

5.7.5 PLS study for 3 components

The 3 components PLS enable the analysis of the strength of the variables targeted by the analysis (Table 5-10).

Table 5-12 which presents the PLS results, determination coefficients and correlation factors, Figure 5-67 which presents the projection graphic and Figure 5-66 which shows the importance factor and are used to explain the results of the 3 components analysis.

We conclude from the analysis that the type of pigment (PCC, GCC, and Clay), the latex (S/B/ACN, SA, S/A/ACN), and the pigment size are the most important variables to explain the results (Figure 5-67 and 5-66). Together, all these variables explain 48 % (table 5-12) of the results. However, if we consider only the 2 first components, 45% of the results are explained.

Table 5-12 Correlation factor R^2 for 3 components – Results

Correlation factor X and Y for 3 components			
Type: PLS Observations (N)=60. Variables (K)=12 (X=7. Y=5), Qualitative (2. expanded=6)			
A	1	2	3
R2X – Cent.	0.207	0.234	0.225
R2X(cum)	0.207	0.441	0.666
Eigen values	1.45	1.64	1.58
R2Y – Cent.	0.299	0.154	0.0287
R2Y(cum)	0.299	0.453	0.482
Q2	0.235	0.185	-0.0361
Limit	0.05	0.05	0.05
Q2(cum)	0.235	0.376	0.354
Significance	R1	R1	R2
Iterations	20	8	23

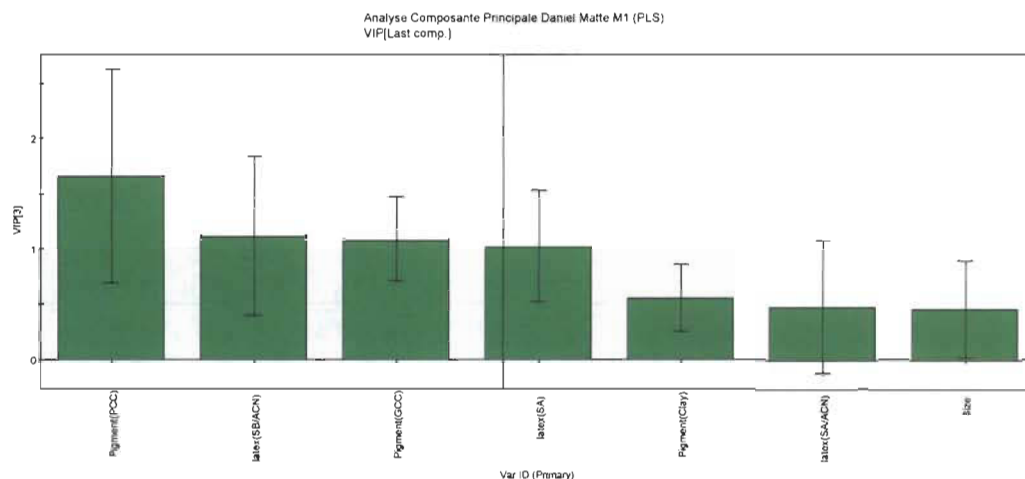


Figure 5-66 PLS Result (3 Components) – Most important variables in order of their importance

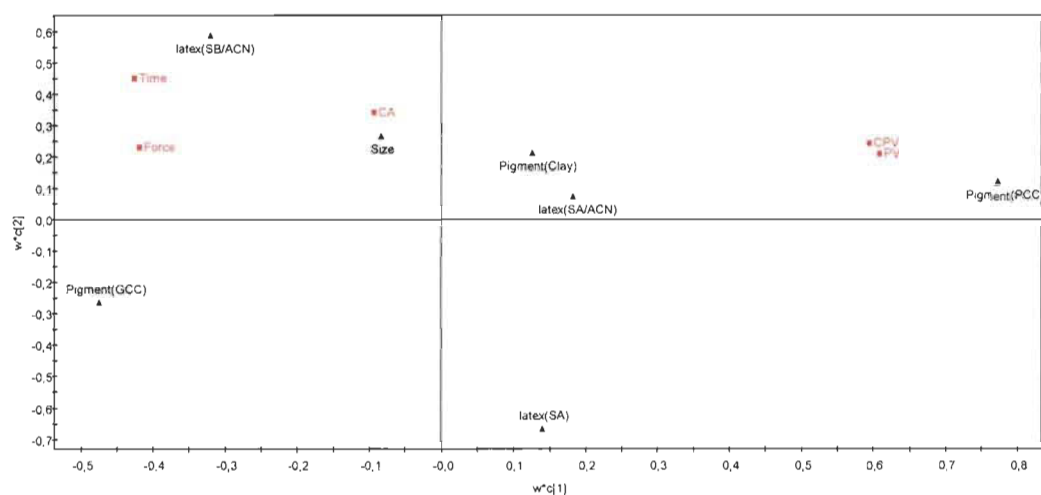


Figure 5-67 PLS Result (3 Components) – Correlation factor R^2 projection graphic

5.7.6 PLS study for 4 components

The PLS analysis with 4 component is the most common way to perform most of the PLS analyses, especially if the results vary widely. We used it initially (0) to evaluate the precoat structural importance; *i.e.* our initial hypothesis. Table 5-13 which presents the PLS results, determination coefficients and correlation factors, Figure 5-70 which presents the projection graphic and Figure 5-69 which shows the importance factor and

are used to explain the results of the 3 components analysis. It should be noted that Figure 5-70 is identical to Figure 5-68 and is presented here to facilitate the analysis. Results in Table 5-13 indicate that the 4 components analysis explains 55.5% of data variations. Therefore, the addition of the 4th component explains approximately 7% more values than the 3 component analysis and 10% more when compared with 2 components (A=2 in table 5-13). This means that the addition of the 4th component has a minor effect and/or works in combination with another parameter of the study. The addition of the 4th component includes all the calendering variables in the PLS study. However, the results related to the calendering are inside and/or very close to the “+/- 0.2 square” area: *i.e.* with a low significance factor. Indeed, we could only see the importance of the pre-calendering when analyzing the factor separately (analysis of Group 2) which seems not to be the case here as all data are included in the PLS study.

Table 5-13 Correlation factor R^2 for 4 components – Results

Correlation factor X and Y for 4 components				
Type: PLS Observations (N)=60. Variables (K)=18 (X=12, Y=6), Qualitative (2. expanded=6)				
A	1	2	3	4
R2X – Cent.	0.183	0.136	0.16	0.162
R2X(cum)	0.183	0.318	0.478	0.64
Eigen values	2.19	1.63	1.91	1.94
R2Y – Cent.	0.312	0.144	0.0571	0.0415
R2Y(cum)	0.312	0.456	0.513	0.555
Q2	0.236	0.106	-0.027	0.0147
Limit	0.05	0.05	0.05	0.05
Q2(cum)	0.236	0.317	0.299	0.309
Significance	R1	R1	NS	R2
Iterations	11	14	29	8

Figure 5-69 shows the variables included in the 4th component analysis by order of importance. Like previous similar graphs, the PCC, GCC type, and the latex S/B/ACN and SA and clay are the most important values. As seen in Table 5-13, they explain over 45% of all the correlations between the data. Not surprisingly, by adding a 4th compo-

ment, the precalendering conditions now reappear in the importance factors. It even has a bigger impact than latex S/A/ACN and the particle size. In the same train of thought, the calendering of the base paper has a larger impact than precoated layer calendering. In addition, it is important to realize that in a 4 dimension space due to the 4 components, one has to analyse various plane projections. Figure 5-70 which shows the projection of the values for the 1st and 2nd component confirms the analysis performed with Figure 5-69. An additional information relates to the importance of the time and force related to tack build-up (DELTACK).

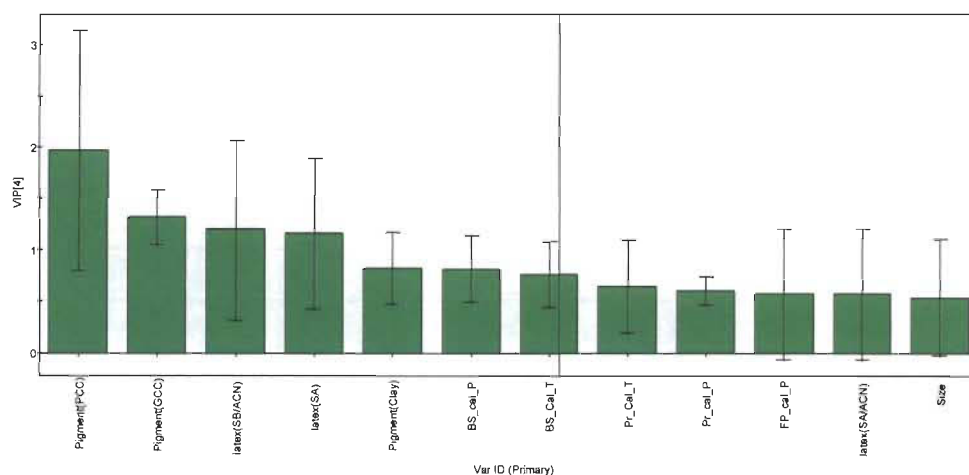


Figure 5-69 PLS Result (4 Components) – Most important variables in order of their importance

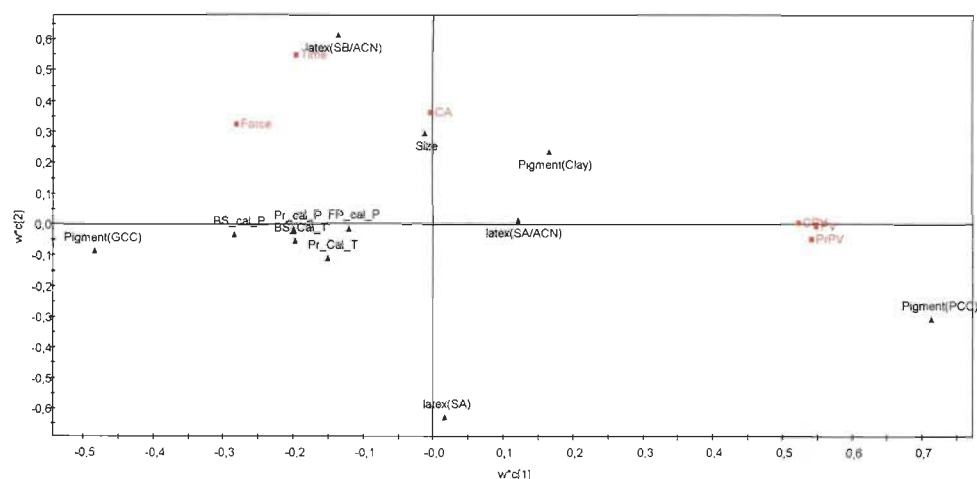


Figure 5-70 PLS Result (4 Components) – Graphic projection for the Component 1 and 2 with precoated variable

It further confirms that the topcoat latex is an important factor when combined with the other analysed values. Figure 5-71 provides the projection for the 3rd and 4th components and also confirms the analysis of the ranking of the various variables.

Figures 5-72 to 5-76 present the correlation coefficient obtained with the Ink Tack Force (5-72), the maximum force (5-73), the pore volume for the uncalendered double-coated paper (5-74), the calendered double-coated paper (5-75), and the contact angle (5-76), respectively and the other dependant variables of the study.

The five graphics simply show how selected dependant variables Y vary for each dependant variables X. The graphics confirm the importance of the 3 first variables appearing in the overall ordering presented in Figure 5-69, namely PCC (type), GCC (type) and S/B/ACN latex.

The other variables have a minor effect for the majority of the dependent variables Y evaluated. Figure 5-76 shows the interesting additional evaluation for the contact angle as we know that the variables affected by the contact angle measurement are very different, depending on both chemical and structural parameters. Indeed, the latexes S/B/ACN and S/A continue to have a key impact on the contact angle value.

Finally, the addition of a 4th component in the PLS analysis clearly demonstrates that the improvement of the determination coefficient (and correlation coefficients) becomes marginal. Although one may conclude that the addition of the variables for the additional 4th component will have a rather low impact on the final results when analysed globally, it mainly means that there is no need to pursue the analysis at the 5th component level.

In conclusion, the PLS analysis has mainly confirmed and validated initial mechanistic and structural analysis we performed. It therefore provides strength and confidence in our proposed mechanisms of precoat structural importance on the double-coated paper properties.

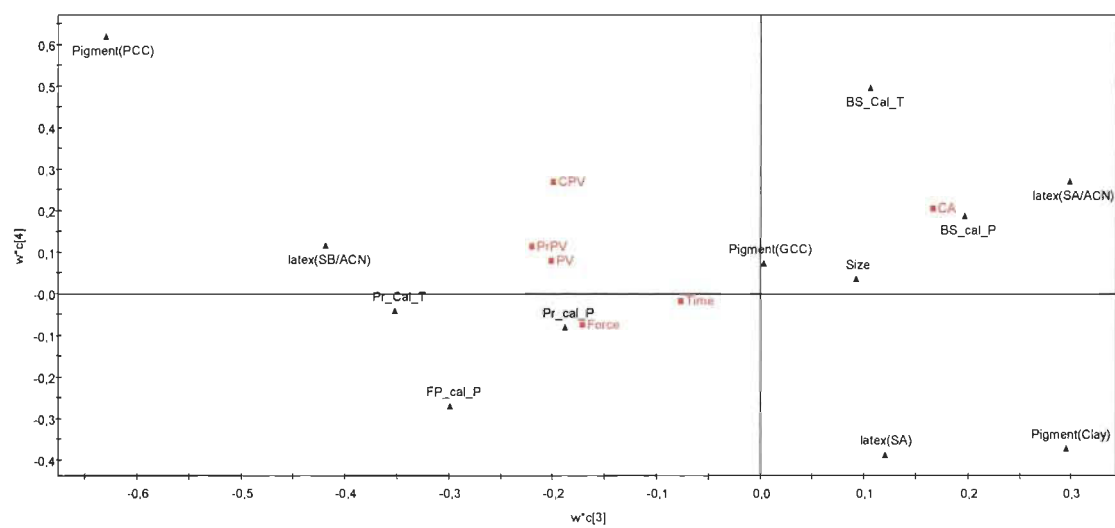


Figure 5-71 PLS Result (4 Components) – Graphic projection for the Component 3 and 4 with pre-coated variable

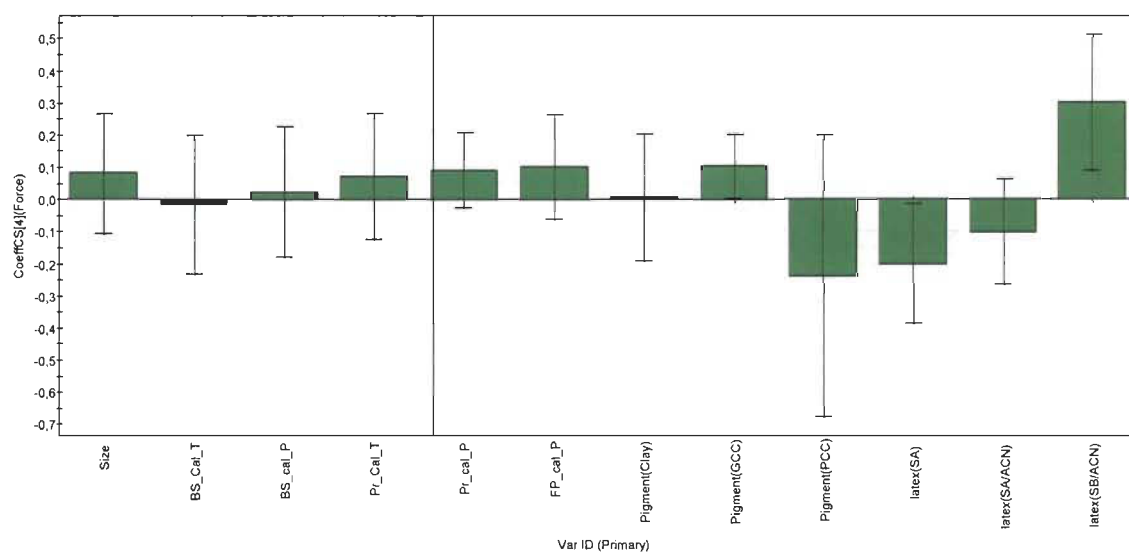


Figure 5-72 PLS Result (4 Components) – Ink Tack Force

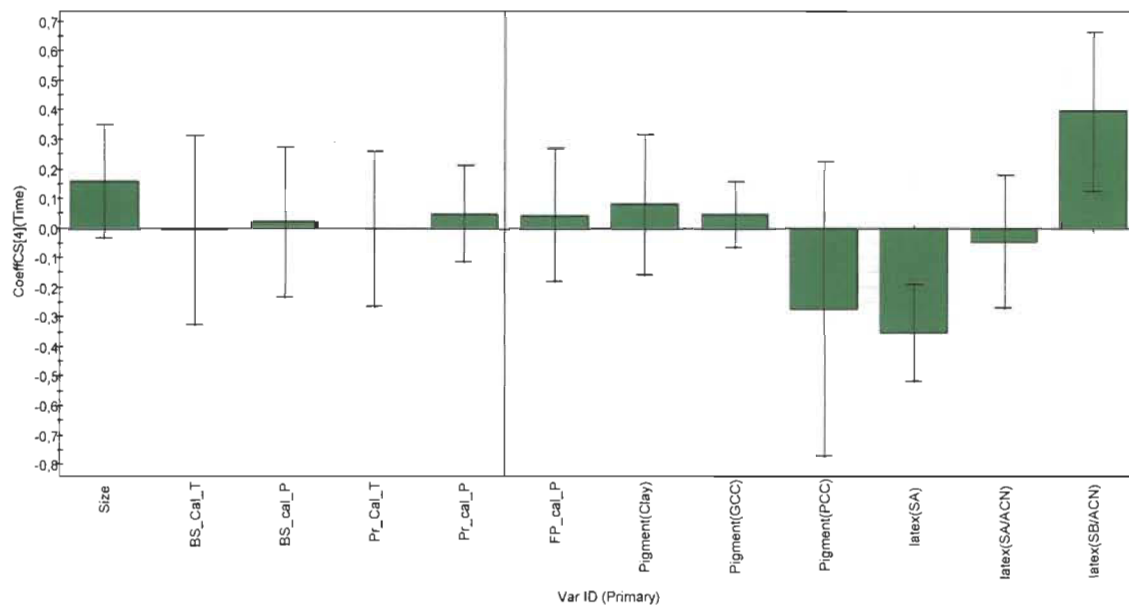


Figure 5-73 PLS Result (4 Components) – Time to get the maximum force with DELTACK

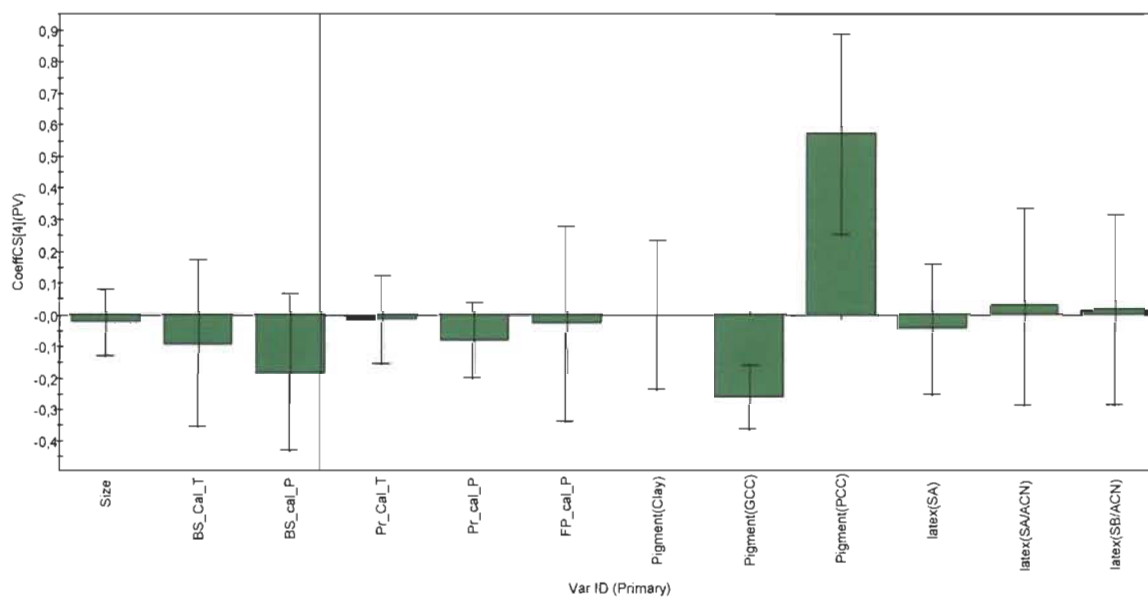


Figure 5-74 PLS Result (4 Components) – Pore Volume for uncalendered paper

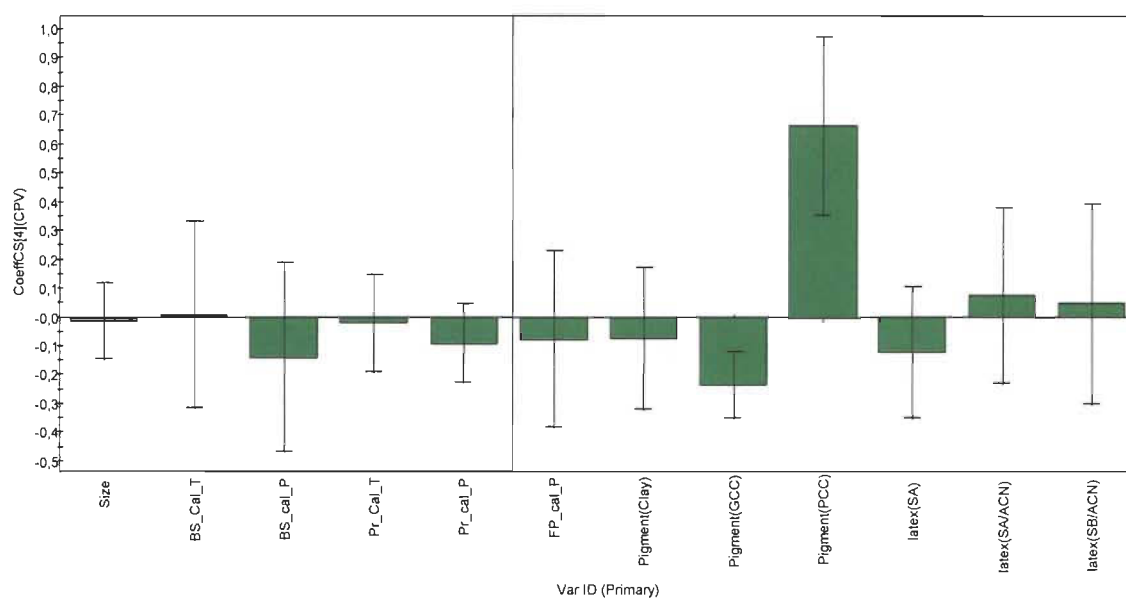


Figure 5-75 PLS Result (4 Components) – Pore Volume for calendered paper

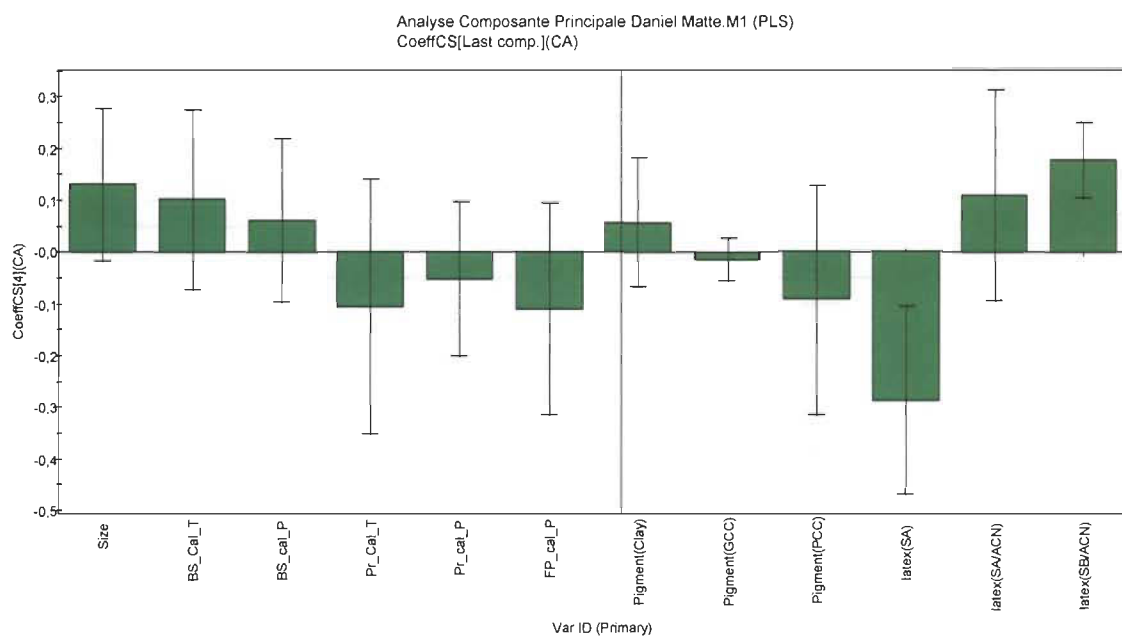


Figure 5-76 PLS Result (4 Components) – Contact Angle

Chapter 6 - Conclusion

The objective of the work was to analyse the effect of the precoat on the properties, mainly structure and printing characteristics as evaluated by the maximum force corresponding to ink build-up upon repeated printing cycles (so-called DELTACK analysis). In order to fully understand the importance of the precoat, we modified the precoat considering potential commercial practices such as substituting 20 parts clay in a 100 parts GCC precoat (Group 1), precalendering either the base paper or the precoated paper (Group 2), substituting either a protein or a S/A latex in the precoat for an SB+CMC combination (Group 3), and changing the various pigments used in the precoating layer (100 parts substitution, Group 4). Our hypothesis was that such modifications would fundamentally modify the structure and even the physico-chemical characteristics of the precoat, thus inducing modification of the topcoat structure, and by consequence, the whole double-coated paper properties. Furthermore, we used 3 commercial standard latexes in the topcoat in order to analyse how the precoat effects would be modulated with different topcoats. The experimental design was developed to permit a full understanding of the different precoat conditions with an additional input created by the topcoat latexes. In essence, the different precoat formulations allowed us to study the modification and/or modulations of the pore structure of the double-coated paper due to changes in the precoat structures and physico-chemical properties.

The present work has permitted an excellent evaluation of different precoat conditions with an additional look on the topcoat latex for double coated paper. The different groups were created to show how the pore structure is modified and/or modulated by changes in the precoat structure (pigments, chemicals, precalendering). The general conclusion related to each groups are:

Present work has clearly demonstrated that substituting 20 parts of clay in 100 parts GCC precoat formulation permits a modulation of the coating structure to obtain the desired structural and printing properties. Similarly, we have shown that the topcoat structure is affected by the precoat and that the most probable explanation is a combination of capillary penetration, a preferential penetration within the precoat structure of the

smallest part of the topcoat pigment particle, *i.e.* a preferential pigment rearrangement, and a forced penetration into the precoat structure by the topcoat coating colour. The forced penetration, or a part of it, probably originates from the rewetting of the precoat layer upon topcoat application.

Another key conclusion related to 20 parts substitution in the precoat (Group 1) is that differences in printing properties as described by the DELTACK analysis are mainly related to the type of latex used in the topcoat layer. The butadiene base latex always presents higher maximum tack force and time than the styrene acrylic. We surmised it was related to the gel content of the latex. The topcoats containing styrene acrylic present similar behaviour when comparing DELTACK curve shapes.

Finally, we demonstrated how the same ink tack could be obtained with very different pore structures, either with equal pore volume and very different average pore size, or on the contrary, with very different pore volume and the same average pore size. We have proposed a fundamental mechanistic approach to explain this particular phenomenon. The mechanism is related to the changes in topcoat structure originating from the different precoat structures. Overall, the structural changes in a complex two layer structure provided by the precoat/topcoat will modify how the ink and/or the ink solvent penetrate preferentially into a two layer structure thus resulting in a thick or thin ink layer with different final compositions which will provide the same tack force.

The second approach to modify the structure of the precoat layer was by precalendering either the base paper or the precoat layer (Group 2). In all cases, precalendering produces lower pore size distribution, and consequently a lower total pore volume, than the reference paper, with no precalendering. Although the analysis of the pore distribution curves indicated no clear trend to easily understand how precalendering specifically affected the structures, it nevertheless led us to the conclusion that the structures thus produced by precalendering are different.

First, we showed that precalendering at 100°C results in a higher precoat pore volume than precalendering at 200°C. As expected, calendering to 200 kN/m also produces smaller total pore volume of the precoat than precalendering at 50 kN/m. More surpris-

ing are the results obtained for the topcoat structure upon precalendering either the base paper or the precoat. Here, we demonstrated that two apparently opposite effects occur. First, when precalendering the base paper, the top coat total pore volume is higher at 100°C than at 200°C. On the opposite, when precalendering the precoat layer, the top coat total pore volume is higher at 200°C than at 100°C.

The mechanism we propose to explain such apparently contradictory results is basically the same as the one we proposed to explain the ink tack. It is related to the filtration and packing of the structure that occurs during the coating operation. It is also related to the movement of the water and materials when a wet coating layer is applied over another surface. Indeed, the surface pore structure being more or less open will control filtration and packing. High temperature precalendering of the precoat layer has a direct impact on the topcoat structure. Precalendering the base paper has the same effect on the precoat structure but the situation is then necessarily reversed when the topcoat is applied in a kind of “domino” effect.

We further explained how it was feasible to obtain the same printing characteristics with the different structures created by precalendering. Here too, the effect of temperature precalendering was the predominant factor. The analysis here developed is a powerful tool to analyse such differences in precalendering. Finally, we demonstrated here that it was possible to control the double-coated layer micro-structure, even down to the nano-structure (at 30 nm and below) through precalendering and thus control the printing characteristics of double-coated papers.

After partial modification of the pigment content and modification of the base paper/precoat structure through calendering, we analysed how chemical modification of the precoat would affect the structures. Accordingly, we showed that, using either a protein or a S/A latex in the precoat to substitute for an SB+CMC combination (Group 3) does not result in significant improvements especially when the S/A latex precoat substitution is concerned. However, the protein substitution case presented an interesting behaviour and we were able to clearly demonstrate the effect of such a substitution on the structure of the coating layer. Indeed, the protein definitively resulted in a

broader pore distribution in the precoat layer. However, it was difficult to generalize as just one condition has been studied.

Finally, considering that the most dramatic commercial change would be to “move to completely another type of pigment”, we looked how different pigment types would modify the precoat structure and therefore the whole double-coated paper structure and properties. The analysis of the structures of the samples obtained when substituting 100 part pigments (Group 4) for different pigments in the precoat layer structure allowed to confirm that the precoat structure greatly impact the final structure of coated paper. We confirmed here the key importance of the particle size distribution and of the average particle size, and how they impact the precoat/topcoat structures. More specifically, we showed and explained how the total pore volume is somehow inversely proportional to the particle size distribution. Not only does the total pore area decrease with particle size but, in the case of the broad particle size distribution pigment, it is inversely proportional to the particle size. Finally, as expected from pigment packing and influence on the coated layer pores, we confirmed that the average pore diameter is directly related to the particle size of pigments used in the precoat.

Last but not least, the mechanism we proposed to explain similar maximum ink tack force, as measured with the DELTACK, with widely different pore structures, namely similar total pore volumes obtained with widely different average pore diameters, and largely different total pore volumes obtained with similar average pore diameters, was fully validated and confirmed with the precoat layers containing very different pigment types. As a reminder, the theory is based on the effect of preferential solvent penetration controlling the ink tack, and the effect of ink transfer controlling the ink thickness.

Present work brings two important contributions to the understanding of the physics and structure of double coated paper, and more specifically on the effect of the precoat layer on the double coated paper structure and properties.

Our first main contribution is the development of a normalisation method to treat the mercury intrusion data in such a way that it is now feasible to extract the maximum amount of structural information on such data sets. The method allowed us to isolate the

coating layers one from the other. It proposes a new way to treat mercury intrusion data sets to analyse the pore structure with good accuracy down to 30 nanometers, and probably lower. The method will be a new powerful tool to understand the flow dynamics at the nano level, for instance, as we have seen, how wet layers behave when applied one on top of the other. The new method enabled to segregate each layer structure separately, providing the potential to fine tune the analysis of multi-layered paper coating. We have thus developed a powerful tool to analyse how various coating colour formulations will affect each layered structure separately.

Our second main contribution is the development and proposal of a mechanism to explain how the same printing characteristics (as indicated by the maximum DELTACK force) can be obtained with two completely different structures, namely structures with the same pore volume but very different average pore diameters, and structures with widely different pore volumes but (almost) identical average pore diameter.

The reasons for obtaining similar printing characteristics when the average pore size of the two structures is widely different are rather complex. The mechanism we proposed, considers that ink transfer, in agreement with previous studies [104, 105], is indeed different because the topcoat structures are different. It should be noted that we have not validated it through modelling of fluid penetration as it was outside of the scope of present study. However, we showed that the low pore size case (case 1) in precoat/topcoat structure corresponds to very fine pores and a very small volume in the topcoat structure. In parallel, referring to the high pore size case (case 2), the precoat/topcoat structure corresponds to a larger pores and larger volume in the topcoat structure. Practically, it means that ink layer remaining of the surface in case 1 will be thicker than in case 2. In addition, considering the actual sizes of these pores, it also means that the structure with very small pores will favour, due to capillary penetration, the preferential absorption of ink solvent. In essence we will end up with a thicker ink film but with less solvent, *i.e.* a tackier ink. In the case of the larger pores, there will be no or less penetration of ink solvent. It is therefore quite feasible that the two effects being opposite, we will end up with the same maximum tack force.

From a commercial standpoint, we have demonstrated that the precoat has a more practical importance than usually accepted by industry practices. Generally, the precoat is more or less considered as a “layer filling-in surface defects and pores”. We have shown here that the precoat is an integral part of the double coated paper structure and printing characteristics. In essence, it could be used to fine tune the desired double coated paper properties. We have also shown that the precalendering has an important effect that goes beyond the usual commercial control of the precoated paper thickness.

For future work, the effect of thickeners on the pore structure and printing properties may be of interest as it may be related to coating improvement, specifically if one needs to understand how such a product modifies the coating structure. It would be of commercial research interest to study the effect of structure/chemistry of the latexes on printing characteristics as the effect on the DELTACK results seen for the thickener substitution were not really different than what was analysed for the structural modification (20 parts substitution and precalendering). Last but not least, the modelling of fluid penetration in double layered structures to further understand ink tack, ink build-up, and there resulting printing characteristics would be both a fundamental and an industry asset.

Bibliography

1. Picollet, M., Piette, P., Morin, V., and LeNest, J.F. *Competition between gravure ink penetration and spreading on LWC coated paper. 1998 TAPPI Coating and papermaker conference.* 1998. New Orleans, Louisiana: Tappi.
2. Gane, P.A.C., Schoelkopf, J., Spielmann, D., Matthews, G.P., and Ridgway, C.J. *Observing fluid transport into porous coating structure: some novel findings. 1999 Tappi coating conference.* 1999. Toronto, Canada: Tappi.
3. Karathanasis, M., Carne, T., Dahlvik, P., Haugwitz, B., and Strom, G., *Importance of coating structure for sheet-fed offset print quality.* *Wochenbl Papierfabr* 2001. **129**(7): p. 426-432.
4. Trefz, M., *Theoretical aspects and practical experiences for film coated offset grades.* *Tappi Journal*, 1996. **79**(1): p. 223-230.
5. Grön, J. and Ahlroos, J., *Effect of base paper filler content and pre-calendering on coating color mist and coverage in MSP coating.* *Journal of Pulp and Paper Science*, 2001. **27**(2): p. 66-73.
6. Grön, J. and Rautiainen, P.J. *Coating solutions for wood-containing and woodfree paper grades. TAPPI Coating Conference.* 1999. Toronto, Canada: Tappi Press.
7. Grön, J., *Significance of paper machine calendering on coating coverage.* *Paperi ja Puu -- Paper and Timber*, 2000. **82**(4): p. 245-249.
8. Gane, P.A.C., Burri, P., Spielmann, D., Drechsel, J., and Reimers, O. *Formulation optimization for improved runnability of high speed pigmented coatings on the metered size press. Tappi Coating Conference.* 1997. Philadelphia: Tappi press, Atlanta.
9. Preston, J.S., Elton, N.J., Legris, A., and Nutbeen, C. *The role of pore density in the settings of offset printing ink on coated paper. 2001 Advanced Coating Fundamentals Symposium.* 2001. San Diego, California: Tappi press.
10. Toivakka, M. and Nyfors, K. *Pore space characterization of coating layers. 2000 TAPPI Coating Conference and Trade Fair.* 2000. Washington, DC: Tappi press.
11. Carter, R.D., Goliber, C., Ishley, J., Barfield, J., and Dreschel, J. *In search of Synergy: Engineering Coatings for Maximum Performance: Optimizing Pigments Combinations for Maximum Performance. 1999 TAPPI Coating conference.* 1999. Toronto, Canada: Tappi press.
12. Hiorns, A.G., Elton, N.J., Coggon, L., and Parsons, D.J. *Analysis of differences in coating structure induced through variable calendaring conditions. 1998 TAPPI Coating / Papermakers Conference.* 1998. New Orleans, Louisiana: Tappi press.

13. Gane, P.A.C., *Skeletal element*. 2006, Omya: Oftrigen, Switzerland. p. Definition of the pore structure with the terminologies.
14. Drage, G., Vaughan, C., Henderson, K., Parsons, D.J., and Hiorns, A.G. *The influence of freesheet and groundwood basepaper formation on coated and printed paper*. TAPPI Coating Conference. 1999. Toronto, Canada: Tappi Press.
15. Zou, X., Vidal, D., and Allem, R. *Film Press for pigments coating: Coated paper quality and basestock effects*. TAPPI Metering Size Press Forum IV. 2002. Orlando, Florida: Tappi Press.
16. Al-Turaif, *The effect of pigment blends on the surface structure and chemistry of pigmented latex coatings*. Tappi Journal, 2006. **5**(8): p. 24-30.
17. Ahlroos, J., Alexandersson, M., and Grön, J. *Influence of base paper filler content and pre-calendering on metered film press coating -- Part II: Paper and print quality*. 1998 TAPPI Coating / Papermaker conference. 1998. New Orleans, Louisiana: Tappi press.
18. Huang, T. and Lepoutre, P. *Effect of base stock absorbency on coating hold out and coated paper properties*. 1996 Tappi Coating conference 1996. Nashville, Tennessee: Tappi press.
19. Gane, P.A.C., Hooper, J.J., and Baumister, M., *A determination of the influence of furnish content on formation and basesheet profile stability during coating*. Tappi Journal, 1991. **74**(9): p. 193-201.
20. Gane, P.A.C., Buri, M., and Blum, R. *Pigment co-structuring: New opportunities for higher brightness coverage and print-surface design*. International Symposium on Paper Coating Coverage. 1999. Helsinki, Finland.
21. Allem, R. and Uesaka, T. *Characterization of paper microstructure: A new tool for assessing the effects of base sheet structure on paper properties*. 1999 Advanced Coating Fundamentals Symposium. 1999. Toronto, Canada: Tappi Press.
22. Gane, P.A.C. and Hooper, J.J. *An evaluation of interactions between coating color and baspaper by coating profile analysis*. Fundamentals of Papermaking, Transactions of the Ninth Fundamental Research Symposium. 1989. London, U.K.: Mech. Eng. Publ.
23. Koivula, H., Fardim, P., and Toivakka, M. *Characterization of pigment particle surfaces by ToF-SIMS*. 2006 TAPPI Advanced Coating Fundamentals Symposium. 2006. Turku, Finland.
24. Lee, D.I., *A fundamental study on coating gloss*. 1974, Dow Chemical Corporation: Midland.
25. Di Risio, S. and Yan, N., *Characterizing the pore structures of paper coatings with scanning probe microscopy*. Tappi Journal, 2006. **3**(11): p. 9-14.
26. David, V. and Bertrand, F. *Recent progress and challenges in the numerical modeling of coating structure development*. 2006 TAPPI Advanced Coating Fundamentals Symposium. 2006. Turku, Finland.

27. Read, D., *Talc SEM Picture*, email, Editor. 2002, Luzenac: South Portland, Maine, USA.
28. Hirai, K. and Bousfield, D.W. *The Correlation Between Coating Penetration And Coating Properties*. TAPPI 2006 Coating And Graphic Arts Conference. 2006. Atlanta, Georgia: Tappi press.
29. Carne, T., Karathanasis, M., Dahlvik, P., Haugwitz, B., and Strom, G. *Importance of Coating Structure for Sheet-fed Offset Print quality*. 19th PTS Coating Symposium. 1999. Munich, Germany.
30. Dahlvik, P., Strom, G., and Salminen, P. *Effect of pH and calcium ion concentration on the flow behavior and structure formation of clay/calcium carbonate suspensions*. 1995 TAPPI Coating fundamentals Symposium. 1995. Dallas, Texas: Tappi press.
31. Järnström, J., Peltonen, J., Sinervo, L., and Toivakka, M. *Topography and gloss of paper coating layer*. 2006 TAPPI Advanced Coating Fundamentals Symposium. 2006. Turku, Finland.
32. Larsson, M. and Engstrom, G. *Interactions in coating colors based on GCC of broad and narrow particle size distribution and their effect on pore structure*. 2004 TAPPI Coating and Graphic Arts Conference and Exhibit. 2004. Baltimore, Maryland: Tappi Press.
33. Okomori, K. and Lepoutre, P. *Effect of pigment size and shape distribution on the cohesion of pigmented coatings*. 1998 TAPPI Coating / Papermakers conference. 1998. New Orleans, Louisiana: Tappi press.
34. Donigan, D.W., Ishley, J.N., and Wise, K.J., *Coating pore structure and offset printed gloss*. Tappi Journal, 1997. **80**(5): p. 163-172.
35. Devisetti, S. and Malla, P.B. *The Effect of Pigment Particle Size, Chemically Structured Kaolin and Coating Pore Structure on Rotogravure Print quality*. 2006 TAPPI Coating and Graphic Arts Conference. 2006. Atlanta, Georgia: Tappi press.
36. Kent, H.J., Climpson, N.A., Coggon, L., Hooper, J.J., and Gane, P.A.C., *Novel techniques for quantitative characterization of Coating structure and coverage*. Tappi Journal, 1986. **69**(5): p. p78-83.
37. Persson, T., Järnström, L., and Rigdhal, M. *Effect of the method of preparation of coating colours on the rheological behaviour and properties of coating layers and coated papers*. 1995 Coating Fundamentals Symposium. 1995. Dallas, Texas: Tappi Press.
38. Conceicao, S., Santos, N.F., Velho, J., and Ferreira, J.M.F., *Properties of paper coated with kaolin: The influence of the rheological modifier*. Applied Clay Science, 2005. **30**(3-4): p. 165-173.
39. Larsson, M., Engstrom, G., Vidal, D., and Zou, X. *Compression of Coating Structures During Calendering*. 2006 TAPPI Advanced Coating Fundamentals Symposium. 2006. Turku, Finland.

40. Gane, P.A.C. *Relaxation-induced dilatancy in separable visco-elastic suspensions: Proposing a novel rheological phenomenon. Tappi Advanced Coating Fundamentals Symposium*. 1997. Philadelphia, Pennsylvania: Tappi press, Atlanta.
41. Gane, P.A.C. *Re: Some explanation*. 2006 December 1st 2006]; Answer to my previous email].
42. Yulong, W. and Zhenlei, C. *Influence of coating pore structure on optical properties of low gloss Coated paper*. 2006 TAPPI Advanced Coating Fundamentals Symposium. 2006. Turku, Finland.
43. Knappich, R., Gerold, L., Burri, P., and Hugener, P. *Wet and dry coating structure of calcium carbonate pigments with narrow particle size distribution*. 1999 TAPPI Coating Conference 1999. Toronto, Ontario: Tappi Press.
44. Fukui, T., Terao, T., and Yamamoto, M. *Effect on porous structure of coated layer on ink setting*. 50th Appita Annual General Conference. 1996. Auckland, New Zeleand.
45. Osterhuber, E.J., McFadden, M.G., and Roman, N.R. *The effect of particle size distribution on the structure and optical properties of calcium carbonate-containing coatings*. International paper and coating chemistry symposium. 1996. Ottawa, Canada.
46. Hagemeyer, R.W., *The influence of chemical composition on the packing of pigment particles*. Tappi Journal, 1964. **47**(10): p. 595.
47. Hagemeyer, R.W., *The efect of particle shape and chemical composition on the packing characteristics of pigment combinaiton*. Tappi Journal, 1964. **47**(2): p. 74.
48. Matsubayashi, H., Miyamoto, K., Tagagishi, Y., and Kataoka, Y., *A Study on Blistering by Coating Structure Analysis*. Tappi Journal, 1990. **73**(5): p. 161-170.
49. Wirth, T. and Lederle, I., *International Customer Seminar Paper Coating Technology*, BASF, Editor. 2006. p. 450.
50. Rättö, P. *Mechanical properties of coating layers*. 2003 5th International paper and Coating Symposium. 2003. Montréal, Canada.
51. Kugge, C., Craig, V., and Daicic, J., *A scanning electron microscope study of the surface structure of mineral pigments, latices and thickeners used for paper coating on non-absorbant substrates*. Colloids and Surface : A Phisiochemical and Engeneering Aspect, 2004. **1**(11): p. 238.
52. Kugge, C., *An AFM study of local film formation of latex in paper coatings*. Journal of Pulp and Paper Science, 2004. **30**(4): p. 105-111.
53. Yamazaki, K., Nishioka, T., Hattori, Y., and Fujita, K., *Print mottle effect of binder migration and latex film formation during coating consolidation*. Tappi Journal, 1993. **76**(5): p. 79-84.

54. Malla, P.B., Starr, R.E., and Werkin, T.J. *The effects of kaolin particle size, structured clay loading and binder level on glossing and offset print properties -- A CLC coating study. 1999 Tappi Coating Conference.* 1999. Toronto, Canada: Tappi press.
55. Audette, H., *Liants.* 2001: Sarnia, Ontario, Canada.
56. Lepoutre, P., *The structure of paper coating: An update*, ed. Tappi. 1989, Atlanta, USA: TAPPI Press.
57. Wallström, A. and Järnström, L. *The influence of thickener on the surface structure of coatings evaluated by pair distribution analysis - Correlation to structure and porosity. 2006 TAPPI Coating and Graphic Arts Conference.* 2006. Atlanta, Georgia: Tappi press.
58. Dimmick, A., *Thesis document comments*, Email, Editor. 2008: Bethlehem.
59. Husband, J.C., Preston, J.S., Gate, L.F., Storer, A., and Creaton, P. *The influence of pigments particle shape on the in-plane Tensile Strenght Properties of Kaolin-based Coating layers. 2006 TAPPI Advanced Coating Fundamentals Symposium.* 2006. Turku, Finland.
60. Fernandez, J.M., Petterson, and Koval, J.C. *Binder influence on rotogravure printability. 1983 Coating Conference.* 1983. Atlanta, Georgia: Tappi press.
61. Laudome, G.M., Matthews, G.P., and Gane, P.A.C., *Distribution of offset ink constituents in paper coating and implications for print quality.* Tappi Journal, 2003. 4(7): p. 9-15.
62. Venkata-Chinnaswamy, H., Aravamuthan, R., and Scheller, B. *Effect of precalendering on surface and printing properties of coated sheets. 1998 TAPPI Coating / Papermakers Conference.* 1998. New Orleans, Louisiana: Tappi press.
63. Suontausta. *The influence of some coating and calendering variables on the smoothness and gloss of LWC paper. International Symposium on Paper Coating Coverage.* 1999. Helsinki, Finland.
64. Kan, C.S., Kim, L.H., Lee, D.I., and Van Gilder, R.L. *Viscoelastic properties of paper coatings: structure/property relationship to end use performance. 1996 TAPPI Coating conference* 1996. Nashville, Tennessee: Tappi press.
65. Koyamoto, H. and Okomori, K. *Effect of surface properties of base paper on print quality. 2006 TAPPI Advanced Coating Fundamentals Symposium.* 2006. Turku, Finland.
66. Steffner, O., Nylund, T., and Rigdahl, M. *Influence of pre-calendering on the properties of a coated woodfree paper and the covering ability of the coating. 1995 TAPPI Coating conference.* 1995. Dallas, Texas: Tappi press.
67. Engsröm, G. and Lafaye, J.F., *Precalendering and its effect on paper-coating interaction.* Tappi Journal, 1998. 75(8): p. p117-112.
68. Nissinen, V. *Effects of Multiple Process Variables on the Quality of Double-Coated Fine Paper. 1995 TAPPI Coating Conference.* 1995. Dallas, Texas.

69. Eng, C., *Double layers coated paper picture*, email, Editor. 2002, Omya: Oftrigen.
70. Renvall, S.V., Rautiainen, P.J., and Rossitto, J.C., *Optimizing the Coating Process for Double-Coated, Wood-Containing Papers*. Tappi Journal, 1990. **73**(5): p. 143-149.
71. Hassell, M.V., Plasted, R.M., and Newberry, V.F., *Study of precoat pigments in double-coated paper and board*. Pulp and paper Canada, 1989. **90**(3): p. 101-102.
72. Burri, P., Bluvol, G., Gane, P.A.C., and Carlsson, R., *Optimising Ink Setting Properties on Doubled Coated Woddfree Paper*: Oftrigen, Switzerland.
73. Hostetler, R.E. *Bent Blade Runnability of Double Coated SBS Paperboard*. Tappi Coating Conference. 2004. Baltimore, USA: Tappi Press.
74. Gagnon, R. and Hiscock, D. *Reducing Backtrap Mottle in Multilayer Coating Systems - Influence of Precoat Composition and Structure*. TAPPI Coating and Graphic Arts Division. 2006. Atlanta, Georgia: Tappi Press.
75. Dullien, F.A.L., *Handbook of porous media: Fluid Transport and Pore Structure*. 1979, San Diego, USA: Academic Press. 171 p.
76. Gane, P.A.C., Schoelkopf, J., Spielmann, D., Mathews, G.P., and Ridgway, C.J., *Fluid Transport into Porous Coating Structures: Some Novel Findings*. Tappi Journal, 2000. **83**(5): p. p. 77-78.
77. Ridgway, C.J. and Gane, P.A.C. *The Impact of Pore Network Structure on the Absorption of Pigmented Inkjet Inks*. 2005 Tappi Coating and Graphic Arts Conference. 2005. Toronto, Canada: Tappi Press.
78. Ridgway, C.J., Schoelkopf, J., Mathews, G.P., Gane, P.A.C., and James, P.W., *The effects of void geometry and contact angle on the absorption of liquids into porous calcium carbonate structures*. Journal of Colloid and Interface Science, 2001. **239**(2): p. 417-431.
79. Schoelkopf, J., Gane, P.A.C., Ridgway, C.J., and Mathews, G.P. *Influence of inertia on liquid absorption into paper coating structures*. Paper and Coating Chemistry Symposium. 2000. Stockholm, Sweden: Tappi Press.
80. Ridgway, C.J. and Gane, P.A.C. *Correlating Pore Size and Surface Chemistry During Absorption into Dispersed Pigmented Network Structures*. 6th International Paper and Coating Chemistry Symposium. 2006. Stockholm, Sweden: Tappi Press.
81. Schoelkopf, J., Gane, P.A.C., and Ridgway, C.J., *A comparison of the various liquid interaction radii derived from experimental and network modelling of porous pigmented structures*. Colloids and Surfaces A: Physiochem. and Eng. Asp. , 2004. **251**(1-3): p. 149-159.
82. Gane, P.A.C., *Re: Theoretical fluid movement*, Outlook, Editor. 2006: Oftrigen. p. Answer to a previous email about fluid movement into a porous structure.

83. Eggli, P., *Angle de raccordement et énergie de surface: introduction*, L. Sàrl, Editor. 2008, aboratoire de REcherche et de Chimie de Bienne: Bienne. p. 6.
84. Darcy, H., *Les Fontaines Publiques de la Ville de Dijon*. 1856, Département des Ponts et Chaussées: Dijon, France. p. 8 pages.
85. Inconnu, *Écoulement d'un fluide dans un lit de particules; Relation entre écoulement et pertes de charge*. n/a. p. 26.
86. Tripathi, P., Joyce, M., and Fleming, P., *New curtain coater thechnology offers benifits for barrier-coated grades*. Solutions, 2006(7): p. 18-22.
87. Urgelli, B. *A quoi correspond l'unité de mesure " Darcy "*. [internet] 2000 [cited 2000 23 mars].
88. Carman, P.C., *Fluid flow through a granular bed*. Transactions of the Institution of Chemical Engineers, 1937. **15**: p. 150-167.
89. Washburn, E.W., *Method of determining the distribution of pore sizes in a Porous Materialsthe dynamics of capillary flow*. Physical Review, 1921. **17**(3): p. 273-283.
90. Ritter, H.L. and Drake, L.C., *Pore Size Distribution in Porous Materials*. Ind. Eng.Chem., 1945(17): p. 782-786.
91. Unknown, *Mercury porosimetry*. 1996, University of Stuuuttgart.
92. Larrondo, L., St-Amour, S., and Monasterios, C. *Porous Structure of Paper Coatings-Comparison of Mercury Porosimetry and Stain-Inhibition Methods of Measurement*. 1995 Coating Conference. 1995. Dallas, Texas: Tappi Press.
93. Yamasaki, H. and Munakata. *Liquid Absorption Model. Products of Papermaking*. 1993. England: Baker, C.F. Ed.
94. Ridgway, C.J. and Gane, P.A.C. *Bulk density measurement and coating porosity calculation for coated paper samples*. 2007 Coating and Graphic Arts Conference. 2007. Miami: TAPPI Press.
95. Gane, P.A.C., Kettle, J.P., Mathews, G.P., and Ridgway, C.J., *Void Space Structure of Compressible Polymers Sphere and Consolidated Calcium Carbonate Paper Coatings Formulations*. Industrial and Engineering Chemistry Research, 1996. **3**(5): p. 1753.
96. Ridgway, C., *RE: Mercury intrusion testing*. 2009, Omya: Oftrigen, Switzerland.
97. *Micromeritics Instrument Corporation*, <http://www.micromeritics.com/library/Application-Notes.aspx>.
98. *Owner Manual, in AutoPore IV 9500*. Operator's Manual V1.01, ed. E. M.I. Corporation: Georgia, USA.
99. Unknown, *Lab Test Method - DELTAC*, Omya, Editor. 2007: Oftrigen, Switzerland. p. 2.

100. Ström, G. *Interaction between offset ink and coated paper - a review of the present understanding. 13th Fundamental Research Symposium*. Cambridge, UK.
101. Rousu, S., Lindström, M., Gane, P.A.C., Pfau, A., Schädler, V., and Eklund, D. *Influence of latex - Oil Interactions on Offset Ink Setting and Component Distribution on Coated Paper. 2002 International Printing and Graphic Arts Conference*. 2002. Bordeaux, France.
102. De Jong, R., *Latex Technologies - Lattices Emulsions polymers*, BASF, Editor. 2008: Charlotte, North Carolina.
103. *Centre International de Couchage, www.coatercic.com, Pilot Coater Facility, Tool Coater, Production of Speciality papers*.
104. De Grace, J.H. and Mangin, P.J., *A mechanistic approach to ink transfer, Part I: Effect of substrate properties and press conditions*. , in *Advanced in Printing Science and Technology*. 1984. p. 312.
105. De Grace, J.H. and Mangin, P.J., *A mechanistic approach to ink transfer, Part II: The splitting behaviour of ink in printing nips*. , in *Advanced in Printing Science and technology*. 1987. p. 146.
106. Dubé, M., Drolet, F., Daneault, C., and Mangin, P.J., *Hydrodynamics of Ink Transfer*. Journal of Pulp and Paper Science, 2008. **34**(3): p. 14.
107. Rousu, S., Lindström, M., Gane, P.A.C., Pfau, A., Schädler, V., Wirth, T., and Eklund, D. *Influence of latex: Oil interactions on offset ink setting and component distribution on coated Paper. 11th International Printing and Graphic Arts Conference*. 2002. Bordeaux, France.
108. Rousu, S., Gane, P.A.C., and Eklund, D. *Influence of coating pigment chemistry and morphology on the chromatographic separation of offset ink constituent. 12th Fundamental Research Symposium*. 2001. Oxford.
109. Van Gilder, R.L. and Purfeest, R.D., *Commercial six-color press runnability and the rate of ink build as related to the latex polymer solubility parameter*. Tappi Journal, 1994. **77**(5): p. 230.
110. Xiang, Y., Bousfield, D.W., Hayes, P.C., and Kettle, J., *A Model to Predict Ink Setting Rates Base in Pore Size Distribution*. Journal of Pulp and Paper Science, 2004. **30**(5): p. 13.
111. Hayes, P.C., Bousfield, D.W., Kettle, J., Yang, X., and Hultgren, L., *Effect on latex swelling on ink setting on coated paper*. Journal of Graphic Technology, 2003. **1**(1): p. 117.
112. Hayes, P.C., Bousfield, D.W., Kettle, J., Yang, X., and Hultgren, L. *Effect on Latex Selling on Ink Tack Build-up and Ink Gloss Dynamics. 2000 International Printing and Graphics Arts Conference*. 2000: TAPPI Press.
113. Vyörykkä, J., *Latex -Chemistry and Use in Paper Coating, Pigment Coating Chemistry Course*. 2007, Åbo Akademi University.

114. Forbes, F. and Ave'Lallemant, T.R., *Modelling the Effects of Styrene-Butadiene-Acrylonitrile Copolymer Latex on Printing Properties of Coated Woodfree Papers*.
115. Lawrenz, D. *International Customer Seminar Paper Coating Technology*. 2006. Ludwigshafen, Germany
116. Wold, S., Eriksson, L., Trygg, J., and Kettaneh, N. *The PLS method -- partial least square projection to latent structures and its applications in industrial RDP (research, development and production)*. COMPSTAT 2004, 16th Symposium of IASC. 2004. Prague, Tchech Republik.
117. Eriksson, L., Johansson, E., Kettaneh-Wold, S., Trygg, J., Wikström, C., and Wold, S., *Multi- and Megavariate Data Analysis Part I: Basic Principles and Applications, Second revised and enlarged edition* Umetrics, ed. U. Academy. 2001, Kinnelon, New Jersey. 425.
118. Jöreskog, K.G. and Wold, H., *System under indirect observation, Volume I and II - Soft modeling. The basic design and some extensions in volume II*, ed. s. Vol. II. 1982, North Amsterdam.
119. Wold, S., Sjöström, M., and Eriksson, L., *PLS Regression - A basic tool of chemometrics*. Chemometrics and Intelligent Laboratory Systems, 2001. **58**(2): p. 109-130.
120. Webb, P.A., *An Introduction To The Physical Characterization of Materials by Mercury Intrusion Porosimetry with Emphasis On Reduction And Presentation of Experimental Data*. 2001, Micromeritics: Norcross, Georgia.
121. Webb, P.A. and Orr, C., *Analatical Method in Fine Particle Technology*, ed. Micromeritics. 1997, Norcross, Georgia.
122. Tenenhaus, M., *La régression PLS: Théorie et Pratique*, ed. Technip. 1998, Paris. 274.
123. Höskuldsson, A., *Prediction Methods in Science and Technology. Vol. 1. Basic Theory*, ed. T. Publishing. 1996, København. 404.

Appendix

Appendix 1 Mercury Intrusion Test Procedure by Micromeritics and calculating values description

“The sample cup has a capillary stem attached and this capillary serves both as the mercury reservoir during analysis and as an element of the mercury volume transducer. Prior to the beginning of each analysis, the sample cup and capillary are filled with mercury. After filling, the main source of mercury is removed leaving only the mercury in the sample cup and capillary stem the combination being referred to as the penetrometer. Pressure is applied to the mercury in the capillary either by a gas (air) or a liquid (oil). The pressure is transmitted from the far end of the capillary to the mercury surrounding the sample in the sample cup. The capillary stem is constructed of glass (an electrical insulator), is filled with mercury (an electrical conductor), and the outer surface of the capillary stem is plated with metal (an electrical conductor). The combination of two concentric electrical conductors separated by an insulator produces a co-axial capacitor. The value of the capacitance is a function of the areas of the conductors, the dielectric constant of the insulator, and other physical parameters. In the case of this particular capacitor, the only variable is the area of the interior conductor as mercury leaves the capillary and enters the sample voids and pores, or as it moves back into the capillary when pressure is reduced. This is mechanically analogous to a mercury thermometer in which case mercury moves in and out of a calibrated capillary from a large bulb at one end. A small volume of mercury entering or leaving a small capillary causes the length (and area) of the mercury column to change significantly, thus providing volume-measuring sensitivity and resolution. In the case of the thermometer, the change in volume is proportional to the change in temperature by the coefficient of volumetric expansion of mercury. The capacitance value of the stem is monitored by a capacitance detector that, similar to the pressure transducer electronics, produces an electrical signal that is proportional to capacitance. Capacitance measurements are transformed into volume measurements by knowledge of the diameter of the precision capillary and the equation governing coaxial capacitors [120]”.

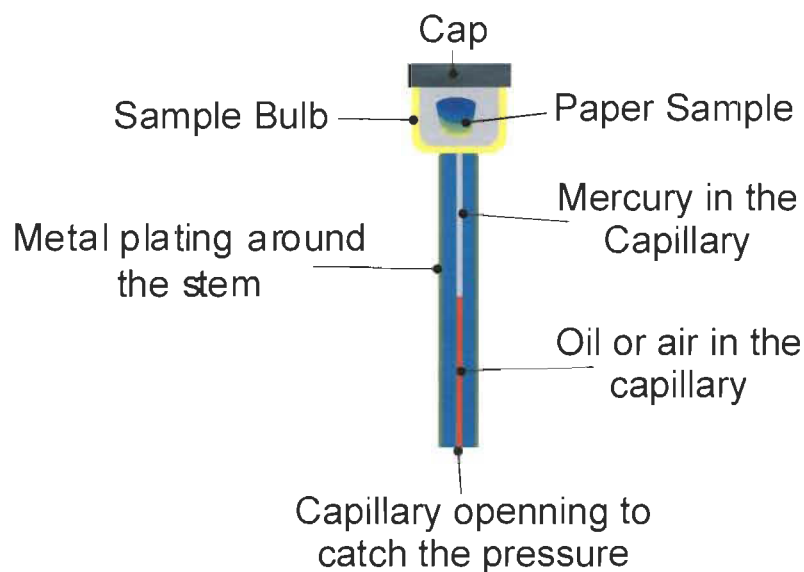


Figure 6-1 Sample bulb and stem – cross section showing the different parts



Figure 6-2 Bulb mounted for low pressure testing and fill with mercury

The test generates many values calculated by the equipment program. The values are calculated considering the weight of the sample. The values obtained by the Micromeritics program are [120, 121]:

1. **Total intrusion volume in mL/g** which is the maximum volume of mercury intrusion (penetration) into the pores for the sample at the indicated pressure.

2. **Skeletal Density in g/cm³** which is the mass of the sample divided by the sum of the volumes of the solid material in the sample and the volume of pores within the sample.
3. **Porosity in %** which is the percentage of pores in the sample or total intrusion divided by the total intrusion + 1/skeletal density x 100
4. **Total Pore area in m²/g** which is the area of the pore walls based on the assumption of cylindrical geometry and summed over the complete pressure range of mercury intrusion.
5. **Median Pore Diameter volume in μm** which is the pore diameter at which equal quantities of pore volume occur at both large and small diameters.
6. **Median Pore Diameter Area in μm** which is the pore diameter at which equal quantities of pore wall area occurs at larger and smaller diameters
7. **Average Pore Diameter – 4V/A in μm** which is based upon the assumption that all pores are right circular cylinders. When the pore volume ($V = \pi d^2 l / 4$) is divided by the pore area ($A = \pi dl$), the pore diameter (d) is $4 V/A$.

To simplify the analysis, the original Autopore data file is imported into an Excel file, regrouping the results in a single table that allow the plotting of required intrusion curves.

Appendix 2 DELTACK Curves

DELTACK Curves for 20 parts clay substitution (Group 1)

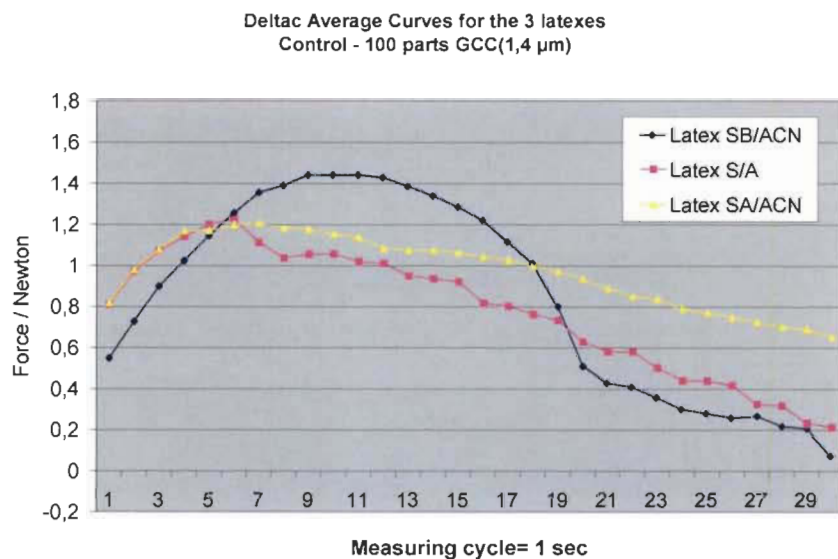


Figure 6-3 DELTACK Average Curves for S/B/ACN latex, S/A latex and S/A/ACN, 100 parts GCC (1.4 μ m)

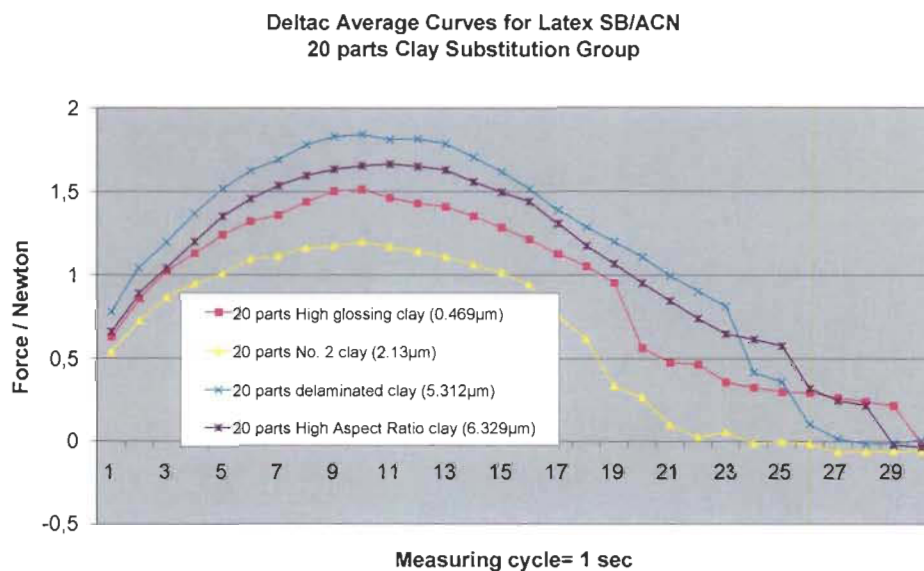


Figure 6-4 DELTACK – 20% clay substitution Group, S/B/ACN latex

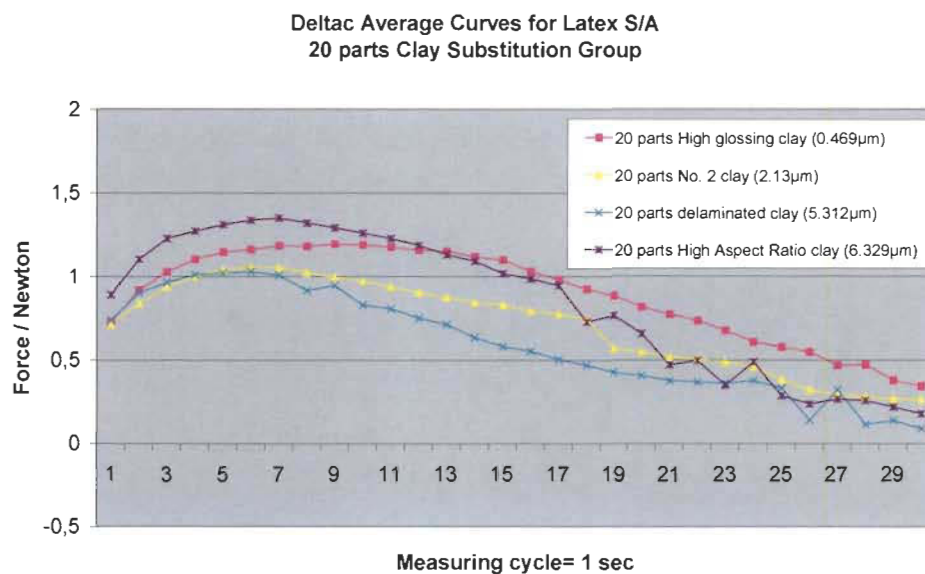


Figure 6-5 DELTACK – 20% clay substitution Group, S/A latex

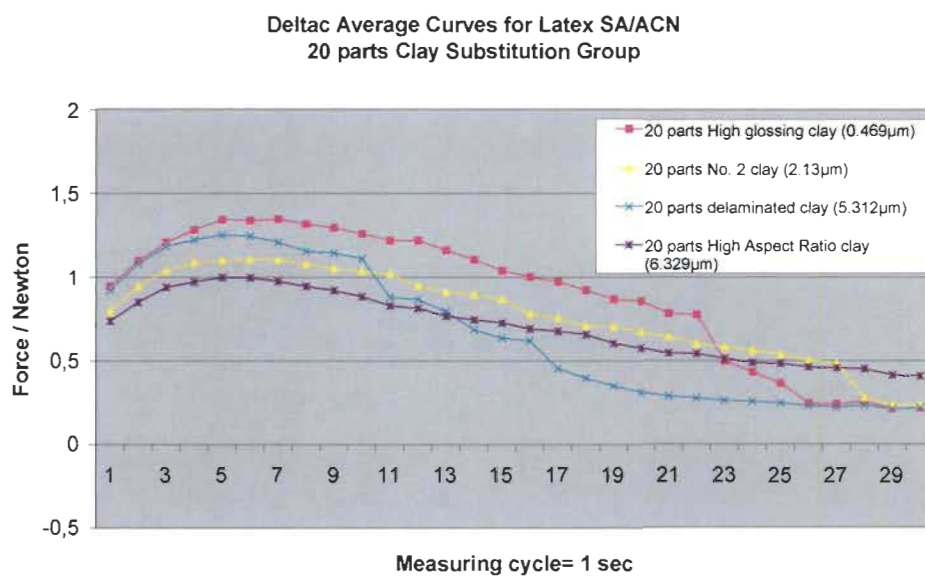


Figure 6-6 DELTACK – 20% clay substitution Group, S/A/ACN latex

DELTACK Curves for Base Paper and Precoat Calendered (Group 2)

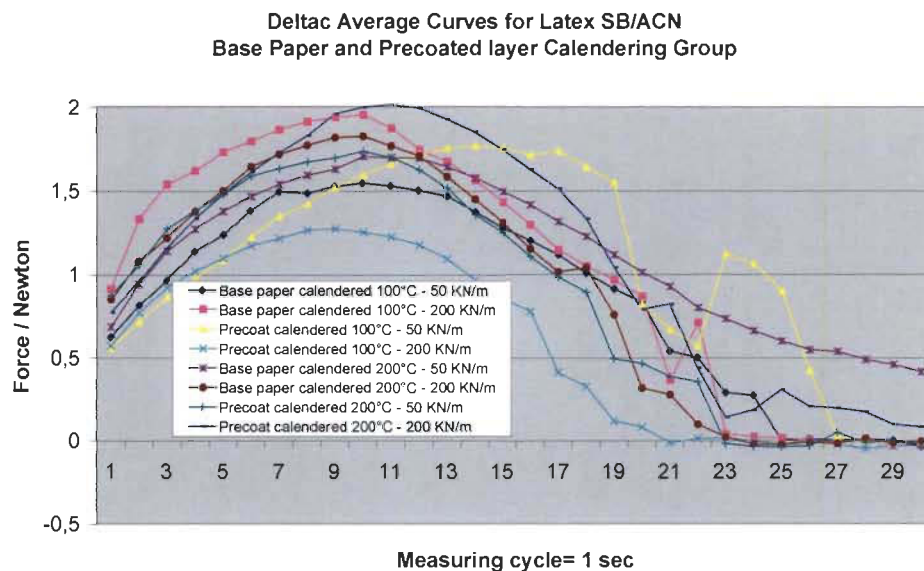


Figure 6-7 DELTACK – Base Paper and Precoated layer Calendering Group, S/B/ACN latex

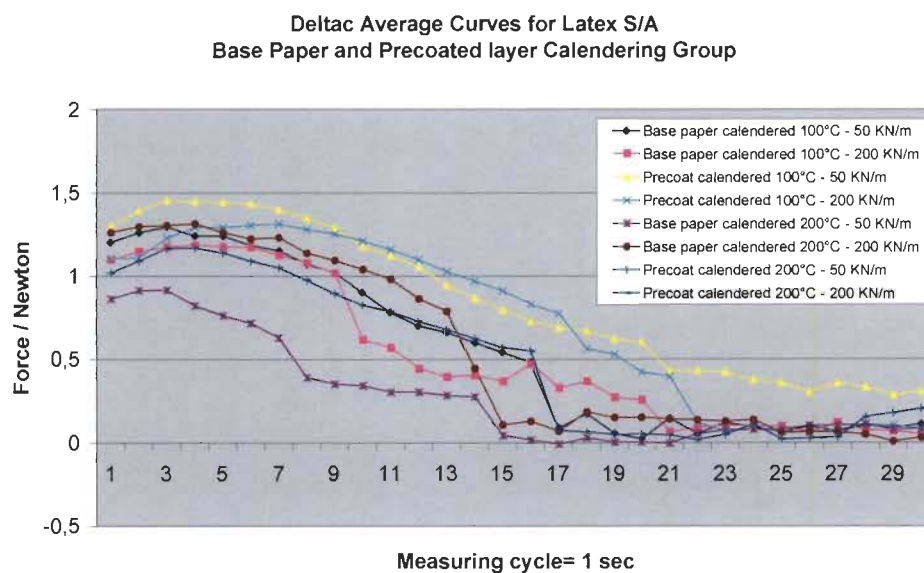


Figure 6-8 DELTACK – Base Paper and Precoated layer Calendering Group, S/A latex

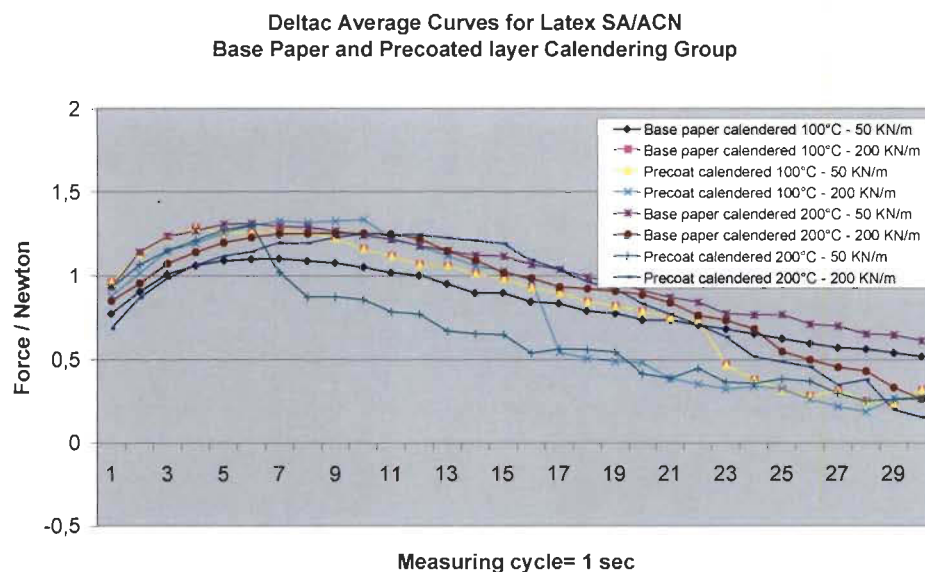


Figure 6-9 DELTACK – Base Paper and Precoated layer Calendering Group, S/A/ACN latex

DELTACK Curves for S/A precoat latex and Thickener substitution (Group 3)

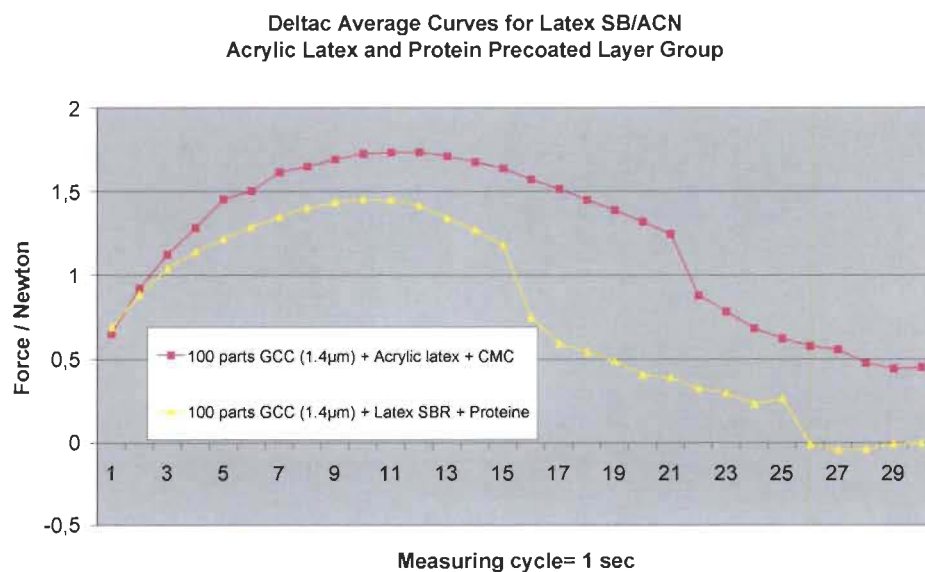


Figure 6-10 DELTACK – S/A Precoating layer and protein Group, latex, S/B/ACN

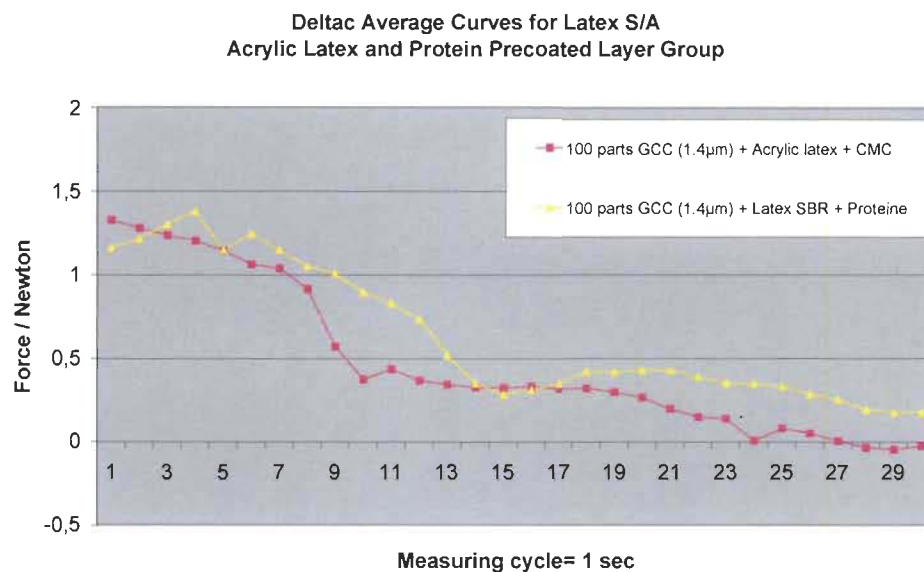


Figure 6-11 DELTACK – S/A Precoating layer and protein Group, S/A latex

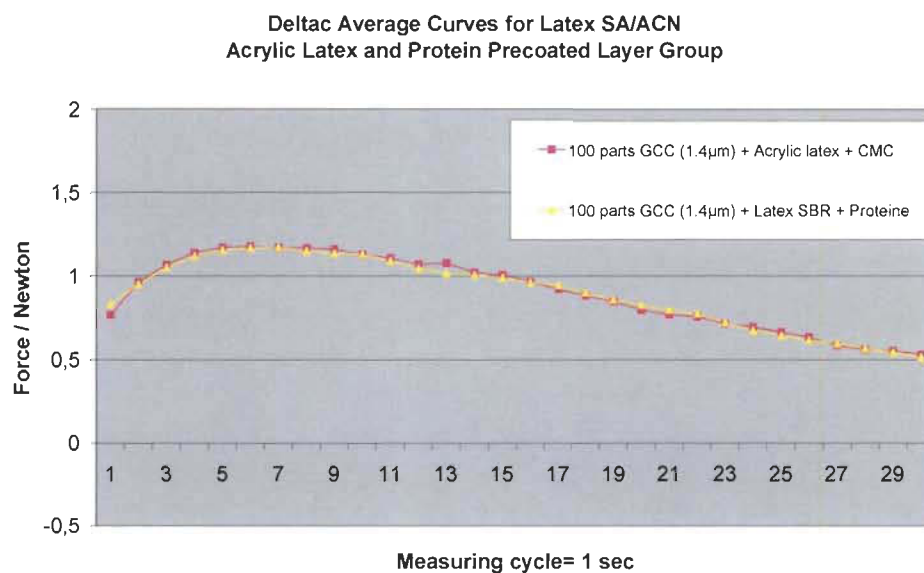


Figure 6-12 DELTACK – S/A Precoating layer and protein Group, latex, S/A/ACN latex

DELTACK Curves for 100 parts pigment substitution (Group 4)

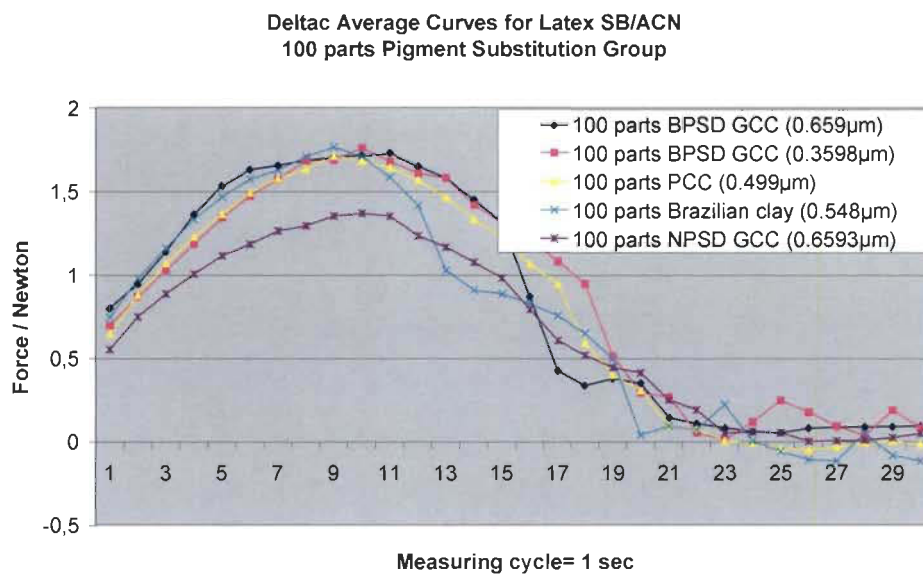


Figure 6-13 DELTACK – 100% Pigment substitution Group, latex, S/B/ACN

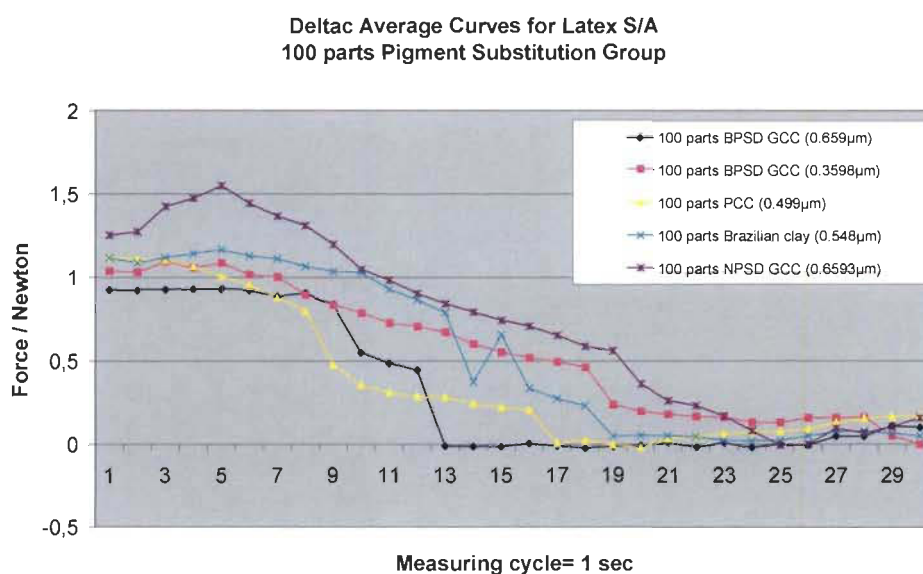


Figure 6-14 DELTACK – 100% Pigment substitution Group, S/A latex

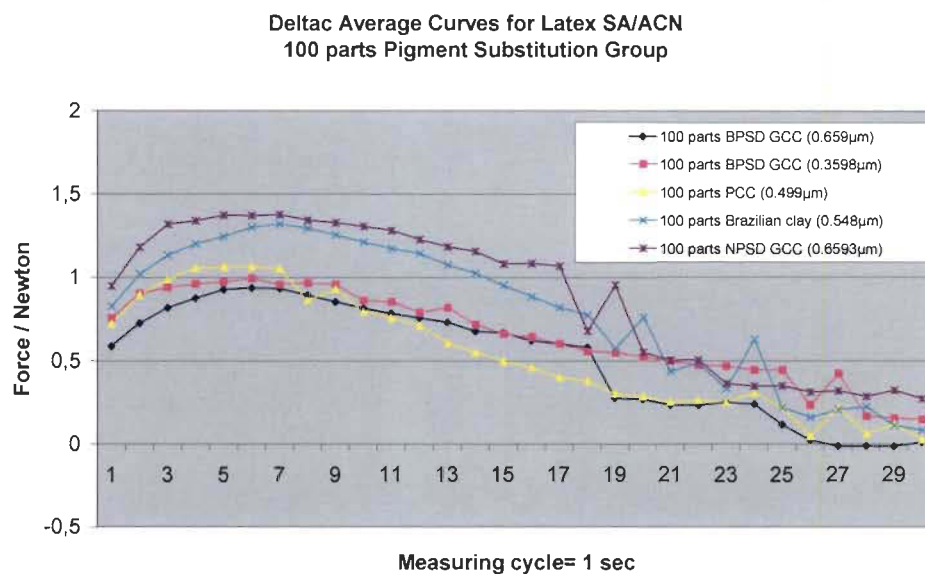


Figure 6-15 DELTACK – 100% Pigment substitution Group, S/A/ACN latex

Appendix 3 Projection on Latent structure (PLS)

Definition of projection on latent structure

Partial least squares regression (PLS-regression) is a statistical method that bears some relation to principal components regression; instead of finding hyper planes of maximum variance between the response and independent variables, it finds a linear model by projecting the predicted variables and the observable variables to a new space. Because both the X and Y data are projected to new spaces, the PLS family of methods are known as bilinear factor models.

It is used to find the fundamental relations between two matrices (X and Y), i.e. a latent variable approach to modeling the covariance structures in these two spaces. A PLS model will try to find the multidimensional direction in the X space that explains the maximum multidimensional variance direction in the Y space. PLS-regression is particularly suited when the matrix of predictors has more variables than observations, and when there is multicollinearity among X values. By contrast, standard regression will fail in these cases.

PLS-regression is an important step in PLS path modeling, a multivariate data analysis technique that employs latent variables. This technique is often referred to as a form of variance-based or component-based structural equation modeling [122].

Theory of the analysis (PLS)

Projection on latent structure (PLS-regression) or partial least squares regression (PLS-regression) is a statistical method that bears some relation to principal components regression; instead of finding hyper planes of maximum variance between the response and independent variables, it finds a linear model by projecting the predicted variables and the observable variables to a new space (Figure 5-60). Because both the X and Y data are projected to new spaces, the PLS family of methods are known as bilinear factor models [117, 119, 122, 123]. The basic equation of the multiple regression model is given by the equation 6-1:

$$Y = b_0 + b_1 X_1 + b_2 X_2 + \dots + b_p X_p \quad \text{Equation 6-1}$$

The PLS-regression is an extension of the multiple regression model. The standard model for a single block is shown in equation 6-2 and 6-3 [123].

$$[X]_N^K = [T]_N^A * [P]_A^K + [E]_N^K \quad \text{Equation 6-2}$$

$$[Y]_N^M = [U]_N^A * [C]_A^M + [F]_N^M \quad \text{Equation 6-3}$$

X is the matrix of N trials where K variables are analysed. Matrix T contains the location of each observation respecting the new system of A latent vectors. The matrix P describes the rotation of latent vectors found by the analysis and respecting the original system. Finally, the residual from the least square fit are in the matrix E. Exactly the same development is done for the variables Y and the matrix are identified U, C and F.

The PLS regression is the analysis of 2 blocks at the same time. A set of K predictor from variables X are compared with a set of M response from variables Y. The latent vector Y is obtained in the same way as X and is shown in equation 6-2 and 6-3 [123].

Equation 6-2 and 6-3 are in relation each other. The objective of the PLS is to use these equations to predict Y from X. Each block are not calculated independently, and the information are exchanged between the 2 blocks to reduce the deviation from the regression line and is described by equation 6-4

$$u_{n,a} = b_a t_{n,a} + h_{n,a} \quad \text{Equation 6-4}$$

Where u is the reduce vector representing X and Y, b the correlation factor between both matrix and finally h, the matrix of the residual data or error.

All these concepts are shown in Figure 6-16 [123]127].

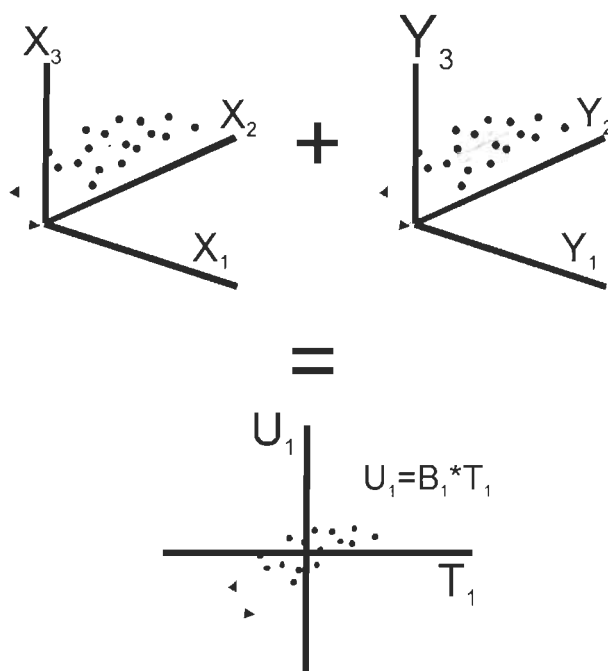


Figure 6-16 Correlation using equation 6-2 and 6-3 and showing correlating latent factor

Projection on latent Structure (partial Least Square) Analysis

In addition to all the analysis done with graphics and tables, a PLS study was performed to verify if the facts and conclusions found are significant and accurate. The PLS study was done with the program SIMCA-P version 11. In statistic analysis, X and Y variables are defined like dependant and independent, accordingly. The PLS analysis refer to input and output variables. The variables X are normally the variables that can be manipulated and the variable Y defined like the answers to the variables X.